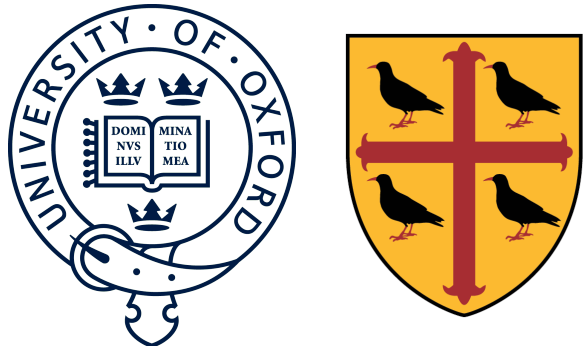


Supernova Neutrinos and Measurement of Liquid Scintillator Backgrounds in SNO+



Jia-Shian Wang
St Edmund Hall
University of Oxford

A thesis submitted for the degree of
Doctor of Philosophy

Hillary 2022

Abstract

Core collapse supernovae (CCSNe) are amongst the most powerful cosmic sources of neutrinos. The extreme environment during the supernova evolution provides opportunities to probe neutrino properties which are not accessible on Earth. In this thesis, the response to supernova neutrinos of the SNO+ experiment is explored as a representative case of neutrino detectors.

SNO+, the successor of the Sudbury Neutrino Observatory (SNO), is a 780-tonne liquid scintillator detector located 2 km underground in Sudbury, Canada. The primary purpose of SNO+ is to detect the neutrinoless double beta ($0\nu\beta\beta$) in ^{130}Te . During the time period covered by this thesis, SNO+ has undergone the transition from water phase to scintillator phase. By performing a bismuth-polonium (BiPo) coincidence study throughout the period, the ^{238}U and ^{232}Th chain, which are important backgrounds to $0\nu\beta\beta$, concentrations in the scintillator have been measured to be $(4.6 \pm 1.2) \times 10^{-17}$ g/g and $(4.8 \pm 0.9) \times 10^{-17}$ g/g, respectively. With the measured radioactive background level and calibrated light yield level, a supernova burst trigger was developed. The study showed that SNO+ has the potential of detecting CCSNe at 100 kpc.

The experience with the coincidence study was also found to be useful in the identification of inverse beta decay (IBD) signals, which is an important supernova neutrino signal common amongst different detectors. One application of this shared neutrino signal is the positioning of supernovae via multi-detector triangulation, which can serve as an alert to other channels of detection. This thesis presents a method using the comparison of light curves to determine the signal arrival time difference between pairs of detectors. The results outperformed existing methods by further reducing the uncertainty by about 30%.

Finally, it was noticed during the triangulation study that the formation of black holes could potentially introduce additional resolution power. Previous studies on the black hole cut-off mostly focused on radial neutrino emissions. To investigate the effect of the black hole, a ray-trace study was performed to give a comprehensive account of the effects of including emissions from all angles upon black hole formation. Both the cases of non-rotating and rotating black holes were discussed. It was discovered that the non-radial emissions contribute a softening to the profile in both cases. Furthermore, extreme rotation introduces significant changes to the tail of the profile, which may be observable with next-generation neutrino detectors.

For my parents

夙
興
夜
寐

無
忝
爾
所
生

Acknowledgements

First, I would like to thank my supervisor, Jeff Tseng, for his guidance, encouragement and all he has taught me. The enlightening conversations often helped me to view things from different angles and helped me through many difficulties along the way. Without his invaluable support and grammar checks, I would not have been able to finish this thesis. It has been a pleasure to work as his student. I would also like to thank Steve Biller and Armin Reichold for their brilliant ideas and suggestions during meetings or whenever I go to them, and making the SNO+ group such a comfortable and friendly place. Also, special thanks to Ed Leming and Valentina Lozza, for their time dealing with the random issues I had and helping me to get started during my first few years.

I would say that I was particularly lucky to have shared the SNO+ office with Jeff Lidgard, Esther Turner, Tereza Kroupová, Iwan Morton-Blake and Josie Paton, who have become great friends of mine during the past years. I really enjoyed all the time we spent together, the office chats and discussions, the drinks and meals, and so on. Thank you for making the whole process so cheerful and pleasant. I am really glad to have your company.

The SNO+ Collaboration is the most friendly collaboration I have ever worked with, and I would like to thank the amazing people from the collaboration for providing all the help and discussions during my studies. In particular, thanks to the members of the supernova working group, who have always made me feel like living in a small village where people took care of each other. I am also appreciative to all the staffs in the sub-department of Particle Physics in Oxford and Teddy Hall for taking such good care of me. On this score, a huge thank you to Sue Geddes and Kim Proudfoot who sorted out all sorts of troubles over the years and got me through in one piece. Additionally, I would like to thank my flatmates and friends in Oxford for always being there for me. Speaking of flatmates, special thanks to Michal Rigan and Iwan for making the freezing mornings of Sudbury so much more bearable and even enjoyable.

Finally and most importantly, I would like to thank my parents for their guidance, teachings and support. Your unconditional support for whatever I decided to do meant everything to me and it is what has been keeping me going. I owe you everything.

Contents

List of Figures	vi
List of Tables	x
1 Introduction	1
2 Neutrino Physics	3
2.1 Neutrino Oscillation	4
2.1.1 Neutrino Mixing	5
2.1.2 Neutrino Oscillation in Vacuum	6
2.1.3 Neutrino Oscillation in Matter	9
2.2 Neutrino Mass	15
2.2.1 Standard Model Neutrino	15
2.2.2 Dirac Neutrino	16
2.2.3 Majorana Neutrino	17
2.3 Neutrinoless Double Beta Decay	20
3 Core-Collapse Supernovae	25
3.1 Stellar Evolution	26
3.2 Supernova Classification	30
3.3 Core-Collapse Mechanisms	33
3.3.1 Iron Core Disintegration	33
3.3.2 Electron Capture Instability	40
3.3.3 Pulsational Pair Instability	40
3.3.4 Photodisintegration	41
3.4 Galactic Supernova	42
3.5 Supernova Neutrino Spectrum	43
3.5.1 Supernova Simulations by the Garching Group	43
3.5.2 Supernova Neutrino Energy Spectrum	44

4 The SNO+ Detector	47
4.1 Detector Hardware	47
4.2 Phases of SNO+	49
4.2.1 Water Phase	49
4.2.2 Pure-Scintillator Phase	49
4.2.3 Tellurium-Loaded Phase	51
4.3 Detector Electronics and Data Processing	54
4.3.1 Photomultiplier Tubes	54
4.3.2 Electronics and Trigger System	54
4.3.3 Event Data Flow	58
4.4 Full Reconstruction	60
4.4.1 Position and Time Reconstructions	60
4.4.2 Energy Reconstruction	61
4.5 Data Analysis and Simulation — RAT	61
5 Measurement of Internal Backgrounds in Liquid Scintillator	62
5.1 ^{238}U and ^{232}Th Decay Chains	62
5.2 Scintillator Fill in SNO+	66
5.3 Bismuth-Polonium Coincidence Tagging	67
5.3.1 Fiducial Volume Cut	67
5.3.2 Nhit Cut	69
5.3.3 Position Difference (Δr) Cut	72
5.3.4 Time Difference (Δt) Cut	74
5.3.5 Tagging Efficiency	75
5.3.6 Misidentification	75
5.4 Measurement of ^{238}U and ^{232}Th	79
5.4.1 Radon Ingress	79
5.5 ^{214}Bi - ^{214}Po Pairs as a Calibration Source	82
5.5.1 Light Yield Verification	82
5.5.2 PPO Mixing	84
5.6 Summary	87
6 Fast Reconstruction	88
6.1 FastZ — Position Reconstruction for Partial Fill	88
6.1.1 Light Path Calculation	89
6.1.2 Performance	92
6.2 TimeCentroid — Spatial Coincidence Identification	93
6.2.1 Topological Similarity in PMT Hit Distributions	93
6.2.2 Weighted Coincidence Classifier	93
6.2.3 Quad with Reduced Iterations	101

6.2.4	Applications	102
6.3	Summary	102
7	Supernova Signal Detection	103
7.1	Supernova Interaction Channels in Liquid Scintillator	104
7.1.1	Inverse Beta Decay	104
7.1.2	Neutrino-Electron Elastic Scattering	106
7.1.3	Neutrino-Proton Elastic Scattering	108
7.1.4	Neutrino-Nucleus Interaction	109
7.2	Multi-Threshold Supernova Burst Trigger	111
7.2.1	Original SNO Burst Trigger	112
7.2.2	SNO+ Burst Trigger	113
7.2.3	Burst Trigger Thresholds	114
7.3	Multi-Detector Supernova Pointing	118
7.3.1	SNEWS Network	118
7.3.2	Multi-Detector Positioning	120
7.3.3	Time Difference Determination	120
7.3.4	Supernova Signal Simulation	123
7.3.5	Result	125
7.4	Summary	129
8	Black Hole Formation in Core-Collapse Supernova	130
8.1	Neutrino Emission upon Black Hole Formation	131
8.2	Non-Rotating Black Hole: the Schwarzschild Geometry	132
8.2.1	The Geodesic Equation	133
8.2.2	Neutrino Travel Time	136
8.2.3	Redshift	140
8.2.4	Ray Tracing and Luminosity Profile	142
8.2.5	Emitters Not in Free-Fall	145
8.3	Rotating Black Hole: the Kerr Geometry	148
8.3.1	The Geodesic Equation	149
8.3.2	Neutrino Travel Time	154
8.3.3	Redshift	160
8.3.4	Ray Tracing and Luminosity Profile	163
8.4	Measurement of the Black Hole Cut-Off	164
8.5	Summary	165
9	Conclusion	167
References		169

List of Figures

2.1	Feynman diagrams for ν coherent forward scattering	10
2.2	Evolution of the effective mixing angle θ_M plotted against the electron density n_e	13
2.3	Beta and double beta transitions for even mass number nuclei	20
2.4	Feynman diagrams for $2\nu\beta\beta$ and $0\nu\beta\beta$	21
2.5	Feynman diagram of $0\nu\beta\beta$ for illustration of the black-box theorem .	22
2.6	Nuclear matrix element $\mathcal{M}_{0\nu\beta\beta}$ values	24
3.1	Hertzsprung-Russell diagram of the stars catalogued by the Hipparcos satellite	27
3.2	Schematic representation of AGB stars	28
3.3	Schematic view of the layered stellar structure	30
3.4	Supernova classification scheme	31
3.5	Types of supernovae according to progenitor properties	34
3.6	Stellar core evolution stages with respect to central temperature T_c and central density ρ_c	35
3.7	Schematic view of the neutrino transport in CCSN	37
3.8	Neutrino luminosity evolution of a $15M_\odot$ progenitor	38
3.9	Galactic supernova probability distribution as a function of distance .	42
3.10	Spectrum pinching versus degeneracy parameter η and shape parameter β	45
4.1	Schematic view of the SNO+ detector	48
4.2	Photo of SNO+ taken on the 26th of March, 2021	50
4.3	Sensitivity of $0\nu\beta\beta$ half-life in SNO+	51
4.4	Effective Majorana mass ($m_{\beta\beta}$) measurement in SNO+	52
4.5	Stack plot of event counts for $0\nu\beta\beta$ in SNO+	53
4.6	Structure of Hamamatsu R1408 PMT	55
4.7	Sketch of SNO+ trigger system	56
4.8	Timing of the SNO+ trigger system	57

4.9	Schematic illustration of the digitised PMT hit information	58
4.10	Flow of the SNO+ data acquisition system	59
5.1	^{238}U decay chain	63
5.2	^{232}Th decay chain	64
5.3	Scintillator fill schedule of SNO+	66
5.4	Decay schemes for ^{212}Bi and ^{214}Bi	67
5.5	Scheme of the BiPo coincidence analysis	68
5.6	MC simulated Nhit spectrum of BiPo214, BiPo212 and BiPo210	70
5.7	Δr distribution of the MC simulated BiPo214 and BiPo212	72
5.8	Δr distributions of the toy model and the MC simulations	73
5.9	BiPo214 Δt fit using data from May 2021	77
5.10	BiPo212 Δt fit using data from May 2021	78
5.11	Tagged number of BiPo214 coincidences from the 11th of February to 11th of April, 2020	80
5.12	Tagged number of BiPo212 coincidences from the 18th of April to 4th of May, 2021	80
5.13	Nhit comparison of ^{214}Bi between data and MC	83
5.14	Nhit comparison of ^{214}Po between data and MC	84
5.15	Nhit distribution and the Nhit distribution plotted against the Z axis of the tagged ^{214}Po from the 16th to 18th of December, 2019	85
5.16	Nhit distribution and the Nhit distribution plotted against the Z axis of the tagged ^{214}Po on the 19th of June, 2021	86
6.1	Light path difference between top and bottom PMTs	89
6.2	The photon angular distribution and emission time of a tagged ^{214}Bi from the 23rd of March, 2021	90
6.3	Fitted resolution and bias of <code>FastZ</code> applied on 2.5 MeV electrons in partial fill with $Z = +4400$ mm	91
6.4	Scintillation photon distribution of a coincidence event	94
6.5	PMT position versus hit time distribution for an example MC BiPo214 pair	95
6.6	PMT position versus hit time distribution for an example BiPo214 pair tagged on the 2nd of April, 2020	96
6.7	ROC curves of <code>TimeCentroid</code> in full-scintillator configuration	98
6.8	ROC curves of <code>TimeCentroid</code> in partial-fill configuration	98
6.9	ROC curves of <code>scintFitter</code> , <code>partialFitter</code> and <code>TimeCentroid</code>	99
6.10	ROC curves of <code>Quad</code> with different number of iterations	101
7.1	Feynman diagrams for νEES	106

7.2	Sensitivity of the original SNO supernova burst trigger	112
7.3	Structure of the SNO+ burst trigger time windows	113
7.4	Sensitivity of the burst trigger in partial-fill phase	115
7.5	Sensitivity of the burst trigger in full-scintillator phase	116
7.6	Schematic representation of multi-detector triangulation	120
7.7	Sketch of light curve matching	121
7.8	Expected IBD event time distribution	123
7.9	IBD event distributions of an average trial for the ls220-s27.0co model at distance 10 kpc	125
7.10	The η distribution per time bin at each $\widehat{\Delta t}$ step for an averaged trial based on the model ls220-s27.0co at 10 kpc	126
7.11	The η distribution per time bin at each $\widehat{\Delta t}$ step for an averaged trial based on the model ls220-s40s7b2c-bh at 10 kpc	128
8.1	Inward and outward trajectories for neutrinos emitted outside the photon sphere	137
8.2	Schematic view of the escape cones	138
8.3	Behaviour of $r^3 - b^2(r - 2M) = 0$ at different b values	139
8.4	Time delays as a function of the emission angle in the free-fall frame	140
8.5	Redshift factor and the fitted decay parameter for outward radial emissions ($b = 0$) and critical emissions ($b = b_c \equiv 3\sqrt{3}M$)	141
8.6	Comparison of cut-off profiles for non-radial and radial emissions	143
8.7	The decay parameter for critical emissions ($b = b_c$) and full emissions	144
8.8	Comparison of three different inward emission scenarios in the non-rotating case	145
8.9	Luminosity and decay parameter profiles for free-fall ($f = 1$) and reduced ($f = 1/4$) shell acceleration	146
8.10	Luminosity and decay parameter profiles for free falling and ρ -shell emitters	147
8.11	Definition of the emission angles ψ and η	153
8.12	Behaviour of $r^3(r^3 - 6Mr^2 + 9Mr^2 - 4Ma^2) + qa^2(r - M)^2 = 0$ with $a = 0.5M$ at different q values	156
8.13	Behaviour of $r^3(r^3 - 6Mr^2 + 9Mr^2 - 4Ma^2) + qa^2(r - M)^2 = 0$ with $a = M$ at different q values	157
8.14	Time delays relative to that of the radial direction for a collapsing ring around a rotating black hole	159
8.15	Example counter-rotating null geodesic emitted close to the event horizon of a rotating black hole	160

LIST OF FIGURES

8.16 Redshift factor and redshift decay parameter of radial emissions for non-rotating ($a = 0$), moderately rotating ($a = 0.5M$) and extremal ($a = M$) Kerr black holes	161
8.17 Redshift factor and redshift decay parameter of critical emissions with $b = 2M$ and $q = 3M^2$ for a $2.5M_\odot$ extremal ($a = M$) Kerr black hole	162
8.18 Luminosity profiles of the neutrino cutoff in Kerr geometry	163
8.19 The three inward emission scenarios in an extreme Kerr black hole	164

List of Tables

2.1	List of naturally occurring candidate isotopes for $0\nu\beta\beta$	23
3.1	List of nuclear fusion channels past hydrogen and helium	29
3.2	List of Garching model light curves	44
5.1	Target purity level of SNO+	65
5.2	Summary on the cuts applied to the BiPo analysis with their respective efficiencies	75
5.3	Measurements on the ^{238}U decay chain concentration	81
5.4	Measurements on the ^{232}Th decay chain concentration	81
6.1	CPU time per event for FastZ and partialFitter	92
6.2	CPU time per event for processing simulated BiPo214 events	100
6.3	CPU time per event for processing simulated BiPo214 events using Quad with different number of iterations	100
7.1	Interaction channels for supernova neutrinos in liquid scintillator . . .	105
7.2	Values of weak coupling constants of neutrinos	108
7.3	Nhit thresholds for burst trigger evaluated in partial-fill phase	114
7.4	Nhit thresholds for burst trigger evaluated in full-scintillator phase .	114
7.5	Neutrino experiments currently connected to SNEWS	119
7.6	Resolutions and biases of the shape comparison method	127
8.1	Null geodesic escape conditions in Kerr geometry of a disc model . .	155

書云 惟克天德 自作元命 配享在下

詩云 維予小子 不聰敬止

曰就月將 學有緝熙于光明

子曰 誠者 天之道也

誠之者 人之道也

Chapter 1

Introduction

This thesis focuses on the features exhibited in the neutrino signals of core-collapse supernovae (CCSNe). Detection of these neutrinos can provide essential information about the evolution of the supernova. Two topics related to the supernova neutrino signal are explored in this thesis: the directional information of the supernova using multiple neutrino detectors and the abrupt termination of the signal associated with the formation of a black hole.

The location of the supernova on the celestial sphere can be inferred by the detection time difference between multiple neutrino detectors, which can be estimated by comparing the features in the detected neutrino time profiles. This provides an accurate and prompt early warning for the optical telescopes, which is one of the major tasks of the upgraded supernova early warning system (SNEWS2.0) [1]. The detection of the supernova neutrinos will be demonstrated with the setup of the SNO+ experiment [2], the successor experiment of the Sudbury neutrino observatory (SNO). SNO+ has been connected to the SNEWS network by the end of 2021.

Amongst the features discussed for the multi-detector pointing, a particularly interesting one is the expected sharp decline in neutrino luminosity when a black hole is formed in the supernova. The large-time-derivative nature of the black hole cut-off could provide strong resolution power in determining the detection time differences. Nonetheless, it will be shown in the work of this thesis that the cut-off turns out to be slightly softer than previous simulations based on radial emissions, and the effect of rotation would further broaden the profile. The measurement of this cut-off could also potentially provide valuable information of the formed black hole and the final stages of the collapse of the stellar progenitor.

The content of the thesis will be arranged as follows: an introduction on the general theoretical aspects of the neutrino is discussed in Chapter 2. Following that, in Chapter 3, the background information regarding stellar evolution, classification of supernovae and the core-collapse mechanism will be introduced.

A description of the setup of the SNO+ detector together with a brief introduction of the goals of the experiment will be given in Chapter 4. As SNO+ is a liquid scintillator experiment, it will be important to study the radioactive backgrounds in the scintillator to estimate the sensitivity to supernova neutrinos. Amongst the backgrounds, the ^{238}U and ^{232}Th decay chains are studied and measured via the identification of the Bismuth-Polonium (BiPo) coincidences, which will be discussed in detail in Chapter 5. This study was carried out through the entire period of transition from water phase to scintillator phase to monitor the background level of the scintillator. It also turned out to be helpful in increasing our understanding on the response of the scintillator. The study in this chapter is internally documented in SNO+ and the results were quoted in various conferences by the collaboration. Though the results are unlikely to appear in the final publications of the collaboration, it is still a crucial intermediate step to establish a thorough understanding of the detector.

Chapter 6 then discusses about two algorithms developed for SNO+ to reconstruct high-level event information from PMT hit data and trigger read-outs in a less time-consuming way. The first is the **FastZ** algorithm designed for rapid position fitting in the transition phase configuration. Then, there is the **TimeCentroid** for tagging spacial coincidences. It is not only useful for the BiPo studies, but also valuable in tagging the inverse beta decay (IBD) signals from supernova neutrinos which requires prompt response. Both of the methods have been incorporated into the SNO+ software.

The detection of supernova neutrino signals will be discussed in Chapter 7. In this chapter, the studies on supernova burst triggers for SNO+ and developments on the multi-detector pointing will be described after a brief introduction on the interaction channels associated to supernova neutrinos. Results presented in this chapter are expected to be included into a later SNO+ publication on supernova detection.

In Chapter 8, a study on the luminosity cut-off associated with black hole formation during a supernova will be presented. The results of this study were published in *Phys. Rev. D* [3]. There are certain overlaps between the content, including text and figures, of the article and this chapter, but both are original works of the author.

Finally, this thesis concludes, in Chapter 9, with a brief summary of the main results from the aforementioned studies.

The original contributions of the author presented in this thesis include: most of Chapters 5 and 7, and all of Chapters 6 and 8. For Chapter 5, Section 5.3 contains content based on the methods developed in [4] together with the improvements designed by the author. In Chapter 7, Section 7.2.2 quotes the SNO+ supernova trigger system designed in [5]. The remaining sections of the chapters are works of the author.

Chapter 2

Neutrino Physics

The idea of the neutrino was initially proposed to salvage the conservation of energy and momentum in nuclear β decay, which exhibits a continuous β energy spectrum yet was hitherto known as a two body decay [6]. In 1930, Pauli postulated an additional weakly interacting neutral fermion participating in the β decay to solve this issue [7]. This idea was further explored by Fermi in 1934 when he described the decay with a four-fermion vertex including the hypothetical neutral fermion to which he assigned the name “neutrino” [8, 9], later known to be the electron anti-neutrino in light of lepton number conservation [10]. Although Fermi’s theory was successful in describing the β energy spectrum, it was not until 1956 when Reines and Cowan first detected reactor electron anti-neutrinos via inverse beta decay that the existence of the neutrino was confirmed [11].

Subsequently, neutrinos of different flavours were discovered. In 1962, the first observation of neutrinos originating from π^\pm decay giving rise to muons carried out by Lederman, Schwartz and Steinberger demonstrated the existence of multiple neutrino flavours [12]. Following the discovery of the tau lepton in 1975 [13], the tau neutrino was observed by the DONUT experiment in 2000 [14].

Meanwhile, the properties of this phantom particle remains an active field of research, amongst which the most intriguing is the mass of the neutrino. Pauli initially made the guess of “same order of the electron mass, and in any event no larger than 0.01 of the proton mass” in his 1930 letter [7]. Later in 1957, following the observations of parity violation in the ^{60}Co β decay [15] and in muon decay [16, 17] a model of massless neutrinos with fixed helicities was proposed [18, 19, 20]. With subsequent observations consistent within experimental uncertainties [21], this model was formulated into the Standard Model of particle physics (SM). The Standard Model was successful in describing all experimental data on electro-weak and strong interactions, until the observation of neutrino flavour oscillation which is direct evidence of neutrino mass.

Pontecorvo first proposed the concept of neutrino oscillations, in the sense of particle/anti-particle transitions, in 1957, with insight gained from Kaon oscillation [22]. The idea was further generalised to neutrino flavour oscillations by Maki, Nakagawa and Sakata in 1962, where the mixing of ν_e and ν_μ was studied [23]. The more modern formulation of neutrino oscillation was established in 1976 by Eliezer and Swift [24], Fritzsch and Minkowski [25], and Bilenky and Pontecorvo [26]. This construction was soon invoked to solve the two famous perplexities in neutrino observation: the solar neutrino problem and the atmospheric neutrino anomaly, where large deficits are observed in the ν_e and ν_μ fluxes, respectively. The theory of neutrino oscillations was eventually confirmed by solar neutrino measurements from the Sudbury Neutrino Observatory (SNO) [27] and atmospheric neutrino measurements from the Super-Kamioka Neutrino Detection Experiment (Super-Kamiokande) [28], and, hence, implying the existence of non-zero neutrino mass.

An open question remaining is the fundamental nature of the neutrinos: Dirac particle or Majorana particle. That is to say, whether the neutrino is its own anti-particle (Majorana) or not (Dirac). The determination of this nature could shed light to the generation and exact value of the neutrino mass. Detection of neutrinoless double beta decay ($0\nu\beta\beta$) is considered the most promising way to determine whether the neutrino is Majorana or not.

This chapter will discuss the neutrino properties that are relevant to the supernova observations. Focus will be put on the neutrino flavour oscillation phenomena in both vacuum and matter, especially in the extreme conditions that would be associated with a collapsing stellar core. In addition, remarks on the neutrino mass and the $0\nu\beta\beta$ process, which is the primary objective of the SNO+ experiment, will be presented.

2.1 Neutrino Oscillation

Neutrino flavour oscillation is a quantum mechanical effect originating from the fact that the flavour eigenstates, associated to the weak interaction, do not coincide with the mass eigenstates. Upon creation in a weak interaction, e.g., β decay, the neutrino will be in a definite flavour eigenstate which is a mixed state of the mass eigenstates. As it propagates, the neutrino will evolve in the mass eigenstates which results in a flavour transition, from ν_α to ν_β , with probability $P_{\nu_\alpha\nu_\beta}$. The preservation of the original flavour is known as the survival probability $P_{\nu_\alpha\nu_\alpha} = 1 - \sum_{\beta \neq \alpha} P_{\nu_\alpha\nu_\beta}$. The probabilities differ in vacuum and matter as the Hamiltonian will be modified by the potential caused by the weak interaction with matter, known as the Mikheyev-Smirnov-Wolfenstein (MSW) effect. Note that this matter effect is more important at higher densities. For instance, when passing the Earth, the matter oscillation pertains to the core, whereas the rest of the travel can be simply described by vacuum

oscillation.

For a complete and consistent derivation, the neutrino oscillations should be derived in the wave packet description [9]. To simplify matters, nevertheless, the derivations in this section will be treated in the plane wave approximation, which is less realistic yet leads to the same results. As shown most clearly in [29], the plane wave approximation can be derived via the wave packet description in the limit of negligible position uncertainty upon production and detection.

2.1.1 Neutrino Mixing

The flavour eigenstates do not have well-defined masses and thus do not coincide with the mass eigenstates $|\nu_i\rangle$, where $i = 1, 2, 3$ is the index for the neutrino masses m_i . The two bases can be related by the unitary mixing matrix U ,

$$\begin{aligned} |\nu_\alpha\rangle &= \sum_{i=1,2,3} U |\nu_i\rangle = \sum_{i=1,2,3} U_{\alpha i} |\nu_i\rangle \\ |\nu_i\rangle &= \sum_{\alpha=e,\mu,\tau} U^\dagger |\nu_\alpha\rangle = \sum_{\alpha=e,\mu,\tau} U_{\alpha i}^* |\nu_\alpha\rangle. \end{aligned} \quad (2.1)$$

where U is known as the Pontecorvo-Maki-Nakagawa-Sakata (PMNS) matrix and is most typically parametrised by the parametrisation inherited from the Cabibbo-Kobayashi-Maskawa (CKM) matrix in quark mixing [30, 31],

$$\begin{aligned} U &= \begin{pmatrix} c_{12}c_{13}e^{i\phi_1} & s_{12}c_{13}e^{i\phi_2} & s_{13}e^{-i\delta_{CP}} \\ -s_{12}c_{23}e^{i\phi_1} - c_{12}s_{23}s_{13}e^{i\delta_{CP}}e^{i\phi_1} & c_{12}c_{23}e^{i\phi_2} - s_{12}s_{23}s_{13}e^{i\delta_{CP}}e^{i\phi_2} & s_{23}c_{13} \\ s_{12}s_{23}e^{i\phi_1} - c_{12}c_{23}s_{13}e^{i\delta_{CP}}e^{i\phi_1} & -c_{12}s_{23}e^{i\phi_2} - s_{12}c_{23}s_{13}e^{i\delta_{CP}}e^{i\phi_2} & c_{23}c_{13} \end{pmatrix} \\ &= \begin{pmatrix} 1 & 0 & 0 \\ 0 & c_{23} & s_{23} \\ 0 & -s_{23} & c_{23} \end{pmatrix} \begin{pmatrix} c_{13} & 0 & s_{13}e^{-i\delta_{CP}} \\ 0 & 1 & 0 \\ -s_{13}e^{i\delta_{CP}} & 0 & c_{13} \end{pmatrix} \begin{pmatrix} c_{12} & s_{12} & 0 \\ -s_{12} & c_{12} & 0 \\ 0 & 0 & 1 \end{pmatrix} \begin{pmatrix} e^{i\phi_1} & 0 & 0 \\ 0 & e^{i\phi_2} & 0 \\ 0 & 0 & 1 \end{pmatrix} \\ &= R_{23}R_{13}R_{12}D \end{aligned} \quad (2.2)$$

with the shorthands $s_{ij} = \sin \theta_{ij}$ and $c_{ij} = \cos \theta_{ij}$. This parametrisation consists of three mixing angles θ_{12} , θ_{13} and θ_{23} ; and three CP symmetry-violating phases δ_{CP} , ϕ_1 and ϕ_2 , where C stands for charge conjugation and P stands for parity. The values of these parameters are estimated by performing a global analysis of all the oscillation data, such as [32], where the values of each parameter depends on different measurements. The mixing angles θ_{12} , θ_{13} and θ_{23} are measured in solar, reactor/accelerator

and atmospheric neutrino experiments, respectively. The CP violating phase δ_{CP} is measured along with θ_{13} in reactor/accelerator neutrino experiments. However, the values are still not well-determined. Depending on the mass hierarchy, CP symmetry can range from being conserved to being maximally violated [32]. Finally, the remaining CP violating phases ϕ_1 and ϕ_2 , which were factored out as a diagonal matrix D in Eq. 2.2, are associated with Majorana neutrinos and non-measurable in oscillation experiments since they cancel out in the probabilities. The diagonal matrix D in Eq. 2.2 will, therefore, be ignored in the subsequent derivations.

2.1.2 Neutrino Oscillation in Vacuum

When a neutrino is created in a weak interaction process, it will initially be in a state of definite flavour, for instance $|\nu_\alpha\rangle$, which is a coherent linear combination of the mass eigenstates

$$|\nu(0)\rangle = |\nu_\alpha\rangle = \sum_{i=1,2,3} U_{\alpha i} |\nu_i\rangle. \quad (2.3)$$

After creation, the neutrino will propagate in mass eigenstates which are the free particle solutions to the time dependent Schrödinger equationⁱ

$$i \frac{d}{dt} |\nu_i(t)\rangle = \mathcal{H}_0 |\nu_i(t)\rangle \quad (2.4)$$

where \mathcal{H}_0 is the neutrino Hamiltonian in vacuum. By applying the plane wave approximation, the evolution of the mass eigenstates can be expressed as

$$|\nu_i(t)\rangle = e^{-i(E_i t - p_i L)} |\nu_i\rangle \quad (2.5)$$

and, hence, the neutrino state

$$|\nu(t)\rangle = \sum_{i=1,2,3} U_{\alpha i} e^{-i(E_i t - p_i L)} |\nu_i\rangle \quad (2.6)$$

where E_i and p_i are the energy and momentum of the given neutrino mass eigenstate, and L is the propagation distance. The flavour composition of the neutrino state after propagating for time t and distance L can be obtained by further decomposing the mass eigenstates in flavour basis

$$|\nu(t)\rangle = \sum_{i=1,2,3} \sum_{\beta=e,\mu,\tau} U_{\alpha i} U_{\beta i}^* e^{-i(E_i t - p_i L)} |\nu_\beta\rangle. \quad (2.7)$$

ⁱThe derivations in this chapter will be done in natural units, where $c = \hbar = 1$.

The oscillation amplitude of one flavour to another is then

$$\begin{aligned}\langle \nu_\gamma | \nu(t) \rangle &= \langle \nu_\gamma | \sum_{i=1,2,3} \sum_{\beta=e,\mu,\tau} U_{\alpha i} U_{\beta i}^* e^{-i(E_i t - p_i L)} | \nu_\beta \rangle \\ &= \sum_{i=1,2,3} U_{\alpha i} U_{\gamma i}^* e^{-i(E_i t - p_i L)}\end{aligned}\tag{2.8}$$

and the corresponding oscillation probability $P_{\nu_\alpha \nu_\gamma}$ is

$$\begin{aligned}P_{\nu_\alpha \nu_\gamma} &= |\langle \nu_\gamma | \nu(t) \rangle|^2 \\ &= \left(\sum_{i=1,2,3} U_{\alpha i} U_{\gamma i}^* e^{-i(E_i t - p_i L)} \right) \left(\sum_{j=1,2,3} U_{\alpha j}^* U_{\gamma j} e^{i(E_j t - p_j L)} \right) \\ &= \sum_{i,j=1,2,3} U_{\alpha i} U_{\gamma i}^* U_{\alpha j}^* U_{\gamma j} e^{-i((E_i - E_j)t - (p_i - p_j)L)}.\end{aligned}\tag{2.9}$$

For nearly vanishing neutrino masses, the following quantities can be approximated, to the order of $\mathcal{O}(m^2/E^2)$, as:

$$\begin{aligned}L &\cong t \\ p_i &= \sqrt{E_i^2 - m_i^2} \cong E_i - \frac{m_i^2}{2E_i}.\end{aligned}\tag{2.10}$$

With these approximations, the phase of the plane waves can be written as

$$\begin{aligned}E_i t - p_i L &\cong E_i t - \left(E_i - \frac{m_i^2}{2E_i} \right) L \\ &= E_i(t - L) + \frac{m_i^2}{2E_i} L \\ &\cong \frac{m_i^2}{2E_i} L.\end{aligned}\tag{2.11}$$

As a result of the different neutrino masses, the energies and momenta of each mass eigenstate varies. Nonetheless, as argued in [33, 34, 35], the equal energy scenario is a good approximation for practical considerations. Therefore, Eq. 2.9 can be expressed as

$$\begin{aligned}P_{\nu_\alpha \nu_\gamma} &= \sum_{i,j=1,2,3} U_{\alpha i} U_{\gamma i}^* U_{\alpha j}^* U_{\gamma j} e^{-i \frac{m_i^2 - m_j^2}{2E} L} \\ &= \sum_{i=1,2,3} |U_{\alpha i}|^2 |U_{\gamma i}|^2 + \sum_{i \neq j} U_{\alpha i} U_{\gamma i}^* U_{\alpha j}^* U_{\gamma j} e^{-i \frac{m_i^2 - m_j^2}{2E} L}\end{aligned}\tag{2.12}$$

where E is the neutrino energy. The unitary condition ($U^\dagger U = 1$) of the mixing matrix leads to the relation

$$\sum_i U_{\alpha i} U_{\beta i}^* = \delta_{\alpha \beta} \quad (2.13)$$

which allows one to finally express the oscillation probability as

$$\begin{aligned} P_{\nu_\alpha \nu_\gamma} &= \left(\delta_{\alpha \gamma} - \sum_{i>j} (U_{\alpha i} U_{\gamma i}^* U_{\alpha j}^* U_{\gamma j} + U_{\alpha j} U_{\gamma j}^* U_{\alpha i}^* U_{\gamma i}) \right) \\ &\quad + \sum_{i>j} (U_{\alpha i} U_{\gamma i}^* U_{\alpha j}^* U_{\gamma j} e^{-i \frac{m_i^2 - m_j^2}{2E} L} + U_{\alpha j} U_{\gamma j}^* U_{\alpha i}^* U_{\gamma i} e^{i \frac{m_i^2 - m_j^2}{2E} L}) \\ &= \left(\delta_{\alpha \gamma} - 2 \sum_{i>j} \Re(U_{\alpha i} U_{\gamma i}^* U_{\alpha j}^* U_{\gamma j}) \right) \\ &\quad + \sum_{i>j} \Re(U_{\alpha i} U_{\gamma i}^* U_{\alpha j}^* U_{\gamma j}) \cdot 2 \cos\left(\frac{m_i^2 - m_j^2}{2E} L\right) \\ &\quad - \sum_{i>j} i \Im(U_{\alpha i} U_{\gamma i}^* U_{\alpha j}^* U_{\gamma j}) \cdot 2i \sin\left(\frac{m_i^2 - m_j^2}{2E} L\right) \quad (2.14) \\ &= \delta_{\alpha \gamma} - 2 \sum_{i>j} \Re(U_{\alpha i} U_{\gamma i}^* U_{\alpha j}^* U_{\gamma j}) \left(1 - \cos\left(\frac{m_i^2 - m_j^2}{2E} L\right) \right) \\ &\quad + 2 \sum_{i>j} \Im(U_{\alpha i} U_{\gamma i}^* U_{\alpha j}^* U_{\gamma j}) \cdot \sin\left(\frac{m_i^2 - m_j^2}{2E} L\right) \\ &= \delta_{\alpha \gamma} - 4 \sum_{i>j} \Re(U_{\alpha i} U_{\gamma i}^* U_{\alpha j}^* U_{\gamma j}) \sin^2\left(\frac{m_i^2 - m_j^2}{4E} L\right) \\ &\quad + 2 \sum_{i>j} \Im(U_{\alpha i} U_{\gamma i}^* U_{\alpha j}^* U_{\gamma j}) \cdot \sin\left(\frac{m_i^2 - m_j^2}{2E} L\right) \end{aligned}$$

where \Re and \Im stands for the real and imaginary parts of a complex number. It is evident from the expression that flavour oscillation will only happen if neutrinos have different masses, i.e., $m_i \neq m_j$, which further excludes the possibility of massless neutrinos.

Experimentally, detectors can be designed to exploit this L/E dependence of the oscillation for sensitivity on the oscillation parameters $\Delta m_{ij}^2 = m_i^2 - m_j^2$, θ_{ij} and δ_{CP} . The experiments are sensitive to the mass-squared splittings only when

$$\frac{\Delta m^2 L}{2E} \sim 1. \quad (2.15)$$

On the contrary, if

$$\frac{\Delta m^2 L}{2E} \ll 1 \quad (2.16)$$

the transition probability will simply vanish, whereas in the case of

$$\frac{\Delta m^2 L}{2E} \gg 1 \quad (2.17)$$

only the average of probability will be observable, yielding information only on the mixing angles θ_{ij} .

As mentioned earlier, neutrino oscillations were first observed in solar and atmospheric neutrino experiments. The results of these measurements revealed the neutrino mass hierarchy as

$$|\Delta m_{atm}^2| \gg \Delta m_{solar}^2 > 0 \quad (2.18)$$

where Δm_{atm}^2 and Δm_{solar}^2 are the mass-squared splittings measured from atmospheric and solar neutrinos [36]. The numbering of the mass eigenstates are then defined as $\Delta m_{solar}^2 \equiv \Delta m_{21}^2$ with $m_2 > m_1$, and $\Delta m_{atm}^2 \equiv |\Delta m_{13}^2| \approx |\Delta m_{23}^2|$ since the atmospheric mass difference is far greater than that of solar [36]. Current experiments are not yet able to determine the precise values of the neutrino masses or the sign of Δm_{13}^2 or Δm_{23}^2 ⁱⁱ. This, in turn, leads to three possible ordering scenarios: normal hierarchy (NH) ($m_3 \gg m_2 > m_1$), inverted hierarchy (IH) ($m_2 > m_1 \gg m_3$) and quasi-degenerate (QD) [37]. The last scheme refers to the case when the lightest neutrino mass is on the order of 0.1 eV or higher, in which case the neutrino masses are much larger than the mass splittings and the mass ordering can be considered as practically degenerate $m_1 \approx m_2 \approx m_3$.

2.1.3 Neutrino Oscillation in Matter

In 1978, Wolfenstein discovered that the presence of matter would introduce a potential to the neutrino due to coherent forward scattering with the particles in the medium [38]. The neutrino Hamiltonian, and thus the oscillation probability, will be modified by this potential.

The neutrino Hamiltonian can be expressed as the sum of the vacuum Hamiltonian \mathcal{H}_0 and the interaction Hamiltonian, i.e., the potential, \mathcal{H}_{int}

$$\mathcal{H} = \mathcal{H}_0 + \mathcal{H}_{int}. \quad (2.19)$$

ⁱⁱNote that the sign of Δm_{21}^2 has been determined via matter resonance measurements for solar neutrinos, see the MSW effect part of Section 2.1.3 for a more detailed discussion.

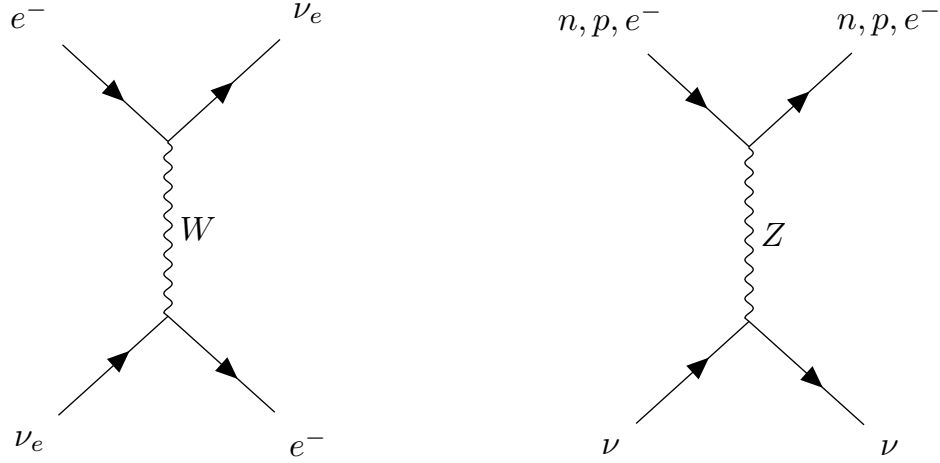


Figure 2.1: Feynman diagrams for the coherent forward scattering via charged current interaction (left) and neutral current interaction (right).

Note that the mass eigenstates $|\nu_i\rangle$ are eigenstates of \mathcal{H}_0 and the flavour eigenstates $|\nu_\alpha\rangle$ are eigenstates of \mathcal{H}_{int} , since the scattering is via weak interaction. One can then write down the eigenvalue equations

$$\begin{aligned}\mathcal{H}_0|\nu_i\rangle &= E_i|\nu_i\rangle \\ \mathcal{H}_{int}|\nu_\alpha\rangle &= V_\alpha|\nu_\alpha\rangle\end{aligned}\tag{2.20}$$

where E_i is the sum of kinetic and rest mass energy of the neutrino mass state $|\nu_i\rangle$, and V_α is the coherent scattering potential experienced by the flavour state $|\nu_\alpha\rangle$.

Weak Interaction Potential

The weak interaction potential V_α of a neutrino of flavour α arising from scattering comprises contributions from both charged-current (CC) scattering and neutral-current (NC) scattering, as shown in Figure 2.1. In the low-energy regime, only electron flavour neutrinos are able to undergo CC scattering, so the potential can be expressed as

$$V_\alpha = \delta_{e\alpha} V_{CC}^e + V_{NC}^e + V_{NC}^n + V_{NC}^p\tag{2.21}$$

where V_{CC}^e is the potential of interacting with electrons via CC scattering; and V_{NC}^e , V_{NC}^n and V_{NC}^p are the potentials arising from interaction with electrons, neutrons and

protons via NC scattering. For CC scattering, the resulting potential per neutrino is

$$V_{CC}^e = \pm \sqrt{2} G_F n_e \quad (2.22)$$

where G_F is the Fermi constant, n_e is the local electron number density, and the “+” and “−” signs correspond to the cases of electron neutrinos and anti-neutrinos, respectively. For NC scattering, on the other hand, the potential takes a rather similar form

$$V_{NC} = V_{NC}^e + V_{NC}^p + V_{NC}^n = \mp \frac{\sqrt{2}}{2} G_F n_n \quad (2.23)$$

where n_n is the neutron number density and the plus sign is, in this case, attributed to the case of anti-neutrinos. Note that the NC potential only depends on neutron density, as contributions from electrons and protons happen to cancel each other.

Flavour Evolution

In the same fashion as in the vacuum case, the evolution of the neutrino is described by the Schrödinger equation

$$i \frac{d}{dt} |\nu(t)\rangle = \mathcal{H} |\nu(t)\rangle \quad (2.24)$$

with

$$|\nu(0)\rangle = |\nu_\alpha\rangle \quad (2.25)$$

where \mathcal{H} is the Hamiltonian as in Eq. 2.19. One can then obtain the evolution equation of the probability amplitude for a transition from ν_α to ν_γ

$$\begin{aligned} i \frac{d}{dt} \langle \nu_\gamma | \nu(t) \rangle &= \langle \nu_\gamma | \mathcal{H}_0 + \mathcal{H}_{int} | \nu(t) \rangle \\ &= \left(\sum_i U_{\gamma i}^* \langle \nu_i | \right) \mathcal{H}_0 | \nu(t) \rangle + \langle \nu_\gamma | V_\gamma | \nu(t) \rangle \\ &= \left(\sum_i U_{\gamma i}^* E_i \left(\sum_\beta U_{\beta i} \langle \nu_\beta | \right) \right) | \nu(t) \rangle + V_\gamma \langle \nu_\gamma | \nu(t) \rangle \\ &= \sum_i \sum_\beta U_{\gamma i}^* E_i U_{\beta i} \langle \nu_\beta | \nu(t) \rangle + V_\gamma \langle \nu_\gamma | \nu(t) \rangle. \end{aligned} \quad (2.26)$$

In light of the ultra-relativistic nature of the neutrino, as in Eq. 2.10, and the fact that the matter potential is nearly negligible compared to the neutrino kinetic energy,

Eq. 2.26 can be expressed as

$$\begin{aligned} i \frac{d}{dL} \langle \nu_\gamma | \nu(L) \rangle &= \sum_i \sum_\beta U_{\gamma i}^* \left(E + \frac{m_i^2}{2E} \right) U_{\beta i} \langle \nu_\beta | \nu(L) \rangle + V_\gamma \langle \nu_\gamma | \nu(L) \rangle \\ &= \left(\sum_i \sum_\beta U_{\gamma i}^* \frac{\Delta m_{ii}^2}{2E} U_{\beta i} \langle \nu_\beta | \nu(L) \rangle + V_{CC}^e \langle \nu_e | \nu(L) \rangle \right) \\ &\quad + \left(E + \frac{m_1^2}{2E} + V_{NC} \right) \langle \nu_\gamma | \nu(L) \rangle \end{aligned} \quad (2.27)$$

where the terms $E + m_1^2/2E + V_{NC}$ are swept aside as they simply cause a common phase shift on all flavours and do not affect the transition probabilities. The reduced equation can then be expressed in matrix form as

$$i \frac{d}{dL} \Psi = \frac{1}{2E} (U^\dagger \mathbf{M}^2 U + \mathbf{V}_{CC}) \Psi \quad (2.28)$$

where

$$\Psi = \begin{pmatrix} \langle \nu_e | \nu(L) \rangle \\ \langle \nu_\mu | \nu(L) \rangle \\ \langle \nu_\tau | \nu(L) \rangle \end{pmatrix}, \quad \mathbf{M}^2 = \begin{pmatrix} 0 & 0 & 0 \\ 0 & \Delta m_{21}^2 & 0 \\ 0 & 0 & \Delta m_{31}^2 \end{pmatrix}, \quad \mathbf{V}_{CC} = \begin{pmatrix} 2\sqrt{2}EG_F n_e & 0 & 0 \\ 0 & 0 & 0 \\ 0 & 0 & 0 \end{pmatrix}. \quad (2.29)$$

The MSW Effect

To simplify matters, the matter effects can be demonstrated most clearly in the two neutrino case. Consider the case of a $\nu_e - \nu_\mu$ mixingⁱⁱⁱ, Eq. 2.28 becomes

$$\begin{aligned} i \frac{d}{dL} \Psi &= \left(\frac{\Delta m_{21}^2}{4E} + \frac{\Delta m_{21}^2}{4E} \begin{pmatrix} -\cos 2\theta_{12} & \sin 2\theta_{12} \\ \sin 2\theta_{12} & \cos 2\theta_{12} \end{pmatrix} + \begin{pmatrix} V_{CC}^e & 0 \\ 0 & 0 \end{pmatrix} \right) \Psi \\ &= \left(\frac{\Delta m_{21}^2}{4E} + \frac{V_{CC}^e}{2} + \frac{\Delta m_{21}^2}{4E} \begin{pmatrix} -\cos 2\theta_{12} + \frac{2EV_{CC}^e}{\Delta m_{21}^2} & \sin 2\theta_{12} \\ \sin 2\theta_{12} & \cos 2\theta_{12} - \frac{2EV_{CC}^e}{\Delta m_{21}^2} \end{pmatrix} \right) \Psi \end{aligned} \quad (2.30)$$

By neglecting the common phase of

$$\exp \left(-i \frac{\Delta m_{21}^2}{4E} L - \frac{i}{2} \int_0^L V_{CC}^e dL' \right), \quad (2.31)$$

ⁱⁱⁱThe case of $\nu_e - \nu_\tau$ is identical as the matter potentials for ν_μ and ν_τ are the same.

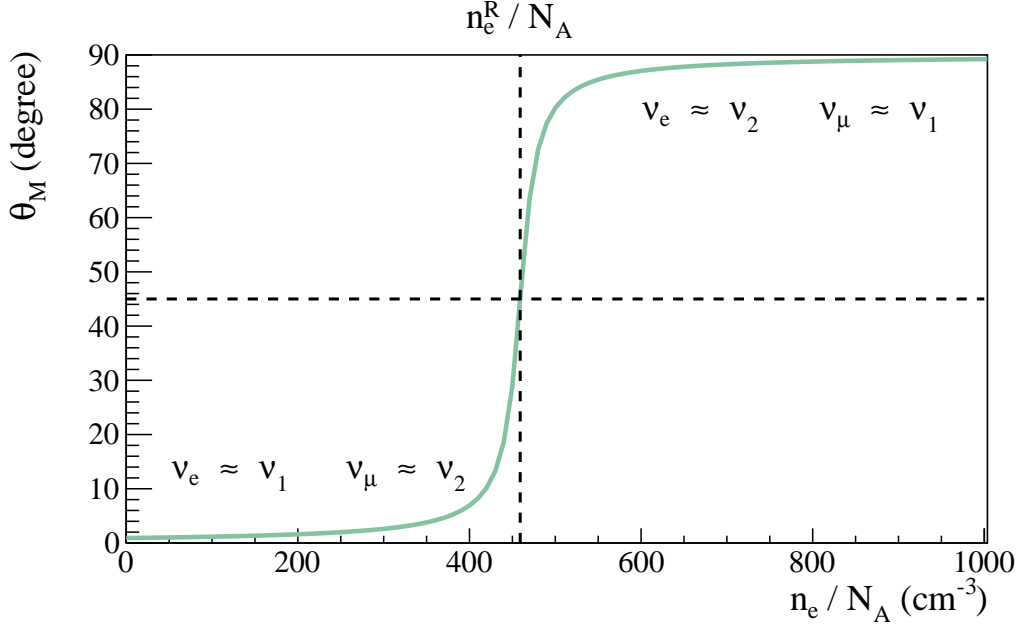


Figure 2.2: Evolution of the effective mixing angle θ_M plotted against the electron density n_e over Avogadro's constant N_A , where $\Delta m_{21}^2 = 7 \times 10^{-5}$ eV 2 , $\sin^2 2\theta_{12} = 10^{-3}$ and $E = 1$ MeV, adapted from [9]. The dashed lines indicate the resonance.

Eq. 2.30 becomes

$$i \frac{d}{dL} \Psi = \frac{\Delta m_{21}^2}{4E} \begin{pmatrix} -\cos 2\theta_{12} + \frac{2EV_{CC}^e}{\Delta m_{21}^2} & \sin 2\theta_{12} \\ \sin 2\theta_{12} & \cos 2\theta_{12} - \frac{2EV_{CC}^e}{\Delta m_{21}^2} \end{pmatrix} \Psi. \quad (2.32)$$

One can then define the effective mixing angles

$$\begin{aligned} \cos 2\theta_M &= \frac{\Delta m_{21}^2 \cos 2\theta_{12} - 2EV_{CC}^e}{\sqrt{(\Delta m_{21}^2 \cos 2\theta_{12} - 2EV_{CC}^e)^2 + (\Delta m_{21}^2 \sin 2\theta_{12})^2}} \\ \sin 2\theta_M &= \frac{\Delta m_{21}^2 \sin 2\theta_{12}}{\sqrt{(\Delta m_{21}^2 \cos 2\theta_{12} - 2EV_{CC}^e)^2 + (\Delta m_{21}^2 \sin 2\theta_{12})^2}} \end{aligned} \quad (2.33)$$

and the effective squared mass difference

$$\Delta m_M^2 = \sqrt{(\Delta m_{21}^2 \cos 2\theta_{12} - 2EV_{CC}^e)^2 + (\Delta m_{21}^2 \sin 2\theta_{12})^2} \quad (2.34)$$

by normalising the Hamiltonian entries. In terms of these effective variables, the effective Hamiltonian can be re-written as

$$\mathcal{H}_M = \frac{\Delta m_M^2}{4E} \begin{pmatrix} -\cos 2\theta_M & \sin 2\theta_M \\ \sin 2\theta_M & \cos 2\theta_M \end{pmatrix}, \quad (2.35)$$

and this leads to the effective mixing matrix

$$U_M = \begin{pmatrix} \cos \theta_M & \sin \theta_M \\ -\sin \theta_M & \cos \theta_M \end{pmatrix}. \quad (2.36)$$

Following from the definitions of the effective mixing angle, it can be observed that a resonance of $\theta_M \rightarrow \pi/4$ can be achieved when

$$\begin{aligned} V_{CC}^e |_R &= \frac{\Delta m_{21}^2 \cos 2\theta_{12}}{2E} \\ n_e |_R &= \frac{\Delta m_{21}^2 \cos 2\theta_{12}}{2\sqrt{2}EG_F} \end{aligned} \quad (2.37)$$

where the subscript R is designated to indicate the resonant values. This shows that with the presence of matter potentials, the mixing can become maximal even when the mixing angle is small. This resonant effect is known as the Mikheyev-Smirnov-Wolfenstein (MSW) effect [39, 40]. The behaviours of the effective mixing angle θ_M and squared mass difference Δm_M^2 plotted against the electron number density n_e are shown in Figure 2.2. In the case of $n_e \gg n_e |_R$, the effective mixing angle approaches $\pi/2$ and an electron neutrino $|\nu_e\rangle = \cos \theta_M |\nu_1\rangle + \sin \theta_M |\nu_2\rangle$ will nearly coincide with $|\nu_2\rangle$.

It should be noted that the symmetry between the signs of the mass splittings^{iv} is broken by the presence of matter, and, hence, the determination of the mass ordering becomes possible with such measurements. From Eq. 2.37, one can see that the sign of the term $\Delta m^2 \cos 2\theta$ dictates whether the resonance is crossed by neutrinos or anti-neutrinos. In fact, this is how the ordering between m_1 and m_2 was resolved. The solar neutrino measurements have constrained the value of $\Delta m_{21}^2 \cos 2\theta_{12}$ to be positive. As a convention, Δm_{21}^2 is set to be positive, designating the lighter electron-flavour-dominant mass state as $|\nu_1\rangle$.

Resonances in Supernovae

The matter density in a supernova [41] far exceeds the maximum solar density [42] by several orders of magnitude, and thus allows the existence of an extra resonance rising from the larger squared mass splitting Δm_{31}^2 . The two resonances are referred to as the High (H) and Low (L) resonances, which corresponds to the electron densities $n_e |_R (\theta_{13}, \Delta m_{31}^2)$ and $n_e |_R (\theta_{12}, \Delta m_{21}^2)$, respectively. The H-resonance is crossed

^{iv}This is, in fact, only true in the case of two-neutrino mixing. It is clear from Eq. 2.14 that for the case of three-neutrino mixing, the oscillation probability will be affected by the change of sign of Δm^2 . Nonetheless, due to the smallness of θ_{13} and $\Delta m_{solar}^2/\Delta m_{atm}^2$, the mixing can be described by the two-neutrino form to leading order in most cases.

by neutrinos or anti-neutrinos, depending on the mass hierarchy, whereas the L-resonance is crossed by neutrinos in both cases [43]. Supernova observations could, therefore, lead to a potential measurement of the neutrino mass hierarchy.

2.2 Neutrino Mass

The discovery of neutrino mass is the only conclusive direct evidence of physics beyond the Standard Model (BSM), as massless neutrinos were postulated in the SM. This mass can be incorporated into the theoretical framework describing the neutrino via two possible scenarios: Dirac spinors and Majorana spinors. The section starts with a review of the mass generation term and neutrino description in the Standard Model. Brief introductions of the masses of Dirac and Majorana neutrinos will then follow.

2.2.1 Standard Model Neutrino

As a fermion, the neutrino is described by the Dirac equation

$$(i\gamma^\mu \partial_\mu - m)\psi = 0 \quad (2.38)$$

where $\partial_\mu = \partial/\partial x^\mu$ and γ^μ are the Dirac matrices. The Dirac matrices in the chiral basis are defined as

$$\gamma^0 = \begin{pmatrix} 0 & I \\ I & 0 \end{pmatrix}, \quad \gamma^k = \begin{pmatrix} 0 & \sigma^k \\ -\sigma^k & 0 \end{pmatrix} \quad (2.39)$$

where σ^k are the Pauli matrices. It is then useful to define a fifth matrix

$$\gamma^5 \equiv i\gamma^0\gamma^1\gamma^2\gamma^3 = \begin{pmatrix} -I & 0 \\ 0 & I \end{pmatrix} \quad (2.40)$$

where chirality is defined upon its eigenvalues ± 1 . The chiral components of eigenvalues $+1$ and -1 are designated as right-handed and left-handed. These components can then be projected by the pair of operators

$$P_L = \frac{1 - \gamma^5}{2}, \quad P_R = \frac{1 + \gamma^5}{2} \quad (2.41)$$

where the labels L and R stands for left-handed and right-handed, respectively. The Dirac equation Eq. 2.38 can, therefore, be written in the form of

$$(i\gamma^\mu \partial_\mu - m) \begin{pmatrix} \phi_L \\ \phi_R \end{pmatrix} = 0, \quad (2.42)$$

and leads to the system of equations

$$\begin{aligned} i\sigma^\mu \partial_\mu \phi_L &= m\phi_R \\ i\bar{\sigma}^\mu \partial_\mu \phi_R &= m\phi_L \end{aligned} \quad (2.43)$$

where $\sigma^\mu = \{I, \sigma^k\}$ and $\bar{\sigma}^\mu = \{I, -\sigma^k\}$; and ϕ_L and ϕ_R are the chiral components of ψ , also known as Weyl spinors or bispinors^v. Eq. 2.43 indicates that the chiral components are coupled to each other for massive fermions. On the contrary, if the fermion is massless, the two equations in Eq. 2.43 will become decoupled

$$\begin{aligned} i\sigma^\mu \partial_\mu \phi_L &= 0 \\ i\bar{\sigma}^\mu \partial_\mu \phi_R &= 0. \end{aligned} \quad (2.44)$$

The equations in Eq. 2.44 are known as the Weyl equations.

When Weyl initially proposed these equations in 1929 [44], they were soon rejected by Pauli on the basis of parity conservation [45]. However, this model was later redeemed by the subsequent discovery of parity violation in 1957, which invalidated Pauli's argument. Furthermore, since there were no evidence for the existence of neutrino mass or right-hand neutrinos at the time, the Weyl description of the neutrino became particularly favourable for constructing the weak interaction model [18, 19, 20]. This framework later became the model for neutrinos that was incorporated into the SM.

2.2.2 Dirac Neutrino

The most straightforward way to incorporate the neutrino mass is to take one step back to Eq. 2.43, and treat it just as any other massive fermion in the SM. In this case, the neutrino mass will be generated through the Dirac mass term in the Lagrangian

$$\mathcal{L}_D = -m_D \bar{\psi} \psi = -m_D (\bar{\psi}_L \psi_R + \bar{\psi}_R \psi_L) = -m_D (\phi_L^\dagger \phi_R + \phi_R^\dagger \phi_L) \quad (2.45)$$

where m_D is the mass of a Dirac neutrino and $\bar{\psi}$ is a shorthand for $\psi^\dagger \gamma^0$. Eq. 2.45 also indicates that both chiral components are needed to generate mass in this scenario.

The main issue with this scenario is that it requires the existence of two additional particles which have not yet been observed: the right-hand neutrino and the left-hand anti-neutrino. These particles are often referred to as “sterile” neutrinos as they do not participate in Standard Model interactions. Note that, however, for massive

^vTo avoid confusion in the notation, the four-dimensional Dirac spinors will always be represented by ψ , whereas the two-dimensional bispinors will be represented by ϕ .

neutrinos, helicity^{vi} states do not coincide with chiral states exactly. Therefore, the neutrinos of left-hand helicity observed thus far will be a combination of mostly left-chiral neutrinos and a small fraction of right-chiral sterile neutrinos in this scenario.

2.2.3 Majorana Neutrino

Another scenario was proposed by Majorana in 1937 [46], when he noticed that Eq. 2.43 does not necessarily require two independent chiral components. It was discovered that fermions can be described by one chiral component if one imposes the Majorana condition

$$\psi = \psi^C \quad (2.46)$$

where $\psi^C \equiv i\gamma^2\psi^*$ is the charge conjugate spinor. This condition indicates the equivalence between the particle and its anti-particle. It is not difficult to verify that this condition is compatible with the Dirac equation Eq. 2.38

$$\begin{aligned} (i\gamma^\mu\partial_\mu - m)\psi^C &= (i\gamma^\mu\partial_\mu - m)i\gamma^2\psi^* \\ &= i(i\gamma^\mu\gamma^2\partial_\mu - \gamma^2m)\psi^* \\ &= i\gamma^2(-i(\gamma^\mu)^*\partial_\mu - m)\psi^* \\ &= 0 \end{aligned} \quad (2.47)$$

where the last equality is simply the conjugate of Eq. 2.38. In terms of chiral components, the Majorana condition Eq. 2.46 becomes

$$\begin{pmatrix} \phi_L \\ \phi_R \end{pmatrix} = i \begin{pmatrix} 0 & \sigma^2 \\ -\sigma^2 & 0 \end{pmatrix} \begin{pmatrix} \phi_L^* \\ \phi_R^* \end{pmatrix} = \begin{pmatrix} i\sigma^2\phi_R^* \\ -i\sigma^2\phi_L^* \end{pmatrix} \quad (2.48)$$

and, hence, the Majorana spinor can be expressed as

$$\psi = \begin{pmatrix} \phi_L \\ -i\sigma^2\phi_L^* \end{pmatrix} \quad (2.49)$$

which is determined by a single bispinor ϕ_L .

^{vi}Helicity is defined as the projection of the spin on the momentum direction $\vec{\Sigma} \cdot \vec{p}$, where $\vec{\Sigma} = \begin{pmatrix} \vec{\sigma} & 0 \\ 0 & \vec{\sigma} \end{pmatrix}$. Helicity coincides with chirality in the case of massless particles, and is what is measured in experiments.

With this construct, the Dirac mass term will then become the Majorana mass term

$$\begin{aligned}\mathcal{L}_M &= -\frac{m_M}{2}(\bar{\psi}\psi) = -\frac{m_M}{2}(\bar{\psi}_L^C\psi_L + \bar{\psi}_L\psi_L^C) \\ &= -\frac{m_M}{2}(\phi_L^T \cdot i\sigma^2 \cdot \phi_L - (\phi_L^*)^T \cdot i\sigma^2 \cdot \phi_L^*)\end{aligned}\quad (2.50)$$

where the m_M is the Majorana mass and the extra factor of $1/2$ was introduced to compensate double counting^{vii}. Though the mass term is still composed of the coupling of right and left-handed components, the right-handed component is now ψ_L^C which behaves as the anti-particle of ψ_L . In this case, the Majorana neutrino will be, in a sense, a mixture of particle and anti-particle in contrast to the neutrino and sterile neutrino combination in the Dirac case.

See-saw Mechanism

The discussion of the Majorana neutrino has thus far focused on the left-hand component ψ_L , because this is what has been observed and formulated in the Standard Model. On the other hand, the Majorana construction leaves the right-hand component ψ_R at liberty, for it is independent of ψ_L . Though the right-hand neutrino ν_R has never been observed, it is, in principle, not forbidden. Many BSM theories have postulated the existence of ν_R . One of them is the see-saw mechanism [47, 48, 49] which is particularly interesting as it explains the almost vanishing neutrino mass in a way that is theoretically attractive.

If ν_R also exists, the Lagrangian can contain both the Majorana mass terms

$$\mathcal{L}_M = -\frac{m_L}{2}(\bar{\nu}_L^C\nu_L + \bar{\nu}_L\nu_L^C) - \frac{m_R}{2}(\bar{\nu}_R^C\nu_R + \bar{\nu}_R\nu_R^C)\quad (2.51)$$

and Dirac mass terms

$$\mathcal{L}_D = -m_D(\bar{\nu}_L\nu_R + \bar{\nu}_R\nu_L)\quad (2.52)$$

where m_L and m_R are the Majorana masses of left and right-handed neutrinos, respectively. Note that ψ is now replaced by ν , for the discussion is now specifically for neutrinos. It is then convenient to write the mass terms in a basis of left-handed chiral fields and its Hermitian conjugate (H.c.)

$$\mathcal{L}_{M+D} = -\frac{1}{2} \begin{pmatrix} \bar{\nu}_L^C & \bar{\nu}_R \end{pmatrix} \begin{pmatrix} m_L & m_D \\ m_D & m_R \end{pmatrix} \begin{pmatrix} \nu_L \\ \nu_R^C \end{pmatrix} + \text{H.c.}\quad (2.53)$$

^{vii}Since the left-handed and right-handed components of a Majorana field ψ , as in Eq. 2.49, are not independent, the Lagrangian will be quadratic in ψ_L . Therefore, a factor of $1/2$ will be required to generate the correct equation of motion, viz., the Dirac equation.

By diagonalising the mass matrix, one will then arrive at a basis formed by neutrino states of definite mass. The diagonalisation can be achieved by orthogonal transformations if the masses are real. The mixing of the left-handed chiral states can, therefore, be characterised by a single mixing angle θ

$$\begin{pmatrix} \nu_a^L \\ \nu_b^L \end{pmatrix} = \begin{pmatrix} \cos \theta & -\sin \theta \\ \sin \theta & \cos \theta \end{pmatrix} \begin{pmatrix} \nu_L \\ \nu_R^C \end{pmatrix} \quad (2.54)$$

and the resulting mass eigenvalues can be found to be

$$\begin{aligned} m_a &= \frac{1}{2}\chi \left(m_L + m_R - \sqrt{(m_L - m_R)^2 + 4m_D^2} \right) \\ m_b &= \frac{1}{2} \left(m_L + m_R + \sqrt{(m_L - m_R)^2 + 4m_D^2} \right) \end{aligned} \quad (2.55)$$

where $m_a \leq m_b$ by definition and $\chi = \pm 1$ is a factor to keep m_a positive^{viii}.

The see-saw mechanism considers a particularly interesting case when $m_L = 0$ and $m_R \gg m_D$. This results in

$$m_a \cong \frac{m_D^2}{m_R}, \quad m_b \cong m_R \quad (2.56)$$

in which case m_a is tiny and m_b is relatively heavy. Furthermore, the mixing angle θ is small

$$\tan 2\theta = \frac{2m_D}{m_R} \ll 1 \quad (2.57)$$

that is to say ν_a^L is formed of nearly pure ν_L and ν_b^L is composed mainly of the sterile ν_R . In particular, by setting m_L to zero, one recovers the Standard Model neutrino with ν_L . Additionally, the Dirac mass m_D can be generated by the Standard Model Higgs mechanism. The only component involving BSM physics is the hypothetical sterile neutrino ν_R , whilst its mass m_R is not forbidden by any SM symmetry. This explains the smallness of the observed neutrino masses without assuming an exceptionally small Yukawa coupling as in the case of pure Dirac mass [9].

^{viii} χ can arise from an appropriate choice of phase of ν_R and ν_L .

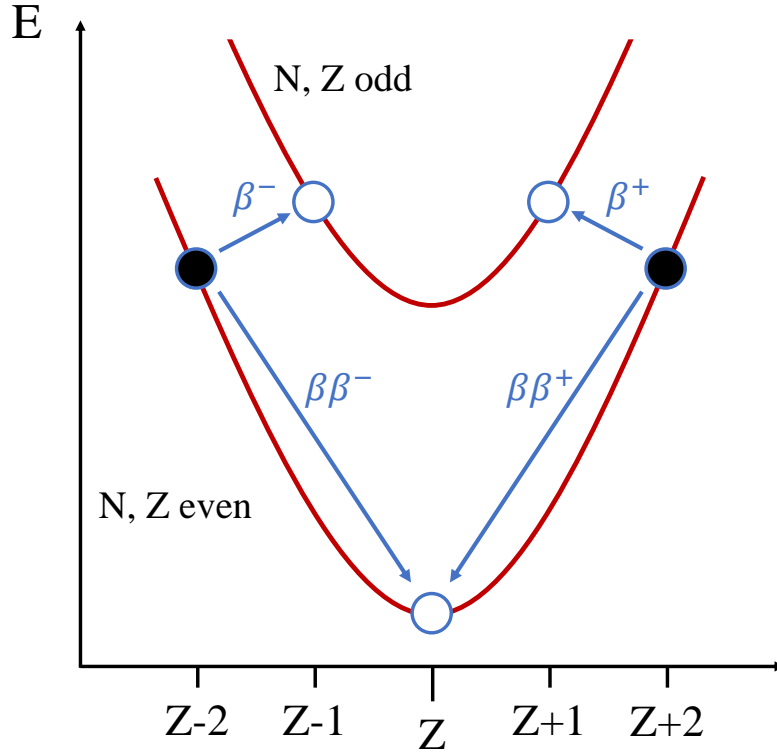


Figure 2.3: Beta and double beta transitions for even mass number nuclei. Adapted from [50].

2.3 Neutrinoless Double Beta Decay

Double beta decay ($2\nu\beta\beta$) is the process of the simultaneous occurrence of two beta decays as some nuclei would reach a more stable state by maintaining an even proton number (Z) and even neutron number (N), as shown in Figure 2.3. The possible existence of such a process was first proposed in 1935 by Goeppert-Mayer [51]. As depicted in Figure 2.4, double beta decay is a second order process and has a much longer lifetime compared to single beta decays. It is, therefore, only observable when the single beta decay is energetically unfavourable whilst the double beta decay is not. In 1987, Elliot *et al.* carried out the first direct observation of $2\nu\beta\beta$ in ^{82}Se decay [52]. Subsequently, it was discovered that there exists 35 naturally occurring nuclei which could possibly undergo $2\nu\beta\beta$, whereas only 20 have been directly measured [53]. Table 2.1 lists some of the naturally occurring $2\nu\beta\beta$ isotopes.

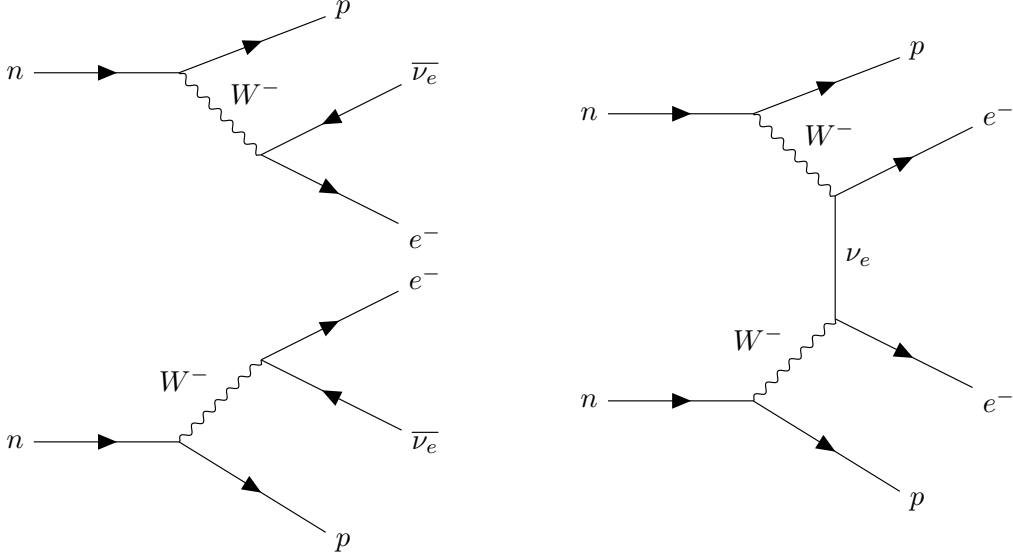


Figure 2.4: Feynman diagrams for ordinary double beta decay (left) and neutrinoless double beta decay (right).

Following the initial proposal, Majorana [46] and Furry [54] suggested that were the neutrino its own anti-particle, viz., a Majorana particle, the results of the process would remain unchanged yet without neutrino emissions, linking Majorana neutrinos to $0\nu\beta\beta$. As it turns out, an observation of $0\nu\beta\beta$ is also a direct indication of the existence of Majorana neutrinos as proved in the black-box theorem [55, 56], depicted in Figure 2.5. The theorem states that if the $0\nu\beta\beta$ process exists, one will then arrive at some vertex with the effect of $2d \rightarrow 2u + 2e^-$, i.e., the “black box”. This “black box” can then always be arranged to give rise to a $\nu \rightarrow \bar{\nu}$ transition, and, hence, the conclusion.

Besides the question of the Dirac or Majorana nature of the neutrino, the measurement of $0\nu\beta\beta$ also addresses the issue regarding the absolute magnitude of the neutrino masses. As described in the previous section, oscillation experiments are able to measure the squared mass differences with increasing accuracy. The precise values of the neutrino masses are, however, unresolvable in these experiments. It is only the upper bound on the masses, of $\mathcal{O}(\text{eV})$, that are currently attainable from measurements in τ , π or tritium decays or cosmological observations [36].

Since the neutrino mass is beyond the scope of the SM, its origin might not arise, or not solely arise, from the Standard Model Higgs mechanism. The see-saw mechanism is currently the most favoured scheme amongst the plethora of proposed mass generation mechanisms [47, 49]. In this scenario, the neutrino mass originates from BSM physics and the violation of lepton number conservation from the Ma-

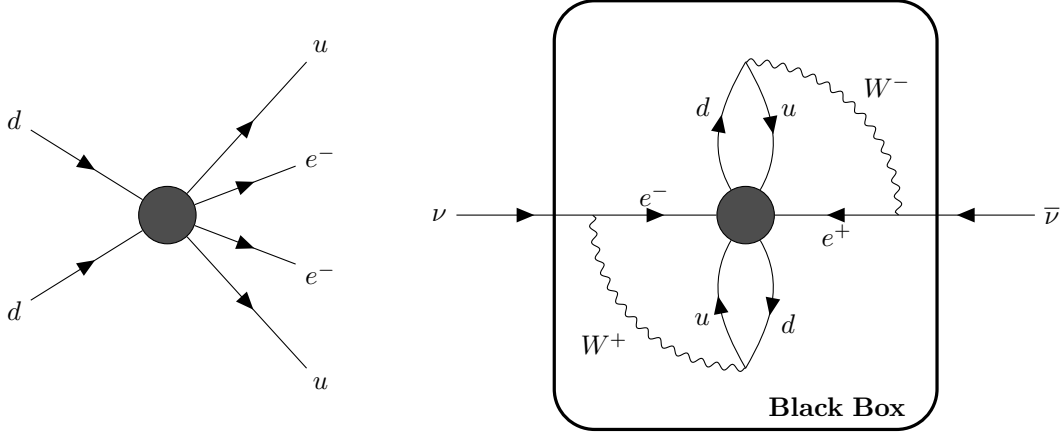


Figure 2.5: Feynman diagram for a general neutrinoless double beta decay (the “black box”) (left) and the $\nu \rightarrow \bar{\nu}$ transition arising from the black box (right).

Dirac mass term happens at scales much higher than the electroweak energy scale. Furthermore, this scheme strongly incline towards neutrinos of the Majorana type. With the presence of the Majorana mass term, the neutrino masses relevant to the measured $\mathcal{O}(0.1 \text{ eV})$ scales can arise without resorting to fine-tuned coupling to the Higgs field. The fundamental nature, Dirac or Majorana, of the neutrino thus plays a crucial role in the determination of the neutrino masses at extremely low energy scales. SNO+ and other large experiments with low backgrounds are, therefore, set in search of the $0\nu\beta\beta$ process to unravel the nature of the neutrino.

Though the Majorana mass is not directly measurable, it can be inferred from the measured $0\nu\beta\beta$ half-life

$$\frac{1}{T_{1/2}^{0\nu\beta\beta}} = G_{0\nu\beta\beta} |\mathcal{M}_{0\nu\beta\beta}|^2 \left(\frac{|m_{\beta\beta}|}{m_e} \right)^2 \quad (2.58)$$

where $G_{0\nu\beta\beta}$ is the phase space factor of the decay, $\mathcal{M}_{0\nu\beta\beta}$ is the nuclear interaction matrix element, and $m_{\beta\beta} \equiv \sum_i U_{ei}^2 m_i$ is the effective Majorana mass which is then normalised to the electron mass m_e [58, 59]. The phase space factor $G_{0\nu\beta\beta}$ is a known integral dependent on the Q -value of the decay. On the other hand, the nuclear matrix element $\mathcal{M}_{0\nu\beta\beta}$ involves the non-trivial treatment of a many-body problem. Methods include: the Energy Density Functional (EDF) method [60], the Quasi-Particle Random Phase Approximation (QRPA) [61], the Interacting Boson Model-2 (IBM-2) [62], the Large-Scale Shell Model (LSSM) [63] and the Projected Hartree-Fock-Bogoliubov (PHFB) approach [64]. The results from these methods are depicted in Figure 2.6. One immediately notices the large uncertainties it introduces to the

2.3. NEUTRINOLESS DOUBLE BETA DECAY

$\beta\beta$ Decay	$G_{0\nu}$ (10^{-14}y^{-1})	Q (MeV)	Nat. Abund. (%)	$T_{1/2}^{2\nu}$ (10^{21}y)
$^{48}\text{Ca} \rightarrow ^{48}\text{Ti}$	6.4	4.27226(404)	0.187	$0.044^{+0.005}_{-0.004} \pm 0.004$
$^{76}\text{Ge} \rightarrow ^{76}\text{Se}$	0.6	2.039061(7)	7.8	$1.84^{+0.09+0.11}_{-0.08-0.06}$
$^{82}\text{Se} \rightarrow ^{82}\text{Kr}$	2.7	2.99512(201)	9.2	$0.096 \pm 0.003 \pm 0.01$
$^{96}\text{Zr} \rightarrow ^{96}\text{Mo}$	5.6	3.35037(289)	2.8	$0.0235 \pm 0.0014 \pm 0.0016$
$^{100}\text{Mo} \rightarrow ^{100}\text{Ru}$	4.4	3.03440(17)	9.6	$0.00711 \pm 0.00002 \pm 0.00054$
$^{116}\text{Cd} \rightarrow ^{116}\text{Sn}$	4.6	2.81350(13)	7.6	$0.029^{+0.004}_{-0.003}$
$^{128}\text{Te} \rightarrow ^{128}\text{Xe}$	0.1	0.86587(131)	31.7	7200 ± 400
$^{130}\text{Te} \rightarrow ^{130}\text{Xe}$	4.1	2.52697(23)	34.5	$0.7 \pm 0.09 \pm 0.11$
$^{136}\text{Xe} \rightarrow ^{136}\text{Ba}$	4.3	2.45783(37)	8.9	$2.165 \pm 0.016 \pm 0.059$
$^{150}\text{Nd} \rightarrow ^{150}\text{Sm}$	19.2	3.37138(20)	5.6	$0.00911^{+0.00025}_{-0.00022} \pm 0.00063$
$^{238}\text{U} \rightarrow ^{238}\text{Pu}$	3.4	1.14498(125)	99.3	2.0 ± 0.6

Table 2.1: List of naturally occurring isotopes that could undergo double beta decay with the corresponding phase space factor $G_{0\nu\beta\beta}$, Q -value, natural abundance and $0\nu\beta\beta$ half-life $T_{1/2}^{0\nu\beta\beta}$. Table adapted from [57].

determination of the effective Majorana mass $|m_{\beta\beta}|$ due to the huge discrepancies between different approaches.

In specific terms of $T_{1/2}^{0\nu\beta\beta}$ measurements, the present day experiments are only able to provide lower bounds. Experimental indications on the existence of $0\nu\beta\beta$ remain inconclusive. The results lead to an upper limit on the effective Majorana mass with KamLAND-Zen currently laying down the most stringent limit of $|m_{\beta\beta}| < 61 - 165$ meV ($T_{1/2}^{0\nu\beta\beta} > 1.07 \times 10^{26}$ years) [65].

Owing to the expected rareness of the $0\nu\beta\beta$ process, approaches taken by experiments can generally fall into two categories. The first is to minimise the sacrifice on the signal by rendering the detector ultra-pure, with nearly no backgrounds, and with particularly fine energy resolution. This includes NEMO-3 and its successor, SuperNEMO, using ^{100}Mo [66]; GERDA [67] using ^{76}Ge ; and CUORE [68] using ^{130}Te . The other is to scale the signal up by pursuing a sizeable detector, though inevitably with slightly enhanced backgrounds. Pioneered by KamLAND-Zen, which uses ^{136}Xe [65], this approach was adapted by SNO+. The SNO+ experiment will be studying $0\nu\beta\beta$ in ^{130}Te . ^{130}Te was chosen for various reasons including the relatively

high energy release in $0\nu\beta\beta$, longer $2\nu\beta\beta$ lifetime and high natural abundance, which makes it more affordable for kilotonne experiments [69]. Details of the SNO+ detector will be described in Chapter 4. In addition, backgrounds arising from bismuth-polonium decays in the uranium and thorium decay chains that fall in the spectral region of interest (ROI) (see Figure 4.5) will be studied in Chapter 5.

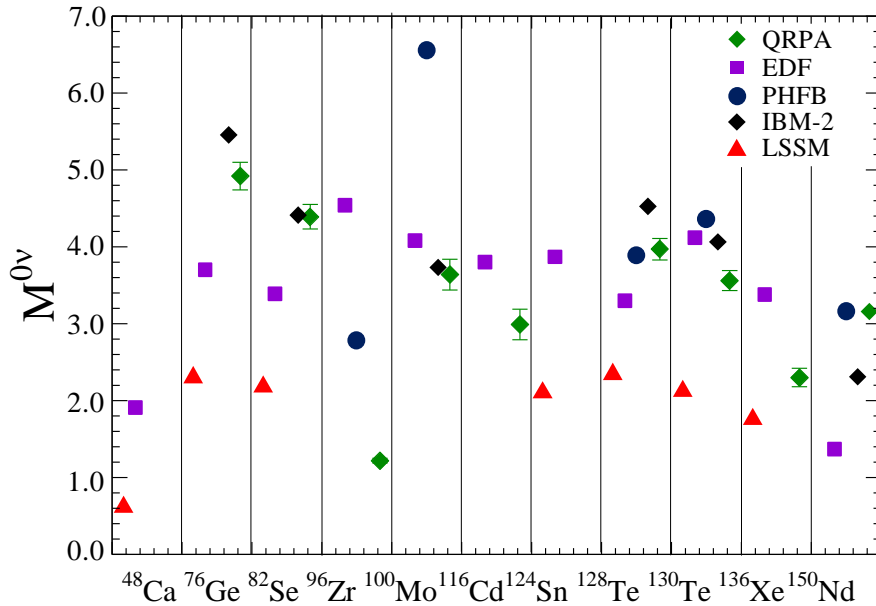


Figure 2.6: Calculated nuclear matrix element $\mathcal{M}_{0\nu\beta\beta}$ values, taken from [70].

Chapter 3

Core-Collapse Supernovae

On the 24th of February, 1987, the blue supergiant Sanduleak -69 202, located in the Large Magellanic Cloud about 50 kpcⁱ from Earth, underwent a supernova explosion and became what is now known as SN1987A [73]. The signals of SN1987A started out with bursts of neutrinos, and was soon followed by the optical signals within 3 hours [73], which was consistent with the expectation for a core-collapse supernova (CCSN). Further studies on the optical spectrum suggested that it was of type II, a type that is believed to release 99% of its energy in the form of neutrino emissions [74].

The neutrino signals of the event were observed in three detectors, one liquid scintillator detector and two water Cherenkov detectors, on Earth: 5 events detected by the Baksan detector [75]; 12 events, in which one of the events was identified as background, detected by the Kamiokande-II experiment [76]; and 8 events observed in the Irvine-Michigan-Brookhaven (IMB) detector [77]. All of these neutrino events were inverse beta decays (IBD), arising from electron anti-neutrinos, though in general all types and flavours of neutrinos are expected from a supernova burst. These 24 neutrino events observed in 13 seconds associated with this super-luminous event were the first, and so far only, confirmed neutrino observations from celestial bodies other than the Sun.

Even though the datasets, containing only a small number of events, were insufficient to result in a measurement of the supernova or neutrino parameters, the observation was still able to set constraints on neutrino properties under extreme conditions and illuminate several aspects of the underlying mechanisms driving the supernova. It clearly demonstrated the enormous potential of supernova neutrino detections in astronomy and astro-particle physics. In this chapter, the evolution of

ⁱA parsec (pc) is defined as $\frac{62800}{\pi}$ astronomical units (au) [71], where an astronomical unit is defined to be exactly 149,597,870,700 metres [72]. Therefore, a kiloparsec (kpc) will be roughly 3260 light-years or 3.086×10^{19} metres.

the stellar progenitor and mechanisms leading to the various types of supernovae will be briefly outlined, in which attention will be put on the CCSN. Furthermore, due to the small cross-sections of neutrino interactions, supernova neutrino detection is practically confined to Galactic supernovae. The occurrence of such events will also be discussed. Finally, the neutrino spectrum will be examined analytically together with a brief review of the numerical simulation of the neutrino luminosity curves obtained from the Garching group [78].

3.1 Stellar Evolution

The formation of stars begins from the condensation of interstellar matter in molecular clouds forming relatively dense proto-stellar cores. As ambient matter continues to accrete onto the proto-stellar core, gravity eventually overcomes the supporting thermal pressure leading to gravitational collapse. The compression from gravity causes the core to further condense and rise in temperature until reaching the point, roughly 10^7 K [79], at which hydrogen fusion ignites. With the energy released from hydrogen fusion balancing gravity, hydrostatic equilibrium is restored. At this stage, the star can be said to have formed. Such a star is known as a “Zero Age Main Sequence” (ZAMS) star, which is when the star first joins the Main Sequence. The Main Sequence is a band of stars on the Hertzsprung-Russell diagram [80, 81] where the majority of stars are to be found in, as shown in Figure 3.1. Stellar masses quoted hereafter will be the ZAMS mass of the stars. A star will leave the Main Sequence once its core is depleted of hydrogen. In general, massive stars tend to exhaust their hydrogen deposits faster and, hence, have shorter Main Sequence lifetimes.

When intermediate-mass stars, of comparable mass to the Sun ($0.5 - 8M_{\odot}$) [79, 82], reach their end in the Main Sequence, the hydrogen in their cores will be replaced by the helium produced from hydrogen fusion, terminating the nuclear fusion in the stellar core. The core then cools down leading to gravitational contraction of the core, causing the core temperature to rise again from the gravitational energy release. As the heat diffuses, the hydrogen shell adjacent to the helium core will reach the critical temperature initiating hydrogen fusion. The hydrogen shell is then “deflagrated”, that is, the burning shell gradually ignites the surrounding hydrogen, which is known as “shell hydrogen burning”. The helium product from shell burning accumulates onto the core, leading to further core contraction. With these additional sources of thermal energy and, hence, increase in internal pressure, one will see a substantial expansion in the outer hydrogen envelope. Along with the expansion, the outer layers will simultaneously cool down, shifting the colour of the star towards the red spectrum. At the end of this process, viz., when the expansion has ceased, the star enters the “red giant phase”.

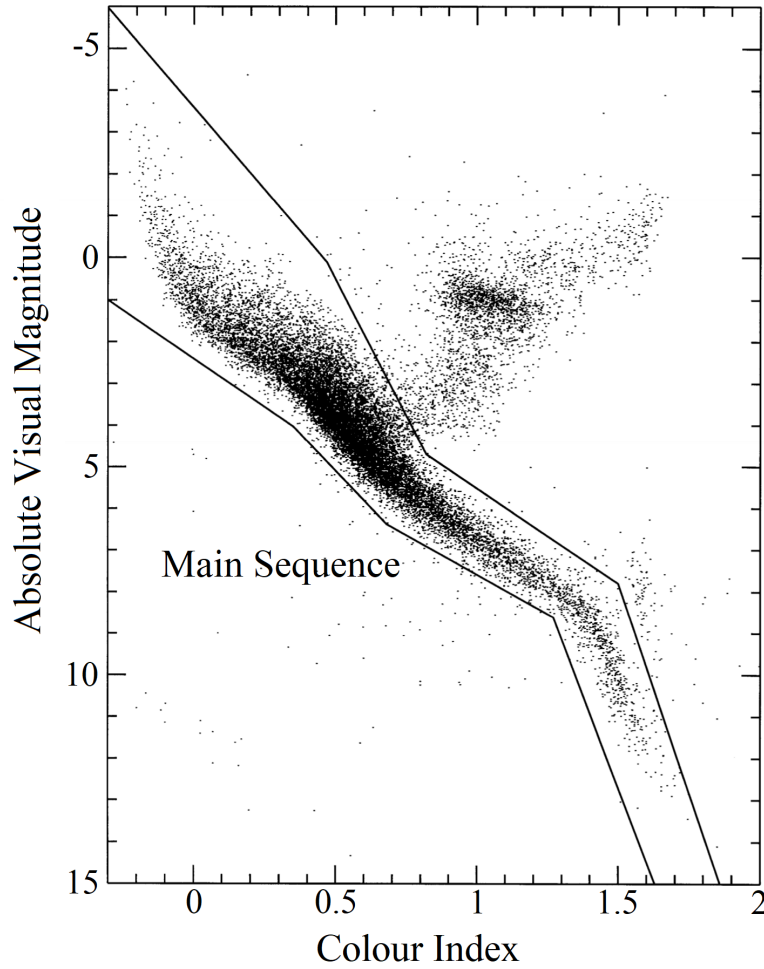


Figure 3.1: Hertzsprung-Russell diagram of the stars catalogued by the Hipparcos satellite. The colour index is a measure of the stellar surface temperature, where smaller indices refer to bluer (hotter) objects and larger indices redder (cooler) [83]. Depending on the mass, stars can enter the Main Sequence at any part of the band. As the stars evolve, they tend to drift towards the top right of the plot, whereas dwarf stars and neutron stars tend to fall below the main sequence. Figure adapted from [84].

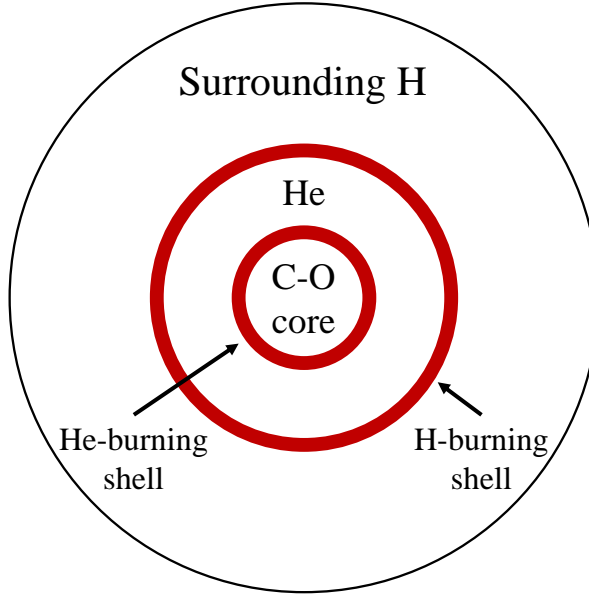


Figure 3.2: Schematic representation of the double shell burning phase, or asymptotic giant branch phase. Figure adapted from [79].

Once the core reaches a temperature of 10^8 K [79], the helium core ignites. Helium fusion produces carbon and oxygen in the core, whilst shell burning is still generating helium that builds on top of the core, creating a layered structure. Note that the ignition of helium would only happen when the star mass is greater than $0.5M_\odot$, below which the core will reach the electron degeneracy density 10^6 g/cm³ before the helium ignition temperature is reached, prohibiting the core temperature from rising further and eventually leading to the formation of a helium white dwarf [79].

For stars of mass greater than $0.5M_\odot$, the helium in the core will eventually be depleted, leaving inertⁱⁱ carbon and oxygen. Unsurprisingly, a process similar to what happened during the end of the Main Sequence takes place: shell helium burning, core contraction and envelope expansion. As it is reminiscent of the red giant phase, stars in this phase are known as the “asymptotic giant branch” (AGB) starsⁱⁱⁱ. This phase is sometimes referred to as the “double shell burning phase” for obvious reasons depicted in Figure 3.2.

The evolution of an intermediate sized star terminates with the end of the AGB

ⁱⁱInert in the sense of nuclear fusion being energetically unfavourable.

ⁱⁱⁱThe term asymptotic is used in the sense that for lighter stars, of mass less than $2.5M_\odot$, the temperature-luminosity relation resembles that of the red giants [85].

Fusion Fuel	Ignition Temperature	Duration	Main Products
Carbon	5×10^8 K	$10^3 - 10^4$ yr	Ne, Na
Neon	8×10^8 K	$10^2 - 10^3$ yr	Mg, O
Oxygen	1×10^9 K	< 1yr	Si, S
Silicon	3×10^9 K	days	^{56}Ni

Table 3.1: List of nuclear fusion channels past hydrogen and helium. The product of silicon burning is ^{56}Ni , of which part will further decay to ^{56}Fe via beta decays, forming the nickel-iron core. Table adapted from [79].

phase. During this stage, AGB stars will develop strong stellar winds due to the expansion and cooling of the outer envelope. As the envelope cools down, gas in the envelope condenses into dust which absorbs radiation more efficiently. These accelerated dust grains will then collide and drag the gas particles in the outer layers along as they escape the relatively weak gravity, creating a stellar wind. Note that although this stellar wind is also present in some red giants, the AGB wind is about 1,000 times greater than that of red giants, earning the AGB phase the name “superwind phase” [86]. This strong stellar wind leads to significant mass loss, which eventually dissipates all outer layers beyond the core. The star, therefore, ends up as a carbon-oxygen white dwarf. It should be noted that the white dwarf, supported by electron degeneracy pressure, is bounded by the Chandrasekhar mass limit of about $1.4M_{\odot}$, corresponding to a ZAMS star mass of roughly $8M_{\odot}$ [87, 88].

Massive stars with masses greater than $8M_{\odot}$, on the other hand, will have core temperatures rising beyond the ignition temperatures for further nuclear reactions, as listed in Table 3.1. Each burning stage is essentially a repetition of what has occurred in the hydrogen and helium burning phases. Note that the ZAMS mass of the star determines which burning phase it reaches. For stars in the mass range $8 - 10M_{\odot}$, the evolution terminates at the stage of neon burning, resulting in an oxygen-neon-magnesium (ONeMg) core. Stars of even higher masses, in the range of $10 - 40M_{\odot}$, will proceed all the way to silicon burning, which ends up with an iron (Fe) core, as depicted in Figure 3.3. Stars with ONeMg cores are designated “super-AGB stars”, whereas the ones that reach silicon burning are known as “supergiants” [89]. In both cases, the stellar cores exceed the Chandrasekhar limit and are expected to undergo a final “core collapse” upon the end of evolution, leading to a core-collapse supernova (CCSN), which will be discussed in more detail in Section 3.3.

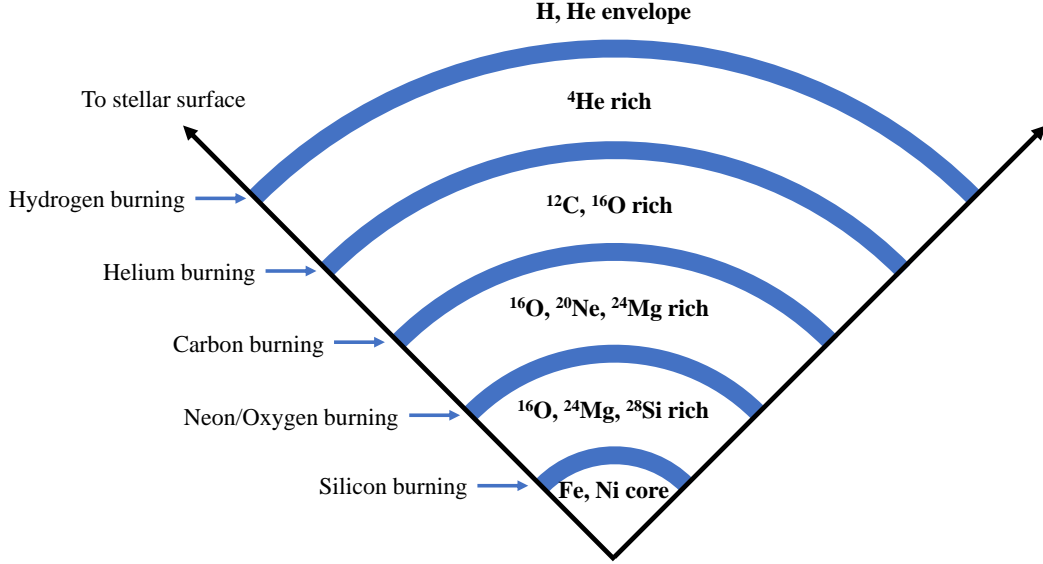


Figure 3.3: Schematic view of the layered structure of stellar progenitors that reach silicon burning. Figure adapted from [95].

Finally, there is the case of stars with masses beyond $40 M_{\odot}$, for which the eventual fate is uncertain. Possibilities include CCSN, pair-instability supernova [90, 91, 92] or direct collapse to a black hole without a supernova-like explosion [93, 94]. Details of these scenarios will also be briefly discussed in Section 3.3.

3.2 Supernova Classification

The astronomical classification for supernovae is summarised and depicted in Figure 3.4. This classification of supernovae is largely based on the absorption lines and further subdivided according to the features of the light curve profiles due to historical reasons. Note that such a division of the supernovae is not necessarily the most suitable for the discussion of neutrino physics. This section shall start with a brief historical review of the classification to introduce the terminology, and conclude in a classification that is more relevant to the discussion of neutrino physics. More detailed information can be found in [96, 97, 98].

The primary division was first established by Minkowski in 1941 [99], when he noticed there are two types of supernovae: the ones lacking hydrogen lines in their spectrum (type I) and the ones with it (type II). The type I could be further cat-

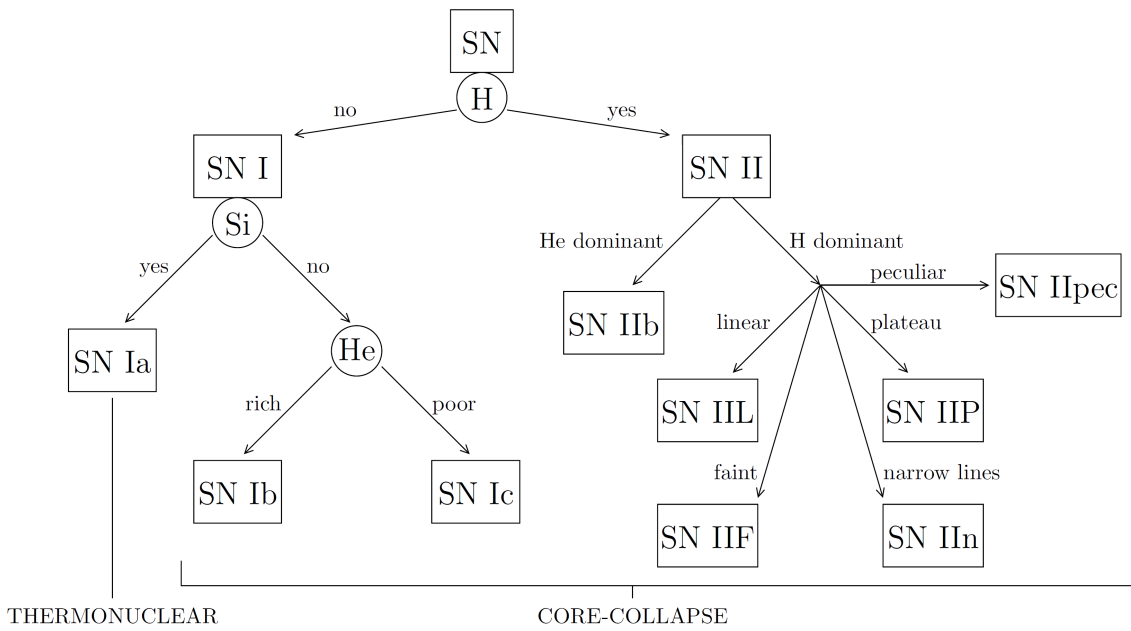


Figure 3.4: Classification scheme of supernovae using spectral line features, luminosity profiles and the corresponding spectral evolution. Figure originally from [9].

egorised into three cases depending on the presence of strong silicon and helium absorption features in the near maximum spectrum ^{iv}. This primitive classification remained as the main spectral division, even though it was discovered as early as the 1960s that there are spectral variations within type I. In 1963, McLaughlin [100] observed particularly strong helium absorption in the spectrum of SN1954A upon near maximum luminosity, which was different from what was regarded as a classical type I, now type Ia, and was later categorised as type Ib. It was not until the 1980s that the necessity to further specify the subdivisions in type I became apparent. With an increasing number of type I supernovae exhibiting spectral features deviating from that of “classical” type I, Elias *et al.*, in 1985, were the first to introduce the designation of sub-types Ia/Ib using broad-band infrared photometry [101]. The more well-known criterion of type Ia showing strong silicon absorption in the near maximum spectrum was proposed slightly later by Branch [102]. Following that, Wheeler and Harkness [103] proposed another division within the non-Ia type according to the helium absorption features, strong in type Ib and weak or none in type Ic.

On the other hand, there is as yet no consensus on spectroscopic sub-classifications of type II. The first attempt to categorise the type II supernovae was by Barbon *et al.*

^{iv}This is the spectrum of the supernova when maximum luminosity is reached.

in 1979 using the light curve shapes [104]. Depending on whether the behaviour of the luminosity profile after maximum is characterised by a plateau or linear decline, the type II supernovae are subdivided into type IIP for the former case and type IIL for the latter. Note that this division is not strict and there are indeed intermediate cases, e.g., see [105]. Furthermore, there is a more recent suggestion of the subclass IIF for supernovae with an overall substantially fainter light curve [106]. In 1988, Filippenko discovered the supernova SN1987K showing strong hydrogen absorption in early stages and starting to resemble the helium-dominated spectral features of type Ib as it evolves, which was then designated as type IIb [107]. Amongst the more regular type II supernovae not displaying obvious helium features, another subclass IIn was proposed by Schlegel for cases when the spectrum exhibits particularly narrow hydrogen lines [108]. Finally, for the type II supernovae that do not exactly fit any of the aforementioned criteria was suggested to be conveniently referred to as IIPec in [109].

Having introduced all the classes outlined in Figure 3.4, there is then the issue of how they affect the detection of the neutrino signal, in other words, how it affects the neutrino flux. The behaviour of the supernova neutrino flux is more related to the structure and final stages of the stellar progenitor, which will eventually lead to different explosion mechanisms. A more suitable distinction should, therefore, be drawn between the thermonuclear supernovae (type Ia), ignited on binary white dwarfs of zero-age masses presumably around $8M_{\odot}$ [110], and CCSNe (type Ib/c, II), for relatively more massive progenitors of masses roughly above $8M_{\odot}$. Herein the focus will be put on CCSNe for the reason that the thermonuclear supernovae would have most of its energy released via heavy element nucleosynthesis, whereas the CCSNe are expected to transfer 99% of its energy in the form of neutrinos [74].

3.3 Core-Collapse Mechanisms

The evolution of massive stars with ZAMS mass greater than $8M_{\odot}$ is expected to end in core collapse. There are several mechanisms that could lead to this eventual implosion of the progenitor core: electron capture instability, iron core disintegration, pair instability and photodisintegration. The stellar progenitor dependence, mainly on mass and metallicity^v, of these scenarios and their corresponding supernova/remnant types are discussed in detail in [93, 111], and concisely summarised in Figure 3.5. It is worth noting, though, that it was pointed out in [112], the compactness^{vi} of the stellar structure serves as a robust parameter in predicting the fate of the supernova remnant. In this section, each of the mechanisms listed above will be briefly outlined, amongst which the case of iron core collapse will be examined in a slightly more thorough manner for it is considered as the classical scenario for CCSNe.

3.3.1 Iron Core Disintegration

To start with, consider the case of the heavier stellar progenitors in the mass range $10 - 100M_{\odot}$. As described in Section 3.1, these progenitors are able to proceed up to silicon burning in their evolution, resulting in a core formed by inert iron-group elements, viz., iron (Fe), cobalt (Co) and nickel (Ni)^{vii}, as in Figure 3.3. In the end, the progenitor is expected to undergo a CCSN, which can be of type II or Ib/Ic. Note the latter case occurs when the star is sufficiently massive and with high enough metallicity, inducing strong stellar winds that dissipates the hydrogen and helium envelopes. Furthermore, depending on the progenitor, the final remnant of the supernova can be either a neutron star or a black hole, where the mass division is usually drawn around $40M_{\odot}$ for solar metallicities.

The CCSNe evolving via the iron core collapse scenario are the most common type of CCSNe, constituting up 60% of the total CCSNe [57], and are, therefore, usually taken as the typical scheme for CCSNe. The development of such supernovae, and in general any CCSNe, can roughly be divided into four stages: core collapse, core bounce, accretion and cooling. The details of each stage and the corresponding neutrino emissions will be described in this section.

^vMetallicity is the mass fraction of elements present in the star that are heavier than hydrogen and helium. The term stems from the astronomical convention of referring to any element besides hydrogen and helium as “metal”.

^{vi}Compactness is defined as $\xi_M = \frac{(M/M_{\odot})}{R}$, where M is a fiducial baryonic mass chosen to be $2.5M_{\odot}$ in [112], and R is the radius enclosing the chosen fiducial mass in units of 1,000 km.

^{vii}These three elements are also known as the “iron triad” [113].

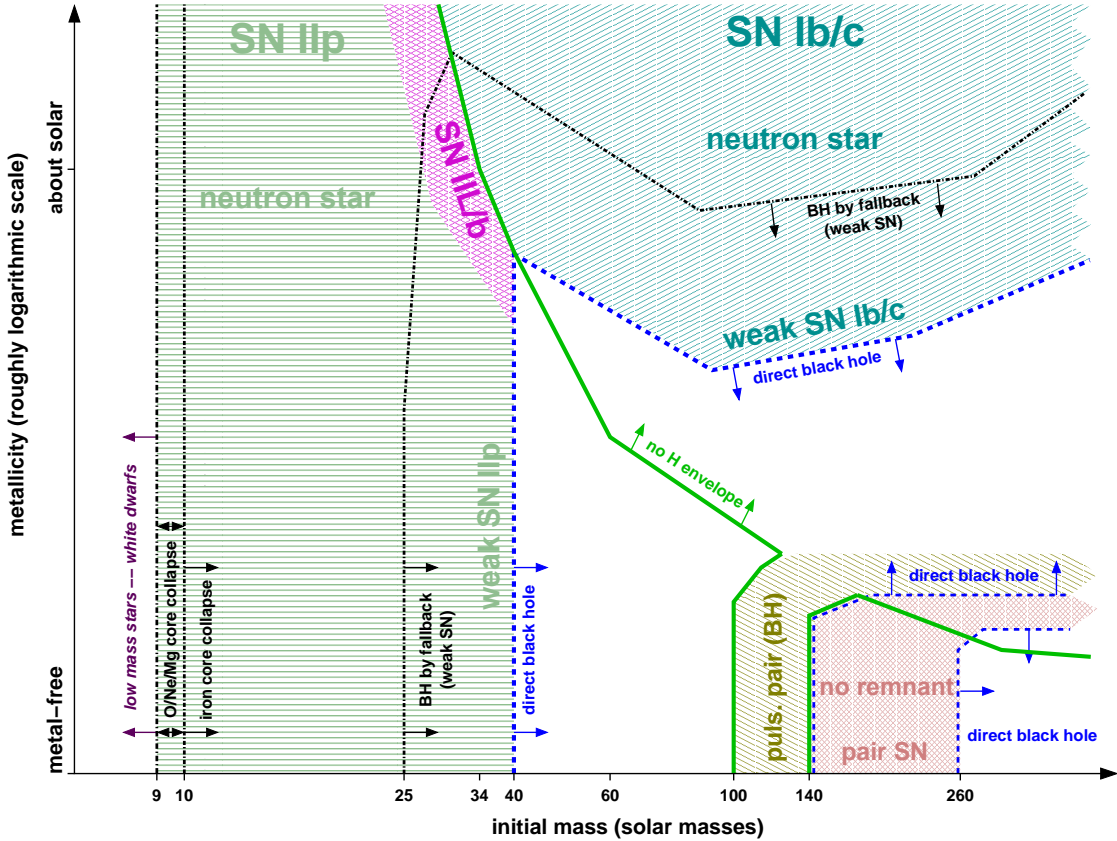


Figure 3.5: Types of supernovae according to the ZAMS mass and metallicity of the stellar progenitors. The white regions on the right of the dotted blue lines indicate the region where no outward shock wave is launched, and, hence, no supernova. Figure adapted from [57], which was originally from [93].

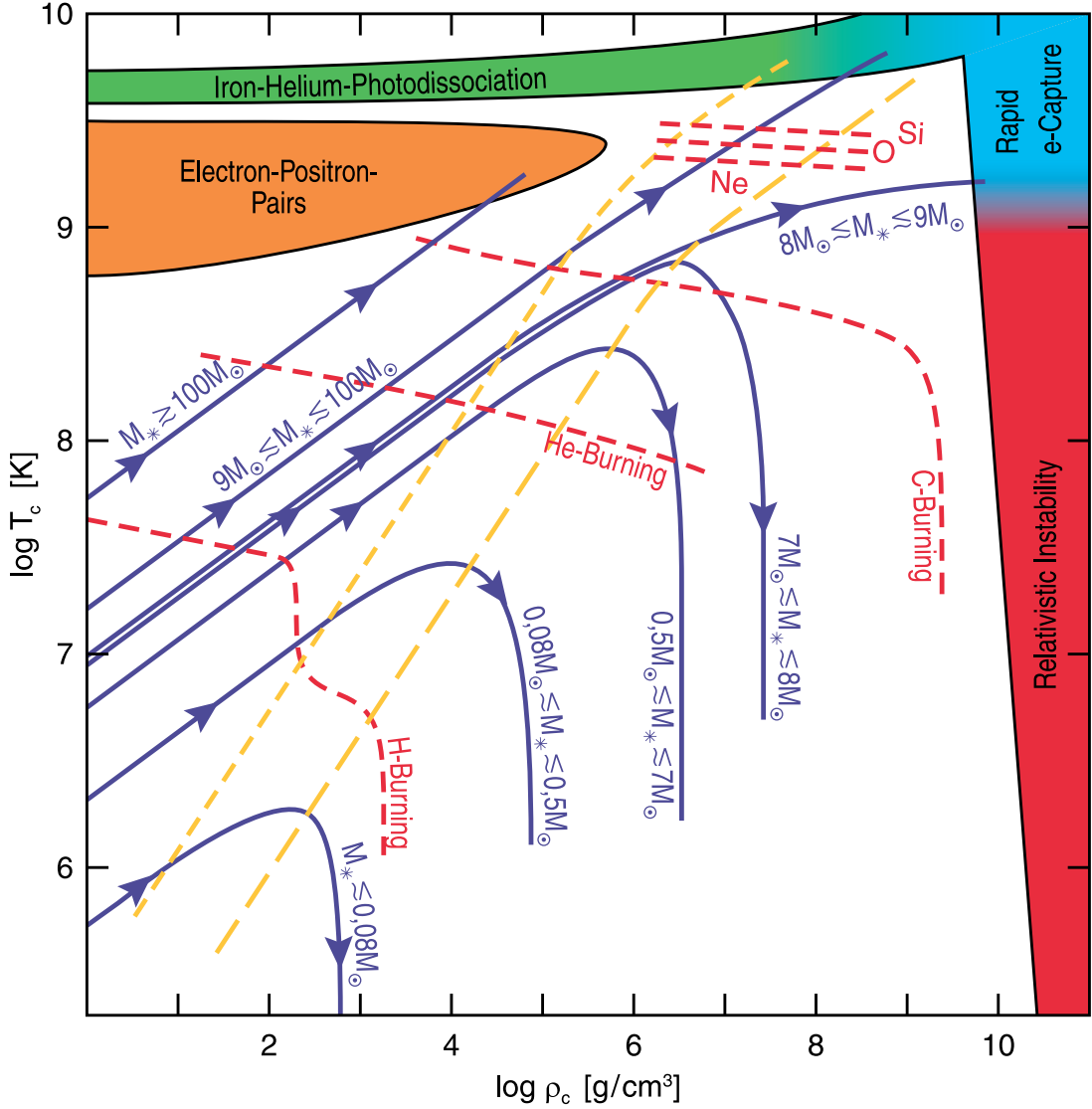


Figure 3.6: Relations between the evolution stages and stellar core configuration as a function of central temperature T_c and central density ρ_c . Coloured regions indicate where the evolution terminates. Blue lines are the evolution paths of the progenitors. Red lines show the boundaries of different fusion phases. Yellow lines mark the initiation of electron degeneracy (short-dashed) and neutron degeneracy (long-dashed). Figure taken from [111].

Core Collapse

As the stellar core enters the phase of silicon burning, the iron-group elements accumulate in the centre of the core, leading to a decrease in thermal pressure support. The core then contracts until electron degeneracy pressure comes into play, halting the collapse temporarily. When the mass exceeds the Chandrasekhar limit, typically when the iron core is of radius near 3,000 km [114], the core once again becomes gravitationally unstable. At this stage, the temperature and density reaches the point to initiate two reactions that would further destabilise the core: photodisintegration and electron capture.

The core temperature now approaches 10^{10} K, at which a state of nuclear statistical equilibrium (NSE)^{viii} is established, favouring free nucleons and alpha nuclei. To disintegrate nuclei as stable as the iron triad, the process must be strongly endothermic, which, in turn, dissipates the thermal pressure further. On the other hand, the rise in density eventually renders electron capture on ^{56}Fe energetically favourable, as indicated in Figure 3.6. In addition, the free protons from NSE in the core accelerates the decline in electron density. At the end, with the two major sources of support diminishing, core collapse begins.

During this process, the neutrinos produced via electron capture will be allowed to freely escape as long as the core density is below $10^{11} - 10^{12}$ g/cm³. This critical density is achieved in the inner regions of the iron core, at radii less than about 100 km, roughly 0.1 s after the outbreak of the instability [114]. The neutrinos will then be concealed until nuclear densities on the order of 10^{14} g/cm³ are reached, which leads to the next phase.

Core Bounce and the Neutronisation Burst

After the onset of the collapse, with little resistance compared to gravity, the core rapidly shrinks to a size of less than 10 km, hitting nuclear densities [114]. The collapse is then suddenly halted by repulsion from the nuclear strong force, and the rebounded material forms a shock front clashing upon the infalling material. The remnant behind the shockwave develops into a proto-neutron star (PNS) with a compact core and growing mantle of material traversing through the shock front. The still collapsing iron-group elements of the outer core will be disintegrated into free nucleons as the shockwave emanates through. The elevated number of liberated protons will induce rapid electron captures creating a copious amount of electron neutrinos trapped behind the shockwave.

The shock front remains opaque to the neutrinos until the shockwave reaches a

^{viii}Nuclear statistical equilibrium is the state at which the rate of photodisintegration and heavy-nuclei synthesis reach equilibrium [115, 116].

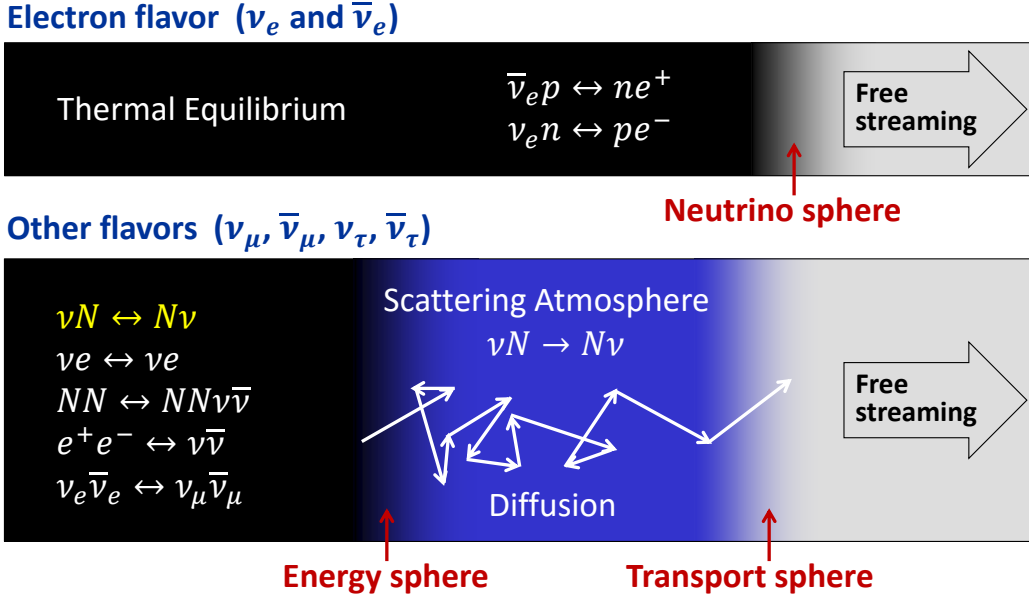


Figure 3.7: Schematic view of the transport properties of electron flavour (top) and non-electron flavour (bottom) neutrinos with corresponding production channels included. Unlike the case of electron flavour neutrinos, where the energy and transport spheres coincide, the energy sphere radius of the non-electron neutrinos are considerably smaller than that of the transport sphere. This is a result of the fact that the main source of opacity for non-electron neutrinos originates from neutrino-nucleon scattering, which is of relatively limited energy exchange. Therefore, the non-electron neutrinos fall out of thermal equilibrium with the stellar material at a much smaller radius. Figure originally from [117].

region of density of about 10^{11} g/cm³, which is expected to happen within 10 ms after the bounce [114]. This surface, beyond which neutrinos are set to stream out unhindered, is named the “neutrinosphere”^{ix}, in analogy to the photosphere in the case of a stellar surface [119]. Upon arrival at the neutrinosphere, the neutrinos confined behind the shock front will suddenly be released creating the most prominent feature in the light curve of supernova neutrinos, the “neutronisation burst”. During the few milliseconds of the burst, the neutrino luminosity is expected to be on the

^{ix}Usually defined as the point where the optical depth of neutrinos reaches unity [117]. The optical depth is defined as the number of mean free paths travelled along a trajectory (see Section 3.5.2). This definition of the neutrinosphere is also often referred to as the “transport sphere” [117, 118]. Another common definition known as the “energy sphere” is defined to be the surface where neutrinos cease to be in thermal equilibrium with the stellar matter [117, 118]. Note that these two definitions do not necessarily coincide, as shown in Figure 3.7.

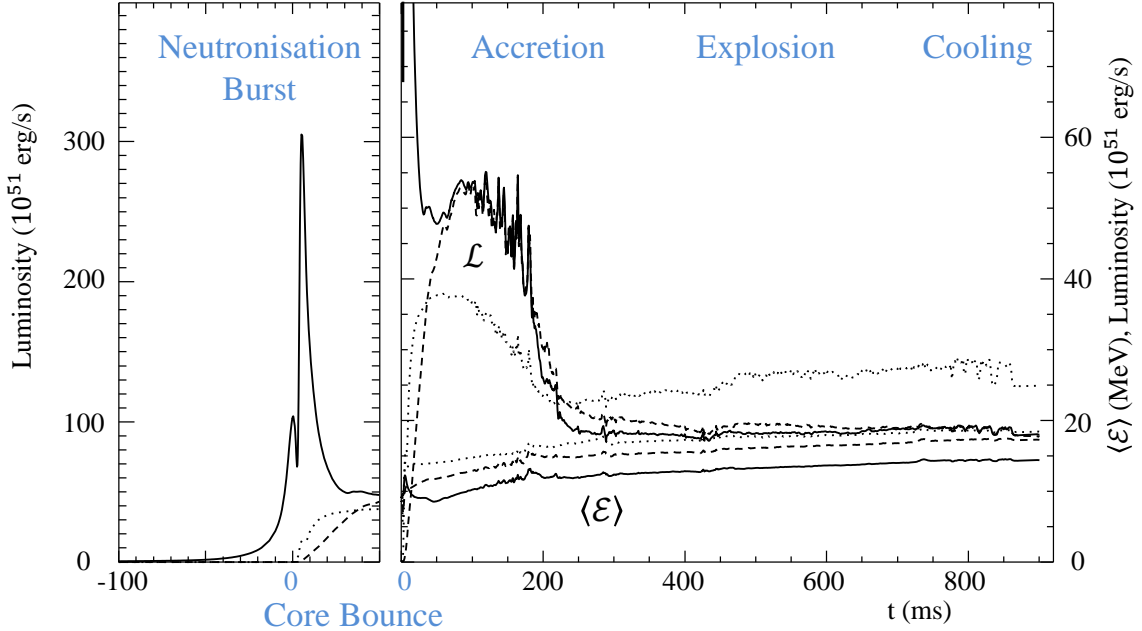


Figure 3.8: Luminosity evolution of ν_e (solid), $\bar{\nu}_e$ (dashed) and ν_x (non-electron flavour neutrinos) (dotted) from simulation of a $15M_\odot$ progenitor. Figure adapted from [57], which was originally from [120].

order of 10^{53} erg/s [120]. Note that the burst does not have strong dependence on the progenitor mass, as a result of the universality in the characteristics of the subsonic collapse and bounce dynamics [121].

The transmission of the shockwave sees severe energy dissipation from the disintegration of iron-group elements, consequently stalling the shock. The shock is expected to stall at the radius between $100 - 200$ km, which happens about 100 ms after the core bounce [114, 117]. In the past, it was thought that the core bounce shock would be able to instantly launch a supernova within several hundred milliseconds. More recent simulations appear to be in agreement with models from the 1980s and 1990s, which disfavours such prompt explosions [114].

Accretion Phase and Shock Revival

As the shock dissipates, the supernova enters the accretion phase. At this stage of the evolution, infalling matter continues to accrete onto the PNS. The amount of mass accreted onto the PNS determines the eventual fate of the remnant. If the PNS, or the later-formed neutron star (NS), mass were to exceed the Tolman-Oppenheimer-

Volkoff limit [122, 123], the analogy of the Chandrasekhar limit, the PNS will implode into a black hole. For progenitors of mass above $40M_{\odot}$, the black hole is expected to form promptly from the core collapse with a core bounce too weak to induce a supernova; whereas in the case of relatively lighter progenitors in the mass range of $20 - 40M_{\odot}$, the black hole might be formed subsequent to a weak supernova from the aggregation of the remnants [124]. In the case of black hole formation, the light curve is expected to terminate abruptly due to the engulfment of the neutrino-rich core together with the strong gravitational redshift. This intriguing phenomenon will be discussed in more detail in Chapter 8.

Alongside the accreting matter, the increasing density and temperature allows thermal generation of neutrinos of all flavours. Moreover, the decrease in electron lepton number caused by the neutronisation burst gives rise to higher concentrations of positrons created from pair production [117], which, in turn, leads to the production of electron anti-neutrinos from positron capture. The channels for the production of different flavours of neutrinos are summarised in Figure 3.7. Since the electron flavour neutrinos can interact via the charged current channels, the luminosity of these neutrinos tend to be higher than that of the non-electron flavours, which is also clear from Figure 3.8.

To successfully launch a supernova, the standing shockwave will have to be revived. The exact mechanism for shockwave revival, possibly a combination of neutrino-heating, convection and magnetic fields, is still unclear and under intensive discussion [111]. At present, the scenario considered most likely is neutrino heating from the nascent PNS. Neutrinos emitted from the PNS are expected to heat up the stalled shockwave by ν_e and $\bar{\nu}_e$ captures on nucleons, as well as neutral current scatterings of all flavours. There is, however, the competing effect of neutrino cooling via neutrino losses from the aforementioned channels listed in Figure 3.7. Since the cooling rate along the radius falls more quickly than that of the heating rate^x, there will be a region in the shockwave of net gain in energy, called the “gain layer”. With sufficient energy deposited, on the order of $10^{50} - 10^{51}$ erg [126], the shockwave will be revived, initiating the final supernova explosion.

Cooling Phase

As the supernova explodes, expelling all the outer envelopes, the accretion phase comes to an end. The remnant PNS is left to collect what was left behind the

^xEnergy gain in the standing shock region is proportional to the inverse of the total area, assuming an isotropic distribution, $\propto R^{-2}$. The cooling rate, on the other hand, is proportional to T^6 (the luminosity $\propto T^4$ and the emission cross section $\propto T^2$), whereas the temperature of the atmosphere of a PNS falls with radius $T \propto R^{-1}$, the “shallow” case in [125]. Therefore, the cooling rate follows $\propto R^{-6}$.

shockwave and cool down. At this phase, the neutrino luminosity is expected to decrease almost exponentially. When the nascent NS becomes transparent to the neutrinos, tens of seconds after the explosion, the luminosity will see an even steeper decline [114]. Luminosities and energies amongst the different flavours are nearly uniform for the entire cooling phase. There are, in general, no further notable features to be expected past this point. Nonetheless, there are speculations that under certain circumstances things such as black hole formation can be postponed to as late as the cooling phase, for instance, see [127].

3.3.2 Electron Capture Instability

Stellar progenitors on the lighter end, $8 - 10M_{\odot}$, form an ONeMg core eventually sustained by the electron degeneracy pressure, as discussed in Section 3.1 and plotted in Figure 3.6. With the core elements remaining inert and shell burning carrying on, the core density, and thus the Fermi energy, continues to increase until the point where electron captures on neon and magnesium become energetically favourable [111]. This capture greatly reduces the degeneracy pressure from the electrons leading to an eventual collapse. Along with the core contraction, the central temperature of the core soon meets the oxygen ignition temperature, initiating oxygen deflagration [128, 129]. The infalling matter is then incinerated at the oxygen deflagration front into a state of NSE. The rate of electron capture will be accelerated in NSE regions, i.e., the core, due to the rapid captures on free protons, which, in turn, further accelerates the process of the core collapse. Finally, a proto-neutron star (PNS) will be formed in the core once it reaches nuclear densities, at which point the collapse is halted by the nuclear strong force. The subsequent evolution, and consequent supernova, proceeds in a similar fashion as in the iron CCSN case described in Section 3.3.1.

This supernova, type II in fact [128], is most commonly known as the “electron-capture supernova”, and it is estimated to constitute around $20 - 30\%$ of the total CCSN rate [111, 130, 131]. It is accompanied by copious neutrino emissions, yet of relatively lower energies compared to that of the iron CCSN, due to the comparatively cooler core [119, 132].

3.3.3 Pulsational Pair Instability

Supermassive stellar progenitors, of masses about $100 - 260M_{\odot}$ and with low metallicity, destabilise via another route. These supermassive stars are able to reach temperatures sufficiently high for electron-positron pair production at relatively lower densities, and thus lower degeneracy suppression on pair production [133]. Typically, when the core temperature reaches 10^9 K, i.e., soon after carbon burning, the pair production sees a strong onset [90, 92]. The conversion of photons into electron/positron

pairs dissipates a significant amount of energy leading to instant destabilisation of the core, followed by gravitational collapse. As the core contracts, similar to the case of the electron-capture supernova in Section 3.3.2, the core temperature rises to the ignition temperature for oxygen. Nonetheless, for such massive stars with extraordinary gravitational pressure, the exothermic oxygen fusion does not lead to immediate expansion of the core, and, hence, further accelerates the fusion by the increased temperature, creating a self-reinforcing loop. This will eventually lead to oxygen “detonation”, viz., an oxygen-induced thermonuclear runaway explosion.

For stars of mass $100 - 140M_{\odot}$, this primary explosion is expected to be merely able to expel some outer layers [92, 93]. After the primary explosion, the remnant core contracts again to resume hydrostatic equilibrium, commencing a new cycle. When pair instability onsets once more, a secondary detonation occurs, ejecting another few solar masses of matter. This repeating process continues until the progenitor mass drops below $100M_{\odot}$, at which point it is expected to either evolve along the normal CCSN route, as described in Section 3.3.1, or be completely unbound by the last thermonuclear runaway explosion [93]. Owing to the repetitive pulsational feature, it has earned the name “pulsational pair-instability supernova”.

On the even heavier side of these stars, $140 - 260M_{\odot}$, it is expected that the progenitor will be obliterated in the first round of thermonuclear explosions, which makes it a pure “pair-instability supernova” [92, 93]. Additionally, metallicity shifts the mass threshold upwards to compensate for the mass loss from stellar wind, as shown in Figure 3.5. The occurrences of pair-instability supernovae are, in fact, quite scarce, only about 2% of CCSNe by including both the pulsational and non-pulsational cases [93].

3.3.4 Photodisintegration

Finally, for stellar progenitors of the absolute highest masses, $> 260M_{\odot}$, the thermally produced photons near the end of carbon burning can become sufficiently energetic to disintegrate the nuclei, strongly endothermic, in the core, inducing an implosion [93, 134]. Due to the exceptionally high mass of the progenitor, the ignition of any fusion will not help in disrupting the collapse. In the end, the star simply collapses into a massive black hole during the first instance of core collapse without any sign of core bounce or supernova explosion.

3.4 Galactic Supernova

Supernovae, in general, are quite common in the universe. In fact, a few hundred such events are catalogued every year using current optical telescopes [135]. Next generation telescopes such as LSST is expecting roughly a million supernova observations per year [136]. A galactic supernova, however, is extremely rare, or at least the observations of such an incident are exceptionally rare. The previous directly observed supernova in our galaxy was in 1604, also commonly known as “Kepler’s supernova”, which was roughly 6.1 kpc from Earth in the constellation Ophiuchus [137]. No further trace, besides remnants, of galactic supernovae have been observed since then.

The rate of galactic CCSN was estimated to be $3.2^{+7.3}_{-2.6}$ per century in [138]. Furthermore, in [138], a modelled probability distribution of galactic supernovae against distance from Earth was carried out. The result is shown in Figure 3.9. The resulting differential distribution peaks at 9 kpc, indicating that it is the most likely distance of the next galactic supernova, and roughly half of the galactic supernovae are expected to occur within that distance. It is, therefore, common practice to set the distance at 10 kpc for supernova sensitivity studies [139, 140, 141]. For the studies conducted in this thesis, the supernova distance is also set at 10 kpc by default unless otherwise specified.

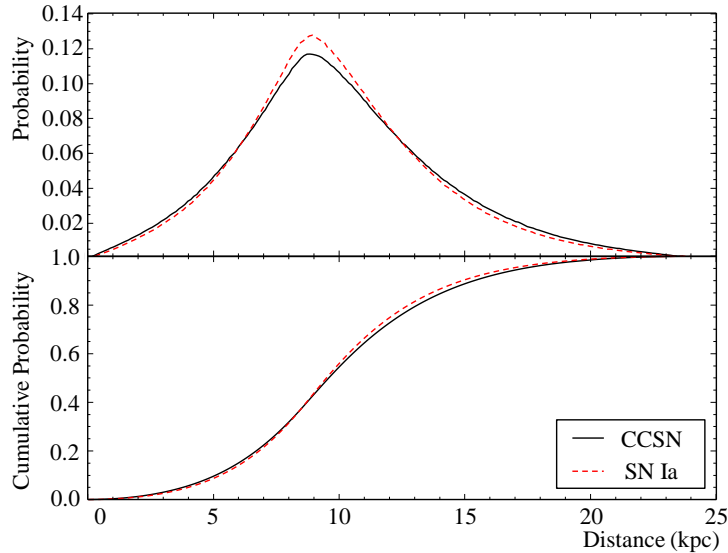


Figure 3.9: The differential (top) and cumulative (bottom) probability distribution of galactic CCSNe (black) and Type Ia supernovae (red) as a function of distance from Earth. Figure adapted from [138].

3.5 Supernova Neutrino Spectrum

This section will discuss the neutrino spectrum upon a supernova burst. A brief overview will be given on the Garching group simulations, which are the supernova models invoked in the studies in this thesis. Following that will be an analytical demonstration of how the neutrino spectrum can be estimated.

3.5.1 Supernova Simulations by the Garching Group

In this thesis, four sets of supernova light curves have been kindly provided by the Garching group at the Max Plank Institute for Astrophysics (MPA). These supernova light curves were simulated using the PROMETHEUS-VERTEX code [142, 143]. The flux simulation covers almost the full neutrino burst, and spherical symmetry is assumed for the entire process. In other words, these are one-dimensional simulations. The light curves are labelled as: ls220-s40.0c-bh, ls220-s40s7b2c-bh, ls220-s27.0co, shen-s8.8. The first two flux models are based on black-hole-forming models, hence the suffix, with progenitors of $40M_{\odot}$ from Woosley and Weaver [144], s40s7b2c, and from Woosley, Heger and Weaver [91], s40.0c. Additionally, the third light curve is based on a $27M_{\odot}$ standard iron core collapse model also from Woosley, Heger and Weaver [91]. All three of these models were carried out using the **ls220** equation of state by Lattimer and Swesty with nuclear incompressibility^{xi} set at 220 MeV [147]. The fourth model, on the other hand, is for an electron-capture supernova of progenitor mass $8.8M_{\odot}$ from Hüdepohl *et al.* [132], which uses a relatively stiffer equation of state labelled **shen** from Shen *et al.* [148]. Details of these models are summarised in Table 3.2. However, it should be noted that these one-dimensional simulations do not in general explode in a spontaneous manner, except for the $8.8M_{\odot}$ electron-capture supernova model. The iron core-collapse supernovae are launched artificially^{xii} at around 0.5 s post bounce.

^{xi}Nuclear incompressibility characterises the energy required per nucleon to compress the nuclear matter from a state of minimum binding energy, known as “saturation”, and is defined as $9n_0^2 \frac{\partial^2(E/A)}{\partial n^2}|_{n=n_0}$, where n is the nucleon number density and $n_0 = 0.16 \text{ fm}^{-3}$ is that upon saturation [145, 146].

^{xii}Popular methods include: the internal energy bomb, the piston-driven explosion and enhanced neutrino heating. The internal energy bomb approach injects significant amounts of heat to certain regions in the star, increasing its thermal pressure [149]. The piston-driven explosion inserts mass points, “pistons”, that follow specified trajectories into the star, which will push and accelerate the stellar material driving an explosion [144]. Finally, there is the enhanced neutrino heating method, where the neutrino opacity of the star is manually reinforced to increase the energy gain from neutrino heating [150].

Model Label	Equation of State	Progenitor Mass	Remnant	Reference
ls220-s40s7b2c-bh	ls220 [147]	$40M_{\odot}$	BH	[144]
ls220-s40.0c-bh	ls220 [147]	$40M_{\odot}$	BH	[91]
ls220-s27.0co	ls220 [147]	$27M_{\odot}$	NS	[91]
shen-s8.8	shen [148]	$8M_{\odot}$	NS	[132]

Table 3.2: List of Garching model light curves studied in this thesis. The remnant neutron stars and black holes are abbreviated as NS and BH, respectively.

3.5.2 Supernova Neutrino Energy Spectrum

Consider the case of neutrinos of flavour α emitted from a hot PNS. At a given luminosity \mathcal{L}_α and mean energy $\langle E_\alpha \rangle$, the rate of neutrinos emitted can be roughly estimated by

$$\frac{dN_\alpha}{dt}(t) = \frac{\mathcal{L}_\alpha(t)}{\langle E_\alpha \rangle(t)}. \quad (3.1)$$

Multiplied by the normalised energy distribution function, one arrives at the differential neutrino flux with respect to time t and energy E

$$\frac{d^2\Phi}{dEdt} = \frac{dN_\alpha}{dt} \times \frac{f_\alpha(E, t)}{\int_0^\infty f_\alpha(E, t)dE} \quad (3.2)$$

where $f_\alpha(E, t)$ is the energy distribution function of ν_α . Though it was predicted in [151] that the neutrino spectrum is likely to deviate from that of a thermal distribution, it was thought that the deviation is not large. The energy distribution can, therefore, still be parametrised in a form based on the Fermi-Dirac distribution [152]

$$f_\alpha(E, t) = \frac{E^2}{1 + \exp(E/T(t) - \eta_\alpha(t))} \quad (3.3)$$

where T is the temperature and η_α is the so-called degeneracy parameter, accounting for the deviation from the thermal distribution.

Indeed, it was then demonstrated in [153] that the neutrino luminosity spectrum is “pinched”, viz., the high and low energy ends are relatively suppressed whilst holding the mean energy constant. This is due to contributions from neutrinospheres associated with different neutrino energies, which are of varying temperatures. Consider the mean free path λ of the neutrino

$$\lambda \propto \rho^{-1}\sigma^{-1} \propto \rho^{-1}E^{-2} \quad (3.4)$$

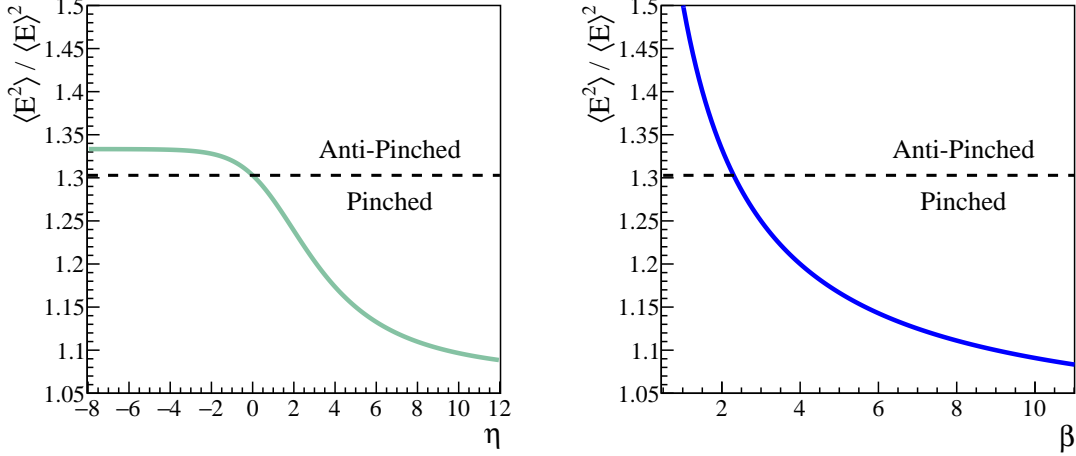


Figure 3.10: Spectrum pinching $\langle E^2 \rangle / \langle E \rangle^2$ versus the degeneracy parameter η (left) and shape parameter β (right). Figure adapted from [57].

where ρ is the density, σ is the cross section, and the relation $\sigma \propto E^2$ comes from ν -nucleon scattering (see Section 7.1.3). By the definition of the neutrinosphere, one then arrives at the expression

$$\int_{r_*(E)}^{\infty} \lambda^{-1} dr = 1 \quad (3.5)$$

where r_* is the radius of the neutrinosphere corresponding to the neutrino of energy E , i.e., the emission radius of the given neutrino. Suppose the matter profiles are of the form $\rho \propto r^{-\delta}$ and $T \propto r^{-\gamma}$, Eq. 3.5 suggests the following relations

$$r_* \propto E^{\frac{2}{\delta-1}}, \quad T_* \propto E^{\frac{-2\gamma}{\delta-1}}. \quad (3.6)$$

This leads to the spectral luminosity distribution

$$\frac{d\mathcal{L}_\alpha}{dE} \propto 4\pi r_*^2 \times \frac{E^3}{1 + \exp(E/T_*)} \propto \frac{E^{3+\frac{4}{\delta-1}}}{1 + \exp(C \cdot E^{1+\frac{2\gamma}{\delta-1}})} \quad (3.7)$$

where C is some proportionality constant. Given that $\delta > 1$ and $\gamma > 0$ [154], it is then clear from Eq. 3.7 that the luminosity of higher and lower energy neutrinos are relatively suppressed.

The degree of pinching in the distribution can be characterised by the pinching parameter p_α , proposed in [155],

$$p_\alpha = \frac{\langle E^2 \rangle / \langle E \rangle^2}{\langle E^2 \rangle / \langle E \rangle^2|_{\eta=0}} \quad (3.8)$$

where the denominator can be calculated without much difficulty [125]

$$\left. \frac{\langle E^2 \rangle}{\langle E \rangle^2} \right|_{\eta=0} \approx 1.3029. \quad (3.9)$$

From the expression of Eq. 3.8, it is obvious that the extremities of the spectrum will be pinched for $p_\alpha < 1$, and enhanced (the so-called “anti-pinching”) if $p_\alpha > 1$.

As it turns out, the thermal picture does not fit the supernova core conditions. The basis for describing the spectrum with a Fermi-Dirac-like form does not stand out as convincing as it initially appeared to be. Therefore, another parametrisation of the energy distribution function, proposed in [125] on the basis of analytical simplicity, is frequently quoted in later studies

$$f_\alpha(E, t) = \left(\frac{E}{\langle E \rangle(t)} \right)^{\beta_\alpha(t)} \exp \left(-(1 + \beta_\alpha(t)) \frac{E}{\langle E \rangle(t)} \right) \quad (3.10)$$

where β_α is called the shape parameter defined by the relation

$$\frac{\langle E^2 \rangle}{\langle E \rangle^2} = \frac{2 + \beta_\alpha}{1 + \beta_\alpha}, \quad (3.11)$$

and thus

$$\beta_\alpha = \frac{2\langle E \rangle^2 - \langle E^2 \rangle}{\langle E^2 \rangle - \langle E \rangle^2}. \quad (3.12)$$

The energy distribution in this form is now simply characterised by the shape parameter β_α and mean energy $\langle E \rangle$. Furthermore, the advantage of parametrising the distribution in the form of Eq. 3.10 is best exhibited in the reproduction of the anti-pinched spectrum. It is evident from Figure 3.10 that $\langle E^2 \rangle / \langle E \rangle^2$ approaches a specific value for $\eta_\alpha < 0$, i.e., the $\langle E^2 \rangle / \langle E \rangle^2$ value becomes practically degenerate. The distribution with respect to β_α , on the other hand, increases without limit.

Finally, by working out the normalisation of Eq. 3.10, the differential flux at the source can be written as

$$\frac{d^2\Phi}{dEdt} = \frac{(1 + \beta_\alpha)^{1+\beta_\alpha}}{\Gamma(1 + \beta_\alpha) \cdot E} \left(\frac{E}{\langle E \rangle(t)} \right)^{1+\beta_\alpha(t)} \exp \left(-(1 + \beta_\alpha(t)) \frac{E}{\langle E \rangle(t)} \right) \times \frac{dN_\alpha}{dt}. \quad (3.13)$$

The flux information can then be carried out via integration. Note that the neutrino oscillations discussed in Chapter 2 would alter the fluxes observed on Earth.

Chapter 4

The SNO+ Detector

The Sudbury Neutrino Observatory (SNO) located in the underground laboratory of SNOLab in Sudbury, Canada, was the deepest underground neutrino detector of its time [156]. SNO+ is the successor of SNO, re-utilising the existing infrastructure of SNO and replacing the heavy water with 780 tonnes of liquid scintillator [2]. Both the hardware and software were upgraded to handle the transition to liquid scintillator. The ultra-pure water, filled by May 2017 [157], was completely removed by April 2021, and the SNO+ target volume is now filled with liquid scintillator, undergoing in-situ inspections of the configuration in order to proceed. For the primary physics goal of SNO+, to detect potential $0\nu\beta\beta$ events from ^{130}Te , tellurium will be loaded into the scintillator soon after the temporary pure-scintillator data-taking phase.

Details of the SNO+ experiment will be briefly outlined in this chapter. It will start with the hardware setup of the SNO+ detector, followed by an introduction to the three phases of data acquisition and the corresponding detection material. Finally, the electronics and software will also be explained.

4.1 Detector Hardware

The SNO+ detector is situated at the Vale Creighton mine 2,092 m below surface, providing 6,010 m.w.eⁱ shielding from cosmic radiations [2]. This results in a muon rate of 63 per day for a circular area of 8.3 m radius, which can be converted to nearly 3 per hour in the SNO+ detector. Within the mine, a cavity of approximately 34 m height and 22 m width was excavated to install the detector. This cavity is filled with roughly 7 kilotonnes of ultra-pure water, which shields the target volume from possible backgrounds emanating from the walls of the cavity.

ⁱMetre water equivalent is a measure of effective attenuation of cosmic rays [158].

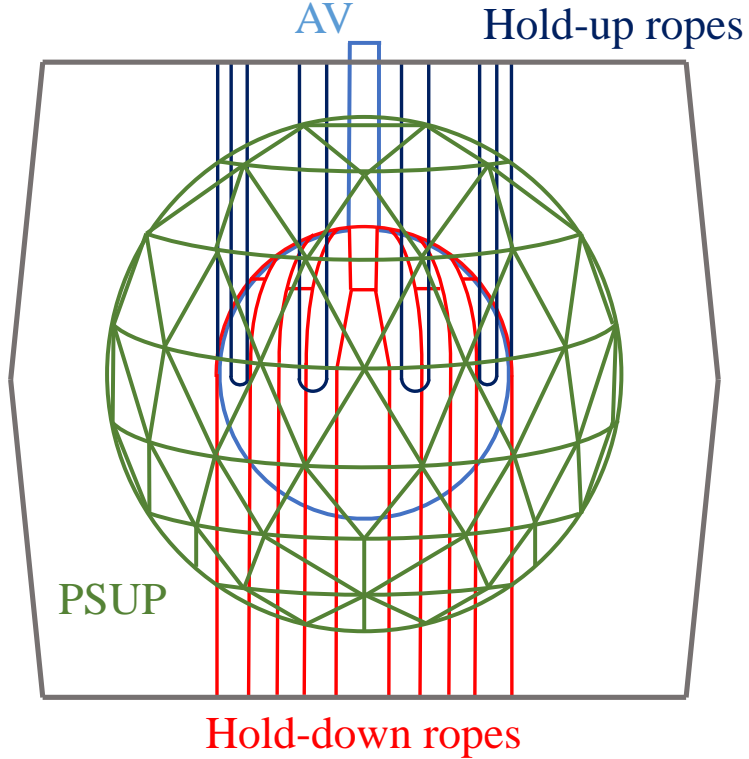


Figure 4.1: Schematic view of the SNO+ detector.

With the infrastructure originally employed in SNO, the detection material is loaded into the target volume isolated within an acrylic vessel (AV). The AV consists of a sphere of 6 m radius and a neck of 6.8 m height, and 1.5 m diameter attached to the top of the sphere. To maintain the entire structure at a fixed position, hold-up and hold-down ropes were installed. Hold-up ropes are a legacy from SNO to keep the AV from sinking, given that it was filled with heavy water. Hold-down ropes, on the contrary, were prepared for SNO+ for the liquid scintillator of about 0.86 g/cm^3 density [159]. The schematic overview of the detector is sketched in Figure 4.1.

The AV is surrounded by 9,455 Hamamatsu R1408 photomultiplier tubes (PMT), of 8-inch diameter, to capture the photon signals of the interactions [156, 157]. These PMTs are attached to the PMT support structure (PSUP), which is a hollow geodesic sphere of 8.9 m radius constructed in stainless steel. According to the way they are mounted, the tubes can be categorised into three classes. First of all, there are the normal PMTs, taking up the majority with 9,362 tubes, that are directed towards the AV covering 54% of the solid angle [157, 160]. There are then 91 PMTs oriented

outwards, often referred to as OWL (outward-looking) tubes, to veto background events emerging from the exterior. Finally, there are the 4 neck PMTs mounted on the AV neck to monitor scintillation light from events within the neck.

4.2 Phases of SNO+

The SNO+ experiment is scheduled to undergo three phases of data taking, each with a different type of detection material loaded into the target volume: ultra-pure water, pure liquid scintillator and tellurium-loaded scintillator. An overview of each phase together with the physical purposes will be described in this section.

4.2.1 Water Phase

Between May 2017 and July 2019, SNO+ started as a water Cherenkov detector in order to re-commission the detector and mitigate radon ingress from the mine air. During this phase, the AV was filled with 905 tonnes of ultra-pure water.

Though it was not the main target of the experiment, physics analyses can still be carried out with the data collected in water phase. The physics goals for water phase were the search for invisible nucleon decays and the measurement of the ${}^8\text{B}$ solar neutrino flux [161]. In addition, various checks on the performance and response of the PMT and data acquisition system together with external backgroundⁱⁱ measurements were also performed during this period.

4.2.2 Pure-Scintillator Phase

SNO+ started its transition to scintillator phase on the 19th of July, 2019. The bulk fill of the 780 tonnes of liquid scintillator was completed by the 26th of March, 2021, as shown in Figure 4.2, with some ultra-pure water remaining in the bottom of the AV, which was finally removed by the 8th of April, 2021. The liquid scintillator adopted by SNO+ is a linear alkylbenzene (LAB) based solution with 2,5-diphenyloxazole (PPO) as the solute [2]. PPO serves as the primary fluor which suppresses the self-absorption by LAB and shifts higher energy LAB fluorescence to wavelengths where the SNO+ PMTs are more sensitive, and thus directly affects the light yield. In order to gain maximum light yield, a target PPO concentration of 2 g/L was determined empirically as a compromise between the self-absorption of PPO and its light yield enhancement. This concentration level is expected to produce a light yield of $11,900 \pm 632$ photons per MeV [157]. By the time writing, the PPO level is about 1.1 g/L.

ⁱⁱThe backgrounds external to the AV. Main sources include the ${}^{208}\text{Tl}$ and ${}^{214}\text{Bi}$ in the ropes, shielding water, AV shell and PMT glass.



Figure 4.2: Photo of SNO+ taken on the 26th of March, 2021.

One of the main purposes for keeping the detector in a configuration of pure scintillator is to measure the radioactive purity of the scintillator. Amongst the internal backgrounds, i.e., the backgrounds within the target volume, the ^{238}U and ^{232}Th decay chains are two prominent sources of radioactivity. As Borexino has demonstrated, the ^{238}U and ^{232}Th levels in liquid scintillator can be brought to concentrations as low as $10^{-17} - 10^{-18}$ g/g [162, 163]. The measurements of the ^{238}U and ^{232}Th chains are studied in Chapter 5.

On top of that, various physics analyses are planned to be conducted in this phase, taking advantage of the substantially lower energy threshold and low background, including the measurements of reactor anti-neutrinos, geo-neutrinos and low energy solar neutrinos; and the search of supernova neutrinos. Relevant studies are discussed in Chapters 6 and 7 of this thesis.

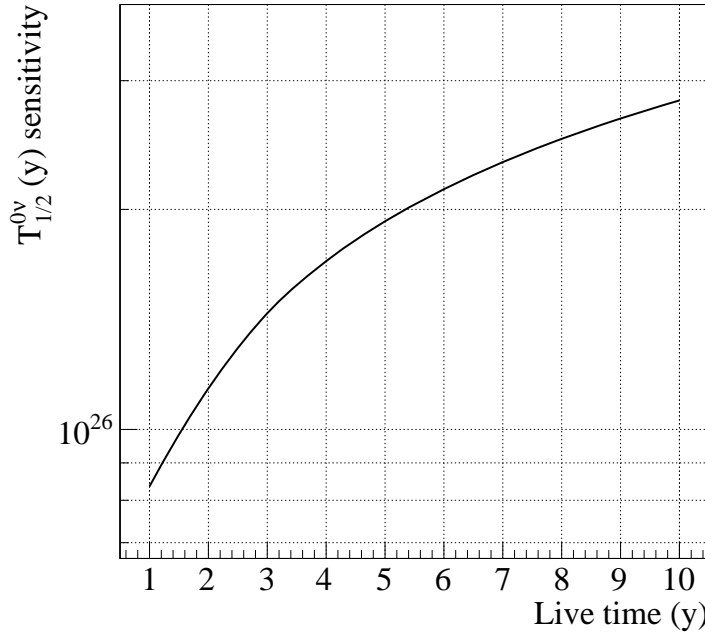


Figure 4.3: Sensitivity of $0\nu\beta\beta$ half-life as a function of the length of data-taking time in SNO+. Figure from [164, 165].

4.2.3 Tellurium-Loaded Phase

Finally, once the relevant planned checks and adjustments are completed, SNO+ will proceed to its major scientific stage — the tellurium-loaded phase. At this stage, the target is to load the scintillator with natural tellurium to the mass concentration of 0.5%.

As mentioned in Section 2.3, the physics goal of this phase, as well as the experiment, is to detect $0\nu\beta\beta$ from ^{130}Te . There are several reasons why ^{130}Te is adopted, as listed in [2]. Firstly, ^{130}Te has a relatively long $2\nu\beta\beta$ half-life, of 8.2×10^{20} years [166], which would help in mitigating this background. In comparison, the other candidate that was initially considered was ^{150}Nd , which also has a $2\nu\beta\beta$ half-life of 9.11×10^{18} years [167]. Following that, ^{130}Te is also a naturally abundant isotope, of 34.08%, allowing loading without enrichment. Finally, the Q -value of the ^{130}Te $0\nu\beta\beta$ process is above 2 MeV, which makes the signal relatively easier to separate from most of the radioactive backgrounds. All of these values for ^{130}Te and other possible candidate isotopes are listed in Table 2.1.

For a data collection period of five years with 0.5% of tellurium load, SNO+ is

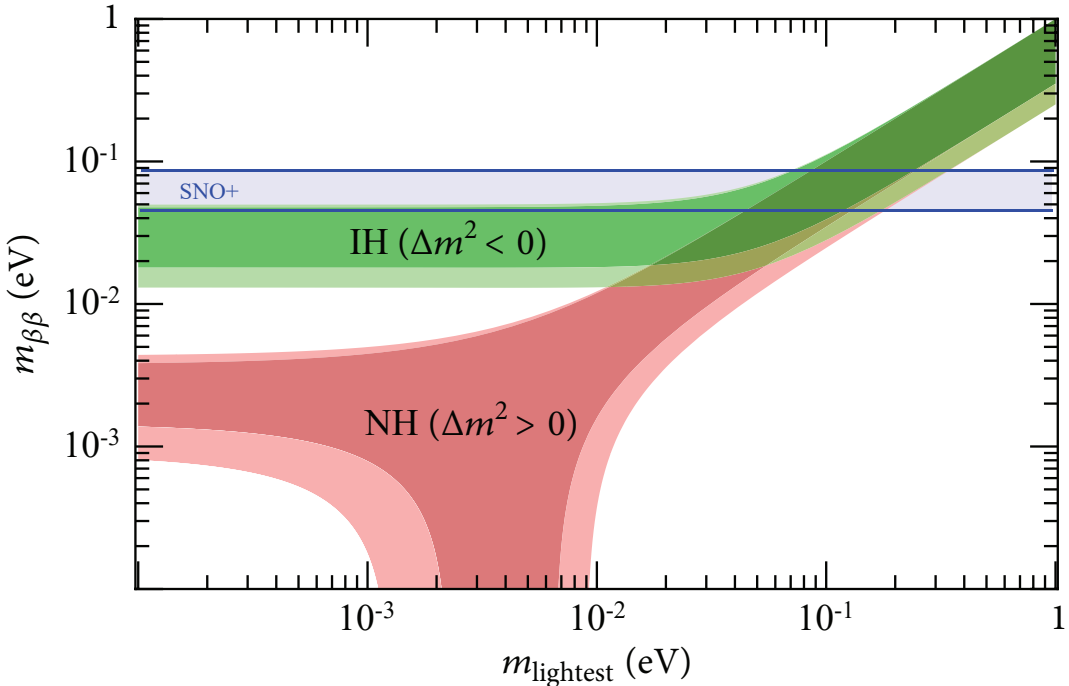


Figure 4.4: The effective Majorana mass ($m_{\beta\beta}$) limit expected to be achieved by SNO+ in five years time. The shaded regions in green and red are the 3σ regions of $m_{\beta\beta}$ given the inverted and normal hierarchy scenarios, which are calculated based on the given lightest neutrino mass and the uncertainties in the oscillation parameters. Figure adapted from [50].

expected to deliver a limit on the $0\nu\beta\beta$ half-life of 1.9×10^{26} years [164], as plotted in Figure 4.3. Converted to effective Majorana mass $m_{\beta\beta}$, this measurement would correspond to a limit of $37 - 89$ meV, as depicted in Figure 4.4. As a demonstration, the resulting spectrum in the case of a Majorana mass $m_{\beta\beta} = 100$ meV in a five-year run using the IBM-2 nuclear matrix element [62] is shown in Figure 4.5.

Though not severe, the introduction of tellurium to the scintillator will lead to a decrease in the light yield and a rise in the background levels. With the relatively lower light yield and higher background level, the physics studies taken during the pure scintillator phase could potentially be affected. The supernova studies, with most events at several tens of MeV, are not expected to be affected to any significant degree, except for the measurement of proton elastic scattering which is of low visible energy and will be further discussed in Chapter 7.

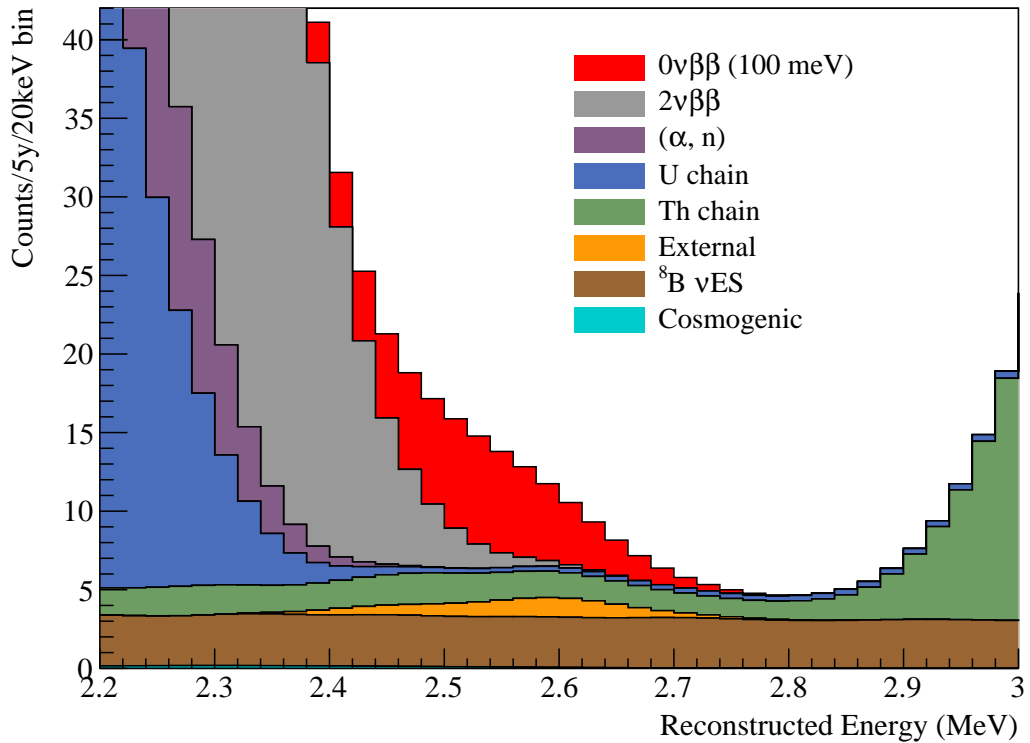


Figure 4.5: Stack plot of event counts for $0\nu\beta\beta$ and all relevant backgrounds expected for five years of data-taking plotted against the visible energy in the detector. This plot uses a Majorana mass $m_{\beta\beta} = 100$ meV and the IBM-2 nuclear matrix element [62]. A spherical fiducial volume of radius 3.3 m is applied. Figure originally from [164, 165].

4.3 Detector Electronics and Data Processing

The detectable physical interactions in SNO+ will yield photons, which will be recorded in the detector in the form of PMT “hits”. When an event is triggered, the time and charge information will be retrieved from the PMTs that have registered a hit. Knowledge about the physics event observed in the detector would then be gathered from this information. This is the basic idea of how signals are converted to data in SNO+. The details of this process will be described in this section.

4.3.1 Photomultiplier Tubes

The 8-inch Hamamatsu R1408 PMTs, shown in Figure 4.6, used in SNO+ were inherited from SNO. When a photon hits the photocathode a photoelectron will be created via the photoelectric effect. This electron is then accelerated by the electric field within the tube, and directed to a series of nine dynodes each inducing secondary photoelectron emissions. In the end, these PMTs are expected to result in a gain of 10^7 electrons per photoelectron [168], generating a measurable signal to be collected at the anode situated at the base of the PMT.

In addition, all of the normal PMTs are equipped with a truncated Winston-cone-shaped reflective concentrator of 27 cm outer diameter [169]. These concentrators lead to an increase in the effective solid-angle coverage of the PMTs by focusing photons onto the photocathodes. Without the concentrators, the coverage would be a mere 31% [156] constrained by the geometry, compared to the 54% with concentrators. The PMT together with the concentrator as a unit are contained in hexagonal cases mounted to the PSUP.

Each of these PMTs is connected to the detector electronics via waterproof BNC cables, providing the high voltage (HV) to the PMTs and also transmitting the anode pulse signals. The cables are of equal length in order to ensure the transmission times from each PMT are the same. These cables connect to electronics crated in the room just above the cavity.

4.3.2 Electronics and Trigger System

To distinguish the events which might possibly correspond to physics interactions worth recording, a trigger system is crated on top of the deck above the detector cavity. A sketch of the electronic signal path is shown in Figure 4.7.

The PMTs are connected to a paddle card with a dedicated channel on it. A total of eight PMTs are connected to each paddle card, with four paddle cards per PMT interface card (PMTIC), i.e., 32 channels per PMTIC. The PMTIC then passes the

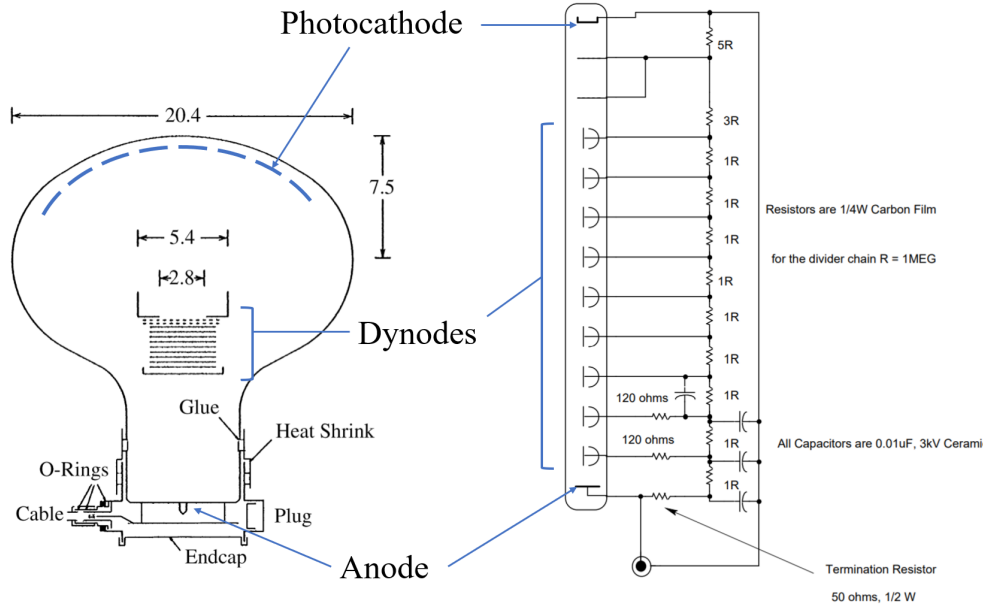


Figure 4.6: Specifics (left) and circuit diagram (right) of the Hamamatsu R1408 PMT. Dimensions of the left plot are in centimetres. Figure adapted from [156] (left) and [168] (right).

signals to the front end card (FEC), in which the PMTIC is linked to the daughterboards (DB) of the FEC. Each DB contains two chips setting the thresholds of discriminators for each channel and two chips to record the PMT times. If the pulse amplitude exceeds the discriminator thresholds, the corresponding PMT channel will be triggered, registering a “hit”. Within the event time window of a single global trigger (GT), only the first hit in each PMT will be registered.

When a channel is triggered, the charge read from individual PMTs will be amplified and integrated over three time windows:

- QHS: high-gain charge integration over a short time window of 60 ns
- QHL: high-gain charge integration over a long time window of 400 ns
- QLX: low-gain charge integration over either time window

All of this information will be temporarily stored on the FEC. Furthermore, each PMT produces four signals for triggering a GT:

- ESUMHI: the high-gain copy of the PMT pulse

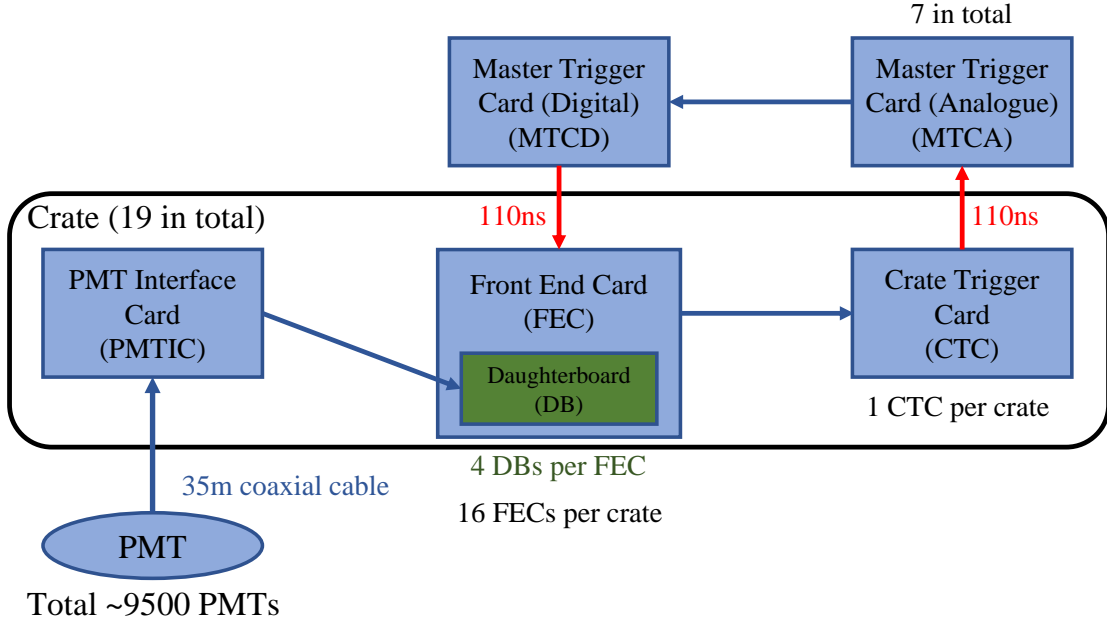


Figure 4.7: Schematic sketch of the signal paths from the PMT to the master trigger cards.

- ESUMLo: the low-gain copy of the PMT pulse
- N100: square pulse of length 100 ns
- N20: square pulse of length 20 ns

Since the N100/N20 signal from each PMT is equal in amplitude, it is essentially a count of the number of PMT hits within the 100/20 ns time window. Note that amongst the four signals related to the issuance of a GT, the N100 is the main GT trigger used in SNO+.

The ESUM signals together with the N100 and N20 signals from each DB will be summed over all the channels by the FEC, and forwarded to the single crate trigger card (CTC). A crate is made up of 16 sets of PMTICs and FECs. In total, there are 19 such crates in SNO+. Each crate will then submit the trigger signals to an analogue master trigger card (MTCA). The MTCA sums the signals from all the individual crates. One MTCA is used for each type of trigger signal. Note that the OWL PMTs, producing only ESUMHI, ESUMLO and N100 signals, are summed separately. There are, therefore, 7 MTCA in total.

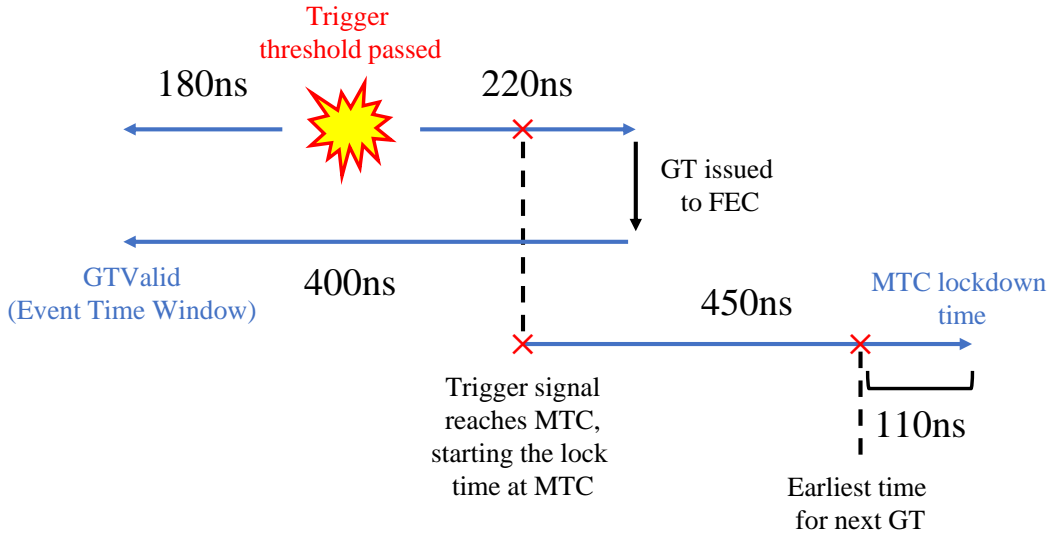


Figure 4.8: Timing of the SNO+ trigger system when the trigger threshold is passed. Since the transmission of signal from FEC to MTC takes about 110 ns, the earliest time for an event at the FEC to initiate the next GT is 110 ns before the MTC lock is lifted.

The summed signals will be passed from the MTCA to the digital master trigger card (MTCD), digitising the signals and detecting if any of the pulses pass the relevant thresholds. If any summed signal passes the thresholds set on the MTCD, a GT, with an unique ID (GTID) assigned, will be issued. Additionally, the trigger time is recorded by a 50 MHz clock, which resets approximately every two days and is synced with the Global Positioning System (GPS) clock.

Once a GT is issued, the MTCD will be forbidden from issuing another GT for a time interval of 450 ns. The GT is sent back to the FECs, and the data held will be read out. The PMT information at each channel are constantly digitised and cached at the FEC by the analogue-to-digital converters (ADCs). These digitised data will be held for a 400 ns time interval known as GTValid, beyond which the data will be discarded. When the FEC receives the GT, all the data within GTValid will be read out, forming an event. GTValid is, therefore, often referred to as the event time window. Furthermore, the time for signal transmission between the FECs and MTCD is 110 ns, so there will be a 220 ns delay between the hit that caused the GT and the time when the GT reaches back to the FECs [170]. The time window thus includes signals within 180 ns prior to the triggering hit. The time intervals and windows just described are summarised in Figure 4.8.

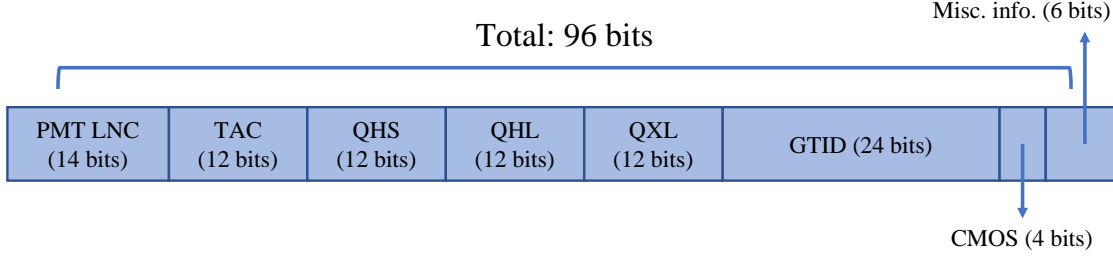


Figure 4.9: Schematic illustration of the 96-bit digitised PMT hit information.

4.3.3 Event Data Flow

When a GT is issued, the digitised PMT information read out from the channels will be stored in a 4 MB FIFO memory on the FEC. The digitised information will be 96 bits long, as depicted in Figure 4.9, comprising the following information:

- PMT logical channel number (PMT LCN) (unique to each PMT): 14 bits
The PMT LNC is also a word with bit fields that is defined as

$$LNC = 512 \times N_{crate} + 32 \times N_{card} + N_{channel} \quad (4.1)$$

where N_{crate} , N_{card} and $N_{channel}$ corresponds to the numbers assigned to a given crate, FEC and channel, respectively.

- Time to amplitude converter (TAC): 12 bits
TAC is the digitised time of the triggering PMT hit, ranging from 0 to 4,095 and giving a resolution of around 0.1 ns.
- QHS: 12 bits
- QHL: 12 bits
- QXL: 12 bits
- GTID: 24 bits

4.3. DETECTOR ELECTRONICS AND DATA PROCESSING

- CMOS cell information: 4 bits

The CMOS cell bits provide information regarding where the analogue data is stored.

- Miscellaneous CMOS information: 6 bits

These final bits stores information related to any error occurring in the CMOS chips, including whether the memory is full.

A customised translator board (XL3) in each crate copies the data from the FEC FIFOs in its crate, and transfers the data to the builder. The builder then constructs files in ZDAB format to store the information. When the ZDAB file reaches a size of 999,940,000 bytes, the file will be closed and a new ZDAB file will be created to carry on if there are remaining data for the given data “run”, which is an hour of data by default. These output ZDAB files are then in a state ready for analysis. They will be further transferred to the Grid [171] for processing to to further convert the data to ROOT-format [172] files for analysis. The data flow is summarised schematically in Figure 4.10.

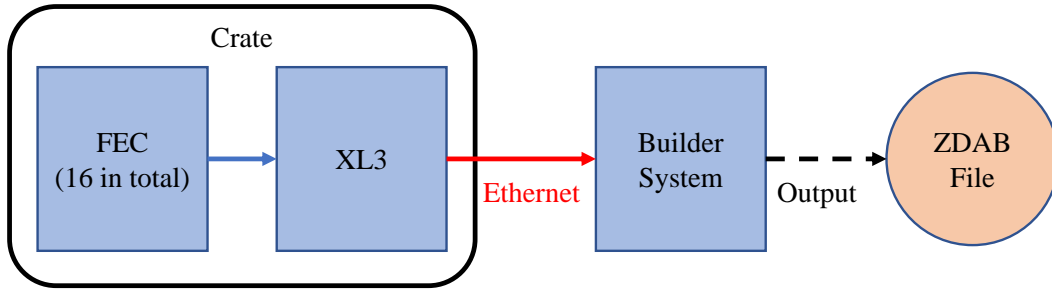


Figure 4.10: Flow of the SNO+ data acquisition system.

4.4 Full Reconstruction

In order to proceed with the physics analyses aimed to be carried out in SNO+, it is necessary to convert the original SNO+ detector events, which consists of trigger read-outs and PMT-hit data, into high-level event information, e.g., position, energy or event time, etc. The process of this conversion is known as reconstruction. Full reconstruction methods in SNO+ reconstruct the position, time and energy of an event. Depending on the configuration, the full reconstructions include: `waterFitter` for water phase, `scintFitter` for scintillator phase, and `partialFitter` for the filling phase. For `partialFitter`, the configuration will be determined by an user-defined interface level, above which is the scintillator volume and below it the water volume. In this section, the focus will be put on the position and time reconstructions, whereas the energy reconstruction will only be briefly described.

4.4.1 Position and Time Reconstructions

Vertex reconstruction in SNO+ is based on the pattern of the PMT hit time distribution. The underlying principle is simple: the PMTs closer to the true event position get hit earlier and the farther the later. Full reconstruction algorithms then decide the position and time by determining the best fit to the recorded hit time pattern. In the case of an ideal detector with uniform material and absolute time resolution, this position can be calculated directly via triangulation

$$\frac{|\vec{r}_{PMT} - \vec{r}_*|}{c} = t_{PMT} - t_* \quad (4.2)$$

where c is light speed in the material, \vec{r}_* and \vec{r}_{PMT} are the positions of the event and PMT hit, respectively; and t_* and t_{PMT} are the event time and PMT hit time. The event vertex can, therefore, be solved with a set of four PMTs.

In practice, however, the electronic noise and the relatively long emission period of the scintillation light introduces uncertainties to the fit results. These uncertainties can be reduced by iterating this process in order to create a large collection of estimated vertices. Information of the true vertex can then be extracted from the overall distribution of this sample set. The `Quad` fitter, developed by I. Coulter [173], is a position reconstruction method built upon this idea, which takes the median of each coordinate distribution as the fit result. The use of the `Quad` fitter will also be discussed in Section 6.2.3.

The fit result of `Quad` is taken as the initial position and time (a seed) for the full reconstruction methods. Starting with this seed vertex, the light path is evaluated by taking into account the light speed difference in different materials. Using this augmented light path model, the emission time profile can be evaluated. The final

vertex is then determined by performing a maximum likelihood fit on the time profile with a probability distribution function (PDF). The PDFs are pre-determined using simulations of evenly distributed electron events.

4.4.2 Energy Reconstruction

Energy in SNO+ is reconstructed based on the number of PMT hits (N_{hit}). The N_{hit} value is first corrected according to the reconstructed position of the event to account for the difference in PMT coverage across the detector. This corrected N_{hit} value is then converted to a number of photo-electrons. Finally, the event energy is estimated by exploiting the proportionality between the energy deposited in the detection material and photo-electrons generated.

4.5 Data Analysis and Simulation — RAT

Data analysis and Monte Carlo (MC) simulations in SNO+ are done by using the Reactor Analysis Tool (RAT) [174]. The RAT framework is written primarily in C++, and invokes GEANT4 [175] and GLG4sim [176] libraries for the MC simulations. GEANT4 is used to simulate the geometry of the detector. The GLG4sim package, on the other hand, is used to generate the primary event process and to simulate the optical photons generated via Cherenkov radiation and scintillation. For simulations, the propagation of every optical photon will be fully modelled from its creation to when it is absorbed. In addition to the physical processes, the electronic responses are also simulated.

The data or simulated events are then passed to the analysis algorithms, such as the reconstruction methods, which are incorporated into the RAT framework. Finally, the resulting analysed events are stored in ROOT-formats [172] for further analysis and handling.

Chapter 5

Measurement of Internal Backgrounds in Liquid Scintillator

The main theme of this chapter is to measure the uranium (^{238}U) and thorium (^{232}Th) decay chain concentrations via bismuth-polonium (BiPo) coincidence tagging. The decay chains are shown in Figures 5.1 and 5.2. The chapter will start with an introduction of the decay chains as a source of internal backgroundsⁱ in the detector. As the results presented here include measurements spanning through the entire period of filling the AV with liquid scintillator, there will be a brief account of the detector configuration evolution during the phase transition. Details of the BiPo coincidence analysis and the resulting measured ^{238}U and ^{232}Th contamination levels will then follow. In addition to its primary purpose of estimating the ^{238}U and ^{232}Th levels, the BiPo coincidence analysis has been proven to be a useful means of in-time monitoring of the detector. The final sections of this chapter will be dedicated to this aspect of the analysis.

Note that although the basic strategy of coincidence tagging is based on the Monte-Carlo (MC) simulation studies of [4], the design and determination of certain cuts applied on data, the functioning analysis script, and the analyses of the data in Section 5.3; and the results presented in Sections 5.4 and 5.5 are original works of the author.

5.1 ^{238}U and ^{232}Th Decay Chains

As shown in Figure 4.5, the ^{238}U and ^{232}Th decay chains constitute a significant fraction of the background in the spectral region of interest (ROI) for $0\nu\beta\beta$ detection. The decay schemes of both decay chains are plotted in Figures 5.1 and 5.2. The

ⁱIn the usage of SNO+, “internal” refers to inside of the AV and “external” for outside of it.

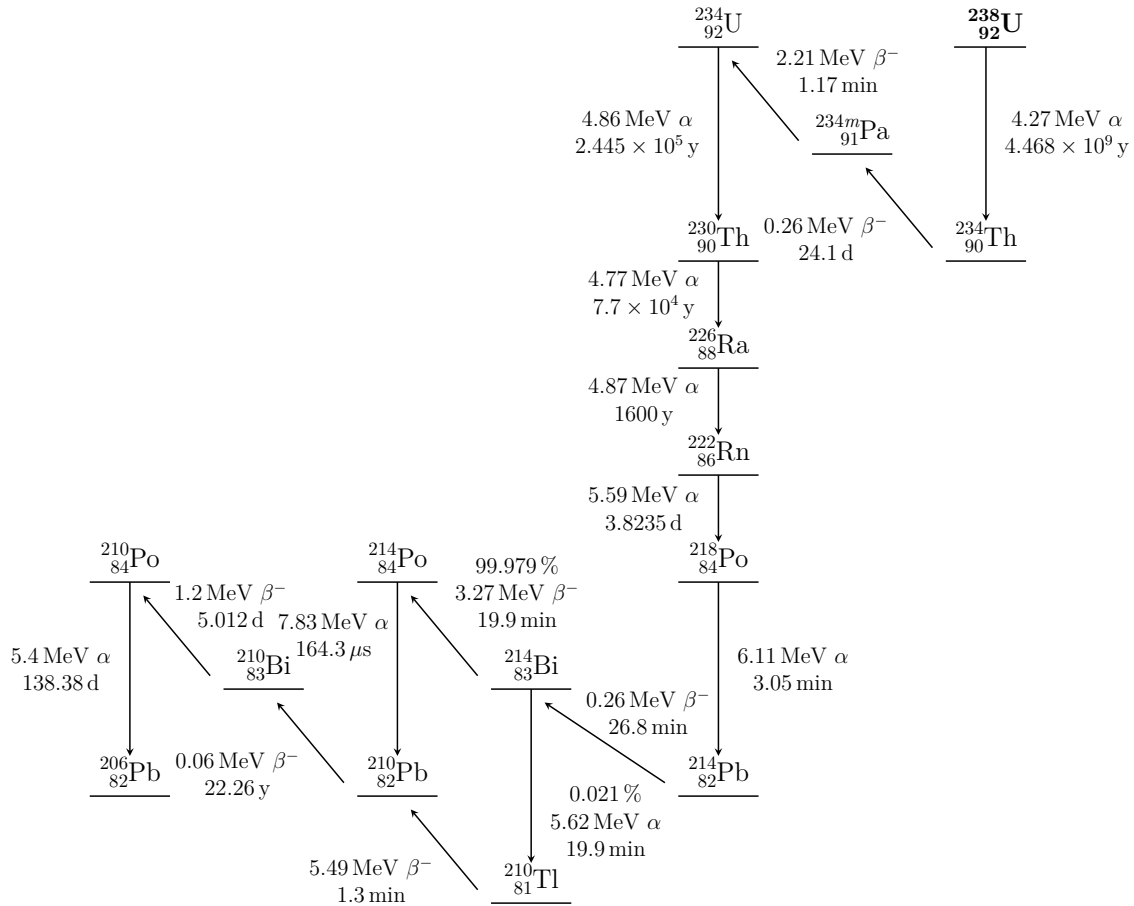


Figure 5.1: ^{238}U decay chain. The energies quoted are the primary channel α energies for the α decays and Q value for the β decays.

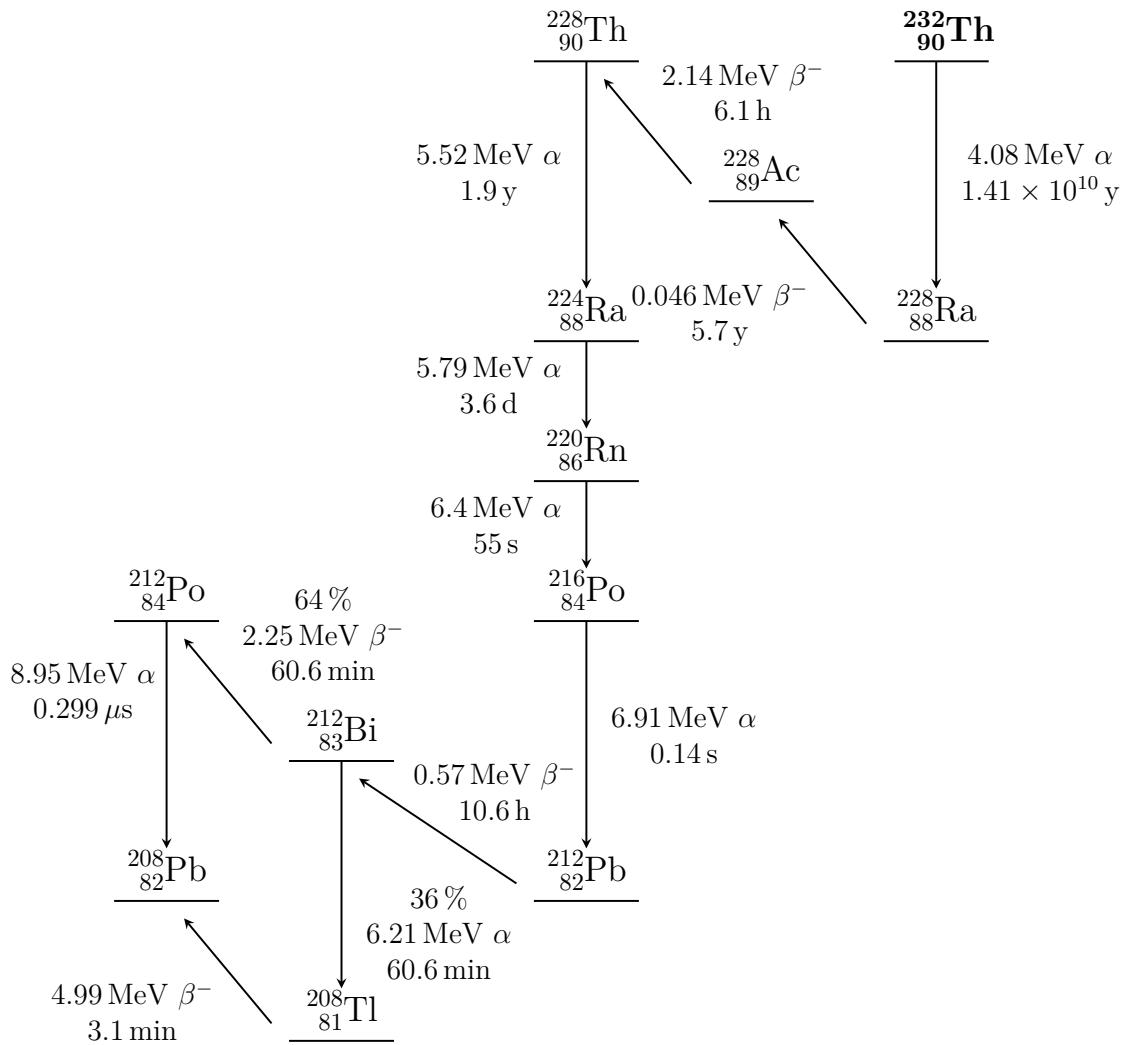


Figure 5.2: ^{232}Th decay chain. The energies quoted are the primary channel α energies for the α decays and Q value for the β decays.

Source	Target Concentration (g/g)	Decay Rate (yr^{-1})
Internal H_2O , Water Phase		
^{238}U Chain	3.5×10^{-14}	1.2×10^7
^{232}Th Chain	3.5×10^{-15}	4.1×10^5
LAB-PPO, Pure Scintillator Phase		
^{238}U Chain	1.6×10^{-17}	4900
^{232}Th Chain	6.8×10^{-18}	700
^{210}Bi	-	7.6×10^8
^{210}Po	-	7.8×10^8
0.3% Te-Loaded Scintillator, Tellurium-Loaded Phase		
^{238}U Chain	2.5×10^{-15}	7.6×10^5
^{232}Th Chain	2.8×10^{-16}	2.8×10^4
^{210}Bi	-	7.9×10^9
^{210}Po	-	9.5×10^9

Table 5.1: Target purity level for different phases of SNO+, adapted from [2]. The units of the $^{238}\text{U}/^{232}\text{Th}$ concentration “g/g” stands for grams of the isotope per gram of detection material.

SNO+ collaboration has set ^{238}U and ^{232}Th chain target purity levels for the detection material in different phases, which are listed in Table 5.1 [2]. These levels were largely based on the purity achieved in Borexino [162, 163] as a realistic preliminary target, where SNO+ is certainly making effort to seek further reductions.

By virtue of their long lifetimes, the ^{238}U and ^{232}Th decay chains can be assumed to be in secular equilibriumⁱⁱ [2]. Provided that all the isotopes are in equilibrium, the ^{238}U and ^{232}Th levels can be inferred by measuring the corresponding BiPo coincidences: $^{214}\text{Bi}-^{214}\text{Po}$ (BiPo214) for ^{238}U chain and $^{212}\text{Bi}-^{212}\text{Po}$ (BiPo212) for ^{232}Th chain. The equilibrium of radioisotopes after ^{222}Rn and ^{220}Rn is often broken by radon ingress when having contact with the surrounding mine air. However, the equilibrium can usually be restored within weeks due to the relatively short lifetimes of the radon and the short-lived daughter-isotopes that follow. The issue of radon ingress will be discussed in more detail in later sections.

ⁱⁱThis is to say that the isotopes in the chain are decaying and being produced at the same rate [177].

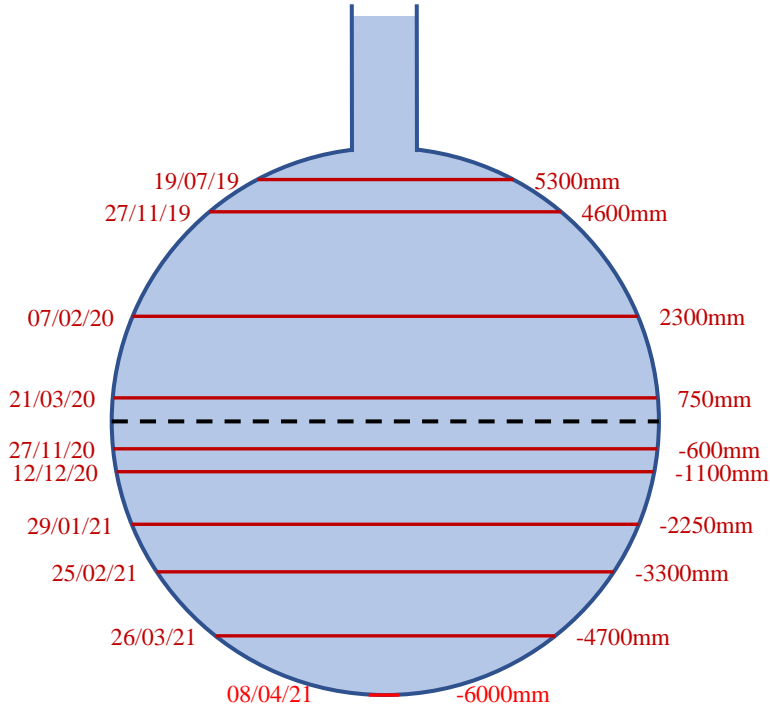


Figure 5.3: The scintillator fill schedule of SNO+. Only interfaces that have remained for more than a week are indicated. The dates labelled on the left are when the scintillator interface first reached that position.

5.2 Scintillator Fill in SNO+

The filling of liquid scintillator started in October 2018. The transition of detection material in SNO+ has been conducted by draining water from the bottom of the AV and replacing the volume on top with liquid scintillator. This transitional period will be referred to as the “partial-fill phase”. As planned, the collaboration performed inspections on the internal background levels of the liquid scintillator during this period. In fact, most of the results exhibited in this chapter are from this phase.

Major stages of the filling progress are shown schematically in Figure 5.3. Scintillator fill in the AV started from July 2019, when neck fill was done, and was eventually completed by April 2021. The final step of the filling is to augment the PPO load from the current 1.1 g/L (as of the 22nd of November, 2021) to the desired 2 g/L, which is expected to be done by March 2022.

Despite the fact that partial-fill was intended to be a temporary state of six

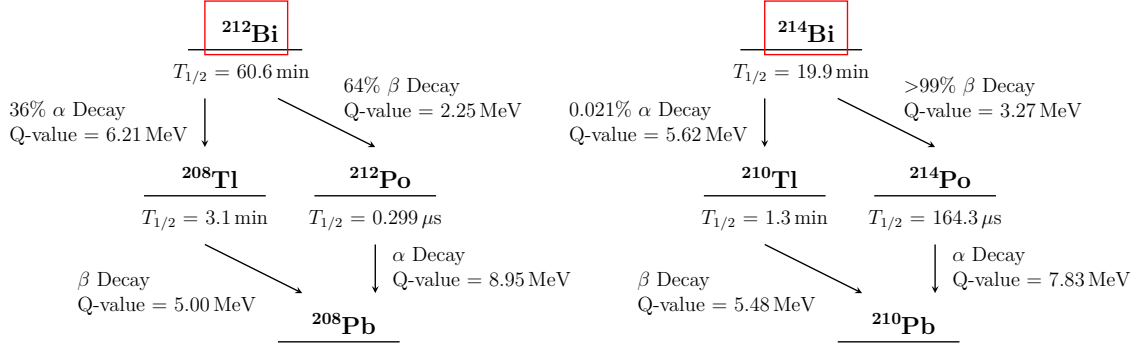


Figure 5.4: Decay schemes for ^{212}Bi (left) and ^{214}Bi (right), adapted from [2].

months for preliminary scintillator assessments, the detector was forced to remain in this state for a considerably longer time due to the pandemic since 2020.

5.3 Bismuth-Polonium Coincidence Tagging

The decay schemes of ^{214}Bi and ^{212}Bi are shown in Figure 5.4. From the decay scheme, one can see that the majority of bismuth decays via the β channel: ^{214}Bi decays to ^{214}Po with 99.979% branching ratio and ^{212}Bi decays to ^{212}Po with 64% branching ratio. The polonium that follows undergoes an α decay with a sufficiently short lifetime, $\tau = 237 \mu\text{s}$ for ^{214}Po and $\tau = 431 \text{ ns}$ for ^{212}Po , suitable for coincidence tagging. Thus, a series of selection cuts can be developed to identify this $\beta - \alpha$ coincidence, i.e. β emission (Bi) with a subsequent α emission (Po).

The selection strategy, depicted in Figure 5.5, can be divided into three main steps: identify a polonium candidate; set constraints on possible parent events by applying inter-event cuts; and, finally, discern the bismuth event out of the eligible parent event candidates. The selection of candidates consists of two cuts: a cut on the number of PMT hits (N_{hit}), serving as a first order estimate of energy; and a fiducial volume cut, rejecting events from the exterior. After identifying the candidates, a time difference (Δt) cut and a position difference (Δr) cut are applied to confine the time and distances between the candidate events.

5.3.1 Fiducial Volume Cut

The fiducial volume cut is essentially the selection of a target volume. Originally in [4], the cut was chosen to be a single radial cut of $r < 4000 \text{ mm}$ designed to reject external backgrounds and reduce the misidentification rate. The study on partial-fill

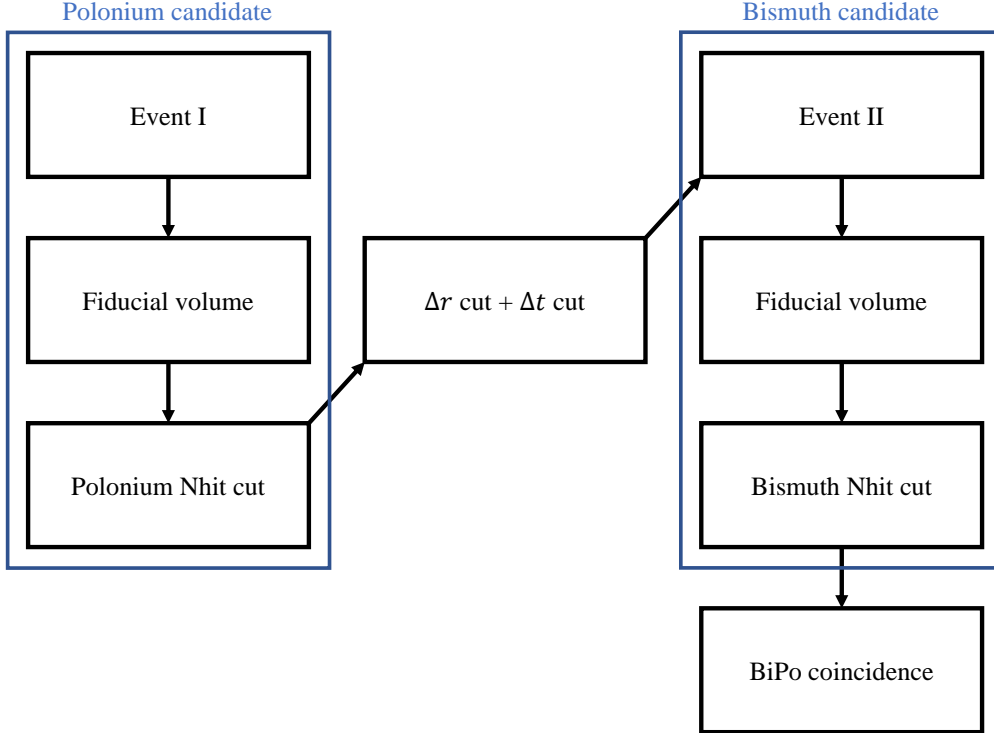


Figure 5.5: Scheme of the BiPo coincidence analysis. If *Event II* did not pass either of the bismuth cuts, then the events prior to *Event I* will continue to be looped through until there is a bismuth candidate or the upper bound of the Δt cut is reached.

phase data has, however, suggested the need for more flexible choices regarding the fiducial volume.

During phase transition, the configuration of the detector was constantly evolving and the scintillator was often not mixed uniformly. To adapt to this situation, a combination of radial cuts, Z cuts and ρ cuts was applied to better study the local behaviour of the detector during filling, where Z is defined along the vertical direction with $Z = 0$ mm at the equator and $\rho = \sqrt{X^2 + Y^2}$ is defined on the horizontal plane. Whenever the results are quoted, the chosen fiducial volume will be indicated in the format of “Radial cut + Z cut + ρ cut”, where the radial cut will be designated with R , the Z cut with Z and the ρ cut with ρ . A fiducial cut of $r < 4000$ mm and $0 < Z < 6000$ mm (the upper hemisphere) will, for instance, be labelled as “ $R4000_Z6000_0$ ”, and the ρ part is neglected since it is not applied.

Assuming isotropic distribution for the isotopes in the liquid scintillator, the fraction of events within the fiducial volume ϵ_{FV} can simply be expressed as

$$\epsilon_{FV} \equiv \frac{N_{FV}}{N_{AV}} = \frac{V_{FV}}{V_{AV}} \quad (5.1)$$

where N_{FV} and N_{AV} are the number of events identified within the fiducial volume and AV; and V_{FV} and V_{AV} are the respective volumes of the fiducial volume and AV.

On a side note, the AV neck, though also filled with scintillator, will not be taken into consideration in this analysis due to its irregular geometry. The terms “scintillator volume” or “AV”, whenever mentioned, only refers to the bulk volume with $r < 6000$ mm, and the neck region shall always be specified as “AV neck” or “the neck”.

5.3.2 Nhit Cut

Nhit is the number of PMT hits, which serves as a preliminary indicator of the event energy. Polonium decays via an α decay and emits an α particle at a specific energy resulting in a distinct and narrow energy, and thus Nhit, spectrum. The bismuth β decay, on the contrary, gives rise to a broad spectrum ranging up to the Q valueⁱⁱⁱ, as a consequence of its three-body nature. Therefore, the broader bismuth Nhit cut will contribute relatively less to the discriminating power of the analysis compared to its polonium counterpart.

The Nhit cut values obtained in this section are based on the MC simulations using **RAT6.18.12**. The actual values applied on the data, however, will have to be adjusted according to the light yield level in the detector. In practice, the upper limit of the cuts are usually relaxed by 20% to adapt the light yield shifts. Figure 5.6 shows the MC simulated Nhit spectra of BiPo214 and BiPo212, together with the high rate internal backgrounds BiPo210, under the configuration with the scintillator interface at $Z = -5950$ mm^{iv} and a 0.5 g/L PPO concentration. One might notice that BiPo210 also forms a $\beta - \alpha$ signal. However, the half-life of ^{210}Po is 138 days, which makes it practically impossible to identify such signals as coincidences.

From Figure 5.6, one will notice that the ^{214}Po and ^{212}Po peaks overlap each other and have Nhit higher than most of the high rate backgrounds, and thus the determination of the polonium cuts should be based upon the discrimination between ^{214}Po and ^{212}Po . As indicated in Table 5.1, the expected activity of the ^{238}U chain

ⁱⁱⁱThe Q value is defined as the energy released or absorbed in a nuclear reaction.

^{iv}Though the actual detector configuration is $Z = -6000$ mm, i.e., fully filled, the processing fitter used is still **partialFitter** (see Section 4.4) which requires an interface value above $Z = -6000$ mm. The interface value for the current data processing is, therefore, set to $Z = -5950$ mm to avoid potential errors.

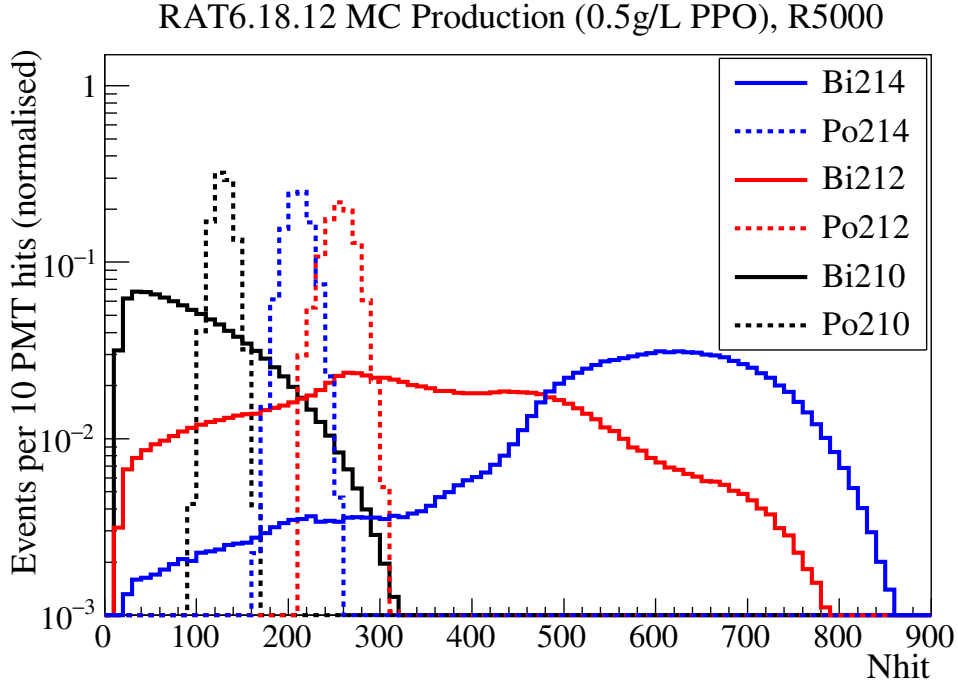


Figure 5.6: MC simulated Nhit spectrum of BiPo214, BiPo212 and BiPo210. A fiducial cut of $r < 5000$ mm is applied to avoid geometric effects close to the AV shell, in particular the light loss around the AV neck. Corrected Nhit cuts will be applied separately to the regions close to the AV shell.

is almost two orders of magnitude higher than the ^{232}Th chain. Consequently, the polonium cuts are designed such that the more abundant ^{214}Po are rejected in the ^{212}Po identification, whereas the ^{214}Po cut can afford overlapping with the ^{212}Po peak. The cuts are, therefore, decided to be (160, 280) for ^{214}Po and (230, 320) for ^{212}Po .

Efficiencies of the polonium cuts are determined by

$$\epsilon_{Po} \equiv \frac{N_{FV}^{Po}}{N_{FV}} \quad (5.2)$$

where ϵ_{Po} is the efficiency of the polonium Nhit cut, and N_{FV}^{Po} is the number of events within the fiducial volume which passes the polonium Nhit cut. In the MC simulation, the efficiencies are found to be 99.996% for ^{214}Po and 90.5% for ^{212}Po .

As for the bismuth cuts, serving more as an auxiliary cut, the primary objective is to remove the high rate backgrounds, mainly BiPo210 and ^{14}C ^v. The ^{214}Bi cut is simply chosen to be (300, 1050) where the lower edge is just above the ^{210}Bi spectrum. On the other hand, a large fraction of the ^{212}Bi spectrum happens to be in a relatively more convoluted region, in which extracting a range for pure ^{212}Bi would be impractical. Eventually, the range for the ^{212}Bi cut is set to be (150, 800) to avoid the ^{210}Po peak, ^{14}C and most of the ^{210}Bi spectrum, whilst rescuing most of the efficiency. The bismuth cut efficiency ϵ_{Bi} is calculated by

$$\epsilon_{Bi} \equiv \frac{N_{FV+\Delta t+\Delta r}^{Bi}}{N_{FV+\Delta t+\Delta r}} \quad (5.3)$$

where $N_{FV+\Delta t+\Delta r}$ is the number of events within the fiducial volume passing the inter-event cuts Δt and Δr ; and $N_{FV+\Delta t+\Delta r}^{Bi}$ is the number of those events passing the bismuth Nhit cut. One would notice that ϵ_{Bi} is defined with a different denominator from ϵ_{Po} owing to the fact that the bismuth cut is applied after the inter-event cuts^{vi}.

Corrections to the Nhit Cut

The Nhit intervals quoted above for the BiPo212 and BiPo214 coincidences are decided based upon the results of MC simulations which assumes a rather idealistic and stable configuration. In practice, however, there are situations that can cause noticeable light yield changes. The two most prominent such situations are PPO stratification and crate failures.

PPO stratification often happens during scintillator fill. The suspected reason for the stratification is the presence of a temperature gradient preventing the scintillator from mixing. When stratification happens, the nominal overall PPO concentration, calculated simply by dividing the total PPO dose with the total scintillator volume, will no longer be indicative of the overall light yield level. In this case, the Nhit cuts will have to be re-tuned for each layer by manually scanning through the Nhit distribution to identify the new Nhit ranges of the bismuth and polonium. Due to the notable difference in activity, the BiPo214 is usually used as a benchmark to determine the light yield and the BiPo212 cut will be scaled accordingly.

Crate failures occur when there are electronics issues in the detector which require the malfunctioned crates to be turned off for maintenance. As a consequence, the PMTs mounted to those crates will stop functioning. This reduces the PMT coverage

^vThis background is not plotted in Figure 5.6 as it is not simulated in the latest MC sample production, but the Nhit spectrum can still be inferred to be up to 60 hits from the previous MC production which also simulates with a 0.5 g/L PPO concentration.

^{vi}Note that although the reverse, i.e., tagging bismuth then polonium, gives the same result, it takes up much more computation time due to the looser Nhit cut of the bismuth.

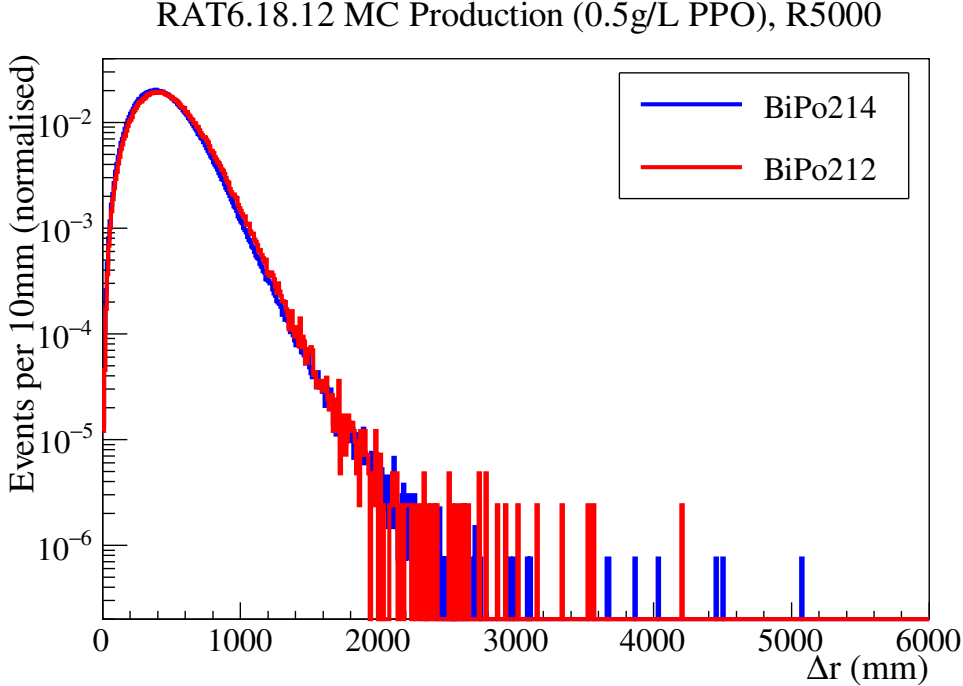


Figure 5.7: Δr distribution of the MC simulated BiPo214 (blue line) and BiPo212 (red line). The slight difference in the two distributions originates from the energy difference of the events, which affects the reconstruction resolution.

and causes the Nhit to decrease accordingly. To cope with this situation, the Nhit cuts are simply scaled down by the fraction of crates turned off.

5.3.3 Position Difference (Δr) Cut

Ideally, the nuclear recoil caused by the bismuth β decay is negligible, and thus the true position of the bismuth and polonium nuclei should be nearly identical. In practice, however, the finite resolution of the position reconstruction, as introduced in Section 4.4, introduces a spatial difference. This position difference between the bismuth and polonium candidates is defined as

$$\Delta r \equiv \sqrt{(x_{Po} - x_{Bi})^2 + (y_{Po} - y_{Bi})^2 + (z_{Po} - z_{Bi})^2} \quad (5.4)$$

where $\{x_i, y_i, z_i\}$ are the reconstructed positions of the candidates $i = \text{Bi}, \text{Po}$.

The Δr cut was decided upon the criterion of preserving roughly 99% of the BiPo pairs. The most straightforward way to determine the cut range is to simulate the BiPo pairs in the corresponding configuration, and examine the simulated Δr

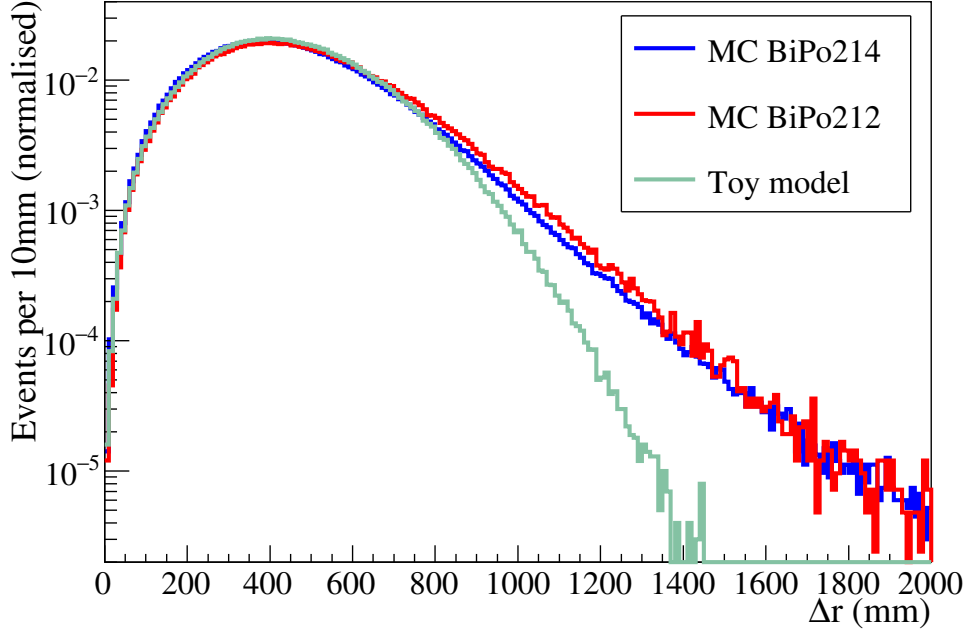


Figure 5.8: Comparison of the Δr distributions of the toy model (green line) and the MC simulations (red and blue lines) shown in Figure 5.7.

distributions, such as Figure 5.7. Based on the simulated result shown in Figure 5.7, a cut value of $r < 1000$ mm was chosen, where the actual efficiency was relaxed to 98% to round up the cut value.

This approach, albeit simple, is often not applicable as detailed simulations are time-consuming and not always available for the constantly evolving partial-fill configuration. In particular, since Δr arises from the position reconstruction uncertainty, the variation in the light yield levels that affects the reconstruction uncertainty will, in turn, affect the efficiency of the Δr cut.

A useful alternative is to model the BiPo pair by two random points in space generated from a normal distribution of the given reconstruction resolution. For instance, Figure 5.8 shows the Δr distribution generated by the toy model with a resolution of 155 mm, quoted from [178], for the same configuration as the MC simulation in Figure 5.7. It is clear that the tail of the toy model distribution is shorter than the simulated distributions. The reason is that the resolution of the reconstruction is not uniform throughout the detector, and it worsens as it approaches the AV shell and especially the AV neck. The toy model, which assumes a gaussian with the average resolution, underestimates the tail of the position reconstruction

and, hence, the tail of the Δr distribution. Regardless of the underestimation in the tail, the point achieving 98% efficiency turns out to be $\Delta r < 990$ mm which is fairly close to the 1,000 mm obtained from simulation. This approach provides a computationally more efficient method to estimate the Δr cut value for a constantly evolving configuration.

5.3.4 Time Difference (Δt) Cut

The other inter-event constraint is the time difference between the bismuth and polonium events. For a BiPo pair, the Δt will be the decay time of the polonium nucleus. The Δt cut can, therefore, be determined based on the polonium lifetime.

The number of nuclei N remaining after a given time t can be described by the exponential decay law

$$N(t) = N_0 \exp\left(\frac{-t}{\tau}\right) \quad (5.5)$$

where N_0 is the initial number of nuclei and τ is the lifetime. For ^{212}Po and ^{214}Po , $\tau_{^{212}\text{Po}} = 431$ ns and $\tau_{^{214}\text{Po}} = 237$ μs respectively. The efficiency of the Δt cut $\epsilon_{\Delta t}$ can then be calculated by

$$\epsilon_{\Delta t} = \frac{\int_{\Delta t_{low}}^{\Delta t_{up}} \exp(-t/\tau) dt}{\int_0^{\infty} \exp(-t/\tau) dt} \quad (5.6)$$

where Δt_{low} and Δt_{up} are the lower and upper limits of the Δt cut. In [4], the upper limit of the Δt cut is selected to achieve a 99.95% efficiency when $\Delta t_{low} = 0$. This sets the upper Δt limit to 1.8 ms for BiPo214 and 4 μs for BiPo212.

The lower Δt limit requires further considerations. For BiPo214, as the lifetime of ^{214}Po is significantly longer than that of ^{212}Po , the lower bound is set to 4 μs which rejects the BiPo212 whilst causing only a slight sacrifice of 1.38%. The case for BiPo212, on the other hand, is more complicated as the ^{212}Po lifetime happens to be of the same order as the SNO+ trigger time window. As described in Section 4.3.2, the event time window in SNO+ is set to 400 ns. If the polonium decay happened within 400 ns after the bismuth decay trigger, it will be written into the bismuth event. For BiPo coincidences, this is known as an “in-window BiPo” event. This analysis will focus only on the out-window BiPo coincidences. Accordingly, the lower Δt bound for BiPo212 is chosen to be 400 ns. The resulting efficiencies calculated with Eq. 5.6 are $\epsilon_{\Delta t}^{\text{BiPo214}} = 98.57\%$ and $\epsilon_{\Delta t}^{\text{BiPo212}} = 48.4\%$.

During scintillator fill, it was soon discovered that these upper bounds are not stringent enough for the high activity in the detector. The misidentification rate, discussed in more detail in Section 5.3.6, was almost of the same level as the BiPo signal, or even higher in the case of BiPo212. To rescue the purity of the tagged

5.3. BISMUTH-POLONIUM COINCIDENCE TAGGING

	BiPo212 Tagging			BiPo214 Tagging		
	Cut Interval		Efficiency	Cut Interval		Efficiency
	Lower Limit	Higher Limit		Lower Limit	Higher Limit	
Po Nhit Cut	230	320	90.5%	160	280	99.996%
Δt Cut	400 ns	800 ns	24%	4 μ s	1 ms	96.8%
Δr Cut	-	1000 mm	97.9%	-	1000 mm	98.3%
Bi Nhit Cut	150	800	69.5%	300	1050	82.3%
Overall Cut Efficiency	14.8%		78.3%			
Branching Ratio	64%		99.979%			
Combined Efficiency	9.5%		78.3%			

Table 5.2: A summary on the cuts applied to the BiPo analysis with their respective efficiencies. The overall cut efficiency is all the individual efficiencies multiplied together, whereas the combined efficiency is the overall cut efficiency further multiplied by the branching ratio.

pairs, the upper bounds were lowered to 1 ms for BiPo214 and 800ns for BiPo212 bringing the efficiencies down to $\epsilon_{\Delta t}^{\text{BiPo214}} = 96.8\%$ and $\epsilon_{\Delta t}^{\text{BiPo212}} = 24\%$, respectively.

5.3.5 Tagging Efficiency

The overall efficiency of the selection cuts is evaluated by combining the individual efficiencies of each cut. Table 5.2 lists the cuts deployed in the analysis and their corresponding efficiencies. Note that the effect of the fiducial cut is not included in the overall efficiency. As mentioned earlier, the detector has often been in a rather agitated state during phase transition giving rise to the need of a more versatile fiducial volume. It is, therefore, desirable to quote the tagging efficiency in a volume-independent form. This is implicitly assuming that the tagging efficiency is uniform within the scintillator volume, which, again, does not apply to regions near the AV neck. Another important factor worth mentioning is the branching ratio. It is included in the final efficiency in Table 5.2 for convenience when converting the coincidence counts to the ^{238}U and ^{232}Th purity level, which can be seen in Section 5.4.

5.3.6 Misidentification

The analysis developed thus far has the potential problem of tagging other background events as BiPo coincidences. A method based on MC simulations to set an upper bound on the misidentification rate was proposed in [4]. Besides that, a simpler method was developed for analysing the data, which simply infers the misidentifica-

tion rate from a fit to the Δt distribution. Both methods will be introduced in this section.

MC Estimation

Recalling the analysis flow in Figure 5.5, the analysis is initiated by the declaration of a polonium candidate, then followed by retracing in time for possible bismuth events. The rate of coincidences can, therefore, be estimated by the rate of polonium events, denoted R_{Po} , multiplied by the probability of finding a bismuth candidate within the given time and position intervals, denoted P_{Bi} .

The rate of polonium candidates originating from a specific isotope i can be simply calculated as

$$R_{Po}^i = R_{all}^i \cdot \epsilon_{FV}^i \cdot \epsilon_{Po}^i \quad (5.7)$$

where R_{all} is the total event rate and the superscript i is designated to associate the terms with the isotope i . The total rate of such candidates is then $R_{Po} = \sum_i R_{Po}^i$.

The bismuth occurrence probability P_{Bi} within a time interval of Δt with an expected number of bismuth candidates of N_{Bi} is expressed as the sum of Poisson probability distribution functions

$$P_{Bi} = \sum_{n=1}^{\infty} \frac{(N_{Bi})^n e^{-N_{Bi}}}{n!} = 1 - e^{-N_{Bi}} \quad (5.8)$$

where N_{Bi} is evaluated by

$$N_{Bi} = \sum_i N_{Bi}^i = \sum_i (R_{all}^i \cdot \Delta t) \cdot \epsilon_{FV}^i \cdot \epsilon_{\Delta r}^i \cdot \epsilon_{Bi}^i. \quad (5.9)$$

When carrying out Eq. 5.9, $\epsilon_{\Delta r}$ can be approximated by

$$\epsilon_{\Delta r} \approx \frac{\frac{4}{3}\pi\Delta r^3}{V_{FV}} \quad (5.10)$$

as an upper limit. Note that ϵ_{FV}^i cannot be evaluated in the same fashion as Eq. 5.1. Since the distribution of the external backgrounds are clearly not uniform, ϵ_{FV}^i has to be evaluated via simulations.

Finally, the misidentification rate is expressed as

$$R_{BiPo}^{false} = R_{Po}^{false} P_{Bi}^{false} + R_{Po}^{false} P_{Bi}^{true} + R_{Po}^{true} P_{Bi}^{false} \quad (5.11)$$

where R_{BiPo} is the rate of coincidence declared, and the superscripts *true* and *false* indicate whether the quantities arise from genuine BiPo pairs or not, viz. whether the isotopes i in Eqs. 5.7 and 5.9 are the corresponding polonium and bismuth.

Data Fit

The MC method was extremely valuable in estimating the upper limit of the misidentification rate without data. Nonetheless, as seen in Section 5.3.3, the dependence on detailed simulations makes it impractical when the detector configuration starts to evolve. Alternatively, it was noticed that the misidentification rate can be evaluated directly by fitting the Δt distribution of tagged BiPo pairs in data. As stated in Section 5.3.4, the Δt distribution of true BiPo pairs is characterised by Eq. 5.5. The misidentified coincidences, as a random accident, should exhibit a uniform Δt distribution. Therefore, the Δt distribution of the tagged BiPo coincidences should be described by a form of

$$A \exp\left(\frac{-t}{\tau}\right) + B \quad (5.12)$$

where A and B are constants reflecting the magnitude of the true and false coincidences.

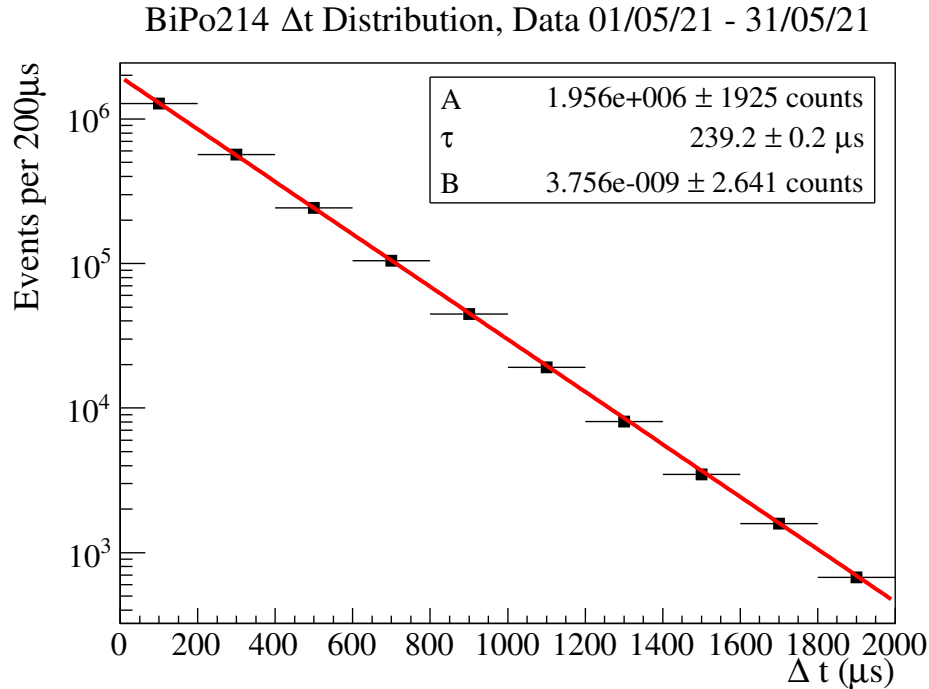


Figure 5.9: BiPo214 Δt fit using data from May 2021. The A and B values are counts per bin.

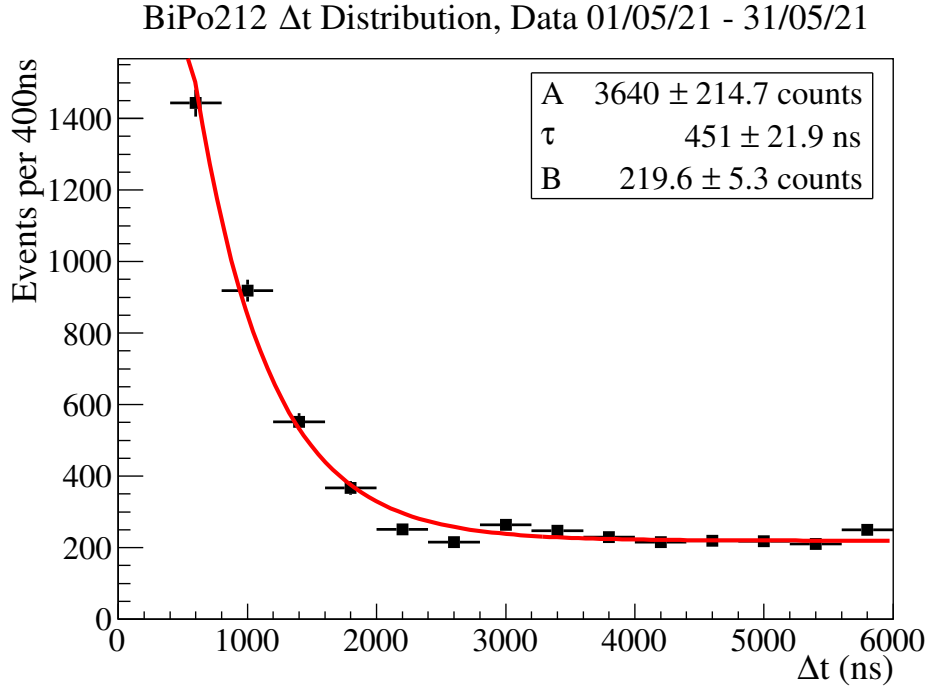


Figure 5.10: BiPo212 Δt fit using data from May 2021. The A and B values are counts per bin.

An example of the fit using data from May 2021 is shown in Figures 5.9 and 5.10. From this example, one can clearly see that, due to the reasons described in Section 5.3.2, the purity of the tagged BiPo214 is much higher than that of the tagged BiPo212.

5.4 Measurement of ^{238}U and ^{232}Th

In this section, the various measurements on the ^{238}U and ^{232}Th performed during the data taking period from July 2019 to May 2021 will be presented and discussed.

Based on the equilibrium assumption of the decay chains, the decay rate of the bismuth is equal to that of the corresponding ^{238}U or ^{232}Th decay chain:

$$\begin{aligned} \frac{1}{\tau_{214\text{Bi}}} N_{214\text{Bi}} &= \frac{1}{\tau_{238\text{U}}} N_{238\text{U}} \\ \frac{1}{\tau_{212\text{Bi}}} N_{212\text{Bi}} &= \frac{1}{\tau_{232\text{Th}}} N_{232\text{Th}} \end{aligned} \quad (5.13)$$

where N is the number of the kind of isotope indicated in the subscript and τ is the lifetime of the corresponding isotope. Eq. 5.13 can be further expanded and expressed in terms of the tagged BiPo rates R_{BiPo} :

$$\begin{aligned} (\epsilon_{FV} \cdot \epsilon_{comb}^{BiPo214})^{-1} \cdot R_{BiPo214} &= \frac{1}{\tau_{238\text{U}}} \cdot \frac{\sigma_{238\text{U}} \cdot M_{AV} \cdot N_A}{m_{238\text{U}}} \\ (\epsilon_{FV} \cdot \epsilon_{comb}^{BiPo212})^{-1} \cdot R_{BiPo212} &= \frac{1}{\tau_{232\text{Th}}} \cdot \frac{\sigma_{232\text{Th}} \cdot M_{AV} \cdot N_A}{m_{232\text{Th}}} \end{aligned} \quad (5.14)$$

where σ is the per material mass concentration of the decay chains; ϵ_{FV} is the volume fraction of the fiducial volume chosen; ϵ_{comb} is the combined efficiency listed in Table 5.2; M_{AV} is the mass of the scintillator in the entire AV; N_A is the Avogadro constant; and m is the molar mass of the isotope. The ^{238}U and ^{232}Th chain concentrations can, therefore, be estimated directly from the number of tagged BiPo coincidences.

5.4.1 Radon Ingress

Ideally, with Eq. 5.14, the estimation of ^{238}U and ^{232}Th levels will be a simple conversion of the number of BiPo coincidences after removing the misidentifications. In reality, however, the infiltration of ^{222}Rn and ^{220}Rn is not rare in the detector, especially during scintillator fill. The radon inevitably enters the scintillator when it gets exposed to air during transport and loading, so a rise in the radon level is almost guaranteed whenever scintillator is loaded into the detector. Many of the rises in BiPo coincidence rates, shown in Figure 5.11, can be attributed to scintillator loading, as indicated by the red arrows.

Radon ingress breaks the assumption of equilibrium and, hence, the validity of Eq. 5.14. Fortunately, the lifetimes of radon and its daughter isotopes are not long,

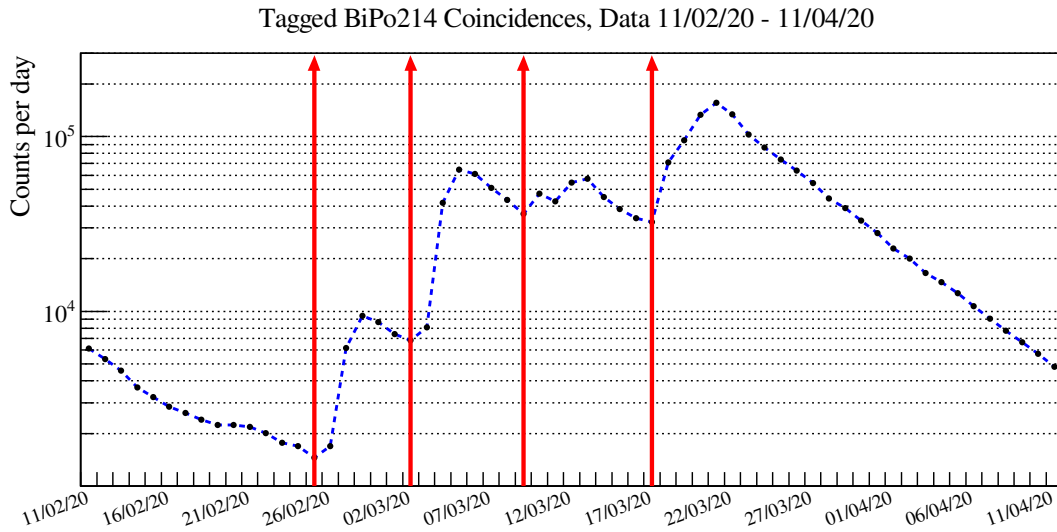


Figure 5.11: Tagged number of BiPo214 coincidences in the scintillator volume from the data taking period of 11th of February to 11th of April, 2020. The red arrows indicate the days of scintillator fill. The decay slopes in the plot matches the lifetime of ^{222}Rn , confirming it as the source of the activity rise.

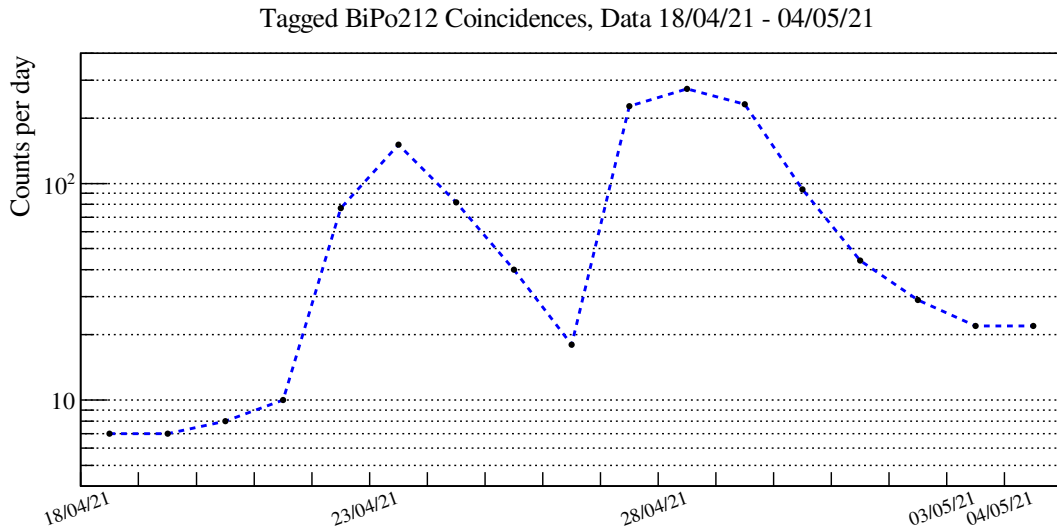


Figure 5.12: Tagged number of BiPo212 coincidences in the scintillator volume from the data taking period of 18th of April to 4th of May, 2021. The decay slopes in the plot matches the lifetime of ^{212}Pb , confirming the ^{220}Rn as the source of the activity rise.

5.4. MEASUREMENT OF ^{238}U AND ^{232}Th

^{238}U Measurement			
Period	Mass (tonnes)	Interface Z (mm)	^{238}U Concentration (g/g)
December 2019 - January 2020	72	+3850	$(9.2 \pm 0.8) \times 10^{-15}$
February 2020	181	+2500	$(7.5 \pm 0.4) \times 10^{-15}$
March - April 2020	355	+750	$(1.9 \pm 0.1) \times 10^{-15}$
June - July 2020	355	+750	$(4.6 \pm 1.2) \times 10^{-17}$

Table 5.3: Measurements on the ^{238}U decay chain concentration hitherto made. Numbers quoted from [179]. The quoted “Mass” is the mass of the scintillator and “Interface Z” is the scintillator interface Z position with respect to the AV equator.

^{232}Th Measurement			
Period	Mass (tonnes)	Interface Z (mm)	^{232}Th Concentration (g/g)
March - April 2020	355	+750	$(9.3 \pm 7.8) \times 10^{-17}$
May 2020	355	+750	$(7.5 \pm 3.4) \times 10^{-17}$
June 2020	355	+750	$(6.5 \pm 2.9) \times 10^{-17}$
July 2020	355	+750	$(5.3 \pm 1.5) \times 10^{-17}$
August - October 2020	355	+750	$(4.8 \pm 0.9) \times 10^{-17}$

Table 5.4: Measurements on the ^{232}Th decay chain concentration hitherto made. The quoted “Mass” is the mass of the scintillator and “Interface Z” is the scintillator interface Z position with respect to the AV equator.

so it is not impractical to wait for the radon to decay away. The decay time scale of the intruding radon will be characterised by the bottleneck in the decay chain. For ^{222}Rn , this will be the ^{222}Rn itself, having a lifetime of 5.51 days. For ^{220}Rn , it is ^{212}Pb which has a lifetime of 15.3 hours. The time profile of the number of tagged BiPo coincidences would then take the form of Eq. 5.12, where τ would become the characteristic lifetime of the radon ingress and the constant component B would now indicate the $^{238}\text{U}/^{232}\text{Th}$ chain contribution to the BiPo coincidence count. The ^{238}U and ^{232}Th chain levels can, therefore, be extracted by performing such a fit. The fit results for the ^{238}U measurement (fitted in collaboration with my colleague I. Morton-Blake [180], where he performed the final fit and the author practiced the BiPo analysis) are listed in Table 5.3. Results for the ^{232}Th measurement, carried out

only during the half-filled period due to higher misidentification rates, are listed in Table 5.4, for which, regardless of the scenario described thus far, the measurement was done by a simple exercise of Eq. 5.14 as there were no evidence of ^{220}Rn ingress for those periods.

It should be noted that in order to perform the measurement in this fashion, a stable period is needed, i.e. no further radon support after the first radon ingress, lasting at least a few characteristic lifetimes of the corresponding radon series. Otherwise, the constant term of the distribution will be concealed by the statistical fluctuations of the overwhelming exponential component. For instance, the stable periods in early March 2020, as depicted in Figure 5.11, or late April 2021, as depicted in Figure 5.12, are apparently too short for fitting. This has been the problem for the more recent data, and, hence, there have not been further measurements made since July 2020.

The most recent measurements listed in Tables 5.3 and 5.4 indicate that the scintillator contamination level of both the ^{238}U and ^{232}Th chains are within one order of magnitude from the target listed in Table 5.1, placing SNO+ in a position capable of executing its primary purpose of detecting neutrinoless double beta decays. Though encouraging, these results were based on the half-filled configuration, and whether the scintillator further loaded into the detector keeps up to this standard awaits confirmation when the detector stabilises.

5.5 ^{214}Bi - ^{214}Po Pairs as a Calibration Source

The implementation of the BiPo214 tagging method has improved the understanding of the detector in various aspects aside from the main objective of serving as a handle for estimating the ^{238}U decay chain concentration. Since the estimated misidentification of BiPo214 is nearly negligible, as demonstrated in the example of Figure 5.9, it has the potential to serve as an in-situ calibration source for various properties of the detector. This section will focus on two aspects: the tracking of PPO mixing and verification of the light yield level. Others have also used the tagged BiPo214 pairs for other purposes, for instance my colleague I. Morton-Blake has carried out a detailed study regarding the liquid scintillator time response to α and β particles using the tagged BiPo214 pairs [180].

5.5.1 Light Yield Verification

As the misidentification rate of the BiPo214 pairs is insignificant, the tagged pairs can be regarded as nearly pure α and β particles. By exploiting the known energies of the corresponding decays, i.e. the 3.27 MeV β decay of ^{214}Bi and the 7.83 MeV α decay of ^{214}Po , one can perform a direct comparison between simulation and data to

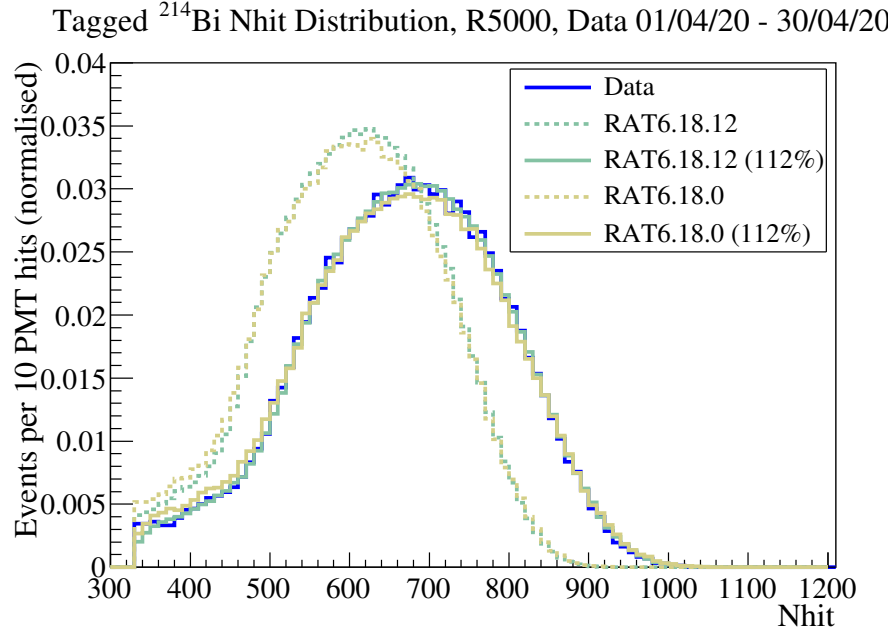


Figure 5.13: The Nhit comparison of ^{214}Bi between data (blue) from April 2020 and MC simulations using **RAT6.18.0** (yellow) and **RAT6.18.12** (green). The original distributions of the simulations are plotted in dashed lines and the scaled distributions of which are plotted in solid lines. Both versions of the simulation agrees well with data after a 12% scale-up in light yield.

estimate the light yield level in the detector. The comparison is done by scaling the MC simulated Nhit distribution to match that of data. To scale the simulation, the Nhit of each event is first multiplied by the chosen scale factor, then smeared by a Poissonian error.

An example comparison of the half-filled data for April 2020 with simulations using **RAT6.18.0** (the RAT version contemporary with the data) and **RAT6.18.12** is shown in Figures 5.13 and 5.14. The simulations used a light yield expected for 0.5 g/L PPO, whereas the data PPO concentration is estimated to be at 0.52 g/L by summing the total amount of PPO loaded in each fill. Results for ^{214}Bi showed overall good agreement with the anticipated light yield, confirming the estimated PPO concentration. This is not too surprising as the scintillator response to electrons is well-understood, and, hence, is handled better in the simulations. The ^{214}Po α emission, on the contrary, involves the phenomenon of quenching^{vii} which is much more complicated and adds difficulty to simulations. As shown in Figure 5.14, the result

^{vii}Processes that reduce the light yield of scintillation are known as quenching. For detailed discussions on the topic, see [57].

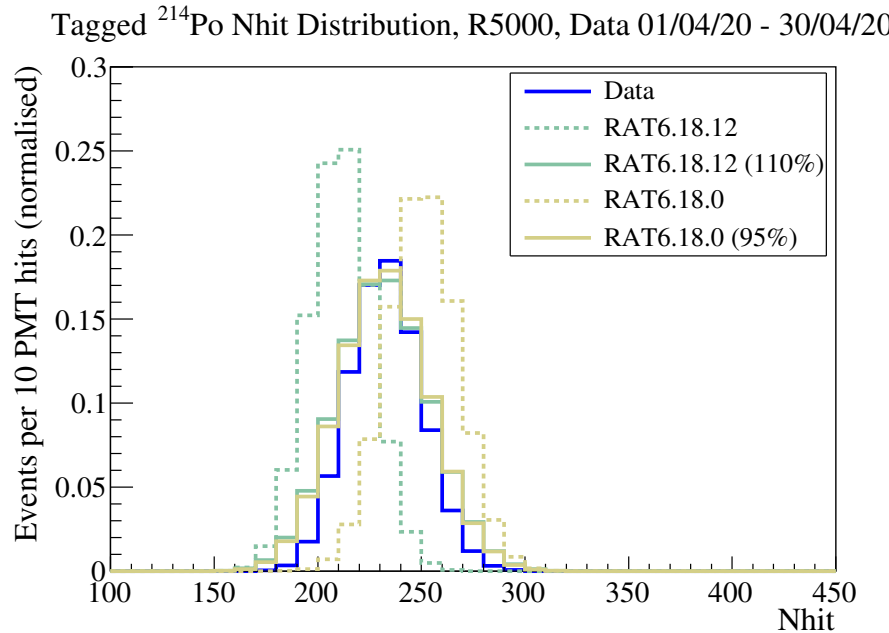


Figure 5.14: The Nhit comparison of ^{214}Po between data (blue) from April 2020 and MC simulations using **RAT6.18.0** (yellow) and **RAT6.18.12** (green). The original distributions of the simulations are plotted in dashed lines and the scaled distributions of which are plotted in solid lines. The discrepancy between data and MC originates from the complications of quenching of the α particle. One can clearly see the improvement in the later **RAT** versions, where the difference between data and simulation has changed from 5% scale-down to 10% scale-up in light yield, matching the results from the ^{214}Bi .

from the comparison between data and the original simulation, using **RAT6.18.0**, suggested that the α particle is more quenched than the model used in that simulation. After that, much effort has gone into improving the model, and it is clear that the simulations done with the more recent versions of **RAT** are agreeing better with data.

5.5.2 PPO Mixing

Due to technical issues during filling, the PPO concentrations in each load of scintillator varied between 0 to 80 g/L rather than being fixed at 2 g/L. This has caused the light yield level to fluctuate over the period. Even worse, the dynamics of mixing between different PPO levels, as previously stated in Section 5.3.2, turns out to be non-trivial. It is, therefore, important to be able to track its state of evolution. The

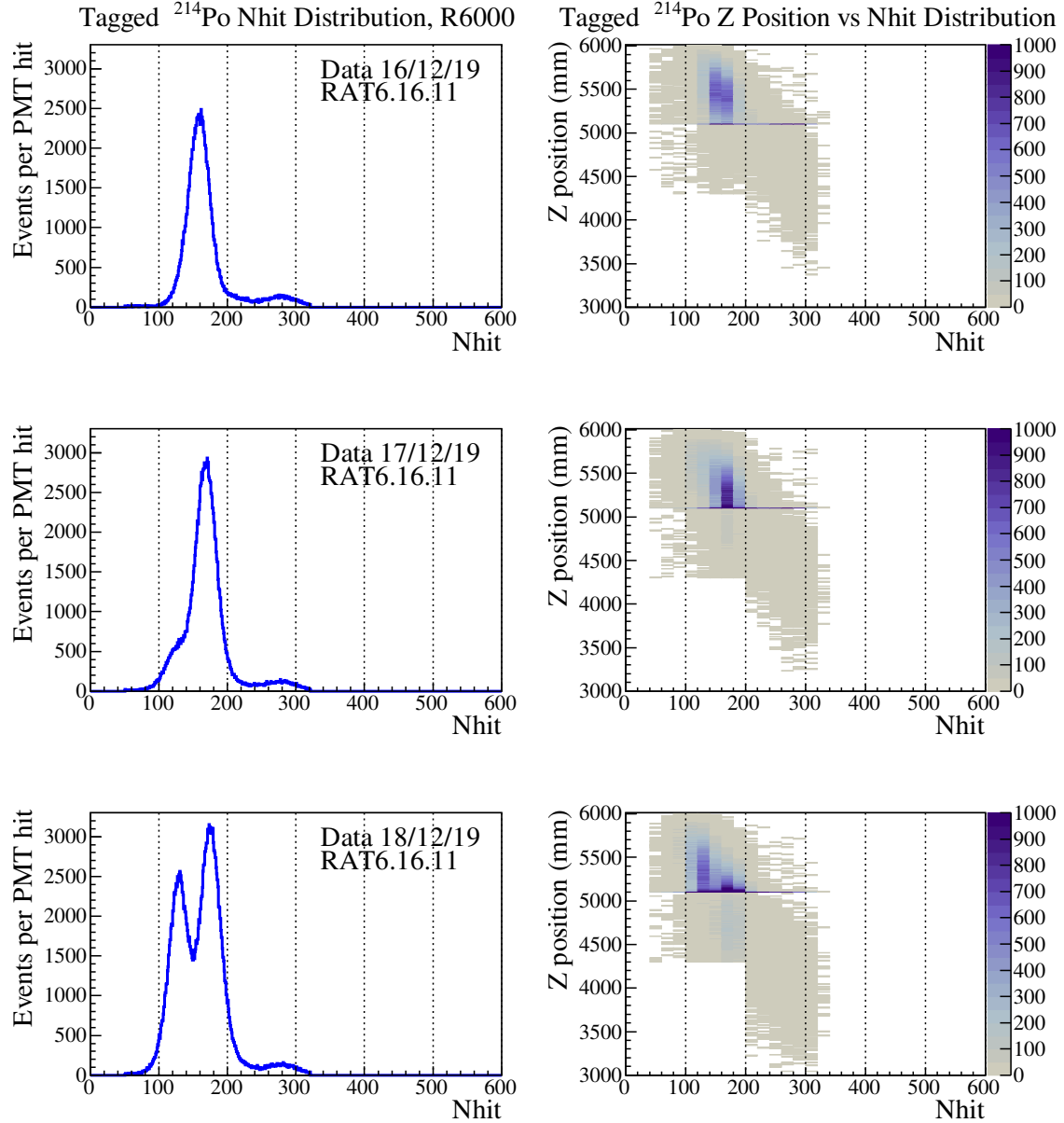


Figure 5.15: The Nhit distribution (left) and the Nhit distribution plotted against the Z axis (right) of the tagged ^{214}Po from data taken from the 16th to 18th of December, 2019. Scintillator with no PPO was loaded during the 17th and 18th of December. This is a typical demonstration of PPO stratification during filling.

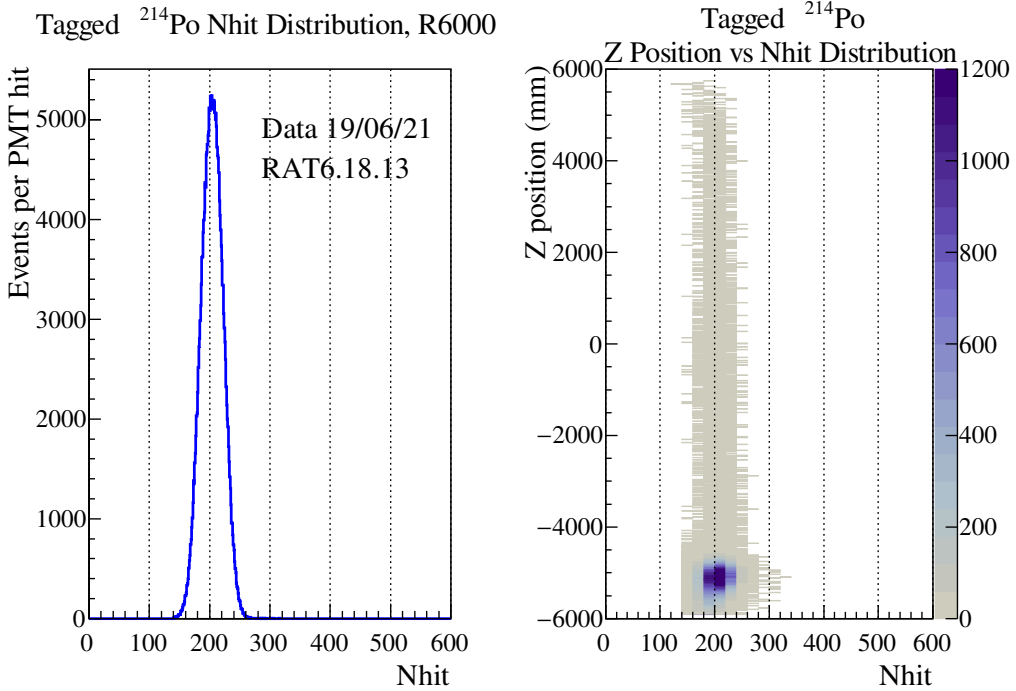


Figure 5.16: The Nhit distribution (left) and the Nhit distribution plotted against the Z axis (right) of the tagged ^{214}Po from data taken on the 19th of June, 2021. This is a recent example of non-uniform ^{222}Rn distribution in a stable light yield configuration.

mono-energetic α particle of ^{214}Po is found to be an efficacious in-time indicator of the local light yield level.

Figure 5.15 is an example of PPO stratification during a scintialltor fill from 16th to 18th of December, 2019. This was one of the first instances of observing PPO stratification in the detector. SNO+ had been troubled with the problem of stratification for long periods during the phase transition. Eventually, it was discovered that the PPO stratification is caused by the existence of temperature gradients in the detector. The gradient can be eliminated by either further proceeding with the filling, which agitates the configuration, or forcibly recirculating the liquid in the AV.

Besides PPO, the distribution of the radon ingress is also non-uniform in many occasions, especially when it just entered. In general, this stratification originates from the same cause. Nonetheless, as shown in Figure 5.16, radon and PPO stratification does not necessarily coincide with each other. In such cases, the PPO was already uniform when the thermal gradient arose.

5.6 Summary

In this chapter, the $\beta-\alpha$ coincidence signals originating from the pairs ^{214}Bi - ^{214}Po and ^{212}Bi - ^{212}Po have been investigated. Using the tagged BiPo pairs, the concentrations of ^{238}U and ^{232}Th decay chains in the liquid scintillator have been measured to be $(4.6 \pm 1.2) \times 10^{-17}$ g/g and $(4.8 \pm 0.9) \times 10^{-17}$ g/g, respectively. These latest measurements suggest that the contamination level of the liquid scintillator is within one order of magnitude from the target initially set for the pure-scintillator phase. Though slightly higher than the target for pure-scintillator phase, it is still well within the limit set for the double beta studies in the tellurium-loaded phase. It should also be noted that this currently achieved purity of the scintillator is by no means final. SNO+ will be carrying out further purification throughout the data-taking period, which is expected to further reduce the contamination level to target, or even lower. Furthermore, the results shown in this chapter are measured in the half-filled configuration ($Z = +750$ mm), and the purity of the scintillator loaded after still await confirmation to ascertain the overall contamination level of the fully filled configuration.

Besides estimating the ^{238}U and ^{232}Th concentrations in the scintillator, the coincidence identification method developed in this chapter has been proven to be valuable in many other aspects. In particular, the high purity of the tagged ^{214}Bi - ^{214}Po pair has been used as a calibration source for the light yield level and time response of the scintillator. During the light yield calibration study, it was also noticed that the mono-energetic α from ^{214}Po is a useful handle in monitoring the local light yields and radon ingress of the detector. Additionally, the method is valuable in itself as a framework for identifying other signals of coincident nature, amongst which the most important is the identification of inverse beta decay (IBD). Indeed, the framework and script developed for this study has been modified to tag IBD events from reactor anti-neutrinos in [180]. With slight modifications to the cut values, the framework established in this study can be easily adapted for the identification of IBD events from supernova neutrinos.

Chapter 6

Fast Reconstruction

In SNO+, the full reconstruction algorithms implemented have achieved good resolution and provided reliable reconstructed information. Full reconstruction is, however, time and resource demanding, currently multiple hours per hour of data. This might be problematic for analyses where prompt response is required, for instance, the detection of supernova bursts and pre-supernova neutrinos. Methods of conducting swift reconstructions, albeit at the risk of losing some resolution, would be desirable for those purposes.

This chapter will serve as an exposition of the algorithms we have developed for fast reconstruction by exploiting the early PMT hit information. The first half of this chapter describes the `FastZ` position reconstruction method developed for partial-fill phase using the earliest PMT hits from the top and bottom regions. This algorithm was developed as an auxiliary method when the full reconstruction, that is, `partialFitter`, was still in its early stages. The second half of the chapter focuses on studies regarding the identification of spatial coincidences. In particular, the development of the `TimeCentroid` coincidence tagger is based on the PMT hit topology, which does not involve actual position reconstruction. Results of this metric-based algorithm will be compared to the position reconstruction methods to demonstrate that a full position reconstruction can be avoided if spatial coincidence identification is the only objective.

6.1 `FastZ` — Position Reconstruction for Partial Fill

When applying the PMT triangulation relation Eq. 4.2, the discontinuity at the partial-fill interface complicates reconstruction and causes the full reconstruction methods to become even more time-consuming. Initially, this did not raise much

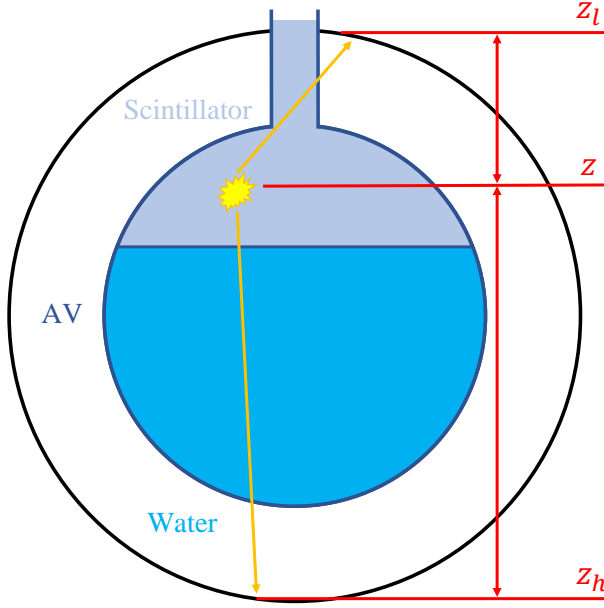


Figure 6.1: Schematic illustration of the light path difference between top and bottom PMTs. This path difference is used in **FastZ** to estimate the Z position of the event.

attention as partial fill was thought to be a transient phase. It became more problematic when the phase transition was prolonged. A proposal to reduce the computation time was to run a swift position estimate along the Z axis and veto the events that are clearly from the water volume. This idea later became the **FastZ** fitter, which utilises the PMT hit time difference between the top and bottom of the detector to conduct a swift and simple Z position estimate.

6.1.1 Light Path Calculation

The basic idea of the **FastZ** fitter is to infer the Z coordinate of the event in a similar fashion as Eq. 4.2 by selecting the PMT hits located in the top and bottom regions of the detector as shown in Figure 6.1, in which top and bottom regions are chosen to be the regions with $Z > +8000$ mm and $Z < -7000$ mm. This idea relies on the basic properties of scintillation light, which is nearly isotropic and usually results in high number of PMT hits. Furthermore, as scintillation light is usually not all emitted at once, only the earliest PMT hit in each region will be selected. These properties of scintillation light can be observed from Figure 6.2. With this selection criterion, it can then be assumed that the photons received are from the first wave of photon emissions and are emitted at roughly the same time which will be denoted as t_0 .

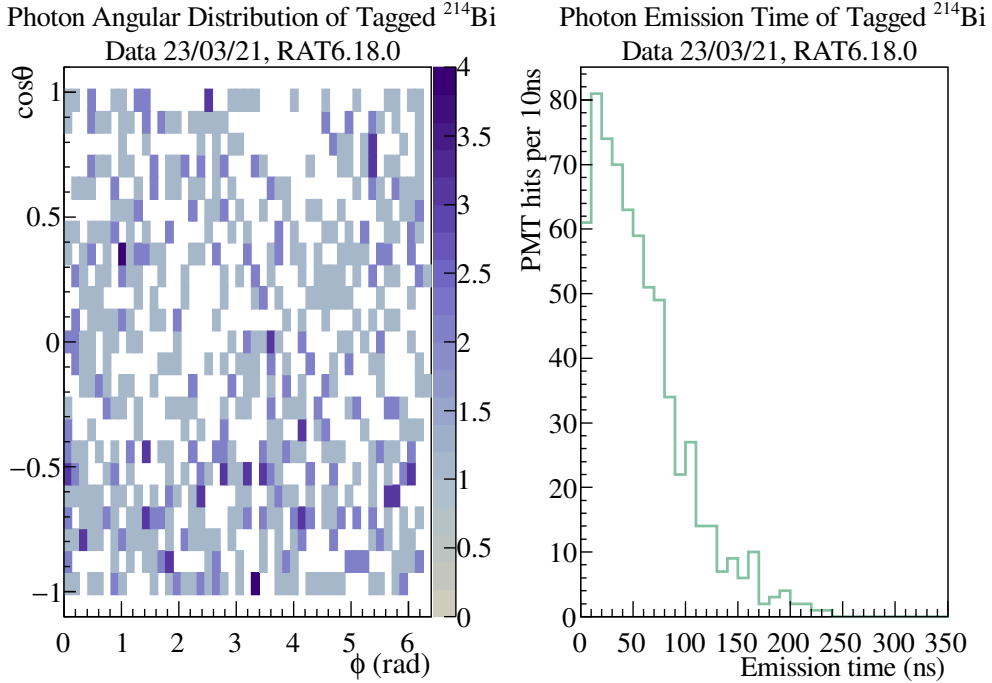


Figure 6.2: The photon angular distribution (left) and emission time (right) of a tagged ^{214}Bi from the 23rd of March, 2021. The (θ, ϕ) coordinates are defined as the usual spherical coordinates with the reconstructed event position (1596.94, 1598.96, 4915.19), in millimetres, as origin. The emission time of the photons is defined as PMT hit time subtracted by the estimated light propagation time, where the zero time is set to the emission time of the photon that first triggered a PMT.

Having selected the two PMT hits in each region, the Z position of the event can immediately be estimated by

$$\begin{aligned} t_{top} &= t_0 + f_s^h \frac{z_h - z}{c_s} + f_w^h \frac{z_h - z}{c_w} \\ t_{bottom} &= t_0 + f_s^l \frac{z - z_l}{c_s} + f_w^l \frac{z - z_l}{c_w} \end{aligned} \quad (6.1)$$

where t_{top} and t_{bottom} are the hit times of each selected PMT; z is the Z coordinate of the true event; c_s and c_w are the light speed in scintillator and water; $\{f_s^h, f_w^h, f_s^l, f_w^l\}$ are the fraction of each path being scintillator or water satisfying $f_s^h + f_w^h = 1$ and $f_s^l + f_w^l = 1$. Eq. 6.1 implicitly assumes that the light path is nearly parallel to the Z axis, which is not completely unreasonable given that the chosen PMT hits are selected from the very top and bottom regions of the detector. To make the expression

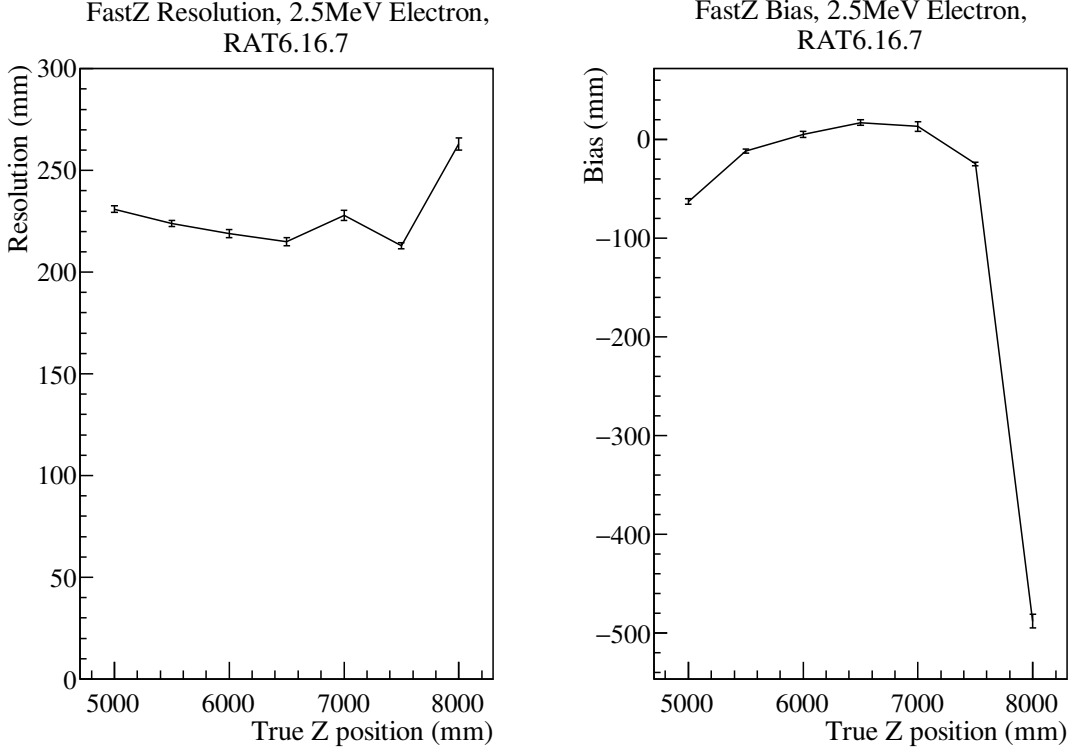


Figure 6.3: The fitted resolution (left) and bias (right) of **FastZ** applied on 2.5 MeV electrons simulated in the scintillator volume of a partial-fill configuration with $Z = +4400$ mm using **RAT6.16.7**.

more realistic, the light speeds are replaced by $c'_s = c_s \cdot \cos \theta_i$ and $c'_w = c_w \cdot \cos \theta_i$, where $\theta_i \in [0, \pi/2]$ ($i = h, l$) are the angles of the travel direction relative to the Z axis. It is, however, not possible to get the precise θ_i for each event without knowing the true event position. Therefore, instead of obtaining an angle for each event, the average angle for the given configuration is applied as an approximation to all events, which is effectively a correction factor to the light speed. By combining the approximations and Eq. 6.1, the reconstructed event Z coordinate can be expressed as

$$z_{recon} = \frac{\left(\frac{f_s^h}{c_s \cos \theta_h} + \frac{f_w^h}{c_w \cos \theta_h} \right) z_h + \left(\frac{f_s^l}{c_s \cos \theta_l} + \frac{f_w^l}{c_w \cos \theta_l} \right) z_l}{\left(\frac{f_s^h}{c_s \cos \theta_h} \right) + \left(\frac{f_w^h}{c_w \cos \theta_h} \right) + \left(\frac{f_s^l}{c_s \cos \theta_l} \right) + \left(\frac{f_w^l}{c_w \cos \theta_l} \right)}. \quad (6.2)$$

Partial Fill, $Z = +4500\text{mm}$	
Method	CPU Time per Event (s)
FastZ	0.00045
partialFitter (RAT6.17.6)	0.75

Table 6.1: CPU time per event for **FastZ** and **partialFitter**.

6.1.2 Performance

The fitter was tested on samples of 2.5 MeV electrons simulated within the scintillator volume using **RAT6.16.7**. The scintillator interface was set to $Z = +4400\text{ mm}$, which corresponds to the 60-tonne configuration initially planned for inspection.

Figure 6.3 shows the resulting resolution and bias of **FastZ** at different positions, where the resolution is defined by the standard deviation of the $z_{\text{recon}} - z_{\text{true}}$ distribution and the bias is the deviation from zero of the $z_{\text{recon}} - z_{\text{true}}$ distribution mean. **FastZ**, being a simple estimate based on only two PMT hits, is obviously not competitive compared to the approximately 90 mm resolution of **partialFitter**. Nevertheless, **FastZ** is able to maintain reasonable resolution and overall stable performance even in regions close to the interface and high up in the AV neck, except for above +8000 mm which is already around the PSUP. Furthermore, Table 6.1 shows that the CPU time per event spent by **FastZ** is about three orders of magnitude faster than **partialFitter**. From these perspectives, it serves its purpose of doing a quick and preliminary estimate on the Z position.

6.2 TimeCentroid — Spatial Coincidence Identification

Coincidence events are one of the most informative types of events within neutrino detectors, for they can be tagged with high purity without much difficulty. Coincidences are identified by pairing events occurring within a specific time window and in neighbouring regions, e.g., the inter-event cuts of the bismuth-polonium (BiPo) analysis in Chapter 5. In spite of the effectiveness of the distance correlation cut (Δr cut), the full position reconstruction is time-consuming. The increase in light yield, e.g., when the PPO load reaches the target 2 g/L, could further aggravate the situation as reconstruction time increases with the number of PMT hits. With the aim of reducing the computation time, this immediately invites the obvious question of whether precise position reconstruction is necessary, or even more radically whether position reconstruction is needed at all, for the purpose of coincidence identification. For this purpose, the `TimeCentroid` algorithm for swift position coincidence tagging based on PMT hit topologies is proposed and investigated.

6.2.1 Topological Similarity in PMT Hit Distributions

The underlying argument for the algorithm is rather simple and intuitive: the topology of the emitted photons, and thus PMT hits, from the same position, as in a coincidence event, should be similar as shown in Figure 6.4. By exploiting this topological similarity, one should, in principle, be able to identify spatial coincidences without performing actual position reconstruction.

In order to verify this hypothesis, BiPo214 pairs in both simulation, randomly distributed in the full-scintillator configuration, and data, from the 2nd of April, 2020, with the scintillator interface at $Z = +750$ mm, are employed for examination. The spatial distribution of PMT hits versus the PMT hit times for an example bismuth and polonium event from both cases are shown in Figures 6.5 and 6.6. From those plots, it is evident that there is some similarity to be exploited between the PMT hit distributions of the BiPo pairs.

6.2.2 Weighted Coincidence Classifier

One of the most prominent features exhibited by the light patterns in Figures 6.5 and 6.6 is the spatial resemblance of the dense cluster of early PMT hits. The `TimeCentroid` tagger is built upon this spatial resemblance. The idea is to evaluate the similarity by locating the central position (mean or median) of the leading light cluster, and use it as a similarity metric.

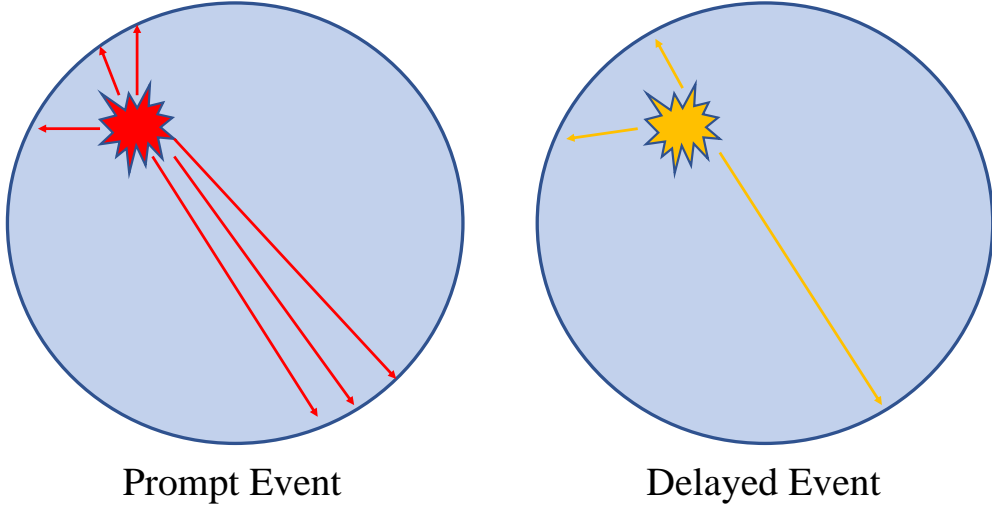


Figure 6.4: Graphical representation of the scintillation photon distribution of a coincidence event.

In **TimeCentroid**, the leading light cluster is defined as the first N PMTs with PMT hit times in the range $250 - 280$ nsⁱ, which can be inferred from Figures 6.5 and 6.6. Note that the number of PMTs chosen, N , is dependent on the light yield level. The central location of the early cluster is then chosen to be a weighted mean of the PMT hit coordinates taking the form of

$$\hat{x}^\mu = \left(\sum_{i=0}^{N-1} w(t_i) x_i^\mu \right) \Bigg/ \left(\sum_{i=0}^{N-1} w(t_i) \right) \quad (6.3)$$

with the weight function

$$w(t) = \frac{1}{t - t_0 + C} \quad (6.4)$$

where $\hat{x}^\mu = \{\hat{x}, \hat{y}, \hat{z}\}$ are the weighted means; i is the index for the PMT hits; $x_i^\mu = \{x_i, y_i, z_i\}$ are the coordinates of the i th PMT hit; t_i is the hit time of the i th PMT hit; t_0 is the hit time of the earliest chosen PMT hit; and C is a time offset for the weight. Note that $i = 0$ corresponds to the earliest PMT, whereas the time ordering of the rest of the cluster is irrelevant. Since the clustering of the leading light is more pronounced for earlier hits and becomes more scattered for later times, the PMT

ⁱThe zero time of the PMT hit time is defined as 280 ns before the PMT trigger threshold is passed [170]. This was arbitrarily chosen such that the zero time is earlier than the lower end of the event time window to keep the PMT times positive.

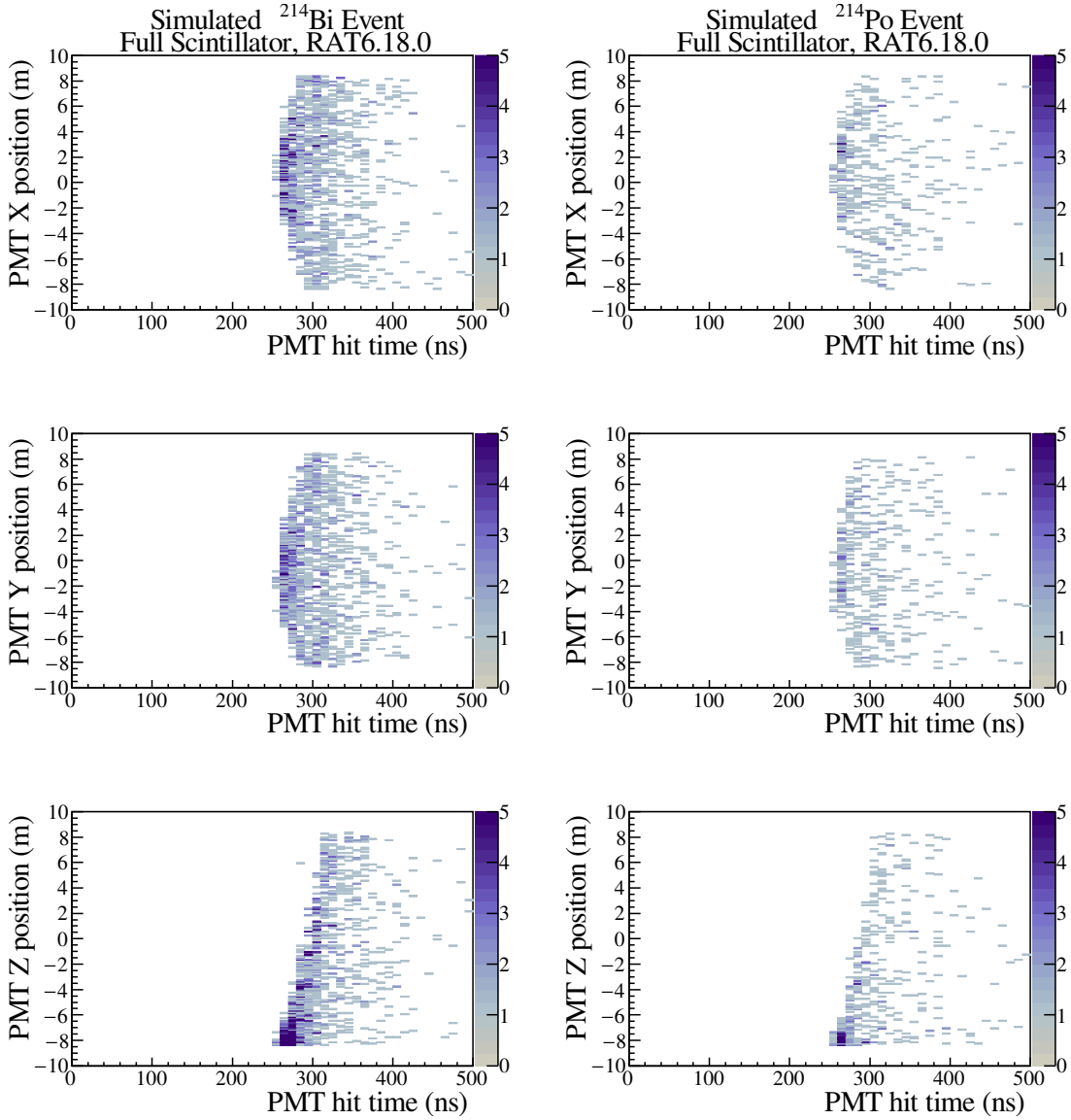


Figure 6.5: PMT position versus hit time distribution for an example ^{214}Bi (left) and ^{214}Po (right) pair simulated in the full-scintillator configuration with RAT6.18.0. The BiPo214 pairs are randomly distributed within the AV. This example BiPo214 pair is positioned at $(x, y, z) = (2664.18, 3207.11, -1968.65)$, in units of millimetres.

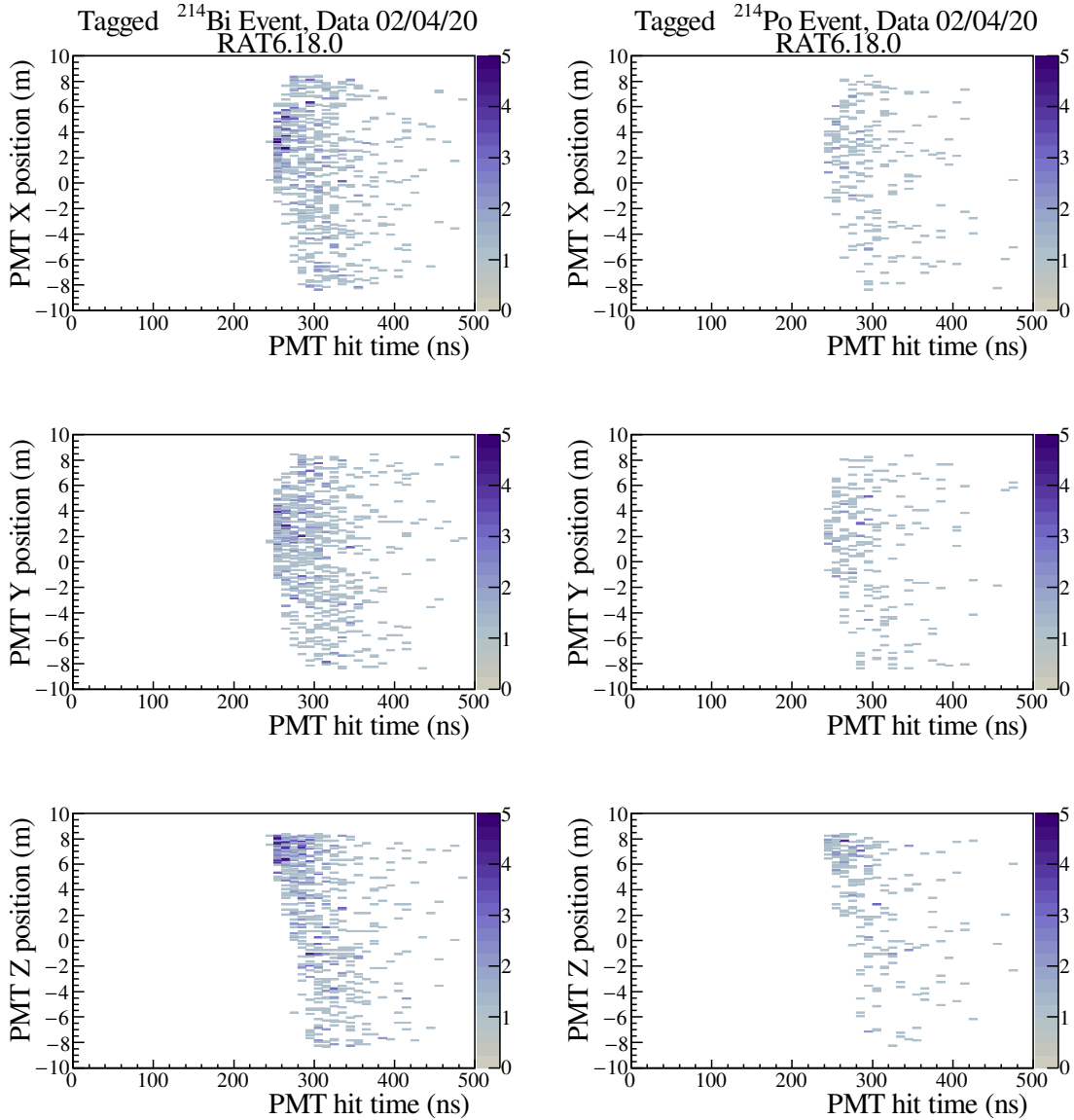


Figure 6.6: PMT position versus hit time distribution for an example tagged ^{214}Bi (left) and ^{214}Po (right) pair from the data taken on the 2nd of April, 2020, which has the scintillator interface at $Z = +750$ mm.

coordinates are weighted by the inverse of the PMT hit time in Eq. 6.3. As weights of the form $1/t$ are dependent on the choice of $t = 0$, the zero time is set to float by adding a time offset C , in units of nanoseconds.

Having obtained the central position $\{\hat{x}, \hat{y}, \hat{z}\}$, the similarity metric can then be evaluated by the Pythagorean sum of the coordinate differences

$$\Delta\hat{r}^2 = \Delta\hat{x}^2 + \Delta\hat{y}^2 + \Delta\hat{z}^2 \quad (6.5)$$

where

$$\begin{aligned} \Delta\hat{x} &= \hat{x}_{prompt} - \hat{x}_{delayed} \\ \Delta\hat{y} &= \hat{y}_{prompt} - \hat{y}_{delayed} \\ \Delta\hat{z} &= \hat{z}_{prompt} - \hat{z}_{delayed}. \end{aligned} \quad (6.6)$$

Note that the carets on the central position variables are used as a reminder that these parameters are *not* event position reconstructions. Instead, these variables serve as an indicator of the position of the early light cluster, and points towards a position around the PSUP which is also apparent from Figures 6.5 and 6.6.

Performance

Performance tests for the algorithm were conducted using samples of 50,000 BiPo214 events simulated in the partial-fill, applying the conditions of the detector configuration as of the 2nd of April, 2020, and full-scintillator configurations. Needless to say, the BiPo214 pairs are regarded as the signal. The background sample, for comparison, is constructed out of unassociated events. For this purpose, two successively simulated ^{214}Bi events, which are independently and randomly distributed within the AV, are paired.

Having defined the signal and background samples, the receiver operating characteristic (ROC) curve can then be constructed to evaluate the performance of each method. Before comparing `TimeCentroid` to the full reconstruction methods `scintFitter` and `partialFitter`, there are two parameters that remain undetermined, namely the number N of PMTs to include in the weighted mean and the time offset C . By inspecting the ROC curves depicted in Figures 6.7 and 6.8, it is found that $\{N, C\} = \{70, 10\}$ is the optimised choice for the full-scintillator configuration and $\{N, C\} = \{50, 10\}$ for the partial-fill case. Finally, Figure 6.9 presents the optimised `TimeCentroid` ROC curves plotted against the `scintFitter` and `partialFitter` curves. Though the full reconstruction methods, without much surprise, clearly deliver the best results, the performance achieved by a method as simple as `TimeCentroid` is still encouraging. At the point of plateau, `TimeCentroid` yields efficiencies greater than 99% for true coincidences with a less than 5% false identification rate.

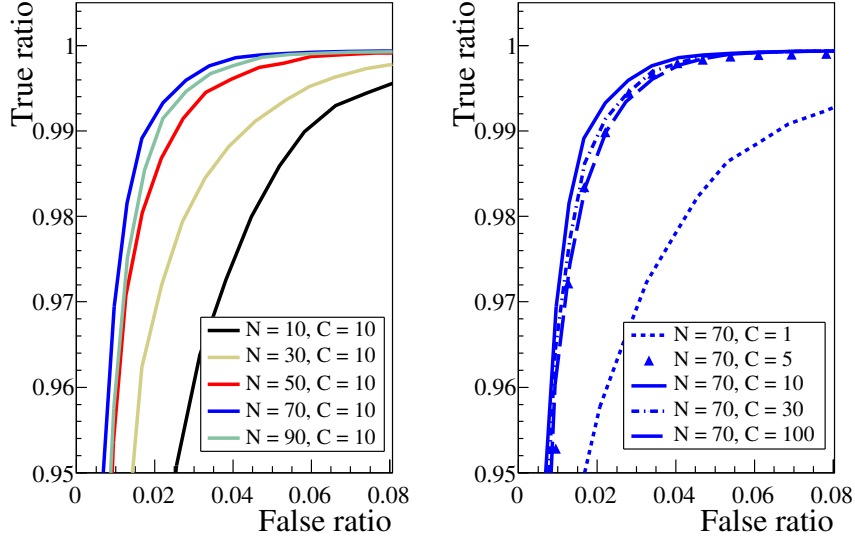


Figure 6.7: ROC curves of TimeCentroid with a range of different N values (left) and C values (right), tested on BiPo214 pairs simulated in the full-scintillator configuration with RAT6.18.0.

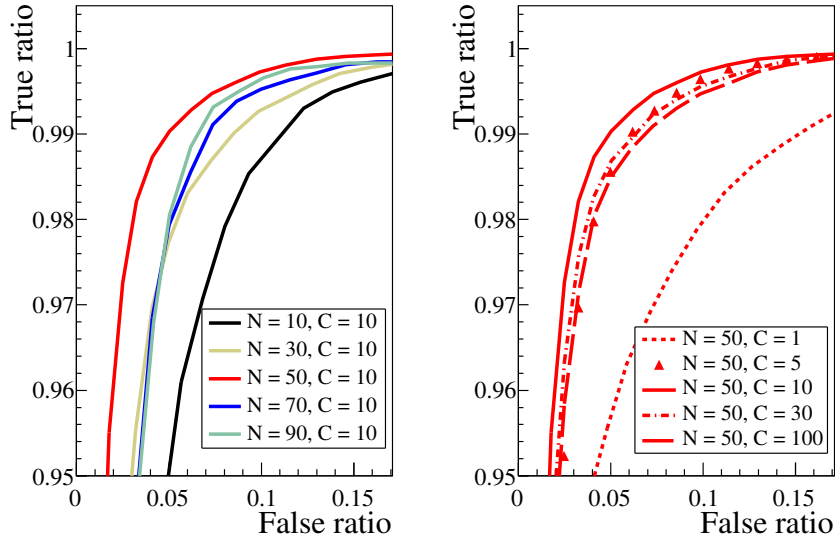


Figure 6.8: ROC curves of TimeCentroid with a range of different N values (left) and C values (right), tested on BiPo214 pairs simulated in partial-fill configuration ($Z = +750$ mm) with RAT6.18.0.

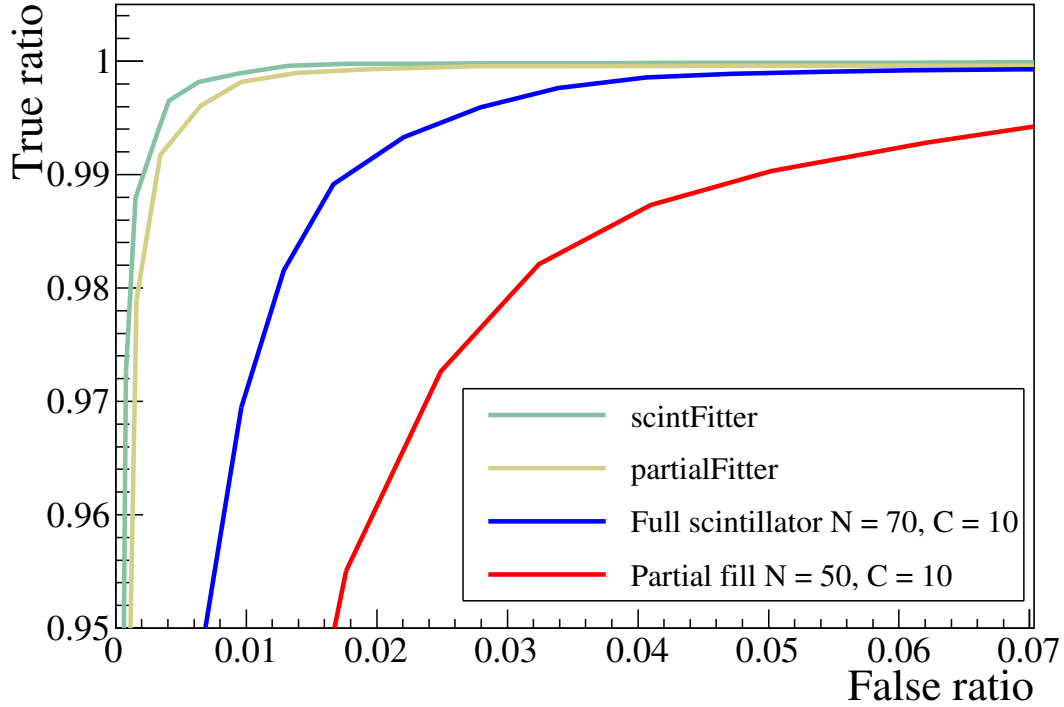


Figure 6.9: ROC curves of `scintFitter`, `partialFitter` and `TimeCentroid` (with optimised parameters).

CPU Time

Besides comparing the identification efficiency to that of the full reconstruction algorithms, another important feature that should also be compared is the CPU time spent when executing these algorithms. Reducing the CPU time is the value and motivation of developing `TimeCentroid`.

Table 6.2 lists the CPU time per event for performing `TimeCentroid` and the position reconstruction methods on the samples of simulated BiPo214 pairs. `TimeCentroid`, being a simple calculation looping through the PMT hits once, is undoubtedly the most time efficient. It is about three orders of magnitude faster than the full reconstruction methods, and one order of magnitude faster compared to the simplest part of the full reconstruction, i.e., `Quad` which was introduced in Section 4.4.1.

Full Scintillator	
Method	CPU Time per Event (s)
<code>scintFitter</code>	2.2
<code>TimeCentroid</code>	0.0015
<code>Quad</code>	0.016

Partial Fill, $Z = +750$ mm	
Method	CPU Time per Event (s)
<code>partialFitter</code>	0.3
<code>TimeCentroid</code>	0.0013
<code>Quad</code>	0.013

Table 6.2: CPU time per event for processing simulated BiPo214 events in full-scintillator (top) and partial-fill (bottom) configurations.

Full Scintillator	
Method	CPU Time per Event (s)
<code>TimeCentroid</code>	0.0015

Method	Iterations	CPU Time per Event (s)
<code>Quad</code>	4000	0.016
<code>Quad</code>	1000	0.0057
<code>Quad</code>	100	0.003
<code>Quad</code>	50	0.0017

Table 6.3: CPU time per event for processing simulated BiPo214 events in the full-scintillator configuration using `Quad` with different number of iterations.

6.2.3 Quad with Reduced Iterations

From Table 6.2, the CPU time spent by `Quad` is, in general, only one order of magnitude higher than `TimeCentroid`. It is, therefore, valuable to take it as an example of a fast primitive position reconstruction, and compare it to the `TimeCentroid` classifier.

Table 6.3 lists the CPU time for running `Quad` with different numbers of iterations on the BiPo214 pairs in full-scintillator configuration, from which one can see that `Quad` with 50 – 100 iterations takes the amount of time comparable to that used by `TimeCentroid`. The resulting ROC curves compared to that of `TimeCentroid` is presented in Figure 6.10. One can observe that the performance of `Quad` with the original 4,000 iterations is slightly better than `TimeCentroid`. As the number of iterations decrease, however, the performance of `Quad` rapidly worsens, e.g., the false rate for 99% efficiency becomes 84% when `Quad` is brought to the same speed as `TimeCentroid`.

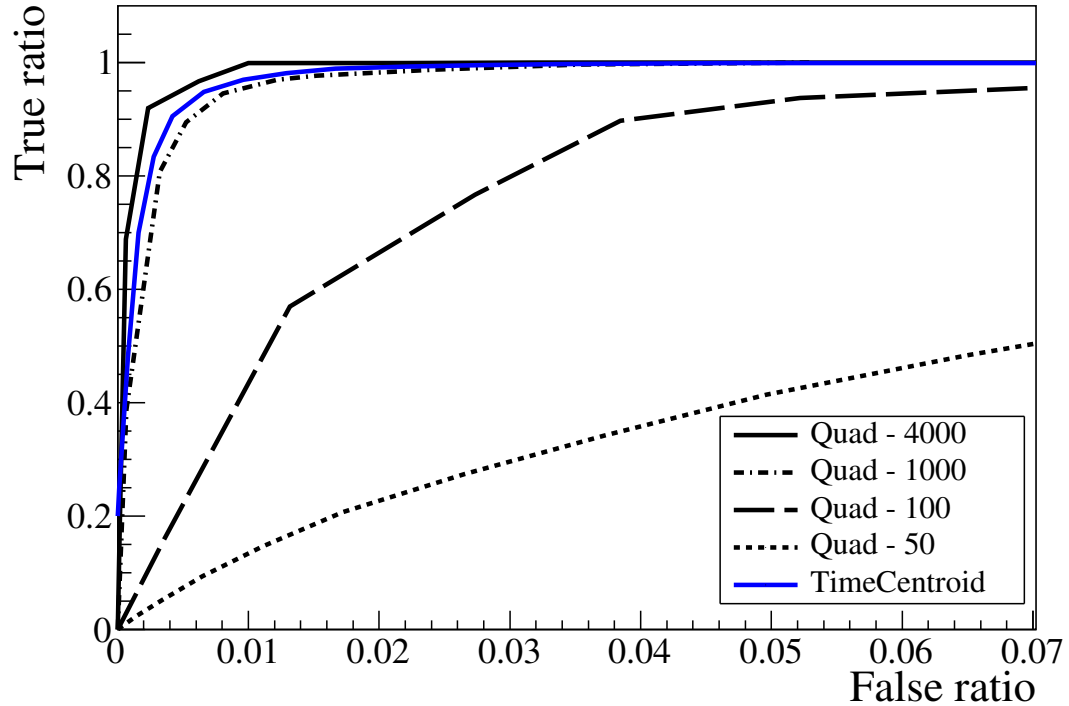


Figure 6.10: ROC curves of `Quad` with different numbers of iterations (n iterations labelled as “`Quad - n` ”). The ROC curve of `TimeCentroid` in full-scintillator configuration is also plotted for comparison.

6.2.4 Applications

With the three orders of magnitude lower CPU time than `scintFitter` and reasonable discriminating power, `TimeCentroid` can be useful in various studies that involve coincidence identification. The two types of coincidences currently of concern are the inverse beta decay (IBD) and Bismuth-Polonium events.

IBD events are the main handles to the detection of pre-supernova $\bar{\nu}_e$ and supernova bursts, where this method can be particularly valuable as supernova-related studies are often constrained for time. Implementation of the classifier in the pre-supernova alert is currently in progress.

`TimeCentroid` has so far only been tested as an event filter to the BiPo identification analysis described in Chapter 5, which could potentially make the BiPo background monitoring more prompt. The basic idea is to run the BiPo tagging cuts with the Δr cut replaced by a `TimeCentroid` cut on the unprocessed data, and process only the events passing those cuts. This can significantly reduce the processing time for each run. To test the effectiveness of this strategy, this event filter is tested on the data runs from the 2nd of April, 2020. This combined event filter was able to preserve 23,155 of the 23,161 events tagged by the original BiPo analysis with only 1,826 additional mistagged events, i.e., the number of events to process per one-hour data run can be reduced from about 300,000 to around 1,000. The processing time spent by the `TimeCentroid` event filter was around a minute, and the processsing time of the full reconstruction using `partialFitter` was reduced to roughly 5 minutes bringing the total reconstruction time down from nearly 6 hours to 6 minutes.

6.3 Summary

The two algorithms, `FastZ` and `TimeCentroid`, developed in the aim of reducing the reconstruction time has been introduced in this chapter. Both of the methods were able to deliver reasonably well results with the CPU time reduced by three orders of magnitude compared to the full reconstruction, fulfilling their initial objectives. The `FastZ` method was designed for a specific period during scintillator fill, and, hence, was not generally applied afterwards. `TimeCentroid`, on the other hand, is generally applicable for coincidence studies, e.g., BiPo and IBD studies. As a result, `TimeCentroid` could come to the aid of the background and supernova studies by making the most time consuming step, namely position reconstruction, in BiPo and IBD identifications nearly prompt. Furthermore, the method has the potential to be applied to a wider range of configurations, as the underlying principles apply to any scintillator detector.

Chapter 7

Supernova Signal Detection

Core collapse supernovae (CCSNe), introduced in Chapter 3, are amongst the most powerful sources of cosmic neutrinos of all flavours. The extreme density and temperature during the supernova evolution provides opportunities to probe neutrino properties which are not accessible on Earth. Furthermore, the detection of these neutrinos are expected to convey information from deep in the core of the supernova that is likely to shed light on the details of the currently not well-known explosion mechanism. Nonetheless, before these exciting features and properties can be explored, one has to be able to detect them. To date, the 24 neutrino detections associated with SN1987A remain the only confirmed observations of supernova neutrinos [75, 76, 77]. It is, therefore, a top priority of the field to secure the neutrino detection of the next supernova.

This chapter will be divided into three sections. The first section will be a brief introduction on the main interaction channels of supernova neutrinos in liquid scintillator. Following that, the next section will discuss how a supernova can be detected in SNO+ and the implementation of a neutrino burst trigger counting high energy events. The final component of the chapter will focus on the utilisation of the time profile of the detected supernova neutrinos from multiple detectors to locate the supernova on the celestial sphere. Given the different arrival times of the various signals originating from the supernova, this directional information would serve as a valuable early warning for optical and gravitational wave telescopes, which constitutes an important part of the tasks of the Supernova Early Warning System (SNEWS).

7.1 Supernova Interaction Channels in Liquid Scintillator

Before discussing the detection and identification of supernova neutrinos, it is important to understand the properties of the interaction channels that are relevant to liquid scintillator detectors. Table 7.1 lists the dominant interaction channels of supernova neutrinos in scintillator, which can be classified into four categories: inverse beta decay (IBD), neutrino-electron elastic scattering (EES), neutrino-proton elastic scattering (PES) and neutrino-nucleus interactions. The kinematics of each channel will be briefly introduced in this section.

7.1.1 Inverse Beta Decay

Inverse beta decay (IBD),

$$\bar{\nu}_e + p \rightarrow e^+ + n \quad (7.1)$$

is the process of an electron anti-neutrino interacting with a proton via charged current interaction producing a positron and a neutron. The theoretical neutrino energy threshold E_ν of the interaction is given by

$$E_\nu = \frac{(m_n + m_e)^2 - m_p^2}{2m_p} \approx 1.806 \text{ MeV} \quad (7.2)$$

where m_e , m_n , m_p are the rest masses of the electron/positron, neutron and proton, respectively.

The signal of IBD consists of two parts: a prompt event originating from the annihilation of the positron, and a delayed signal caused by thermal neutron capture on a proton. The energy visible from the prompt event $E_{vis}^{e^+}$ is given by the sum of the annihilation energy and the positron kinetic energy

$$E_{vis}^{e^+} = T_{e^+} + 2m_e \quad (7.3)$$

where the positron kinetic energy can be approximately expressed as

$$T_{e^+} \approx E_{\bar{\nu}_e} + m_p - m_n - m_e. \quad (7.4)$$

This approximation is valid since the neutron is significantly more massive than the positron, and the resulting neutron recoil energy is only of $\mathcal{O}(10 \text{ keV})$ which can be neglected [181].

The neutron capture event is expected to happen about $200 - 260 \mu\text{s}$ after the positron annihilation [182]. The deuteron resulting from neutron capture will be

Supernova Neutrino Interaction Channels		
Channels	Weak Interaction Type	Event Yield
$\bar{\nu}_e + p \rightarrow e^+ + n$ (IBD)	CC	194.7 ± 1.0
$\nu_e + e^- \rightarrow \nu_e + e^-$	NC/CC	6.4
$\bar{\nu}_e + e^- \rightarrow \bar{\nu}_e + e^-$	NC	2.7
$\nu_x + e^- \rightarrow \nu_x + e^-$	NC	2.1
$\bar{\nu}_x + e^- \rightarrow \bar{\nu}_x + e^-$	NC	1.8
$\nu + p \rightarrow \nu + p$	NC	429.1 ± 12.0
$\nu_e + {}^{12}_6 C \rightarrow {}^{12}_6 C + \nu_e + e^- + e^+$	CC	2.7 ± 0.3
$\bar{\nu}_e + {}^{12}_6 C \rightarrow {}^{12}_6 C + \bar{\nu}_e + e^- + e^+$	CC	7.0 ± 0.7
$\nu + {}^{12}_6 C \rightarrow {}^{12}_6 C + \nu + \gamma$ (15.11 MeV)	NC	43.8 ± 8.7
$\nu_e + {}^{12}_6 C \rightarrow {}^{11}_6 C + e^- + p$	CC	0.16 ± 0.08
$\bar{\nu}_e + {}^{12}_6 C \rightarrow {}^{11}_5 B + e^+ + n$	CC	0.16 ± 0.08
$\nu + {}^{12}_6 C \rightarrow {}^{11}_5 B + \nu + p$	NC	1.6 ± 0.5
$\nu + {}^{12}_6 C \rightarrow {}^{11}_6 C + \nu + n$	NC	0.5 ± 0.16

Table 7.1: Interaction channels for supernova neutrinos in liquid scintillator with the corresponding event yields estimated based on a CCSN at 10 kpc observed in SNO+, adapted from [2]. The CCSN model releases a total energy of 3×10^{53} ergs equally partitioned amongst the neutrino flavours. The errors on the event yields are derived from the uncertainties of the interaction cross sections. Note that the uncertainties of the electron scattering cross-sections arising from Standard Model calculations are less than 1%, and are, therefore, neglected in the yield count.

formed in an excited state, and will quickly de-excite to the ground state via emission of γ rays. These γ rays then constitute the delayed signal. More than 99% of the thermalised neutrons will be captured on the Hydrogen nuclei producing a characteristic 2.23 MeV γ . Besides that, the remaining less than 1% of the neutrons will be captured on the ^{12}C nuclei with a 4.945 MeV de-excitation γ emission.

The high tagging efficiency and large cross section of IBD makes it the most important and reliable signal for supernova neutrino detection, e.g., all of the events detected in SN1987A were IBD events. In the discussions of this chapter, the IBD signals will often be taken as a conservative estimate for the least yield scenario to demonstrate the efficiencies of the methods developed.

7.1.2 Neutrino-Electron Elastic Scattering

Neutrinos of all flavours and energies are able to scatter elastically on electrons via weak interactions known as the neutrino-electron elastic scattering (EES). Being a purely leptonic process, the cross section of this interaction can be calculated analytically with the Standard Model. The leading order Feynman diagrams of all the possible channels are depicted in Figure 7.1. As shown in the Feynman diagrams, both the neutral and charged current interaction channels are available for ν_e and $\bar{\nu}_e$, whereas the muon and tau flavours can only interact via Z boson exchange.

The leading order cross sections of each channel of the EES interaction can be

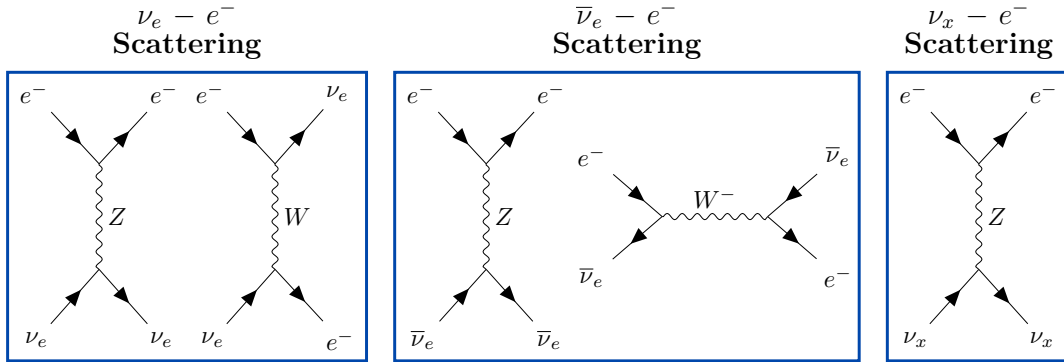


Figure 7.1: The EES Feynman diagrams for ν_e , $\bar{\nu}_e$ and $\nu_x = \{\nu_\mu, \nu_\tau, \bar{\nu}_\mu, \bar{\nu}_\tau\}$.

7.1. SUPERNOVA INTERACTION CHANNELS IN LIQUID SCINTILLATOR

calculated by [9]

$$\sigma_{\nu}^{NC} = \frac{G_F^2 2m_e E_{\nu}}{\pi} \left(\left(\frac{1}{2} - \sin^2 \theta_W \right)^2 + \frac{1}{3} \sin^4 \theta_W \right) \quad (7.5)$$

$$\sigma_{\nu}^{CC} = \frac{G_F^2 2m_e E_{\nu}}{\pi} \cdot 2 \sin^2 \theta_W \quad (7.6)$$

$$\sigma_{\bar{\nu}}^{NC} = \frac{G_F^2 2m_e E_{\nu}}{\pi} \left(\frac{1}{3} \left(\frac{1}{2} - \sin^2 \theta_W \right)^2 + \sin^4 \theta_W \right) \quad (7.7)$$

$$\sigma_{\bar{\nu}}^{CC} = \frac{G_F^2 2m_e E_{\nu}}{\pi} \cdot \frac{2}{3} \sin^2 \theta_W \quad (7.8)$$

and the total cross section can be expressed as

$$\sigma_{tot} = \frac{G_F^2 2m_e E_{\nu}}{\pi} \left(c_1 \left(\frac{1}{2} \pm \sin^2 \theta_W \right)^2 + c_2 \sin^4 \theta_W \right) \quad (7.9)$$

where G_F is the Fermi coupling constant; θ_W is the Weinberg angle; the “+” sign is for the electron flavour neutrinos/anti-neutrinos; the “−” sign is for the muon and tau flavour neutrinos/anti-neutrinos; and c_1 and c_2 depends on the type of the neutrino with $c_1^{\nu} = c_2^{\nu} = 1$ and $c_1^{\bar{\nu}} = c_2^{\bar{\nu}} = \frac{1}{3}$.

The visible energy of the interaction is induced by the kinetic energy of the electron in the laboratory frame

$$T_e \equiv E_e - m_e = \frac{2m_e E_{\nu}^2 \cos^2 \theta}{(m_e + E_{\nu})^2 - E_{\nu}^2 \cos^2 \theta} \quad (7.10)$$

where θ is the scattering angle of the electron. The differential cross section with respect to the visible energy distribution is then given by

$$\frac{d\sigma}{dT_e} = \frac{G_F^2 2m_e}{\pi} \left(g_1^2 + g_2^2 \left(1 - \frac{T_e}{E_{\nu}} \right) - g_1 g_2 \frac{m_e T_e}{E_{\nu}^2} \right), \quad (7.11)$$

and the differential cross section for the electron scattering angle can be derived via the relation in Eq. 7.10,

$$\frac{d\sigma}{d \cos \theta} = \frac{G_F^2 2m_e}{\pi} \cdot \frac{4m_e E_{\nu}^2 (m_e + E_{\nu})^2 \cos \theta}{((m_e + E_{\nu})^2 - E_{\nu}^2 \cos^2 \theta)^2} \cdot \left(g_1^2 + g_2^2 \left(1 - \frac{T_e}{E_{\nu}} \right) - g_1 g_2 \frac{m_e T_e}{E_{\nu}^2} \right) \quad (7.12)$$

where the values of g_1 and g_2 for each flavour and type of neutrino are listed in Table 7.2 [9].

ν flavour	g_1	g_2
ν_e	$\frac{1}{2} + \sin^2 \theta_W$	$\sin^2 \theta_W$
$\bar{\nu}_e$	$\sin^2 \theta_W$	$\frac{1}{2} + \sin^2 \theta_W$
ν_x	$-\frac{1}{2} + \sin^2 \theta_W$	$\sin^2 \theta_W$
$\bar{\nu}_x$	$\sin^2 \theta_W$	$-\frac{1}{2} + \sin^2 \theta_W$

Table 7.2: Values of g_1 and g_2 for each neutrino flavour.

7.1.3 Neutrino-Proton Elastic Scattering

Neutrino-proton elastic scattering (PES) is the process of neutral current interaction between a neutrino and proton, which is identical for all flavours of the neutrino. Unlike the case of the EES, PES involves hadronic interaction and, hence, its cross section cannot be fully determined analytically. The total cross section and differential cross section with respect to the proton recoil energy T_p can be expressed as

$$\sigma_{tot} = \frac{G_F^2 E_\nu^2}{\pi} (c_V^2 + 3c_A^2) \quad (7.13)$$

$$\frac{d\sigma}{dT_p} = \frac{G_F^2 m_p}{2\pi E_\nu^2} ((c_V + c_A)^2 E_\nu^2 + (c_V - c_A)^2 (E_\nu - T_p)^2 - (c_V^2 - c_A^2)m_p T_p). \quad (7.14)$$

where c_V and c_A are the vector and axial-vector neutral current coupling constants between the Z boson and proton [183]. At supernova neutrino energies, the expressions of the neutral current coupling constants can be approximately written as [183]

$$c_V = \frac{1 - 4 \sin \theta_W}{2} \quad (7.15)$$

and

$$c_A = \frac{1.27 - \Delta_s}{2} \quad (7.16)$$

where Δ_s is the strange quark nucleon spin contribution which is not measured to good precisionⁱ. Although the measured cross section of PES is only a third of that of the IBD, the PES event yield is still the highest since all six flavours of neutrinos are involved.

Similar to EES, the visible energy of PES is induced by the recoiled charged particle, i.e., the proton. The visible energy is, however, strongly quenched due to the higher mass of the proton which ionises more scintillator molecules and, in turn,

ⁱThe currently best value is 0.152 ± 0.0889 [184]

suppresses the prompt emissions in scintillationⁱⁱ. As a consequence, the visible energy of most of the PES events, converted to electron equivalent energy, is scaled below 0.5 MeV. In this case, only about 30% of the signal events are left within the detection window given a 0.2 MeV energy threshold [57].

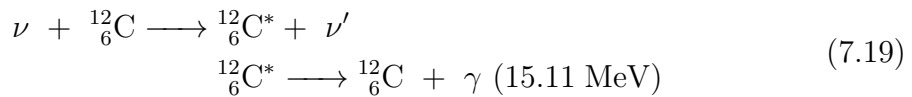
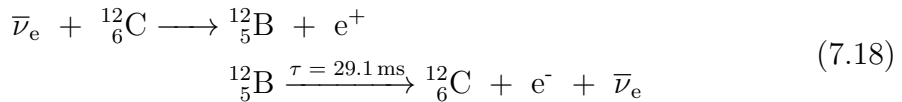
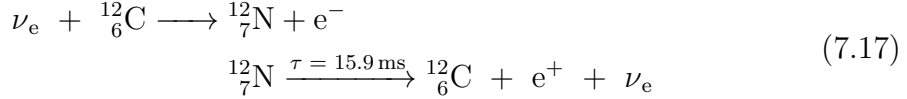
Since neither the EES nor PES signals can be tagged by any characteristic signature or coincidence, the only remaining method to discriminate the two is via pulse shape discrimination (PSD). This method, however, requires knowledge regarding the time response of the protons in scintillator which is hitherto unmeasured. In this case, the two channels form an irreducible background for each other.

7.1.4 Neutrino-Nucleus Interaction

For supernova neutrino energies, the neutrinos are often energetic enough to surpass reaction thresholds to interact with the ^{12}C nucleus which is abundant in the organic liquid scintillators. As the nucleus is involved, the cross sections of this interaction has to be either estimated via nuclear network calculations or empirically measured [185, 186]. In this section, the seven channels listed in Table 7.1 for neutrino- ^{12}C interaction, in which three are super-allowed transitions and four forbidden transitions, will be briefly introduced.

Super-Allowed Transition

The three super-allowed transitions with substantially higher cross sections are



where Eqs. 7.17 and 7.18 are charged current interactions, and Eq. 7.19 is a neutral current interaction.

ⁱⁱThis phenomenon is known as ionisation quenching [57]. The ionised scintillator molecules causes relatively delayed emissions, known as phosphorescence, compared to the prompt emissions, known as fluorescence. Since the light yield from phosphorescence is lower than that of fluorescence, the total light yield is reduced.

7.1. SUPERNOVA INTERACTION CHANNELS IN LIQUID SCINTILLATOR

As suggested by Eqs. 7.17 and 7.18, both of the charged current channels form a coincidence signal with the e^\pm pair. The coincidence consists of a prompt electron(positron) signal originating from electron neutrino(anti-neutrino) capture followed by a delayed positron(electron) emitted by the relatively short-lived nucleus via beta decay. These reactions have high energy thresholds that can be calculated as

$$E_{\nu_e} = \frac{(m_{^{12}\text{N}} + m_e)^2 - m_{^{12}\text{C}}^2}{2m_{^{12}\text{C}}} \approx 17.86 \text{ MeV} \quad (7.20)$$

and

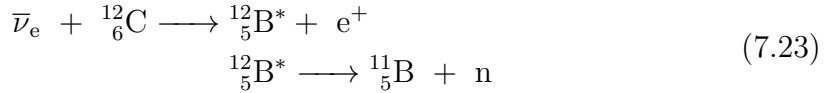
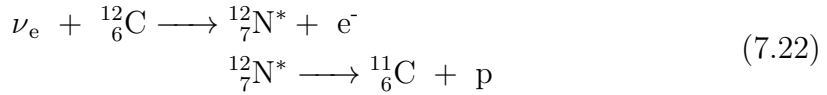
$$E_{\bar{\nu}_e} = \frac{(m_{^{12}\text{B}} + m_e)^2 - m_{^{12}\text{C}}^2}{2m_{^{12}\text{C}}} \approx 13.89 \text{ MeV} \quad (7.21)$$

where $m_{^{12}\text{N}}$, $m_{^{12}\text{B}}$ and $m_{^{12}\text{C}}$ are the masses of the ^{12}N , ^{12}B and ^{12}C nuclei, respectively. The visible energy of the signals depend on the particle type. If the signal is from an electron, the energy is simply the kinetic energy of the electron, whereas for positrons the energy becomes the sum of the positron kinetic energy and annihilation energy as in Eq. 7.3.

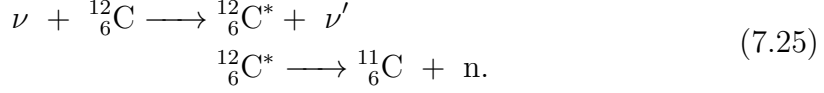
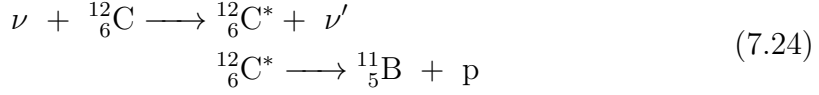
The neutral current interaction, on the other hand, is identified by the distinct signature of a prompt 15.11 MeV de-excitation γ . With a mono-energetic γ , the signal would appear as a well defined peak corresponding to the 15.11 MeV visible energy. Due to the neutral current nature, just as the PES, this channel is insensitive to the neutrino flavour.

Forbidden Transition

With the supernova neutrino energies, the neutrinos are energetic enough to cause the ^{12}C nuclei to eject a nucleon [187, 188]. The event yield contribution of these interactions is not significant, and only the processes with relatively larger cross sections are listed here. This involves two charged current channels



and two neutral current channels



Each of these processes consists of two stages: a neutrino scatter that excites the nucleus followed by a de-excitation nucleon emission. The signals of these interactions form backgrounds for other channels, e.g., the emitted protons constitute a source of background for PES interactions, and Eq. 7.23 is essentially an IBD reaction. Since the final state nuclei ${}_{6}^{11}\text{C}$ and ${}_{5}^{11}\text{B}$ are relatively stable and do not create a coincidence signal, these backgrounds are difficult to reject and should be taken into account when measuring the corresponding signals.

In general, the neutrino-nucleus interactions have high reaction thresholds. If channel discrimination with high precision were possible, the interactions could provide useful flavour information of the neutrino flux for the high energy spectrum. This is, however, not relevant to the main theme of this chapter, and is mentioned just to illustrate the possible prospects of study for this interaction mode.

7.2 Multi-Threshold Supernova Burst Trigger

In the event of a galactic supernova, the primary signature in neutrino detectors is expected to be the emergence of a burst of hundreds to thousands of high energy neutrino-induced events within a short time interval of seconds. It is, therefore, possible to identify the supernova by implementing a burst trigger targeting at high energy events. The original supernova burst trigger in SNO+ was inherited from SNO, which was designed for the water phase and to comply with the conservative once-per-century false alarm rate of the Supernova Early Warning System (SNEWS) [189]. Now, with scintillator loaded, the trigger thresholds for both energy and multiplicity should be re-evaluated. In addition, with the more tolerant attitude of the astronomical community towards false bursts, it is possible to explore the lower energy ranges to maximise the physics value of the SNO+ data. Inclusion of the lower energy ranges might reveal signs of the PES events, which SNO+ will be in a unique position to detect amongst all the neutrino detectors around the globe.

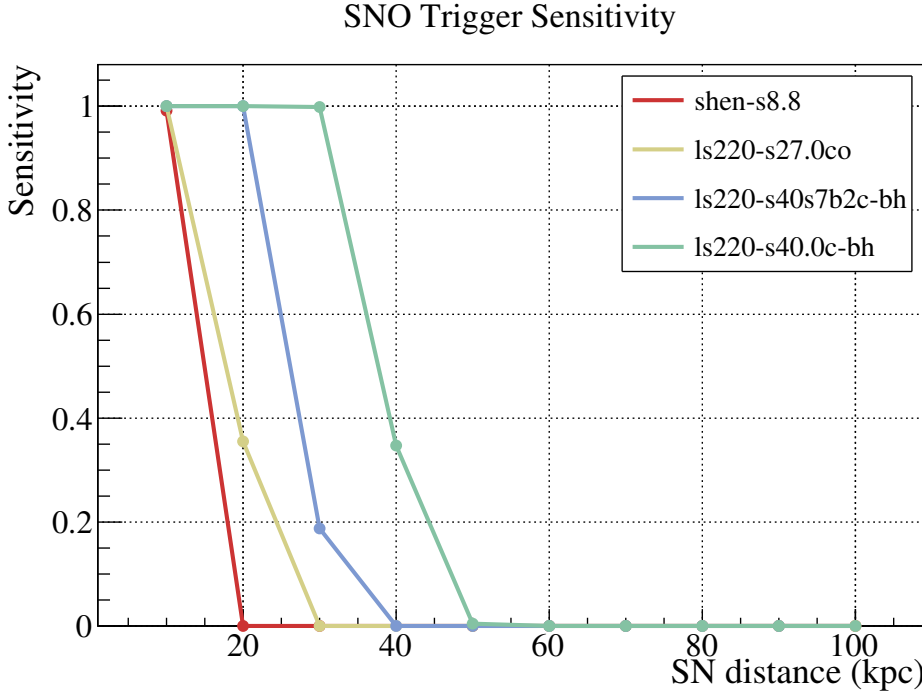


Figure 7.2: Sensitivity of the original SNO supernova burst trigger versus supernova distance for the models: $8.8M_{\odot}$ (Shen) (red), $27M_{\odot}$ (LS220) (yellow), $40M_{\odot}$ (LS220) forming a black hole after 0.5 s (blue), and $40M_{\odot}$ (LS220) forming a black hole after 2 s (green). The sensitivities are calculated by assuming a Poisson distribution using the expected event yields from the quoted models.

7.2.1 Original SNO Burst Trigger

In the original settings of the SNO supernova burst trigger, the trigger was divided into three distinct levels [190]. Level 1 was the event burst monitor which surfs through the datastream and declares bursts if the threshold of 30 events with greater than 35 PMT hits, equivalent to 4 MeV in SNO [189], occur in a 2 s window. When a burst is declared, the events would be written into a file and transferred to the Level 2 trigger where data-cleaning cuts are applied to remove the detector instrumental noise. Finally, if more than 35% of the events survived the data-cleaning cuts, the burst would be passed to Level 3. From Level 3, an alert would be sent to SNEWS. The SNO burst trigger group would also be notified to analyse the fitted vertices and obtained directional information to infer the possible direction of the observed supernova.

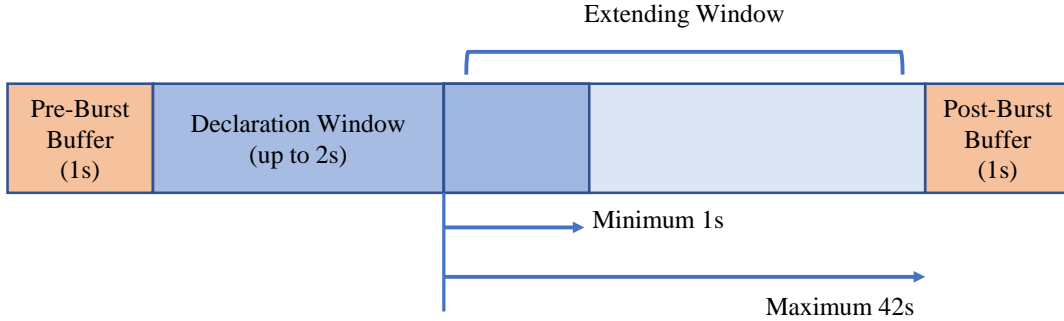


Figure 7.3: Structure of the SNO+ burst trigger time windows.

This study will focus on the trigger thresholds applied in the event burst monitor. The original design consists of only a single high energy and high multiplicity trigger, which guarantees the purity of the declared bursts. This, however, sacrifices the sensitivity of the trigger as indicated in Figure 7.2, where the sensitivity for typical CCSNe is limited beyond 30 kpc. Possibilities of lowering the event multiplicity threshold to improve the detection sensitivity for SNO has been discussed in [191], though the energy thresholds are still maintained at a relatively high level. Besides lowering the event multiplicity threshold, the possibility of lowering the energy thresholds will also be explored in this chapter for the SNO+ scintillator phase burst trigger.

7.2.2 SNO+ Burst Trigger

The SNO+ burst trigger system, designed by M. Rigan [5], is developed based on the original trigger system. In the SNO+ burst trigger system, Level 1 refers to the data acquisition and event trigger system. The burst monitor, originally Level 1 in the SNO burst trigger system, is now defined as Level 2. The new burst logic starts with a burst declaration time window up to 2 s, during which the events are subjected to the burst thresholds to determine whether a burst should be declared. Once the burst thresholds are passed, a burst will be declared and an “extending window” of 1 s starts. If any event during the 1 s extending window has N_{hit} above 700 PMT hits, the extending window will be renewed and reads in another second after that event. The extending window can then be maximally extended to 42 s. The declaration window and extending window forms the main body of the burst. Besides that, the new logic also includes a pre-burst and post-burst buffer to keep track of the overall trend, which records all events 1 s before the beginning of the declaration window and 1 s after the end of the extending window. The basic structure of the burst trigger time windows is illustrated schematically in Figure 7.3.

Partial Fill SN Burst Trigger					
Multiplicity	3	5	7	10	20
Nhit	1630	1000	795	700	380

Table 7.3: Nhit thresholds for each burst trigger evaluated in partial-fill phase (26th of June to 27th of August, 2020). The background burst rates are not exactly one burst per month as the values are rounded up to steps in 5 PMT hits.

Full Scintillator SN Burst Trigger					
Multiplicity	3	5	7	10	20
Nhit	1630	1200	885	835	460

Table 7.4: Nhit thresholds for each burst trigger evaluated in full-scintillator phase (17th of August to 17th of September, 2021). The background burst rates are not exactly one burst per month as the values are rounded up to steps in 5 PMT hits.

The burst file will then be passed to Level 3 for data cleaning. The cleaned events will be re-evaluated again by the burst logic. If it still constitutes a burst, this Level 3 burst will be sent out for manual review. In the future, the SNO+ supernova working group is planning to set up an automatic message sent to SNEWS when Level 3 bursts occur.

7.2.3 Burst Trigger Thresholds

In this study, the new thresholds of the Level 2 burst monitor are tuned such that the false burst rate from the radioactive backgrounds is once per month. In order to expand the sensitivity range and explore the lower energy signals, a design of an augmented multi-threshold burst trigger is implemented. The current implementation of the burst trigger consists of a four-fold multiplicity threshold of 3, 5, 7 and 10 events in a 2 s window. Table 7.3 lists the Nhit thresholds currently implemented for each multiplicity trigger. These values are determined by examining the background rates of the partial-fill data from the 26th of June to the 27th of August, 2020.

Figure 7.4 shows the sensitivity of these triggers for different supernova models at different distances. The sensitivity is estimated via a Poisson distribution based on the expected event yield passing the thresholds for each supernova model. To derive the event yields, a toy simulation is performed. This simulation is based on the distance-scaled neutrino luminosity profiles quoted from the supernova models.

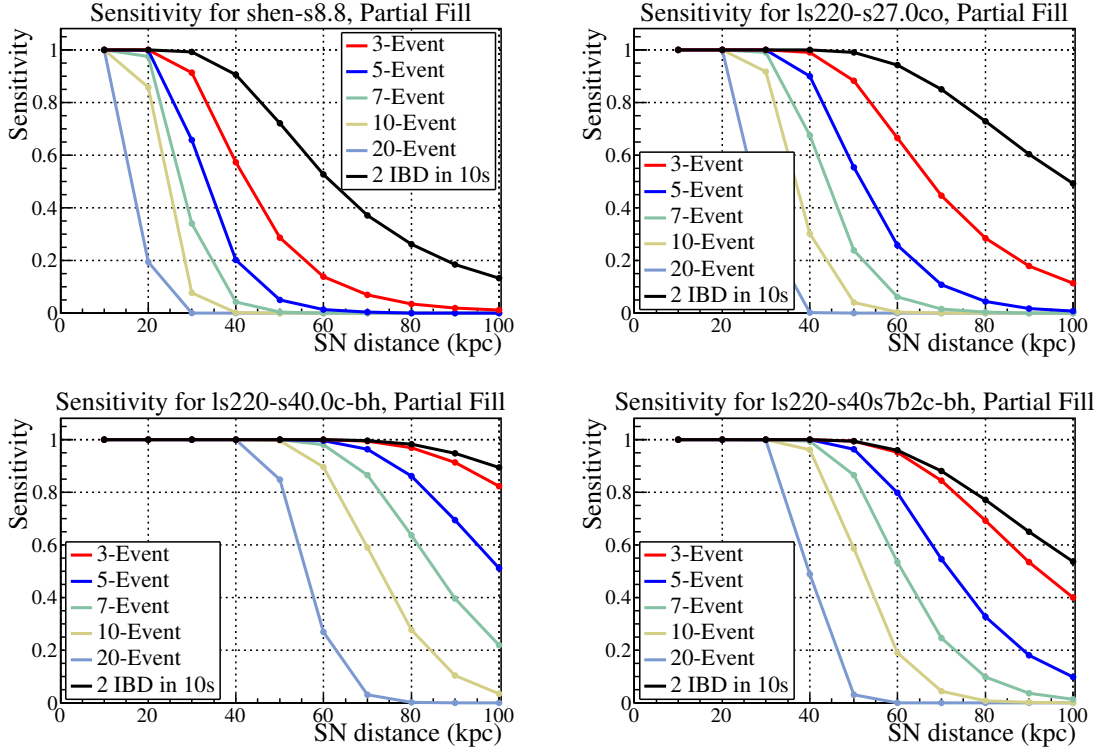


Figure 7.4: Sensitivity of the burst trigger in partial-fill phase versus supernova distance for the models: $8.8M_{\odot}$ (Shen) (top left), $27M_{\odot}$ (LS220) (top right), $40M_{\odot}$ (LS220) forming a black hole after 2 s (bottom left), and $40M_{\odot}$ (LS220) forming a black hole after 0.5 s (bottom right). The sensitivities are calculated by assuming a Poisson distribution using the expected event yields from the quoted models.

The interaction channel, listed in Table 7.1, is then randomly assigned according to their respective cross sections in liquid scintillator. Finally, the generated visible energy is converted to Nhit by the light yield, which has been determined to be 320 ± 15 PMT hits per MeV for the chosen data period with the method introduced in Chapter 5. In general, the burst trigger sensitivity with respect to supernova distance follows the pattern of lower multiplicity thresholds leading to higher sensitivities and vice versa. The 3-event burst trigger, accordingly, has the highest sensitivity in all cases. The higher multiplicity triggers, though slightly inferior in sensitivity, are still valuable in different aspects. The initial intention of implementing higher multiplicity thresholds was to introduce triggers that are more resilient against the radioactive backgrounds and electronic noise. However, the final decision of tuning all of the triggers to a fixed background burst rate shrouded this advantage of the

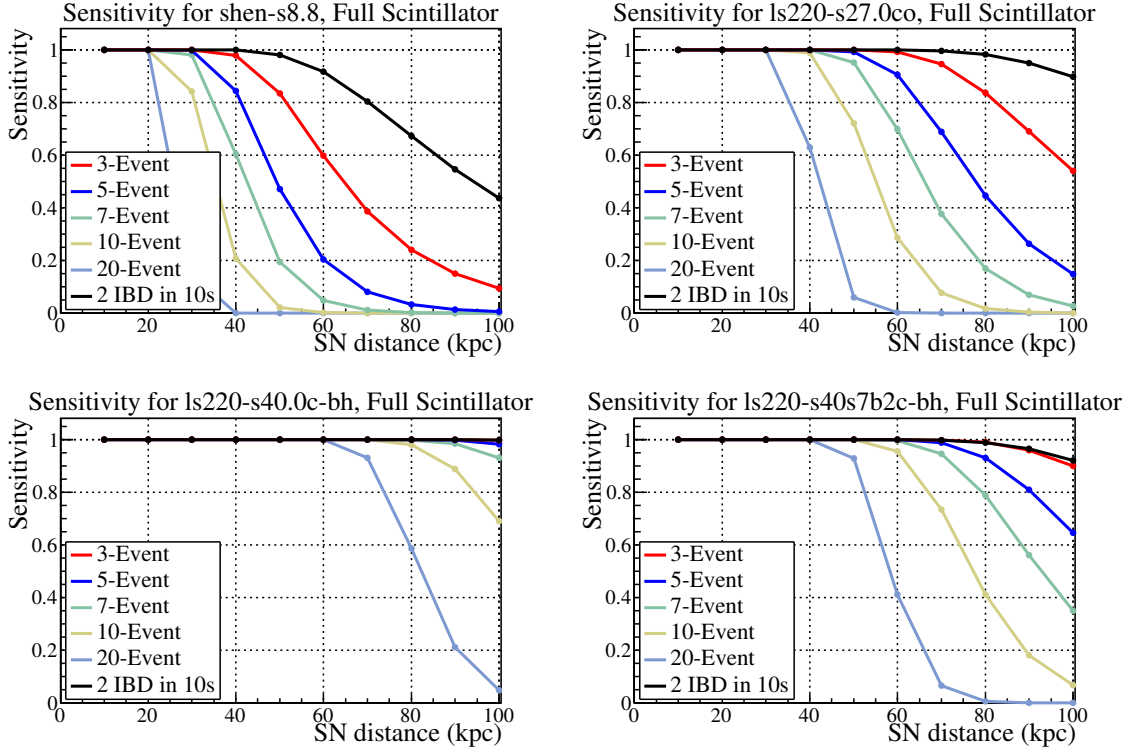


Figure 7.5: Sensitivity of the burst trigger in full-scintillator phase versus supernova distance for the models: $8.8M_{\odot}$ (Shen) (top left), $27M_{\odot}$ (LS220) (top right), $40M_{\odot}$ (LS220) forming a black hole after 2 s (bottom left), and $40M_{\odot}$ (LS220) forming a black hole after 0.5 s (bottom right). The sensitivities are calculated by assuming a Poisson distribution using the expected event yields from the quoted models.

high multiplicity triggers. Besides resisting backgrounds, the lower energy thresholds associated with these triggers allow the burst to record interactions of lower visible energy such as PES. For instance, the 10-event trigger is expected to be able to utilise nearly 5% of the PES signal.

Apart from the triggers currently implemented, one will notice there are two supplementary triggers plotted in Figure 7.4 that are not yet in operation. They are studied out of the interest of improving the sensitivity range and recording low energy signals. The additional burst triggers include a trigger with a multiplicity threshold of 20 events in the 2 s time window and a trigger of 2 IBD events in a 10 s time window. The motivation of testing a 20-event trigger is simply to increase the acceptance fraction of the PES signal. With the threshold listed in Table 7.4 for the 20-event trigger, it is expected that almost 20% of the PES signal will be preserved

constituting a third of the expected event yield. On the other hand, the 2-IBD trigger is devised to test the maximum sensitivity one could possibly exploit from burst detection. Since the IBD signal is essentially free of background and SNO+ expects only 5 IBD events per month, the lowest possible multiplicity threshold for a burst can thus be set to 2 IBD events. Indeed, this trigger sets the upper limit of the sensitivity as shown in Figure 7.4.

As SNO+ reached full-scintillator phase, the background rate of the detector nearly doubled. Consequently, the triggers currently implemented, using thresholds obtained from partial-fill phase, fire much more often than the original once-per-month target false alarm rate. The thresholds were, therefore, re-evaluated using the more recent data from the 17th of August to the 17th of September, 2021. The new values and their corresponding sensitivities are listed in Table 7.4 and Figure 7.5. Though the thresholds were forced to be raised, the sensitivities still improved as the event yield is also expected to be doubled with the extra scintillator.

7.3 Multi-Detector Supernova Pointing

Whereas supernovae are extremely luminous optically, the optical signals are expected to be heavily attenuated by the cosmic dust along their paths. To capture these attenuated signals, dedicated observations using large telescopes will be needed. However, the angular coverage of the relevant telescopes are, in general, of only several degrees [1]. An early warning with prompt and accurate directional indication is, therefore, valuable and necessary for the detection of the supernova electromagnetic signals. In addition, this warning will also be essential for possible gravitational wave signals, whose waveform is uncertain and likely to be lost otherwise.

The SNEWS network is thus proposed to serve this demand by utilising the neutrino signals that are expected to arrive at the Earth tens of minutes to a few days prior to the electromagnetic waves [1, 189]. The question is then how could the directional information be extracted from the neutrinos before they could be optically located. Two approaches were explored in [192]: single detector in-situ directionality and multi-detector triangulation. The first approach requires in-situ directionality information from the detector, which usually relies on the Cherenkov light and is currently mainly performed in water detectors. Though this approach gives the best angular resolution, it is relatively more time-consuming, usually on the order of tens of minutes [193], and might be at the risk of not being able to provide prompt enough warning for the telescopes. This is where the second approach of multi-detector triangulation demonstrates its value. The supernova direction in this case is inferred from the time difference between the neutrino detectors by simple calculations that can be done nearly instantly. This approach has, until recently, been considered unfeasible owing to the low yield of past neutrino detectors. Nonetheless, with the new generation of kilotonne detectors envisaged to observe thousands of events during a supernova explosion, this method has been brought back to the attention of the astrophysical community.

7.3.1 SNEWS Network

The supernova early warning system (SNEWS), operating since 1998 and automated since 2005, is a network combining a wide range of neutrino detectors across the globe [1, 189]. The basic idea of the SNEWS network is to issue prompt alerts to the astronomical community based on the coincidence of neutrino bursts across multiple neutrino detectors within a short time window (10 s by default). Member experiments currently connected to SNEWS are listed in Table 7.5 with NO ν a, KM3NET and Baksan preparing to join.

Experiment	Material	Main Interaction Channel
Super-Kamiokande	water (32 kt)	$\bar{\nu}_e + p \rightarrow n + e^+$
Daya Bay	scintillator (20 t)	$\bar{\nu}_e + p \rightarrow n + e^+$
LVD	scintillator (1 kt)	$\bar{\nu}_e + p \rightarrow n + e^+$
Borexino	scintillator (300 t)	$\bar{\nu}_e + p \rightarrow n + e^+$
KamLAND	scintillator (1 kt)	$\bar{\nu}_e + p \rightarrow n + e^+$
SNO+	scintillator (0.8 kt)	$\bar{\nu}_e + p \rightarrow n + e^+$
IceCube	water (Antarctic ice)	noise excess
HALO	Lead (76 t)	$\nu_e + Pb \rightarrow e^- + Bi^*$

Table 7.5: Neutrino experiments currently connected to SNEWS [1]. Note that SNO+ joined recently by the end of 2021, and is in the testing channel by the time of writing.

Participating neutrino experiments will execute their own supernova monitors. The SNEWS client will then send the necessary information, such as the experiment name, time of first burst event and burst quality parameter, to the SNEWS coincidence servers located at the Brookhaven National Laboratory and the University of Bologna. Directionality and burst size information is optional depending on its availability at each experiment upon supernova explosion. Alerts are further categorised into “gold” and “silver”, where “gold” alerts satisfies all the burst quality criteria and are automatically sent out to the subscribers; and “silver” alerts are those that fail at least one of the criteria and will only be sent to the experiments for manual review. This design is largely driven by the target one-per-century false alert rate allowing only coincidences of extremely high quality.

With the advancements of astro-particle physics in various fronts, such as the successful detection of gravitational waves [194] and possible neutrino observation of a blazar [195], multi-messenger astronomy has acquired wide attention amongst the astronomical community. Consequently, the SNEWS network is aiming for an upgrade, known as SNEWS 2.0, to become more suitable for multi-messenger astronomy. The focus of the system is shifted from purity of the signal to maximising the possible information that can be extracted from the future supernova. The main changes introduced by SNEWS 2.0 include [1]: sacrifice of burst purity for sensitivity; reducing alert latency; implementation of multi-detector triangulation; and implementation of a pre-supernova alert. These upgrades will make SNEWS 2.0 the most comprehensive neutrino multi-messenger alert system.

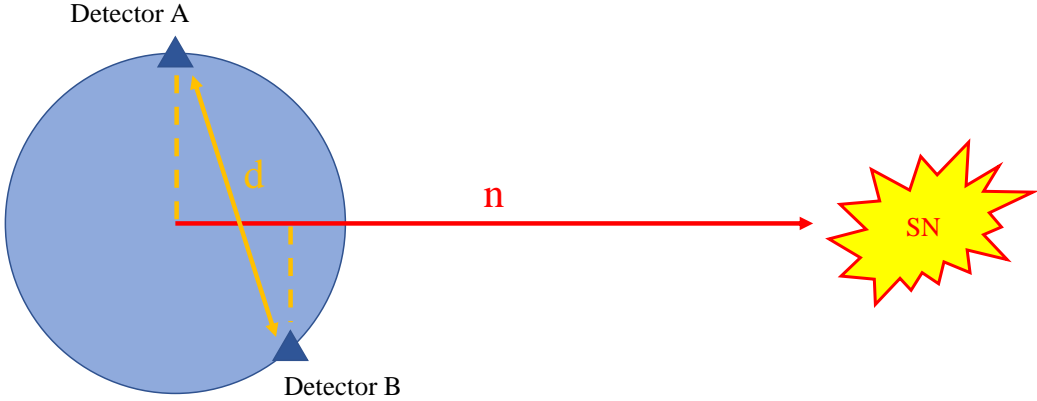


Figure 7.6: Schematic representation of multi-detector triangulation with a pair of neutrino detectors.

7.3.2 Multi-Detector Positioning

The whole idea of multi-detector triangulation is to reconstruct the supernova direction from the time differences between different pairs of spatially separated neutrino detectors connected to SNEWS. Figure 7.6 is a schematic illustration of the concept with a single pair. The relation between the detector time difference Δt and the supernova direction can be expressed as

$$\Delta t = \frac{|\vec{d} \cdot \hat{n}|}{c} \quad (7.26)$$

where \vec{d} is the displacement between the detectors, \hat{n} is the directional unit vector of the supernova with the origin chosen to be the centre of the Earth, and c , without surprise, is the speed of light. Note that this implicitly assumes that the distance between the Earth and the target supernova is far greater than $|\vec{d}|$, which is clearly the case.

7.3.3 Time Difference Determination

Time difference determination is the central piece of supernova triangulation. It is clear from Eq. 7.26 that the problem can be reduced to finding the time difference, since Δt is the only unknown variable besides the supernova direction. There are, in general, two approaches to the problem: model-dependent and model-independent.

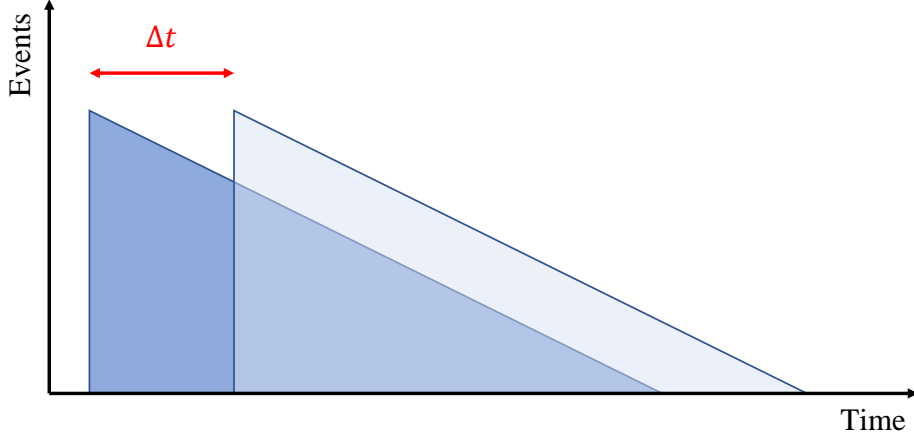


Figure 7.7: Sketch of light curve matching.

In the former approach, a likelihood fit on the signal would elegantly solve the issue. The only problem with it is which model, out of the ocean of supernova models, should be used or, even worse, whether the models are applicable at all. This is another complicated topic that is beyond the scope of this thesis.

The model-independent approach, on the contrary, will rely on the exploitation of the time lapse between the detections of notable features within the time series. The question is, then, of which feature should one focus on. An immediately apparent choice is the use of the time difference between the first or first few events of the time series, which has been studied in [196]. This simple method provides surprisingly good resolution. For instance, the combination of JUNO and Super-Kamiokande yields a Δt resolution of 5.7 ms. It is, however, less resilient against background events and has a relatively larger bias.

Another option, which will be discussed in more detail, is to match the overall profile of the two time series, as depicted in Figure 7.7. By comparing the entire profile, it is expected to introduce a smaller bias and be more robust against background events as more data points are taken into account. The basic idea is to make use of the shape similarity between the light curves. Assuming an identical underlying time distribution, which should be the case for comparable detectors, shifting one of the profiles by the correct time offset Δt should, in principle, result in the minimisation of some difference metric between the two distributions. Conventional metrics such as χ^2 and cross-correlation have been explored in [197]. The time resolution is im-

proved with this method, e.g., the JUNO plus Super-Kamiokande pair now gives a resolution of 2.73 ms using χ^2 and 2.75 ms using cross-correlation. After examining these conventional methods, it appears that the resolution power mainly comes from the edges, i.e., large derivatives, of the time distributions.

This observation is consistent with the Cramer-Rao theorem [192, 198, 199] which is used to estimate the theoretical limit of the true event time resolution $(\delta t_0)_{min}$:

$$\frac{1}{(\delta t_0)_{min}^2} = N \int dx \frac{[\partial f(x)/\partial x]^2}{f(x)} \quad (7.27)$$

where N is the total number of events, and $f(x)$ is the time profile. For binned distributions, Eq. 7.27 can be approximately expressed as

$$\frac{1}{(\delta t_0)_{min}^2} \approx N \sum_i \frac{[\Delta b_i/\Delta x]^2}{b_i} \quad (7.28)$$

where the subscript i denotes the bin index; b_i is the bin content of the normalised profile; Δx is the bin width; and $\Delta b_i/\Delta x$ is the average slope at bin i . The limit of the time difference resolution for a pair of detectors can then be simply calculated via error propagation

$$\delta(\Delta t) = \sqrt{(\delta t_0)_{min}^2 + (\delta t'_0)_{min}^2} \quad (7.29)$$

where $(\delta t_0)_{min}$ and $(\delta t'_0)_{min}$ are the individual resolution limits of the pair of detectors. This motivates one to consider weighted-difference metrics that emphasize more on the edge.

To demonstrate this idea, a simple parameter η is devised for the binned time series $F = \{t_j\}_{j=1}^N$ and $F' = \{t'_j\}_{j=1}^{N'}$:

$$\begin{cases} \eta_i = |b_i - b'_i|(b_i + b'_i) & \text{if both bins are non-zero} \\ \eta_i = |b_i - b'_i|(b_{max} + b'_{max}) & \text{if one of the bins is empty} \\ \eta_i = 0 & \text{if both bins are empty} \end{cases} \quad (7.30)$$

where b_i and b'_i are the bin contents of the normalised distributions of F and F' ; $b_{max} = \max\{b_i\}$ and $b'_{max} = \max\{b'_i\}$. This metric is designed to accentuate the edge feature of the metric profile by assigning greater weight to the bin difference when there is an actual displacement, that is, when a non-empty bin of one light curve is compared to an empty bin of the other. The metric value calculated by Eq. 7.30 is per bin, and the resulting metric value is the sum of all such values

$$\eta = \sum_i \eta_i. \quad (7.31)$$

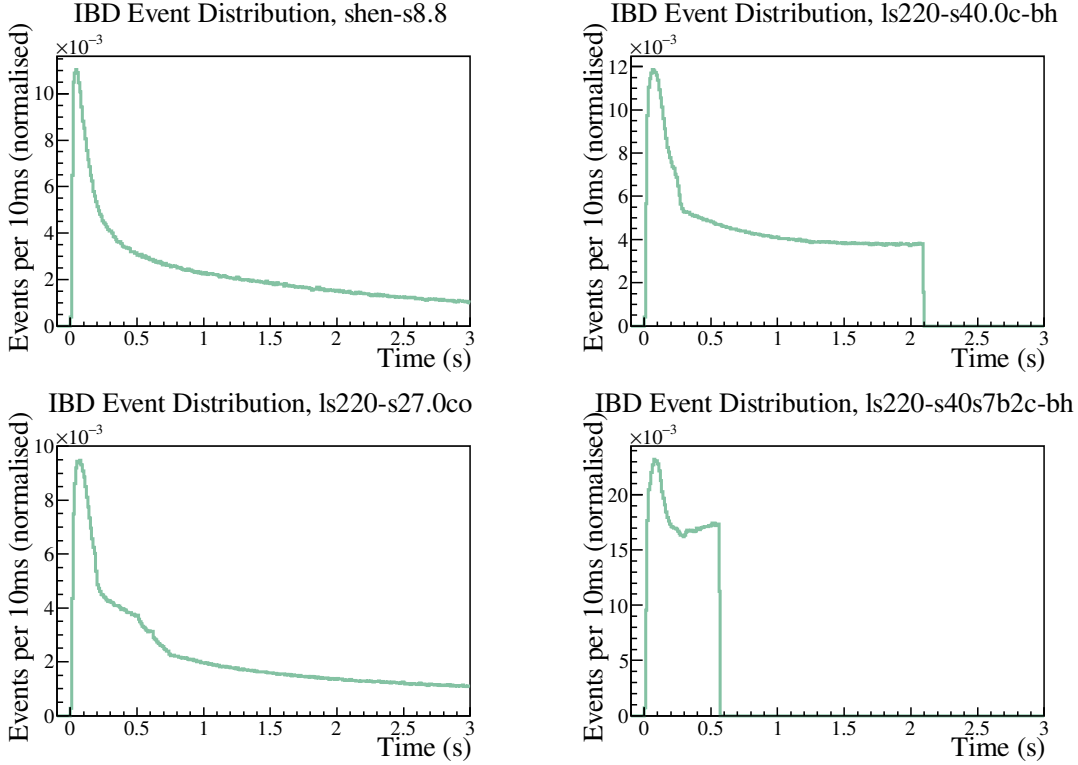


Figure 7.8: Expected IBD event time distribution for the supernova models: $8.8M_{\odot}$ (Shen) (top left), $27M_{\odot}$ (LS220) (bottom left), $40M_{\odot}$ (LS220) forming a black hole after 2 s (top right), and $40M_{\odot}$ (LS220) forming a black hole after 0.5 s (bottom right).

7.3.4 Supernova Signal Simulation

In order to test the metric, realistic simulations of the observed supernova signal time series in each detector are needed. The simulation is divided into three stages: event yield calculation, event interaction simulation and, finally, detector response. For this study, four supernova models from the Garching group [78, 132, 200] were employed: an electron capture supernova with a progenitor mass of $8.8M_{\odot}$ (shen-s8.8); an iron-core CCSN with progenitor mass of $27M_{\odot}$ (ls220-s27.0co); two $40M_{\odot}$ progenitor mass supernovae forming black holes in 0.5 s (ls220-s40s7b2c-bh) and 2 s (ls220-s40.0c-bh) after core bounce.

The event yield calculation was done with the SNOwGLoBES event rate calculator [201]. SNOwGLoBES multiplies the neutrino flux, derived from the luminosity and mean energies of the supernova models, by the corresponding interaction cross-sections of each channel to obtain the interaction rate. The interaction rate of a given

channel i can then be expressed as:

$$R_i = \frac{\mathcal{L}}{\langle E \rangle \cdot 4\pi D^2} \sigma_i = \Phi \sigma_i \quad (7.32)$$

where \mathcal{L} and $\langle E \rangle$ are the luminosity and mean energies obtained from the supernova models, respectively; D is the distance of the supernova, 10 kpc by default; Φ is the derived flux; and σ_i is the interaction cross-section. The total rate is then simply the sum of all possible channels:

$$R = \sum_i R_i = \sum_i \Phi \sigma_i. \quad (7.33)$$

The total event yield obtained from SNOwGLoBES is then fed to the simulation as the total number of events to simulate. For each event, a time is randomly generated by taking the time dependent interaction rate as the probability distribution function. Once the time series is generated, each event is assigned a neutrino energy following the energy spectrum according to its time label. The neutrino energy spectrum is described by Eq. 3.10 in Section 3.5.2.

Now, with the incident time and incoming neutrino energy assigned, the next step is to assign an interaction channel to the simulated event. The channel is randomly assigned based on the relative expected event rates, calculated by Eq. 7.32, at the given time and energy. Depending on the assigned interaction channel, the visible energy of each event can be calculated as discussed in Section 7.1.

Finally, Gaussian smearing is applied to the resulting visible energies to approximate the effect of the energy resolution of the detectors. This smeared visible energy is compared to the energy threshold of the detector subjected to the simulation, and the event will be discarded if it happens to fall below threshold.

For this study, JUNO and Super-Kamiokande are the only detectors investigated, and their respective energy resolutions are 3% [202] and 4.5% [203]. Furthermore, for the discussions in this section, IBD will be the only interaction channel considered due to its high purity. Figure 7.8 shows the expected IBD event time distribution for the four supernova models, where the incident time is defined as the prompt event time of each pair. Note that IBD tagging in Super-Kamiokande is slightly different from that in scintillator detectors since the delayed 2.2 MeV γ is below the water detection threshold, and, hence, is not eligible for coincidence tagging. To cope with this issue, in [204], it was proposed to dope Gadolinium into the Super-Kamiokande detector, so that 90% of the IBD events will result in neutron captures on Gadolinium leading to a γ cascade with a total energy of 8 MeV. This will be the scenario considered in this study, and, hence, Super-Kamiokande will refer to Super-Kamiokande-Gd whenever mentioned hereafter.

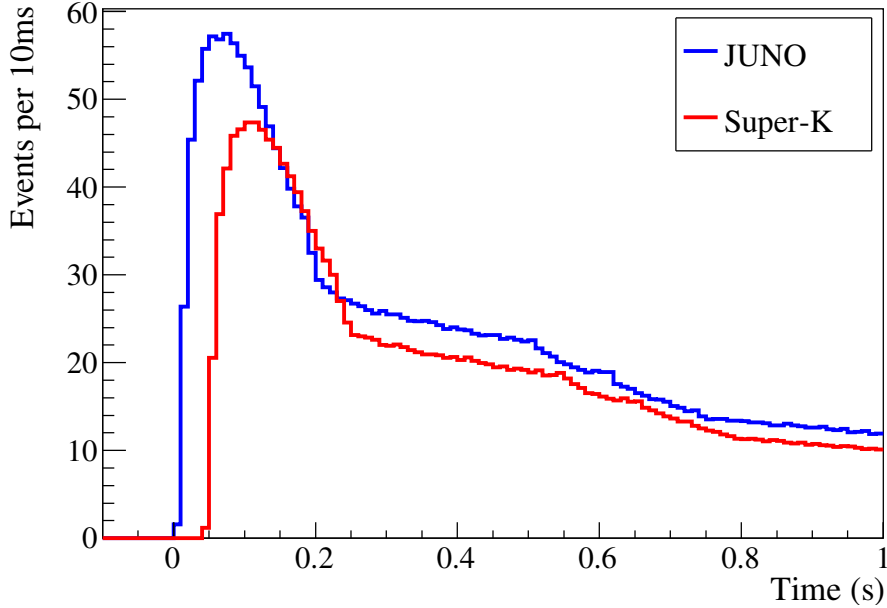


Figure 7.9: The IBD event distributions of an average trial for the ls220-s27.0co model at distance 10 kpc, where the Super-Kamiokande histogram is shifted by $\Delta t_0 = 10$ ms.

7.3.5 Result

With the JUNO and Super-Kamiokande IBD time series simulated following the description in Section 7.3.4, an artificial time offset Δt_0 will be applied to one of the time series. For convenience of presentation, results shown in this section are carried out with the artificial time delay fixed at +10 ms, which is the maximum time difference possible for this pair of detectors, and always applied to the Super-Kamiokande time series. The reverse and different offset values have both been tested, and are confirmed to have no effect on the results. Figure 7.9 shows the time series distribution of an averaged trial of the model ls220-s27.0co.

The time window for comparison is chosen to be from -0.2 to 4 s after core bounce. The bin size is event-yield dependent and is optimised for each model and distance. Each time entry in the time series will then be filled into the corresponding histograms. Whilst being binned, the entries of one of the series, the JUNO series in this case, will be shifted by a scanning time offset $\widehat{\Delta t}$. This scanning offset $\widehat{\Delta t}$ will scan through a range of -60 to 60 ms in steps of 0.1 ms, and the shifted series will be re-binned at each step. Presumably, the total metric value η should be minimised when $\widehat{\Delta t}$ matches up with the true offset Δt_0 . Figure 7.10 shows the resulting η_i values per time bin at each $\widehat{\Delta t}$ step for an averaged trial based on the model ls220-s27.0co.

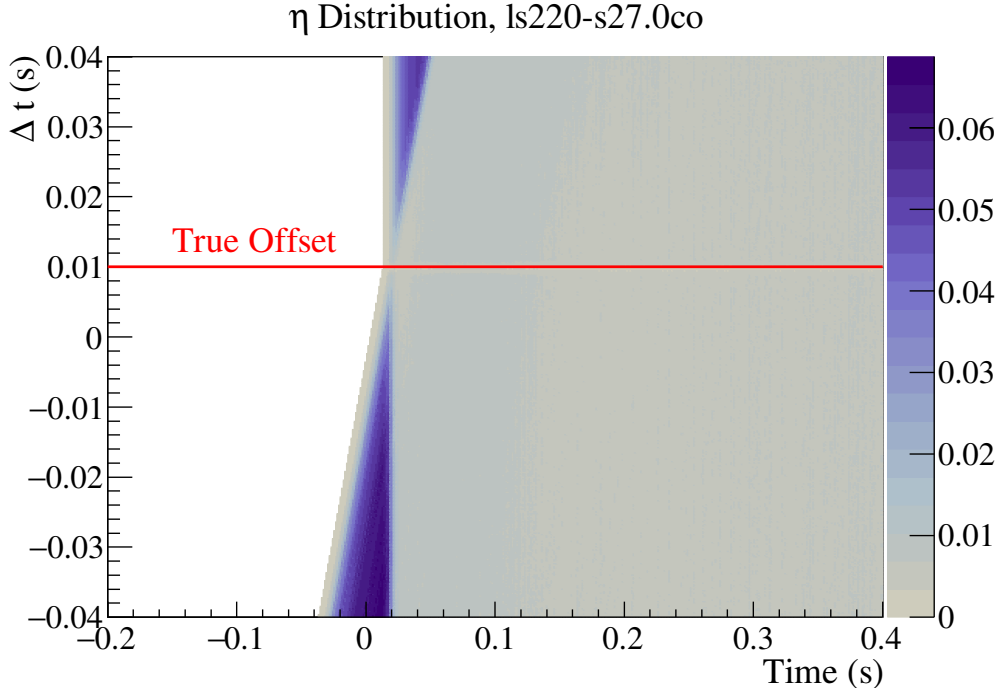


Figure 7.10: The η distribution per time bin (η_i) at each $\widehat{\Delta t}$ step for an averaged trial based on the model ls220-s27.0co at 10 kpc. The colour scale indicates the η contribution of a given time bin.

The final Δt that one obtains should, in principle, be the value with the minimum summed η . Nonetheless, the summed η distribution against $\widehat{\Delta t}$ is rugged due to the binning of discrete time entries. The η distribution is, therefore, smoothed by a fourth order polynomial, and the final Δt will be determined from the overall trend of the distribution.

This method is tested with 1,000 trials for each supernova model simulated as described in Section 7.3.4. The resulting Δt distribution is further fitted by a Gaussian to determine the resolution and bias, which are defined as the standard deviation of the distribution and $|\langle \Delta t \rangle - \Delta t_0|$, respectively. Results are listed in Table 7.6. One can clearly see that this method outperforms the aforementioned existing methods: 3.4 ms compared to the 5.7 ms resolution of the first-event method using the shen-s8.8 model [196]; and 1.83 ms compared to the 2.73 ms resolution of the χ^2 method using an analytical model equivalent to a $27M_\odot$ CCSN [197]. This demonstrates that there is further mileage to be gained from unconventional metrics focusing on the large derivatives.

Shape Comparison		
Models	Resolution (ms)	Bias (ms)
shen-s8.8	3.4	0.6 ± 0.17
ls220-s27.0co	1.83	0.04 ± 0.15
ls220-s40.0c-bh	0.95	0.02 ± 0.08
ls220-s40s7b2c-bh	0.56	0.15 ± 0.04

Table 7.6: Resolutions and biases of the shape comparison method for each supernova model at the default 10 kpc distance.

Background

As mentioned earlier, all the results hitherto obtained are solely based on the expected IBD signals of each target detector. The coincident nature of the signal assures that accidental detections arising from the radioactive backgrounds are expected to be negligible. There are, nonetheless, authentic IBD backgrounds in each detector caused by geo-neutrinos and reactor anti-neutrinos. JUNO is foreseeing a rate of about 64 IBD events per day [205], and the IBD event rate for Super-Kamiokande is around 13 per month [206]. For the 4.2 s time window under consideration, the expected IBD background rate is thus far lower than one for both of the detectors. The worst case scenario would, therefore, simply be the occurrence of one, or at most two, such event. This might cause trouble to the relatively simple first-event method, but should not affect the shape comparison method which invokes a significant portion of the time series.

To test the robustness of the method, one and two randomly generated background events within the time window of comparison are added to the simulated 1,000 trials. For the case of the ls220-s27.0co model, the change in resolution is minor: 1.85 ms for one background event and 1.86 ms for two background events, compared to the original 1.83 ms. The biases are largely unaffected in both cases, confirming the reliability of light curve matching against backgrounds.

Black Hole Cut-Off Feature

Another notable feature when studying the light curve matching method is the black hole cut-off. From Table 7.6, it is clear that the resolution is much better in the cases of the two models where the supernova explosion is accompanied with black hole formation. This is not only because the slight increase in event yield due to the heavier progenitor, but is also an effect of the presence of a sharp cut-off at the end when the black hole forms, as depicted in Figure 7.8. Figure 7.11 demonstrates the

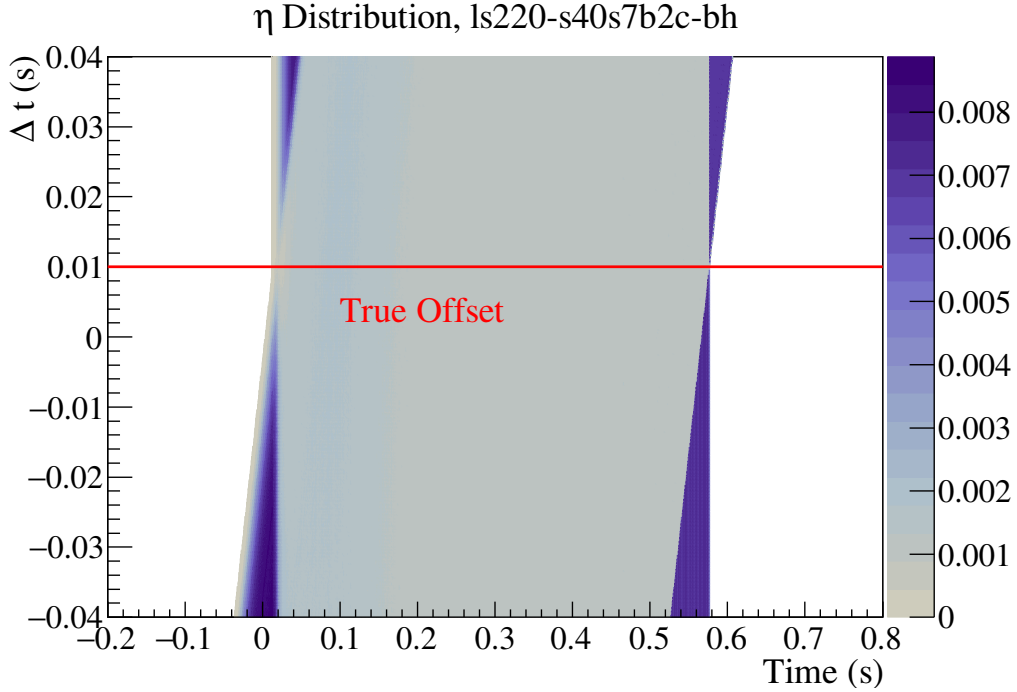


Figure 7.11: The η distribution per time bin (η_i) at each $\widehat{\Delta t}$ step for an averaged trial based on the model ls220-s40s7b2c-bh at 10 kpc. The colour scale indicates the η contribution of a given time bin.

additional resolution power contributed by the sharp cut-off.

The formation of the black hole is expected to cause this cut-off in luminosity as it engulfs the core which is the source of the neutrinos. In the black-hole-forming models invoked in this study, namely the ls220-s40.0c-bh and ls220-s40s7b2c-bh, the cut-off is a perfect discontinuity in the sense that the simulation was manually terminated upon black hole formation. If this was the case, then it might be more efficient to perform a last-event comparison for the determination of the time difference when black hole formation is identified. The black hole cut-off, however, might be slightly softer than many have expected, which will be investigated in the next chapter. Light curve matching is thus currently still the most reliable method for obtaining the time difference between detectors, where the ending edge caused by the black hole could play an important role.

7.4 Summary

Supernova neutrino detection in the SNO+ detector and the multi-detector SNEWS network has been discussed. Based on the light yield and background levels determined in Chapter 5, a multi-threshold burst trigger is developed for SNO+ in the aim of identifying the high energy neutrino burst upon supernova explosion. With the simulated neutrino fluxes based on the Garching models [91, 132, 144], it is discovered that SNO+ is able to maintain higher than 50% sensitivity at 100 kpc for the standard iron-core CCSNe (ls220-s27.0co, ls220-s40.0c-bh, ls220-s40s7b2c-bh) using the currently implemented burst triggers, whereas the sensitivity for the lighter electron-capture supernovae (shen-s8.8) is slightly lower. Additionally, the practical maximum sensitivity in SNO+ can be estimated using a 2-IBD trigger, where the sensitivity for iron-core CCSNe reaches an overall 90% at 100 kpc and 45% for the electron-capture supernovae at the same distance. In order to achieve this sensitivity or to implement the 2-IBD trigger, a prompt IBD identification will be need, in which the `TimeCentroid` method developed in Chapter 6 could play an important role.

With IBD events identified in a timely manner, this valuable signal can be communicated amongst different neutrino detectors across the globe as an important handle in supernova detection, owing to its high purity and relatively high energy emission. These comparable signals synchronised via the SNEWS network could be utilised for many purposes. One main application discussed in this chapter is the positioning of the supernova on the celestial sphere via multi-detector triangulation. To determine the detection time difference between detectors, a light curve matching method based on a simple metric focusing on the large time-derivatives in the luminosity profile has been developed. The results, based on the same set of supernova models, shows that this simple method outperforms the existing methods: 3.4 ms uncertainty compared to the 5.7 ms in [196] for the shen-s8.8 model and 1.8 ms uncertainty compared to the 2.7 ms in [197] for a $27M_{\odot}$ model (equivalent to ls220-s27.0co). Furthermore, by introducing randomly generated events to the luminosity profile, it is demonstrated that the method is resilient to possible backgrounds.

During the study, it was noticed that the sharp decline associated with black hole formation could potentially provide strong resolution power. In fact, if the sharp decline is indeed a perfect cut-off, a last-event method would deliver the most accurate result. Nevertheless, as it will become clear in the next chapter, the cut-off is slightly smoother than is usually expected. The light curve matching method is, therefore, still the most reliable way of identifying the detection time differences between different detectors.

Chapter 8

Black Hole Formation in Core-Collapse Supernova

Black holes are expected to form in the event of a core-collapsing supernova (CCSN) when the proto-neutron star (PNS) exceeds the neutron star mass limit of $2.1\text{--}2.4M_{\odot}$. Though the formation of such a PNS is expected to result from a massive stellar progenitor, further details of the criteria still remain debated [110]. In such an event, the neutrino, and possible gravitational wave, signals might not be accompanied by subsequent visible electromagnetic signals. The observation of black hole formation following a CCSN would, therefore, solely rely on the detection of its neutrino signals. One distinct indication of such an end result is an abrupt cut-off in the neutrino luminosity profile. This abrupt drop in luminosity is due to the engulfment of the main neutrino-producing regions of the PNS as well as the strong gravitational redshift of those neutrinos that just managed to escape.

The cut-off was first explored in the case of photon emissions from a collapsing stellar surface. In 1964, Podurets was the first to work out the asymptotic behaviour of such cut-offs in studying the optical luminosity of a free-falling non-rotating mass shell [207]. It was discovered that the late-time behaviour of the light curve is dictated by photons trapped for an extended period around the unstable circular orbit at a critical radius of $3M^i$, where M is the total mass confined within the collapsing surface, resulting in the luminosity approaching a decaying exponential of time constant $3\sqrt{3}M$. Later in the same year, Zel'Dovich and Novikov demonstrated that radial emissions alone would lead to a luminosity decline characterised by a time constant of $4M$ [208]. Following these enlightening advancements, Ames and Thorne presented the expressions of the redshift factor and the resulting spectral profile in

ⁱHere, and hereafter, the so-called geometric units are used in which $c = G = 1$. In SI units, the expression for such distance will be $3GM/c^2$.

1968 [209]. In the event of a CCSN, the photons would, of course, barely escape and this cut-off would only be evident in the neutrino channel. Therefore, these results have been widely applied in later studies of neutrinos emerging from growing black holes, such as [210, 211].

In terms of the evolution of the black hole, it remains unclear how much of the PNS is involved in the first instance due to uncertainties in its structure. Nonetheless, the formation of the event horizon is likely to initially take place below the surface of the PNS, leaving the most neutrino-producing fertile layers outside. If this is the case, the layers outside will continue to emit neutrinos in all directions, rather than radially, before they themselves fall behind the event horizon. Indeed, it was suggested in [212] that the radial treatment, hitherto adopted by most ray-tracing studies, is expected to be an underestimate, and that a full treatment would require detailed ray-tracing through a highly curved spacetime.

As the indicative signature of the incident black hole formation, the final rapidly declining behaviour of the neutrino light curve is an intriguing feature for its clarity and distinctiveness. In addition, it also reflects the events shrouded deep in the turbulent and violently evolving CCSN core upon black hole formation, and could potentially provide extra statistical power in the multi-detector triangulation of CCSNe as mentioned in Chapter 7 [192, 199, 213]. Detailed modelling of this phenomenon involves computationally intensive hydrodynamic simulations, which, of necessity, simplify neutrino transport to various degrees and approximate or incorporate full general relativity, for instance [214, 215]. In many cases, however, the formation of a black hole presages the end of the validity of such simulations.

Previous analyses of the subject have focused on either specific trajectories or simplified neutrino transport models. In this chapter, we aim to present a comprehensive account of the effects of non-radial geodesics on the neutrino luminosity cut-off by performing a ray-trace study. This idealised scenario is clearly a drastic simplification within a complex domain, but as a toy model it can highlight broad features and be a useful check for more detailed simulations. Null geodesics from non-rotating collapsing stars have been investigated in [209, 216, 217] for photons, as well as in [218, 219] for neutrinos, upon which we will base our studies of the cut-off profile arising from non-rotating black holes. Furthermore, we also present the first ray-tracing study on rotating black holes using the Kerr metric with much of the formulation derived for the first time. The results of this study have been published in [3].

8.1 Neutrino Emission upon Black Hole Formation

The hot dense core of the CCSN is the main source of the neutrinos. As described in Chapter 3, the core undergoes rapid neutronisation during the early stages of the core

collapse, leading to the neutronisation burst consisting of ν_e . Later stages see the thermal production of all neutrino flavours within the coalescing PNS as it continues to accrete matter from the collapsing star. Two scenarios are envisaged to result in the formation of a black hole [220]. The first is where the PNS is further compressed by accretion until sufficient matter is confined within a sufficiently small radius such that the null geodesics start to curve back on themselves, viz., formation of an event horizon. For the case of a non-rotating black hole, this horizon will appear at the radius $2M$, which is clear from the metric listed in Section 8.2. In the second, a part of the PNS undergoes a nuclear phase transition, leading, again, to higher densities sufficient of forming an event horizon.

In either case, it is worthwhile to note that the formation of the event horizon, and thus the black hole itself, is a global observable irrelevant to any neutrino travelling beyond the evolving mass distribution. Suppose that the neutrino were to pass through the environment, the neutrino will only be sensitive to the local curvature determined by the mass distribution around it. As mass re-distributes, generally “inwards” in a global sense, the geodesics bend accordingly. For distant observers, the only indication that a black hole has formed is the disappearance of some, yet by no means all, neutrinos that follow trajectories which bend back on themselves prohibiting their escape.

Furthermore, the timescale of this geodesic bending is not altogether sudden. As the black hole forms, the mass accretion rate onto the PNS is expected to be on the order of $1M_\odot/\text{s}$ [215]. If we use this as the estimate of the growth rate of the black hole, the critical radius of the unstable circular orbit of the null rays will correspondingly grow at the rate of $3M_\odot/\text{s}$, or perhaps more intuitively, on the order of kilometres per second. On the contrary, neutrinos travel at speeds near the speed of light, which is greater by five orders of magnitude. From this perspective, the relatively slow increase in the size of the black hole should clearly not affect the neutrino path to any significant extent.

8.2 Non-Rotating Black Hole: the Schwarzschild Geometry

To start the discussion, the case of neutrinos emitted, or perhaps undergoing their last scatter before escaping, from a shell of matter free-falling towards an inner non-rotating black hole is considered. Spacetime in such a scenario would be described by the Schwarzschild metric. The Schwarzschild metric, solved in 1916 by Schwarzschild as the name suggests [221], is an exact solution of the Einstein field equations that

describes the exterior gravitational field of a non-rotating static spherical body of mass M . In standard spherical coordinates (t, r, θ, ϕ) , the Schwarzschild metric reads out as

$$ds^2 = -\left(1 - \frac{2M}{r}\right)dt^2 + \left(1 - \frac{2M}{r}\right)^{-1}dr^2 + r^2d\theta^2 + r^2\sin^2\theta d\phi^2. \quad (8.1)$$

Since the metric is spherically symmetric, one may restrict attention to study geodesics in the equatorial plane, $\theta = \pi/2$, to simplify matters without loss of generality.

8.2.1 The Geodesic Equation

In this study, there are two particles that should be taken into consideration: the free-falling emitter and the emitted neutrino. The motion in both cases are described by the geodesic equation, since the emitter is assumed to be free-falling and the neutrino trajectory is presumably ballistic, that is, free of any force other than gravity.

To tackle the geodesic equations directly from the general form will be rather laborious. A conventional alternative approach to avoid the tedious computations involving the Christoffel symbols is to invoke the conservation relations associated with the Killing vectors [222]. In the case of the Schwarzschild metric, the quantities can be expressed as

$$\begin{aligned} E &\equiv -g_{\alpha\beta}\left(\frac{\partial}{\partial t}\right)^\alpha\left(\frac{\partial}{\partial \tau}\right)^\beta = C(r)\frac{dt}{d\tau} \\ L &\equiv g_{\alpha\beta}\left(\frac{\partial}{\partial \phi}\right)^\alpha\left(\frac{\partial}{\partial \tau}\right)^\beta = r^2\frac{d\phi}{d\tau} \end{aligned} \quad (8.2)$$

where τ is the proper time, or an affine parameter in the case of a null geodesic, and

$$C(r) \equiv 1 - \frac{2M}{r}. \quad (8.3)$$

In the coordinate frame, that is, the frame of a distant observer, the conserved quantities E and L can be regarded as the total energy and total angular momentum per unit rest mass of a time-like particle. For null rays, similarly, $\hbar E$ and $\hbar L$ can be interpreted as the total energy and angular momentum of the particle.

Observation Frames

Before proceeding to the velocities, it will be beneficial to state explicitly the frames in which the velocities are observed. In this study, there are three frames which will be frequently referred to. The first is, obviously, the aforementioned coordinate

frame which is the frame of the distant observer, e.g., observers on Earth. All of the expressions shown so far are derived in this frame. For consistency, observables are presumably in this frame unless otherwise specified. The second frame is the proper frame of the free-falling emitter. This frame will be referred to as the “free-fall” (*FF*) frame hereafter, and the observables of this frame will be indicated by the subscript *FF*. Finally, there is the frame of a stationary observer in which the metric is invariant in time [223], that is to say it is at rest with respect to the t -hypersurfacesⁱⁱ, and coincides in position with the falling emitter. Since this stationary observer turns out to be staticⁱⁱⁱ, the variables observed in this “static” (*S*) frame will be labelled with the subscript *S*.

Velocities

The normalisation of the tangent vector of a geodesic can be expressed as

$$\kappa = \xi^\alpha \xi_\alpha = -C \left(\frac{dt}{d\tau} \right)^2 + C^{-1} \left(\frac{dr}{d\tau} \right)^2 + r^2 \left(\frac{d\phi}{d\tau} \right)^2 \quad (8.4)$$

where

$$\kappa = \begin{cases} -1 & \text{time-like geodesics} \\ 0 & \text{null geodesics} \end{cases}.$$

By substituting the conservation relations in Eq. 8.2, the normalisation condition becomes

$$\kappa = -C^{-1} E^2 + C^{-1} \left(\frac{dr}{d\tau} \right)^2 + \frac{L^2}{r^2} \quad (8.5)$$

and with some rearrangement of the terms one will arrive at

$$\left(\frac{dr}{d\tau} \right)^2 = E^2 + C \left(\kappa - \frac{L^2}{r^2} \right) \quad (8.6)$$

which is precisely the radial geodesic equation. It will, however, be slightly more informative written in terms of the velocity rather than proper velocity

$$\left(\frac{dr}{dt} \right)^2 = C^2 + C^3 \left(\frac{\kappa}{E^2} - \frac{b^2}{r^2} \right) \quad (8.7)$$

where $b \equiv L/E$ is known as the apparent impact parameter in the case of null rays, for it will be the distance of closest approach were the spacetime flat [222]. In this case, it becomes apparent that the null geodesics will be solely determined by the impact parameter b .

ⁱⁱThis means the four-velocity of the observer will be proportional to $\nabla^\alpha t = g^{\alpha\beta}(\nabla_\beta t) = g^{\alpha\beta}(dt)_\beta$. In Schwarzschild geometry, this reads out as $\frac{\partial}{\partial\tau} \propto -C^{-1} \frac{\partial}{\partial t} \propto \frac{\partial}{\partial t}$.

ⁱⁱⁱThe static observer is defined as a strictly time-like observer, i.e., $\propto \frac{\partial}{\partial t}$.

Free-Falling Emitter

Consider the case of a free-falling emitter initially at rest at $r = r_0$. Free-falling from rest suggests that the emitter has no angular momentum, i.e., $L = 0$ at all times. The geodesic equation Eq. 8.6 then becomes

$$\left(\frac{dr}{dt}\right)^2 = C^2 \left(1 - \frac{C}{E^2}\right). \quad (8.8)$$

By inserting the initial condition that the emitter is at rest at r_0 , one can solve for E^2 without much labour

$$E^2 = C_0 \quad (8.9)$$

where $C_0 \equiv C(r_0)$. Therefore, the free-falling velocity of the emitter in coordinate frame is

$$\frac{dr}{dt} = C \sqrt{1 - \frac{C}{C_0}}. \quad (8.10)$$

It is also useful to express this velocity in the static frame. The conversion between the coordinate and static frames can be figured out by comparing the metric tensor transform between the coordinates $x^\mu = \{t, r, \theta, \phi\}$ and $x_S^\mu = \{t_S, r_S, \theta_S, \phi_S\}$

$$\begin{aligned} (g_{\alpha\beta})_S (dx_S^\alpha)_a \otimes (dx_S^\beta)_b &= g_{ab} = g_{\alpha\beta} (dx^\alpha)_a \otimes (dx^\beta)_b \\ &= g_{\alpha\beta} \left(\frac{\partial x^\alpha}{\partial x_S^\gamma}\right) \left(\frac{\partial x^\beta}{\partial x_S^\delta}\right) (dx_S^\gamma)_a \otimes (dx_S^\delta)_b \end{aligned} \quad (8.11)$$

where the abstract index notation has been invoked [222]. In the abstract index notation, indices in Greek letters are used to indicate the scalar components of the tensors, and Latin indices are used to keep record of the tensor bases, for which the outer product will no longer be explicitly written henceforth. For instance, a rank 2 mixed tensor will be written as $T_b^a = T_\beta^\alpha (\partial_\alpha)^a (dx^\beta)_b$.

Since a local observer will find the local spacetime flat, the metric in the static frame will simply be the Minkowski metric. Bearing that in mind, a simple comparison of the left hand side and right hand side of Eq. 8.11 leads to the following observations

$$\frac{\partial t}{\partial t_S} = C^{-\frac{1}{2}}, \quad \frac{\partial r}{\partial r_S} = C^{\frac{1}{2}}, \quad \frac{\partial \theta}{\partial \theta_S} = 1, \quad \frac{\partial \phi}{\partial \phi_S} = 1. \quad (8.12)$$

Finally, with these relations the static frame velocity can be expressed as

$$\beta_S \equiv \frac{dr_S}{dt_S} = \left(\frac{\partial t}{\partial t_S}\right) \left(\frac{\partial r_S}{\partial r}\right) \left(\frac{dr}{dt}\right) = \sqrt{1 - \frac{C}{C_0}}. \quad (8.13)$$

Neutrino Trajectory

Since the neutrino mass is nearly vanishing, null geodesics can describe the neutrino trajectories to a fairly high degree of accuracy. In this case, the geodesic equation describing the neutrino motion will be

$$\left(\frac{dr}{dt}\right)^2 = C^2 \left(1 - C \frac{b^2}{r^2}\right). \quad (8.14)$$

Following similar transformations as in Eq. 8.13, the radial velocity of the neutrino in the static frame is found to be

$$\left(\frac{dr}{dt}\right)_S = \cos \psi_S = \sigma_r \sqrt{1 - C \frac{b^2}{r^2}} \quad (8.15)$$

where ψ_S is the angle relative to the outward radial direction as observed in the static frame; and σ_r is +1 for radially outward trajectories and -1 for inward trajectories as measured in, again, the static frame. Note that since the null geodesic is invoked, the total velocity is always fixed at $c = 1$ and the radial velocity can simply be identified as $\cos \psi_S$ in the static frame.

Another important quantity in the considerations of the neutrino emission is the neutrino radial velocity in the free-fall frame, for this will be the frame in which emission is isotropic. The free-fall frame only differs from the static frame by an inward boost of β_S . Therefore, one can obtain the neutrino radial velocity in free-fall frame through a simple exercise of velocity addition

$$\left(\frac{dr}{dt}\right)_{FF} = \cos \psi_{FF} = \frac{\cos \psi_S + \beta_S}{1 + \cos \psi_S \cdot \beta_S} \quad (8.16)$$

where ψ_{FF} is now the angle relative to the outward radial direction in the free-fall frame. Eqs. 8.15 and 8.16 also showed that there is a bijective relation between the impact parameter b and the emission angle ψ from which one can calculate the other whenever one of the quantities are known, e.g., $b = 0$ obviously leads to radial emissions.

8.2.2 Neutrino Travel Time

With the trajectory determined, the travel time of the neutrino as observed on Earth can then be estimated by integrating Eq. 8.14, leading to the expression

$$T(b, r_*; r_E) \equiv \int_{t_*}^{t_E} dt = \int_{r_*}^{r_E} \frac{r^{5/2} dr}{(r - 2M) \sqrt{r^3 - b^2(r - 2M)}} \quad (8.17)$$

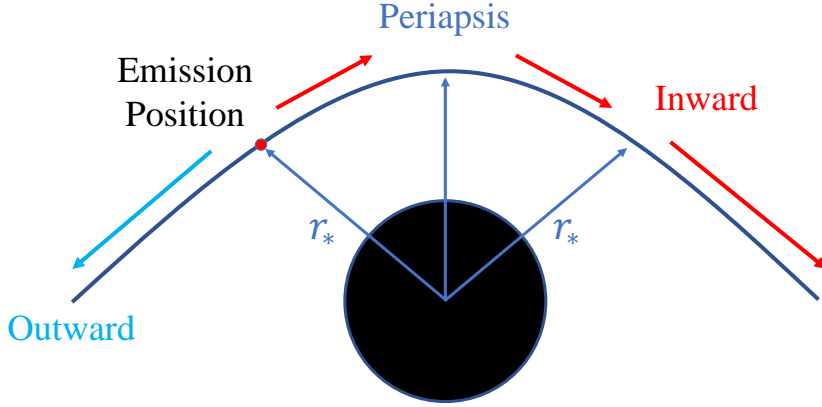


Figure 8.1: Inward and outward trajectories for neutrinos emitted outside the photon sphere. Outward trajectories escape directly, whilst inward trajectories reach periapses before joining the outward trajectory.

where t_* and t_E are the times of emission and observation; and r_* and r_E are the emission radius and the distance to Earth, respectively. This expression can be further simplified in the case of radial emissions

$$\begin{aligned} T(b = 0, r_*; r_E) &= \int_{r_*}^{r_E} \frac{r dr}{r - 2M} \\ &= (r_E - r_*) + 2M \ln \left(\frac{r_E - 2M}{r_* - 2M} \right). \end{aligned} \quad (8.18)$$

When calculating the travel time of the neutrinos, there are two cases that should be taken into consideration, as depicted in Figure 8.1. For a neutrino appearing to be emitted outwardly in the static frame, the time delay compared to a neutrino travelling radially outward from the initial radius is

$$\Delta T_+(b, r_*) = T(b, r_*; r_E) - T(0, r_0; r_E) \quad (8.19)$$

where the “+” label indicates the outward travel direction. The inward oriented path, on the other hand, will acquire an extra Shapiro-like time delay [224] as it passes the periapsis. The expression of the time delay then becomes

$$\Delta T_-(b, r_*) = 2T(b, r_p; r_*) + \Delta T_+(b, r_*) \quad (8.20)$$

where r_p is the periapsis distance

$$r_p = \frac{2b}{\sqrt{3}} \cos \left(\frac{1}{3} \arccos \left(-\frac{\sqrt{27}M}{b} \right) \right) \quad (8.21)$$

which can be solved from the right hand side of Eq. 8.14 at given b .

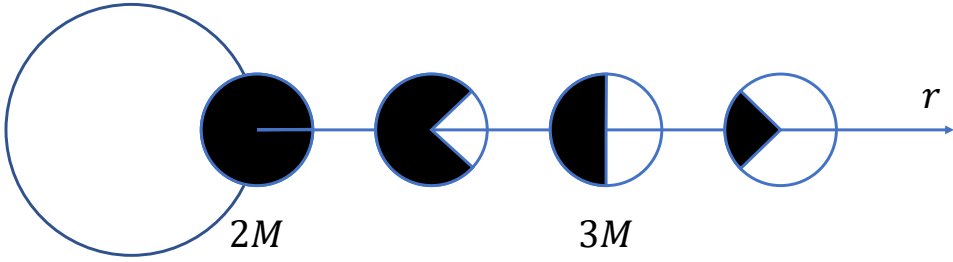


Figure 8.2: Schematic view of the escape cones (unshaded region) for null geodesics in Schwarzschild spacetime. At $r_* = 2M$, only radial geodesics can escape. For $2M < r_* \leq 3M$, only outward-oriented geodesics are able to escape. Beyond $r_* = 3M$, some of the inward-oriented geodesics can also escape to infinity.

Escape Cone and Photon Sphere

It is evident from the integrand in Eq. 8.17 that not all trajectories lead to infinity. There are two occasions when the integrand diverges: $r = 2M$ and $r^3 - b^2(r - 2M) = 0$. The first is simply the event horizon, whereas the second condition introduces an unstable circular orbit at $r = 3M$ known as the “photon sphere”, for which paths are characterised by the “critical impact parameter” $b_c \equiv 3\sqrt{3}M$. The photon sphere is the only possible circular orbit for null rays in Schwarzschild geometry, for it is the only instance when both the radial velocity and acceleration vanishes outside the event horizon

$$\left. \frac{d^2r}{dt^2} \right|_{r^3 - b^2(r - 2M) = 0} = \sigma_r \frac{(r - 2M)(r - 3M)}{r^3}. \quad (8.22)$$

The photon sphere creates a boundary at $r = 3M$, outside which only outward oriented geodesics and inward directed geodesics with b

$$b_c < b \leq \sqrt{\frac{r^3}{r - 2M}} \quad (8.23)$$

are able to reach infinity. Between the photon sphere and the event horizon, only outward travelling paths of $b < b_c$ are able to escape. These “escape cones”^{iv} are shown in Figure 8.2. The reason behind this is that, as shown in Figure 8.3, the equation $r^3 - b^2(r - 2M) = 0$ is solvable outside the event horizon only when $b \geq b_c$. Therefore, the paths of $b < b_c$ will either escape to infinity if oriented outwards or

^{iv}The opposite of what Chandrasekhar referred to as the “cone of avoidance” [225].

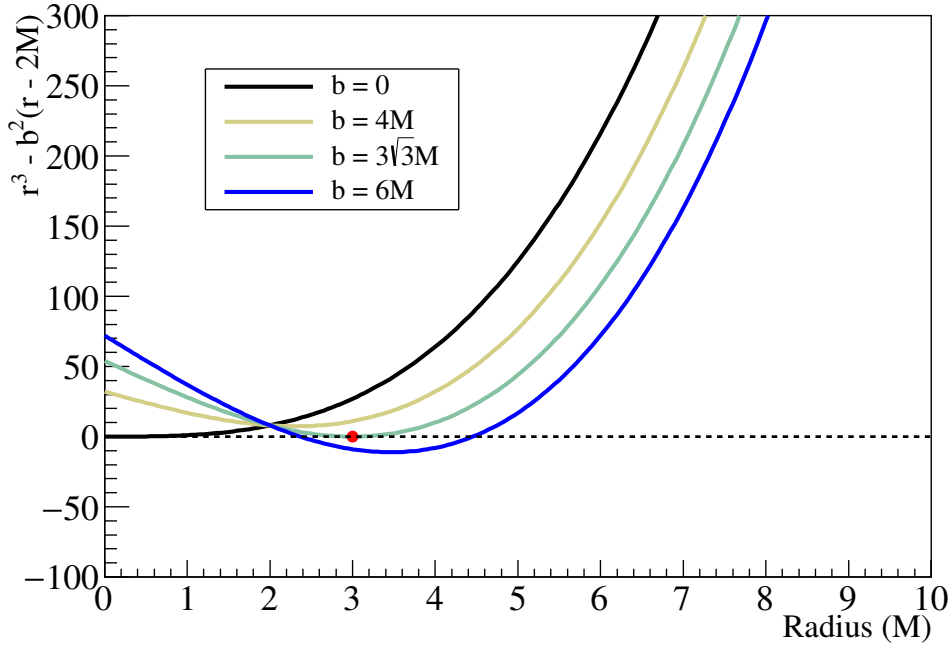


Figure 8.3: Behaviour of $r^3 - b^2(r - 2M) = 0$ at different b values. Roots beyond the event horizon only exist when $b > b_c = 3\sqrt{3}M$.

plunge into the black hole if oriented inwards. The case for paths of $b > b_c$ is slightly more intricate. The outward trajectories beyond the photon sphere simply escapes, and the inward trajectories within the range $2M < r < 3M$ will be absorbed by the black hole. Besides these straightforward cases, the outward paths for $2M < r < 3M$ and the inward paths for $r > 3M$ will eventually pass their respective apoapsis and periapsis at the roots of $r^3 - b^2(r - 2M) = 0$ then reverse course as the acceleration will always be non-zero in the opposite direction, which can be easily verified from Eq. 8.22.

Emission Angle and Travel Time

Figure 8.4 shows the emission angle dependence of the time delay for a surface free-falling from rest at radius $10M$ towards a black hole of mass $2.5M_\odot$. Note that the emission angle in Figure 8.4 is that observed in the free-fall frame. The time delay is zero at $\psi_{FF} = 0$ by definition, since ψ_{FF} is defined with respect to the outward radial direction. As the emission direction deviates from the radial direction, the time delay increases accordingly and will eventually diverge as the periapsis radius approaches the photon sphere radius at $r = 3M$. The escape cone shrinks in accordance with the

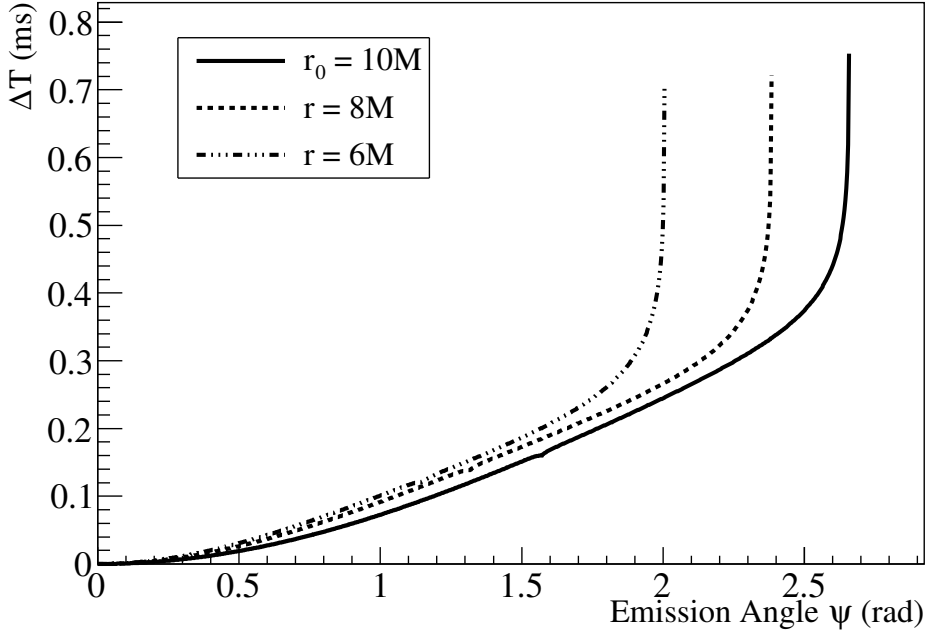


Figure 8.4: Time delays, relative to that of the outward radial emission for a given radius, as a function of the emission angle in the free-fall frame. The curves are shown for the initial radius $r_0 = 10M$ and for subsequent radii $8M$ and $6M$, for a Schwarzschild black hole with mass $2.5M_\odot$.

receding radius. Moreover, the increasing velocity of the falling shell will introduce a further contraction in the coverage of the escape cone due to relativistic beaming.

With close inspection on Figure 8.4, one will notice that a large fraction of the trajectories lead to time delays of fractions of a millisecond. This time delay is expected to lead to the softening of the black hole cut-off.

8.2.3 Redshift

The cut-off profile of the luminosity of a collapsing surface as a function of the observation time t_E is governed by the number of neutrinos reaching the observer as well as by the redshift, first worked out in [209],

$$\zeta(b, r_*, \sigma_r) = \frac{\nu_E}{\nu_*} = \sqrt{C(r_*)} \times \frac{\sqrt{1 - \beta_S^2}}{1 + \beta_S \cos \psi_S} \quad (8.24)$$

where ν_E and ν_* are the neutrino energies upon observation at Earth and upon emission measured in free-fall frame. The first factor of the right hand side of Eq. 8.24

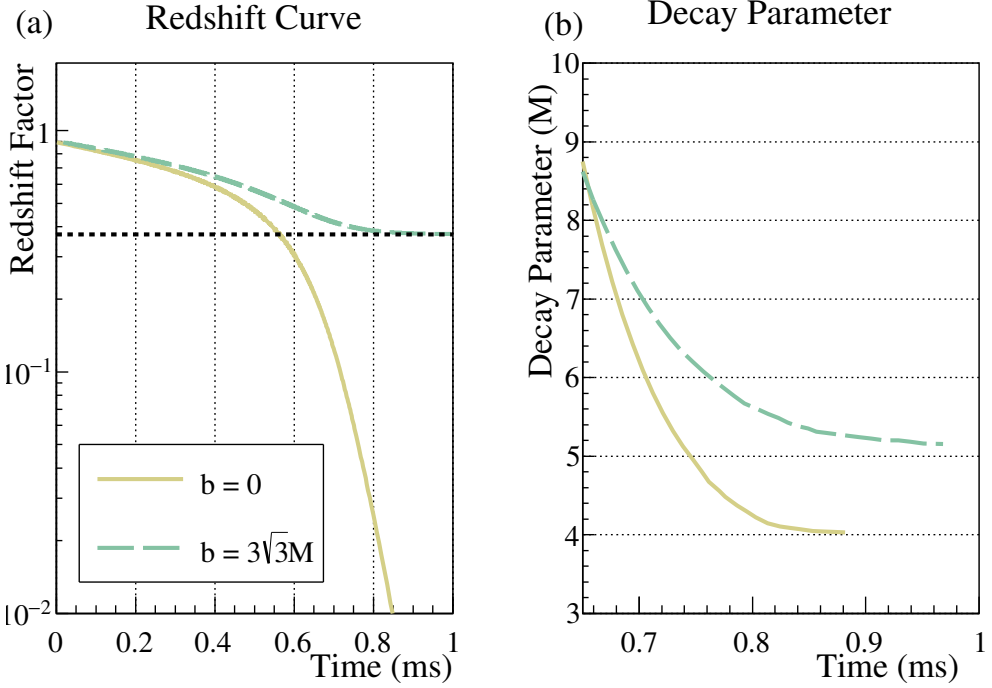


Figure 8.5: (a) Redshift factor and (b) the fitted decay parameter for outward radial emissions ($b = 0$, solid/yellow line) and critical emissions ($b = b_c \equiv 3\sqrt{3}M$, dashed/green line) plotted against observation time for a $2.5M_\odot$ Schwarzschild black hole. The curves are calculated for a shell falling from $10M$ to $2.1M$ (for $b = 0$) or $3M$ (for $b = b_c$). The observation time is taken relative to the observation of the first neutrino received from the shell when it was at $10M$. The dashed black line in (a) is the redshift at the unstable circular orbit at $r = 3M$, Eq. 8.28.

is the gravitational redshift, assuming $r_E \gg r_*$, between the energy upon emission measured in the static frame and the energy measured on Earth

$$\frac{\nu_E}{\nu_S} = \sqrt{\frac{C(r_*)}{C(r_E)}} \approx \sqrt{C(r_*)} \quad (8.25)$$

where ν_S is the neutrino energy upon emission measured in static frame. The second part, on the other hand, is simply the Doppler shift between the neutrino emission energy measured in the static and free-fall frames.

Figure 8.5 (a) shows the redshift factor for outward radial emissions ($b = 0$) and “critical emissions” ($b = b_c$) as a function of their observation times, relative to the arrival of the first neutrino emitted from the initial radius. Since the behaviours of the redshift curves are expected to approach exponentials, the curves are fitted by the form

$$A \exp\left(-\frac{t}{\tau}\right) \quad (8.26)$$

where τ is what will be referred to as the “decay parameter” plotted in Figure 8.5(b). At late times, the radial redshift curve approaches an exponential of decay constant $4M$, which is precisely what was demonstrated in [208]. Meanwhile, the redshift curve for the critical emission takes a slightly different asymptotic form of an exponential plus a constant

$$A \exp\left(-\frac{t}{\tau}\right) + B. \quad (8.27)$$

This constant floor is a result of the presence of the photon sphere. Since the critical emissions from $r \leq 3M$ will not escape, the late-time behaviour will be dominated by the emissions just beyond the critical radius, where the redshift factor will approach

$$\zeta(b_c, r_* \approx 3M, +1) \approx \sqrt{C(3M)} \times \sqrt{1 - (\beta_S(3M))^2}. \quad (8.28)$$

By subtracting this asymptotic offset, the fitted decay parameter will eventually approach $3\sqrt{3}M$, which is the results of [207, 209].

8.2.4 Ray Tracing and Luminosity Profile

Finally, the energy contribution of a neutrino of impact parameter b emitted at time t from radius r that reaches the observer at time t_E can be written as

$$d\epsilon(t_E) = \zeta(b, r, \sigma_r) \times \frac{\mathcal{L}_0 \cdot dt}{4\pi r^2} \times r^2 d\Omega, \quad (8.29)$$

where $d\Omega$ is the solid angle element of the emitting shell, and \mathcal{L}_0 is the total luminosity of the surface. The total luminosity is assumed to be constant throughout the collapse.

The luminosity profile as a function of the observation time is then evaluated by a simple ray-tracing Monte Carlo. At each time step in coordinate time t , a fixed number of neutrino emissions isotropic in direction are generated from the collapsing shell. The emission angle ψ_{FF} is randomly assigned and used to determine the impact parameter b via the relations in Eqs. 8.15 and 8.16

$$b = \sqrt{\frac{r^2}{C} \cdot \left(1 - \left(\frac{\cos \psi_{FF} - \beta_S}{1 - \cos \psi_{FF} \cdot \beta_S}\right)^2\right)}. \quad (8.30)$$

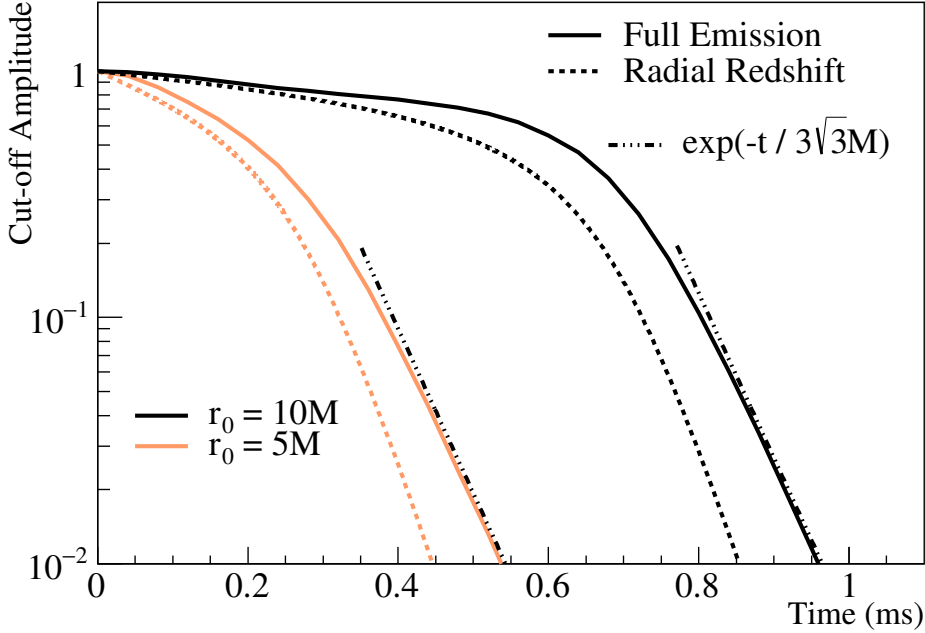


Figure 8.6: Comparison of cut-off profiles for non-radial (solid) and radial (dotted) emissions for initial radii $10M$ (black) and $5M$ (orange). The amplitudes of the profiles are normalised to unity at $t_E = 0$. The late time behaviours approach falling exponentials with decay parameters $3\sqrt{3}M$, which are indicated with black dotted-dashed lines.

The corresponding observation time t_E , if applicable, and the redshift factor ζ will then follow. Additionally, the simulation is further simplified, in light of the spherical symmetry of the metric, by simulating the neutrino from a single point on the shell regardless of where the trajectory intersects the outer sphere of radius r_E . The results are shown in Figure 8.6 for initial radii of $10M$ and $5M$. The general feature of the profiles consists of an initial slow drop in luminosity for several tenths of milliseconds, soon followed by a steepening which rapidly approaches an exponential characterised by a decay parameter of $3\sqrt{3}M$. The $3\sqrt{3}M$ decay parameter thus characterises much of the cut-off rather than only the end, where dominance by nearly critical emissions ($b \approx b_c$) has long been expected [207]. Moreover, it is evident that consideration of all emission directions softens the overall cut-off. Figure 8.7, for example, shows that the decay parameter of the full emissions curve exceeds that of critical emissions at all times.

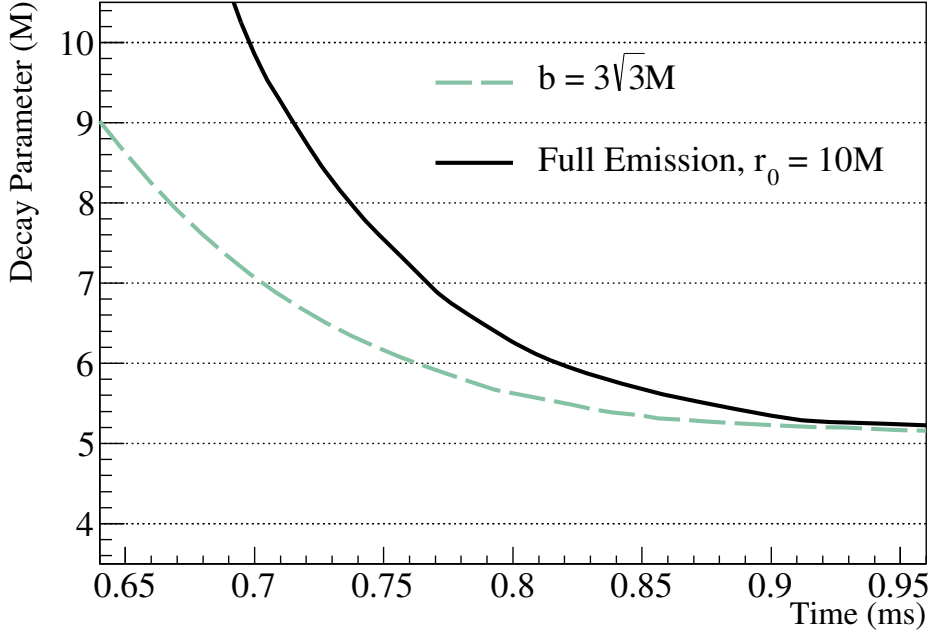


Figure 8.7: The decay parameter for critical emissions ($b = b_c$) (dashed/green) and full emissions (solid/black), with initial radius $r_0 = 10M$.

Emission Schemes

It should be noted that Figure 8.6 shows the result of all the neutrino emissions included in the distant observation, i.e., the surrounding medium is transparent to the neutrinos. If, on the contrary, the inner medium is assumed to be completely opaque to neutrinos, then only those neutrinos appearing to be emitted outwards in the free-falling frame will escape. The cut-off profiles of this ‘opaque shell’ scenario are shown in Figure 8.8. Note that the opaque shell scenario is different from that of allowing only outward emissions in the static frame. The opaque shell scenario includes the contribution from neutrinos which appear to be directed inward in the static frame, whilst lagging behind the collapsing opaque shell, viz., when the inward radial velocity of the neutrino is less than β_S . As it turns out, the modification of the opaque shell correction is rather mild compared to the full emission scenario, and only introduces minor changes to the decay timescale.

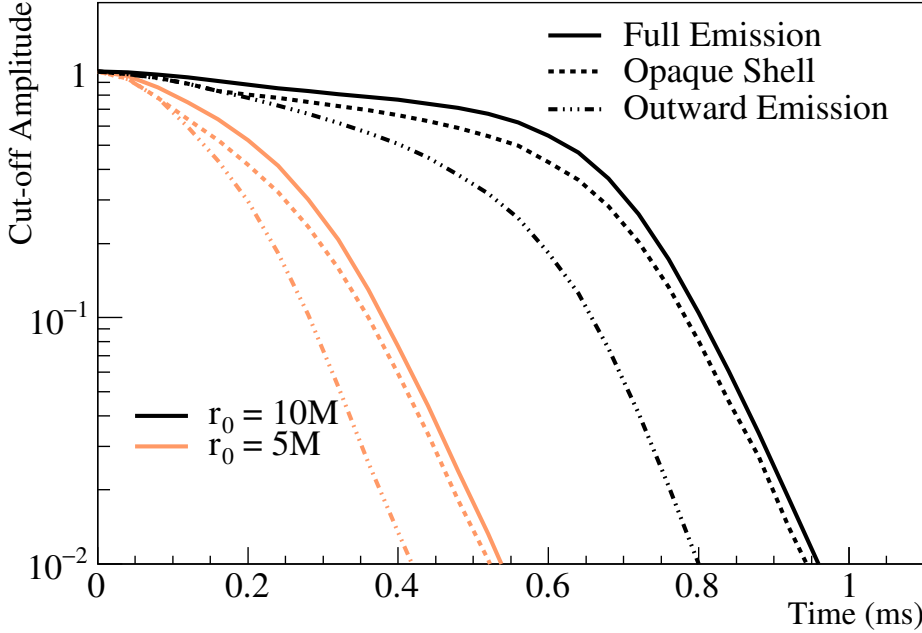


Figure 8.8: Comparison of three different inward emission scenarios for initial radii $10M$ (black) and $5M$ (orange): transparent medium, with emissions allowed in all directions (solid); opaque inner medium, allowing only emissions which are outward in the free-fall frame (dotted); and allowing only emissions which are outward in the static frame (dashed-dotted).

8.2.5 Emitters Not in Free-Fall

The neutrino-emitting surface is hitherto assumed to be in free-fall, yet it is generally expected that free-fall is an overestimate of the collapsing speed of the shell. To introduce a little more realism to the toy model, one can consider reducing the acceleration of the shell by a constant factor f to mimic residual pressure support. The proper velocity will then be

$$\frac{dr}{d\tau} = \sqrt{f \cdot (C - C_0)}. \quad (8.31)$$

As the motion no longer follows a geodesic, the Killing equations will not apply. The conversion to ordinary velocity will then rely on the normalisation relation given in Eq. 8.4 which results in the expression

$$\frac{dt}{d\tau} = \sqrt{(1 - f)C^{-1} + fC_0C^{-2}} \quad (8.32)$$

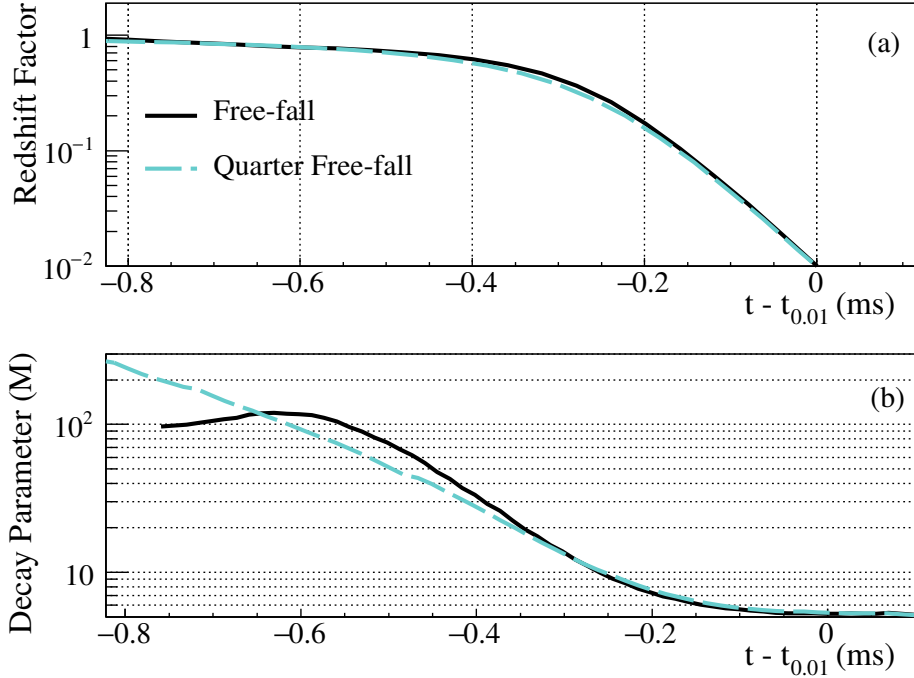


Figure 8.9: (a) Luminosity and (b) decay parameter profiles for free-fall ($f = 1$, solid/black) and reduced ($f = 1/4$, dashed/blue) shell acceleration. The curves are shifted in time to meet at $t = t_{0.01}$, when the luminosity has fallen to 1% of its value at $t = 0$.

and leads to the velocity in coordinate frame

$$\frac{dr}{dt} = C \cdot \sqrt{\frac{C_0 - C}{C_0 + (\frac{1}{f} - 1)C}}. \quad (8.33)$$

In the static frame, it becomes

$$\beta_S = \sqrt{\frac{C_0 - C}{C_0 + (\frac{1}{f} - 1)C}}. \quad (8.34)$$

The resulting luminosity profile for $f = 1/4$, corresponding to a doubling of the collapse time relative to the free-fall case, is shown in Figure 8.9. This slower velocity profile leads to an extension of the initial slow drop by approximately 0.8 ms before the onset of the rapid decay. In order to compare the rapid decays, the luminosity profiles in Figure 8.9 are aligned at the point where they have decreased to 1% of the initial amplitude. The quarter free fall decay parameter profile starts from a

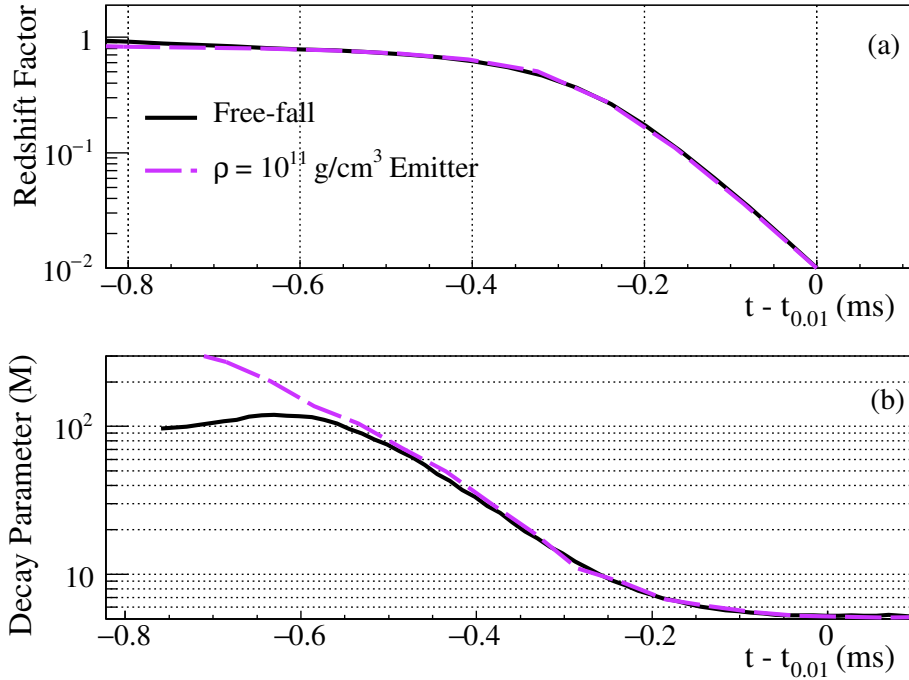


Figure 8.10: (a) Luminosity and (b) decay parameter profiles for free falling (solid/black) and ρ -shell (dashed/violet) emitters. The curves are shifted in time to meet at $t = t_{0.01}$, when the luminosity has fallen to 1% of its value at $t = 0$.

higher value and decreases more gradually throughout. Once the rapid decay begins, however, it approaches a decay parameter of $3\sqrt{3}M$ in a manner fairly similar to the free-fall case.

Another variation of the opaque shell model is to allow the shell radius to fall at a speed different from that of the emitters themselves. In this case, the surface is drawn by the density of the matter below which the emitted neutrino is expected to scatter or be absorbed, known as the “neutrinosphere” [226]. The emitters, on the other hand, fall through this radius as they emit. The values of shell radii and emitter velocities as a function of time come from outside the present toy model. They are calculated from a GR1D [227] general relativistic hydrodynamic simulation, with modern neutrino transport and interaction rates. This simulation is based on a $40M_\odot$ progenitor model [228] using the Lattimer & Swesty equation of state with nuclear incompressibility of 220 MeV, which collapses to a $2.25M_\odot$ black hole [214]. As mentioned in Section 3.3.1, this shell is usually chosen to be at the density of $\rho = 10^{11} \text{ g/cm}^3$, as the optical depth of the neutrino reaches unity at that density [229].

Simulations are carried out until black hole formation. This corresponds to a

shell collapsing from roughly $7M$ to $3.5M$ and attaining a final maximum speed of approximately $0.35c$ in the static frame. When the simulation is terminated, no further emissions will be generated, though the neutrinos already emitted on escaping trajectories will continue to propagate to the observer. The resulting profiles are shown in Figure 8.10. The slowly decaying part of the luminosity profile is significantly elongated compared to the free-fall case. In the end, nonetheless, the decay parameter still approaches $3\sqrt{3}M$, as a result of neutrinos emitted inwards and subsequently trapped near the photon sphere at $r = 3M$.

8.3 Rotating Black Hole: the Kerr Geometry

In this section, the neutrino luminosity profile of a collapsing surface around an uncharged rotating black hole will be discussed. The geometry of an uncharged rotating black hole^v is described by the Kerr metric, discovered by Kerr in 1963 as a generalisation of the Schwarzschild metric [230]. The metric expressed in Boyer-Lindquist coordinates (t, r, θ, ϕ) ^{vi} is [231]

$$\begin{aligned} ds^2 = & - \left(1 - \frac{2Mr}{\Sigma} \right) dt^2 - \frac{4aMr \sin^2 \theta}{\Sigma} dt d\phi \\ & + \frac{\Sigma}{\Delta} dr^2 + \Sigma d\theta^2 + \left(r^2 + a^2 + \frac{2Mra^2 \sin^2 \theta}{\Sigma} \right) \sin^2 \theta d\phi^2 \end{aligned} \quad (8.35)$$

where

$$\begin{aligned} a &\equiv J/M \\ \Delta &\equiv r^2 + a^2 - 2Mr \\ \Sigma &\equiv r^2 + a^2 \cos^2 \theta \end{aligned} \quad (8.36)$$

and J is the angular momentum of the black hole. Since the Kerr metric is only axially symmetric, the geodesics are not, in general, planar and one is no longer at liberty to restrict attention to the equatorial plane without loss of generality.

^vThis will be simply referred to as a rotating black hole hereafter.

^{vi}These are ellipsoidal coordinates.

8.3.1 The Geodesic Equation

Similar to the case of the Schwarzschild metric, the geodesics are, again, characterised by the conserved quantities E and L as defined in Eq. 8.2

$$\begin{aligned} E \equiv -g_{\alpha\beta} \left(\frac{\partial}{\partial t} \right)^\alpha \left(\frac{\partial}{\partial \tau} \right)^\beta &= \left(1 - \frac{2Mr}{\Sigma} \right) \frac{dt}{d\tau} + \frac{2Mar \sin^2 \theta}{\Sigma} \frac{d\phi}{d\tau} \\ L \equiv g_{\alpha\beta} \left(\frac{\partial}{\partial \phi} \right)^\alpha \left(\frac{\partial}{\partial \tau} \right)^\beta &= -\frac{2Mar \sin^2 \theta}{\Sigma} \frac{dt}{d\tau} + \frac{A \sin^2 \theta}{\Sigma} \frac{d\phi}{d\tau} \end{aligned} \quad (8.37)$$

with the useful shorthand

$$A \equiv (r^2 + a^2)^2 - \Delta a^2 \sin^2 \theta. \quad (8.38)$$

In addition, another conserved quantity was discovered by Carter in 1968, by performing a separation of variables of the Hamilton-Jacobi equation [232]. This conserved quantity is known as the Carter constant Q , which can be thought of as characterising the non-planar motion. Soon after, Walker and Penrose identified the Carter constant with a rank 2 Killing tensor, a generalisation of the Killing vector [233]. The resulting equations of motions are [232]

$$\begin{aligned} \frac{\Sigma}{E} \left(\frac{dt}{d\tau} \right) &= \frac{1}{\Delta} (A - 2Mrab) \\ \frac{\Sigma}{E} \left(\frac{d\phi}{d\tau} \right) &= \frac{b}{\sin^2 \theta} + \frac{a}{\Delta} (2Mr - ab) \\ \frac{\Sigma}{E} \left(\frac{d\theta}{d\tau} \right) &= \sigma_\theta \sqrt{\Theta} \\ \frac{\Sigma}{E} \left(\frac{dr}{d\tau} \right) &= \sigma_r \sqrt{R} \end{aligned} \quad (8.39)$$

with the abbreviations

$$\begin{aligned} R &\equiv ((r^2 + a^2) - ab)^2 - \Delta \left(q + (a - b)^2 - \frac{\kappa}{E^2} r^2 \right) \\ \Theta &\equiv q - \cos^2 \theta \left(\frac{b^2}{\sin^2 \theta} - a^2 \left(1 + \frac{\kappa}{E^2} \right) \right) \end{aligned} \quad (8.40)$$

where κ is defined as in Eq. 8.4; σ_r and σ_θ indicate the direction of motion relative to the r and θ axes; and the impact parameters $b \equiv L/E$, as before, and $q \equiv Q/E^2$. Additionally, the direction of the azimuthal motion can be read from b , in that $b > 0$ indicates co-rotation with the black hole and $b < 0$ indicates counter-rotation.

Locally Non-Rotating Frame

As in the non-rotating case, the observables will be discussed in three observation frames, of which the notions of the coordinate and free-fall frames remain the same. The stationary observer in Kerr spacetime is, however, no longer static due to the effects of inertial-frame dragging. This frame of stationary observers in Kerr spacetime is known as the locally non-rotating frame (LNRF), proposed by Bardeen in 1972 [234]. In this section, the LNRF will be used in place of the static frame of the non-rotating case, and, hence, the subscript S will be re-purposed to represent observables in the LNRF for convenience.

By definition, as the stationary observer is at rest with respect to the t -hypersurfaces, the four-velocity of the observer will be proportional to

$$\begin{aligned}\nabla^a t &= g^{ab}(\nabla_b t) = g^{ab}(dt)_b = g^{\alpha t} \left(\frac{\partial}{\partial x^\alpha} \right)^a = g^{tt} \left(\frac{\partial}{\partial t} \right)^a + g^{\phi t} \left(\frac{\partial}{\partial \phi} \right)^a \\ &= \frac{-1}{\Sigma \Delta} \left(A \left(\frac{\partial}{\partial t} \right)^a + 2aMr \left(\frac{\partial}{\partial \phi} \right)^a \right) \\ &= \frac{-1}{\Delta \sin^2 \theta} \left(g_{\phi\phi} \left(\frac{\partial}{\partial t} \right)^a - g_{\phi t} \left(\frac{\partial}{\partial \phi} \right)^a \right)\end{aligned}\tag{8.41}$$

where the components of the metric are

$$g_{tt} = \frac{2Mr - \Sigma}{\Sigma}, \quad g_{\phi\phi} = \frac{A \sin^2 \theta}{\Sigma}, \quad g_{t\phi} = g_{\phi t} = -\frac{2Mra \sin^2 \theta}{\Sigma}.\tag{8.42}$$

The four-velocity of the observer can, therefore, be written as

$$Z^a = \left(\frac{\partial}{\partial \tau} \right)^a = Z_0 \left(\left(\frac{\partial}{\partial t} \right)^a - \frac{g_{\phi t}}{g_{\phi\phi}} \left(\frac{\partial}{\partial \phi} \right)^a \right)\tag{8.43}$$

where Z_0 is the normalisation constant and $\tau = t_S$ is the proper time of the observer. The “angular momentum” L of the observer, as defined in Eq. 8.37, can then be evaluated by

$$L = g_{ab} Z^a \left(\frac{\partial}{\partial \phi} \right)^b = Z_0 \left(g_{\phi t} + g_{\phi\phi} \left(-\frac{g_{\phi t}}{g_{\phi\phi}} \right) \right) = 0.\tag{8.44}$$

For this reason, the LNRF observer is also known as the zero angular momentum observer (ZAMO)^{vii} [235].

^{vii}Note that, strictly speaking, the term ZAMO actually encompasses a wider class of observers that are not necessarily stationary. Nonetheless, this term is usually attributed to the LNRF observer in most usages.

Furthermore, Eq. 8.44 shows that the basis of the LNRF is

$$\left\{ Z_0 \left(\left(\frac{\partial}{\partial t} \right)^a - \frac{g_{\phi t}}{g_{\phi\phi}} \left(\frac{\partial}{\partial \phi} \right)^a \right), \left(\frac{\partial}{\partial r} \right)^a, \left(\frac{\partial}{\partial \theta} \right)^a, \left(\frac{\partial}{\partial \phi} \right)^a \right\}. \quad (8.45)$$

The transformation between the LNRF $\{t_S, r_S, \theta_S, \phi_S\}$ and the coordinate frame $\{t, r, \theta, \phi\}$ can then be carried out in a similar fashion as in Eq. 8.11. This results in the transforms

$$\frac{\partial t}{\partial t_S} = \sqrt{\frac{A}{\Sigma\Delta}}, \quad \frac{\partial r}{\partial r_S} = \sqrt{\frac{\Delta}{r^2 + a^2}}, \quad \frac{\partial \theta}{\partial \theta_S} = 1, \quad \frac{\partial \phi}{\partial t_S} = \frac{2Mra}{\sqrt{A\Sigma\Delta}}, \quad \frac{\partial \phi}{\partial \phi_S} = \sqrt{\frac{r^2 + a^2}{A}}. \quad (8.46)$$

Based on these relations, it is also useful to define the orthonormal tetrad basis in the LNRF $\{t_S, x_S^r, x_S^\theta, x_S^\phi\}$ [234], in which the local metric takes the form of a Cartesian Minkowski metric, viz., $diag(-1, 1, 1, 1)$. The relations in Eq. 8.46 then become

$$\frac{\partial t}{\partial t_S} = \sqrt{\frac{A}{\Sigma\Delta}}, \quad \frac{\partial r}{\partial x_S^r} = \sqrt{\frac{\Delta}{\Sigma}}, \quad \frac{\partial \theta}{\partial x_S^\theta} = \frac{1}{\sqrt{\Sigma}}, \quad \frac{\partial \phi}{\partial t_S} = \frac{2Mra}{\sqrt{A\Sigma\Delta}}, \quad \frac{\partial \phi}{\partial x_S^\phi} = \sqrt{\frac{\Sigma}{A \sin^2 \theta}}. \quad (8.47)$$

Free-Fall in Kerr Geometry

For free-fall in Kerr geometry, the emitter initially at “rest” coincides with the ZAMO at $r = r_0$ with $L = 0$. The equations of motion in Eq. 8.39 then become

$$\begin{aligned} \frac{\Sigma}{E} \left(\frac{dt}{d\tau} \right) &= \frac{A}{\Delta} \\ \frac{\Sigma}{E} \left(\frac{d\phi}{d\tau} \right) &= \frac{2Mra}{\Delta} \\ \frac{\Sigma}{E} \left(\frac{d\theta}{d\tau} \right) &= \sigma_\theta \sqrt{q + a^2 \left(1 - \frac{1}{E^2} \right) \cos^2 \theta} \\ \frac{\Sigma}{E} \left(\frac{dr}{d\tau} \right) &= \sigma_r \sqrt{(r^2 + a^2)^2 - \Delta \left(\frac{r^2}{E^2} + q + a^2 \right)}. \end{aligned} \quad (8.48)$$

With the initial conditions

$$\left. \frac{\partial r}{\partial \tau} \right|_{r=r_0} = 0, \quad \left. \frac{\partial \theta}{\partial \tau} \right|_{r=r_0} = 0 \quad (8.49)$$

and the fact that for ZAMOs, from Eq. 8.47,

$$\left. \frac{dt}{d\tau} \right|_{r=r_0} = \sqrt{\frac{A}{\Sigma\Delta}}, \quad (8.50)$$

one can solve the constants of motion

$$Q = a^2(1 - E^2) \cos^2 \theta \quad (8.51)$$

and

$$E = \sqrt{\frac{\Sigma_0 \Delta_0}{A_0}} \quad (8.52)$$

where $\Sigma_0 = \Sigma(r_0)$, $\Delta_0 = \Delta(r_0)$ and $A_0 = A(r_0)$. After some algebra, the free-fall velocity can finally be shown to be

$$\frac{dr}{dt} = \frac{\Delta}{\sqrt{A}} \cdot \sqrt{1 - \frac{\Sigma \Delta / A}{\Sigma_0 \Delta_0 / A_0}} \quad (8.53)$$

which in the LNRF becomes

$$\beta_S = \sqrt{1 - \frac{\Sigma \Delta / A}{\Sigma_0 \Delta_0 / A_0}}. \quad (8.54)$$

Neutrino Trajectory

As in the Schwarzschild case, the null geodesics are characterised by the impact parameters and emission angles. Now, since the geometry is not spherically symmetric, two emission angles are required to specify the emission direction, as depicted in Figure 8.11. The emission angle ψ is reserved for the angle relative to the outward radial direction. The other emission angle η is then defined as the angle in the $\theta - \phi$ plane from the θ axis with $\eta \in [0, 2\pi)$, where \hat{n} is defined as the cross product $\hat{n} \times \hat{\psi}$ between the emission direction (\hat{n}) and the positive ψ direction ($+ \hat{\psi}$). $\eta \in (0, \pi)$ indicates a co-rotating trajectory and $\eta \in (\pi, 2\pi)$ counter-rotating.

From the equations of motion Eq. 8.39, the radial velocity can immediately be read out to be

$$\frac{dr}{dt} = \frac{\sigma_r \sqrt{RA}}{A - 2Mrab}, \quad (8.55)$$

which in the LNRF, using Eq. 8.47, can be written as

$$(v_r)_S = \frac{dx_S^r}{dt_S} = \cos \psi_S = \frac{\sigma_r \sqrt{RA}}{A - 2Mrab}. \quad (8.56)$$

The radial velocity in the free-fall frame can be expressed in the exact same form as Eq. 8.16. The velocity of the neutrino in the LNRF can then be determined by the

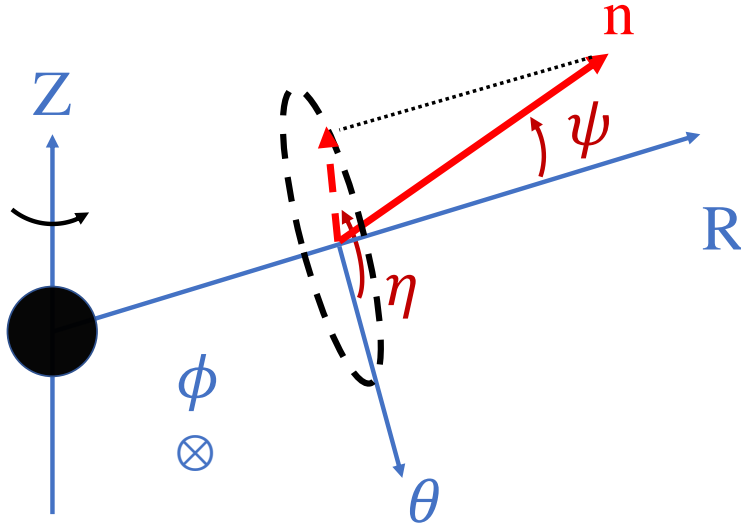


Figure 8.11: Schematic view of the definition of the emission angles ψ and η . $\eta \in (0, \pi)$ corresponds to the $+ \phi$ direction and $\eta \in (\pi, 2\pi)$ corresponds to the $- \phi$ direction.

velocity component along the θ direction^{viii}

$$(v_\theta)_S = \frac{dx_S^\theta}{dt_S} = \sin \psi_S \cos \eta_S = \frac{\sigma_\theta \sqrt{\Theta \Delta A}}{A - 2Mr_{ab}}, \quad (8.57)$$

whereas the corresponding velocity observed in the free-fall frame will be

$$(v_\theta)_{FF} = \sin \psi_{FF} \cos \eta_{FF} = \frac{\sqrt{1 - \beta_S^2} \sin \psi_S \cos \eta_S}{1 + \beta_S \cos \psi_S}. \quad (8.58)$$

Note that $\kappa = 0$ for null geodesics, so the R and Θ in Eqs. 8.55 – 8.57 are

$$\begin{aligned} R &= ((r^2 + a^2) - ab)^2 - \Delta(q + (a - b)^2) \\ \Theta &= q - \cos^2 \theta \left(\frac{b^2}{\sin^2 \theta} - a^2 \right). \end{aligned} \quad (8.59)$$

As in the case of the Schwarzschild metric, the impact parameters b and q , and, hence, the trajectory, can be inferred from the given emission direction (ψ, η) . Since

^{viii}It can, of course, also be the ϕ component, but it is slightly more laborious to work with as it involves both dt and $d\phi$ (dx_S^ϕ) as shown in Eq. 8.46 (Eq. 8.47).

the emissions are always generated in the free-fall frame, the calculation always start from the emission angles (ψ_{FF}, η_{FF}) . From these variables, one can calculate the quantities

$$\begin{aligned} B &\equiv a^2 - \frac{\Delta}{\sin^2 \theta} \\ (v_r)_S^2 &= \cos \psi_S = \frac{\cos \psi_{FF} - \beta_S}{1 - \beta_S \cos \psi_{FF}} \\ (v_\theta)_S^2 &= \sin \psi_S \cos \eta_S = \frac{\sin \psi_{FF} \cos \eta_{FF} (1 + \beta_S \cos \psi_{FF})}{\sqrt{1 - \beta_S^2}} \\ \mu^2 &\equiv (v_r)_S^2 + (v_\theta)_S^2 = \cos^2 \psi_S + \sin^2 \psi_S \cos^2 \eta_S \end{aligned} \quad (8.60)$$

from which the impact parameter can be calculated

$$b = \frac{A \left(2Mra(1 - \mu^2) - \sigma_b \sqrt{(1 - \mu^2)(4M^2r^2a^2 - AB)} \right)}{AB - 4M^2r^2a^2\mu^2}, \quad (8.61)$$

where $\sigma_b \equiv b/|b|$ is the rotating direction relative to the rotation of the black hole, and

$$q = \cos^2 \theta \left(\frac{b^2}{\sin^2 \theta} - a^2 \right) + \sin^2 \psi_S \cos^2 \eta_S \frac{(A - 2Mrab)^2}{\Delta A}. \quad (8.62)$$

8.3.2 Neutrino Travel Time

The neutrino travel time can now be calculated from Eq. 8.55 in a manner similar to Eq. 8.17

$$T(b, q, a, r_*; r_E) = \int_{t_*}^{t_E} dt = \int_{r_*}^{r_E} \frac{A - 2Mrab}{\sigma_r \sqrt{R} \Delta} dr. \quad (8.63)$$

Furthermore, since the integrand in Eq. 8.63 depends implicitly on θ via A , and θ is not in general constant, the propagation of θ along r has to be accounted for when evaluating the travel time. By equating the θ and r equations in Eq. 8.39, one can write down the propagation as

$$\begin{aligned} \int_{r_*}^r \frac{dr}{\sigma_r \sqrt{R}} &= \int_{\theta_*}^\theta \frac{d\theta}{\sigma_\theta \sqrt{\Theta}} \\ &= \int_{\cos \theta_*}^{\cos \theta} \frac{-\sigma_\theta d \cos \theta}{\sqrt{q + (a^2 - q - b^2) \cos^2 \theta - a^2 \cos^4 \theta}}. \end{aligned} \quad (8.64)$$

The time delays ΔT_\pm are carried out in the same fashion as in Eqs. 8.19 and 8.20. For the inward case, the periapsis position r_p is the largest real root of R for some given b and q .

r_*	q	$b (\sigma_r = +)$	$b (\sigma_r = -)$
$r_H < r_* < r_e^+$	$0 \leq q < 27M^2$	$b_c^- < b < b_c^+$	N/A
$r_e^+ \leq r_* < 3M$	$0 \leq q < q_*$	$b_c^- < b \leq b_{max}^+$	$b_c^+ < b < b_{max}^+$
	$q_* \leq q < 27M^2$	$b_c^- < b < b_c^+$	N/A
$3M \leq r_* < r_e^-$	$0 \leq q < q_*$	$b_c^- < b \leq b_{max}^+$	$b_c^+ < b < b_{max}^+$
	$q_* \leq q < 27M^2$	$b_{max}^- \leq b \leq b_{max}^+$	$b_{max}^- < b < b_c^-, b_c^+ < b < b_{max}^+$
	$27M^2 \leq q < q_{max}$	$b_{max}^- \leq b \leq b_{max}^+$	$b_{max}^- \leq b \leq b_{max}^+$
$r_* \geq r_e^-$	$0 \leq q < 27M^2$	$b_{max}^- \leq b \leq b_{max}^+$	$b_{max}^- < b < b_c^-, b_c^+ < b < b_{max}^+$
	$27M^2 \leq q < q_{max}$	$b_{max}^- \leq b \leq b_{max}^+$	$b_{max}^- \leq b \leq b_{max}^+$

Table 8.1: Null geodesic escape conditions in Kerr geometry of a disc model. Table adapted from [236]. r_H is the event horizon.

Escape Conditions

The escape conditions for the Kerr metric are much more complicated than those for the Schwarzschild metric and entail a number of cases, which are tabulated in [237] for a full Kerr space and [236] for a disc model.

Whilst the relations thus far derived are generally applicable to the entire Kerr space, the results will only be calculated for the case of emissions from an equatorial disc, namely $\theta_* = \pi/2$, to reduce computation time. Therefore, the discussions in this section will only focus on the escape conditions of the disc model, in which the collapsing surface would become a ring of matter. Table 8.1 lists the escape conditions from [236]. Moreover, the discussion will only consider the case of $a > 0$ as it will simply become the Schwarzschild metric when $a = 0$.

By observing the integrand of Eq. 8.63, one immediately identifies two conditions that would lead to the divergence of the integrand: $\Delta = 0$ and $R = 0$. These two conditions correspond to the two conditions in the Schwarzschild case, where $\Delta = 0$ is evidently the event horizon and $R = 0$ is the equivalent of $r^3 - b^2(r - 2M) = 0$.

Suppose one is to consider the restrictions on b first. For some given q , one can obtain the photon sphere^{ix} by solving $R = 0$ and $\partial R / \partial r = 0$, which results in the

^{ix}Note that in the rotating case it is not exactly a sphere any more.

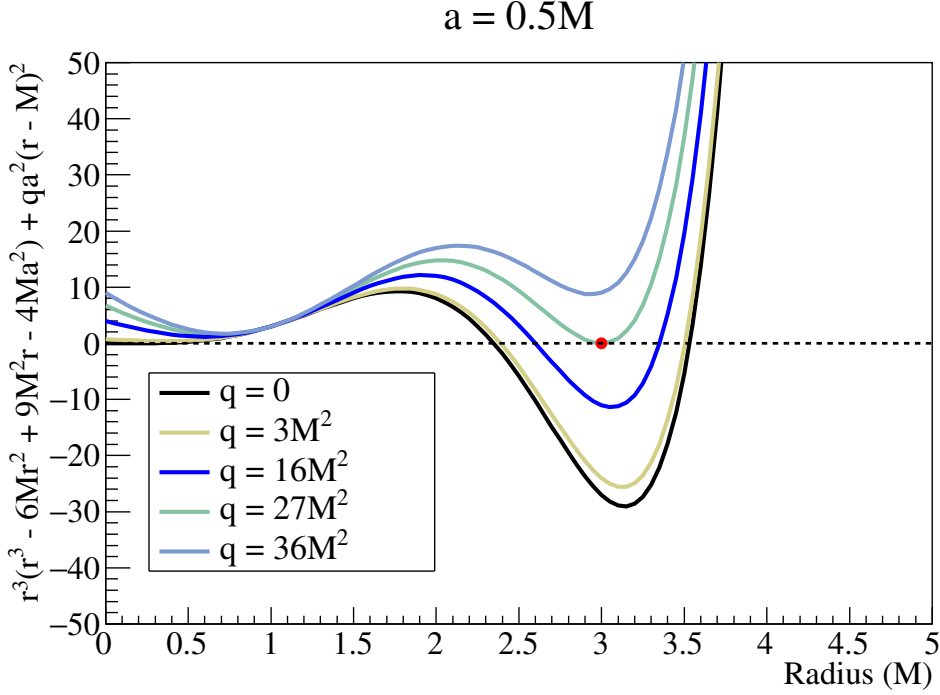


Figure 8.12: Behaviour of $r^3(r^3 - 6Mr^2 + 9M^2r - 4Ma^2) + qa^2(r - M)^2 = 0$ with $a = 0.5M$ at different q values. Real roots, corresponding to r_c^\pm , only exist when $q \leq 27M^2$.

relations

$$q = -\frac{r_c^3(r_c^3 - 6Mr_c^2 + 9M^2r_c - 4Ma^2)}{a^2(r_c - M)^2} \quad (8.65)$$

and

$$b_c = -\frac{r_c\Delta - M(r_c^2 - a^2)}{a(r_c - M)} \quad (8.66)$$

where r_c is the critical radius which can be solved from Eq. 8.65 and b_c the critical impact parameter, corresponding to the $3\sqrt{3}M$ in the Schwarzschild case. From Figures 8.12 and 8.13, one will notice a boundary at $q = 27M^2$, at which the co-rotating and counter-rotating critical radii coincide at $r = 3M$. For $q < 27M^2$, there will always be at least two real roots where the smaller root, denoted by r_c^+ , is the critical radius for co-rotation and the larger root, denoted by r_c^- , for counter-rotation. On the other hand, if $q > 27M^2$, there will be in general no critical radii at all. This is not to say that the emissions will plunge into the black hole. In fact, the opposite is true: $R = 0$ will always have a real root in the range $r \geq 3M$ regardless of the b value when $q \geq 27M^2$, viz., a periapsis always exists.

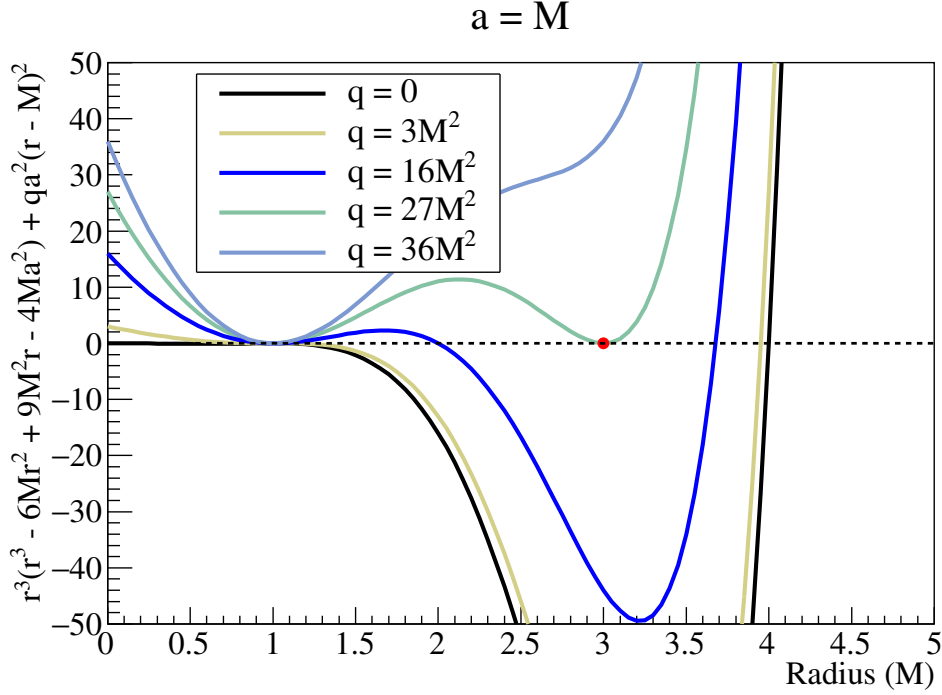


Figure 8.13: Behaviour of $r^3(r^3 - 6Mr^2 + 9Mr^2 - 4Ma^2) + qa^2(r - M)^2 = 0$ with $a = M$ at different q values. $r = M$ is a root regardless of the q value. When $q > 27M^2$, $r = M$ will be the only real root. When $q \leq 27M^2$, there will be an extra pair of real roots corresponding to r_c^\pm . When $q = 3M^2$, the root for r_c^+ will coincide with $r = M$ and will fall behind it if $q < 3M^2$.

At any given a , the extremal critical radii r_e^\pm will happen when $q = 0$, and can be expressed as

$$r_e^\pm = 2M \left(1 + \cos \left(\frac{2}{3} \arccos \left(\frac{\mp a}{M} \right) \right) \right). \quad (8.67)$$

Note that in the case of extreme rotation $a = M$, as shown in Figure 8.13, the co-rotation critical radius will fall behind $r = M$, the event horizon, when $q < 3M^2$, and, hence, the r_c^+ will effectively be at $r = M$.

These critical radii will lead to the escape conditions similar to those of the non-rotating case. For $r \leq r_c$, only outward directed geodesics with $|b| < |b_c|$ will escape. For $r > r_c$, all outward travelling geodesics and inward travelling geodesics of $|b_c| < |b| \leq |b_{max}|$ will reach infinity, where b_{max} can be solved from $R = 0$ by rearranging the equation as an quadratic equation of b

$$(2Mr - r^2)b^2 - 4Mrab + (r^4 + (a^2 - q)r^2 + 2M(a^2 + q)r - a^2q) = 0 \quad (8.68)$$

resulting in

$$b_{max}^{\pm} = \frac{-2Mar \pm \sqrt{r\Delta(r^3 - q(r - 2M))}}{r(r - 2M)}. \quad (8.69)$$

In order to make sure b_{max} is real, the condition $r^3 - q(r - 2M) \geq 0$ has to be imposed on q . With the experience from the Schwarzschild case, one can immediately conclude that $q < 27M^2$ for $r \leq 3M$ and $q \leq q_{max}$ for $r > 3M$, where

$$q_{max} = \sqrt{\frac{r^3}{r - 2M}}. \quad (8.70)$$

Furthermore, the fact that $\theta_* = \pi/2$ leads to a restriction on q

$$\Theta(\theta = \theta_*) = q - \cos^2 \theta_* \left(\frac{b^2}{\sin^2 \theta_*} - a^2 \right) = q \geq 0. \quad (8.71)$$

Finally, there is one last notable value of q , which is $q_* = q(r_c = r_*)$. At this q value, the emission radius coincides with one of the critical radii: $r_* = r_c^+$ for $r_* \leq 3M$ and $r_* = r_c^-$ for $r_* > 3M$. With all these special values identified, the escape conditions as in Table 8.1 follow simply.

Emission Angle and Travel Time

The time delays ΔT , defined as in the non-rotating case and plotted against the emission angles in the free-fall frame (ψ_{FF}, η_{FF}) for the cases of $a = 0.5M$ and $a = M$, are shown in Figure 8.14. In each case, the rotation is in the direction of increasing azimuthal angle ϕ . The overall behaviour of the time delays is, in general, quite similar to that of the case of a non-rotating black hole: increased time delays at larger ψ_{FF} , and escape cone contraction alongside the collapse. The boundary between the white and black regions in Figure 8.14 indicates the critical emission directions of divergent time delays, and so the trajectories in the white region dive into the black hole. Nonetheless, the presence of rotation introduces an asymmetry in the emission directions. As mentioned earlier, the emissions with $\eta_{FF} \in (0, \pi)$ are classified as co-rotating and $\eta_{FF} \in (\pi, 2\pi)$ as counter-rotating. From Figure 8.14, one notices that at each given ψ_{FF} the counter-rotations tend to induce relatively longer time delays. Figure 8.15 illustrates an example path of a counter-rotating geodesic.

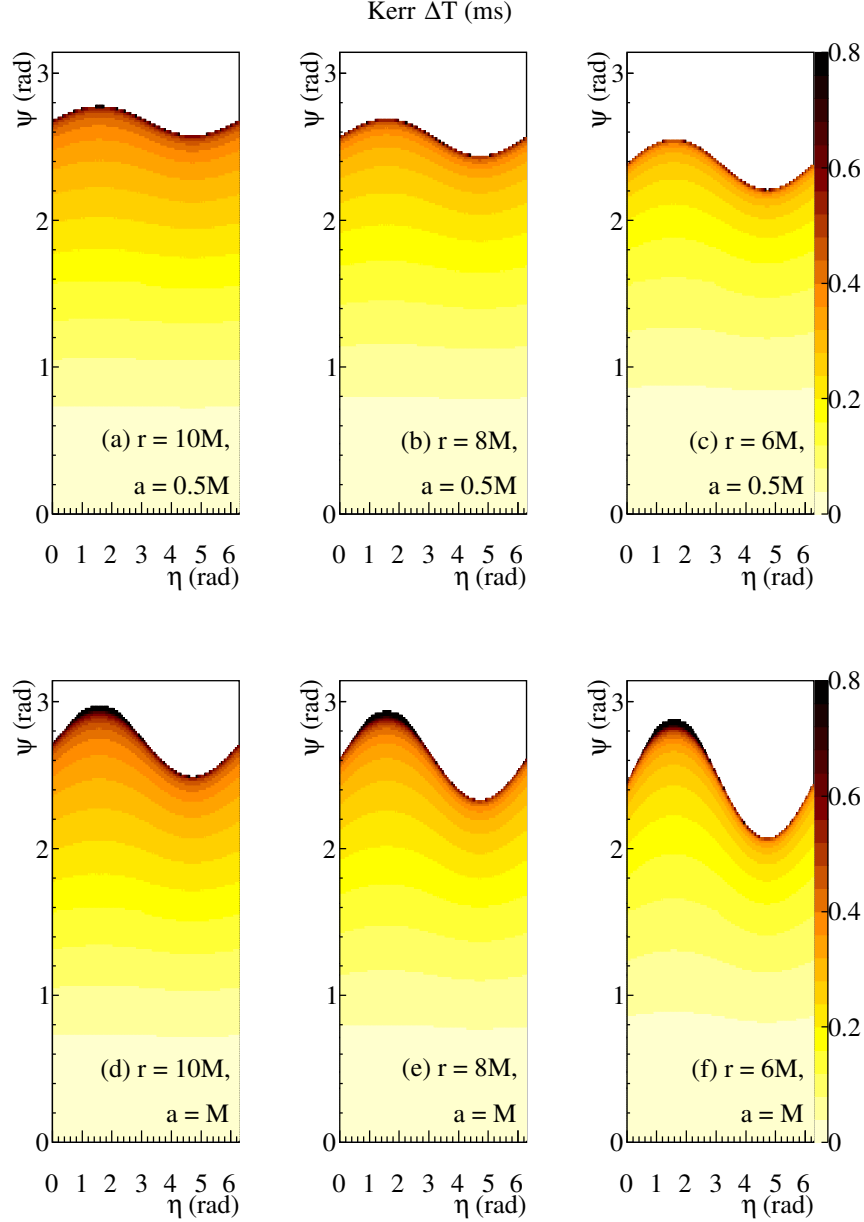


Figure 8.14: Time delays relative to that of the radial direction, as a function of the emission direction in the free-fall frame, at different emission radii for a collapsing ring around a rotating black hole. The white region at large ψ_{FF} indicates plunging directions, and the border between the white and black regions is the photon sphere. The black hole mass is $M = 2.5M_\odot$, and the ring starts from rest at $10M$. Top row: sub-extreme rotation $a = 0.5M$. Bottom row: extreme rotation $a = M$.

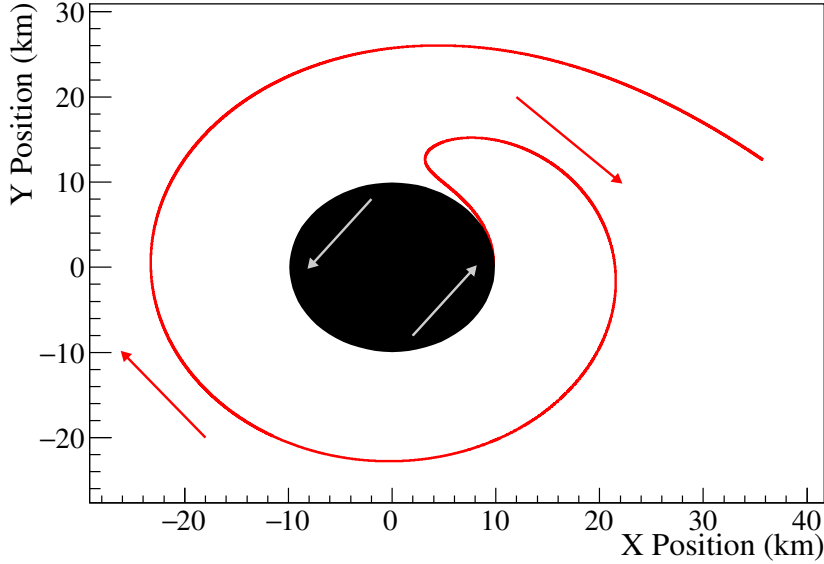


Figure 8.15: An example counter-rotating null geodesic emitted close to the event horizon of a rotating black hole. Near the event horizon the strong local frame dragging causes the geodesics to appear in the same direction as the black hole rotation in the coordinate frame, though not so in the LNRF.

8.3.3 Redshift

The redshift of the neutrino emissions from the collapsing surface in the case of a rotating black hole can be derived in a manner similar to the non-rotating case. The redshift can, again, be factored into contributions from gravitational redshift and Doppler shift, in which the Doppler shift component remains unaltered. It is the gravitational redshift in Kerr spacetime that is to be derived.

Following the standard derivation of gravitation redshift in Schwarzschild spacetime [222, 238], one starts out by considering two ZAMOs at r_* and r_E . The four-velocity of the ZAMO shown in Eq. 8.43 can be expressed explicitly as

$$Z^a = Z_0 \left(\left(\frac{\partial}{\partial t} \right)^a - \frac{g_{t\phi}}{g_{\phi\phi}} \left(\frac{\partial}{\partial \phi} \right)^a \right) = \sqrt{\frac{A}{\Delta\Sigma}} \left(\frac{\partial}{\partial t} \right)^a + \frac{2Mr a}{\sqrt{A\Sigma\Delta}} \left(\frac{\partial}{\partial \phi} \right)^a. \quad (8.72)$$

The four-wavevector k^a of the neutrino, on the other hand, will be the tangent vector of the null geodesic [222, 238]

$$k^a = \frac{dx^\mu}{d\tau} \left(\frac{\partial}{\partial x^\mu} \right)^a. \quad (8.73)$$

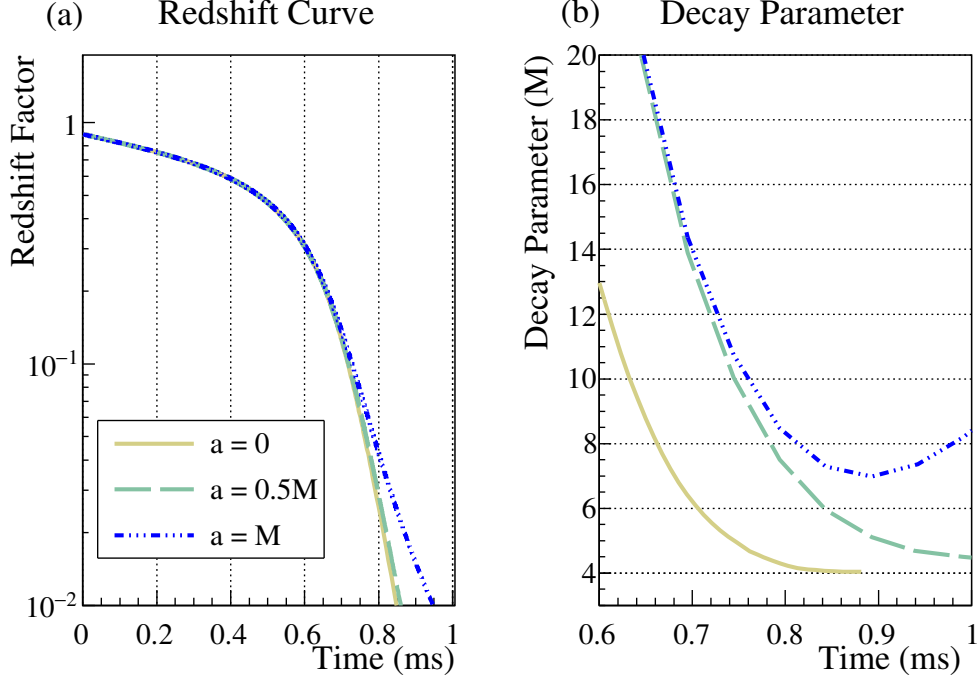


Figure 8.16: (a) Redshift factor and (b) redshift decay parameter of radial emissions for non-rotating ($a = 0$), moderately rotating ($a = 0.5M$) and extremal ($a = M$) Kerr black holes.

Subsequently, the observed energy by the ZAMO becomes

$$\begin{aligned}
 \nu &= k^a Z_a = k^a \cdot Z_0 \left(-\frac{\Sigma \Delta}{A} \right) (dt)_a \\
 &= \frac{dt}{d\tau} \cdot Z_0 \left(-\frac{\Sigma \Delta}{A} \right) \\
 &= \frac{A - 2Mrab}{\Sigma \Delta} E \cdot \sqrt{\frac{A}{\Sigma \Delta}} \left(-\frac{\Sigma \Delta}{A} \right) \\
 &= -E \cdot \sqrt{\frac{A}{\Sigma \Delta}} \left(1 - \frac{2Mra}{A} b \right),
 \end{aligned} \tag{8.74}$$

and the gravitation redshift ($r_E \gg r_*$)

$$\frac{\nu_E}{\nu_S} \approx \sqrt{\frac{\Sigma \Delta}{A}} \left(1 - \frac{2Mra}{A} b \right)^{-1}. \tag{8.75}$$

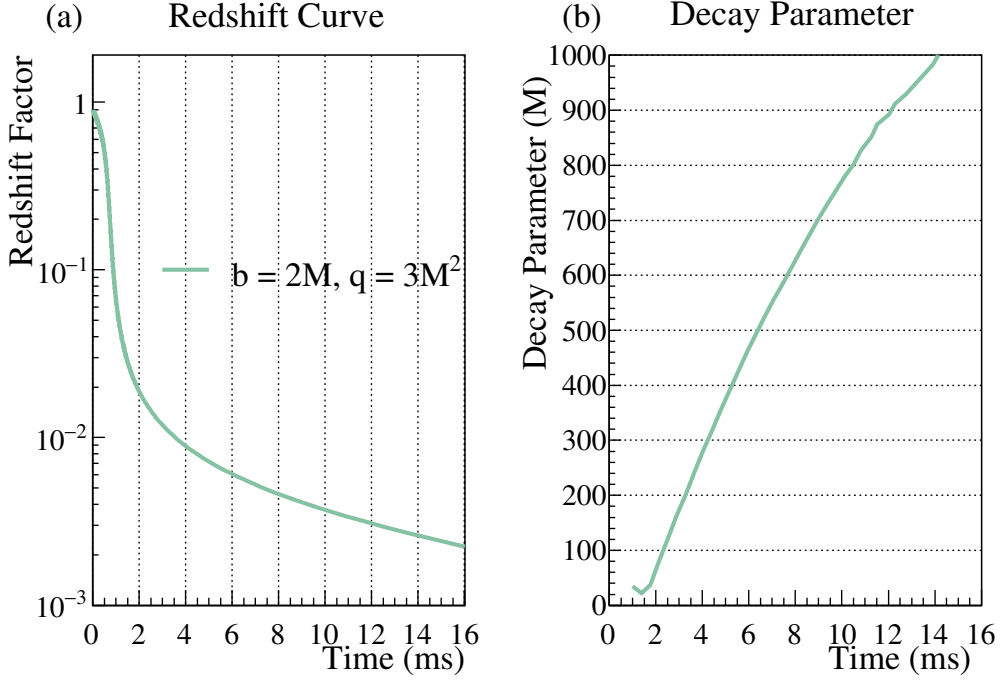


Figure 8.17: (a) Redshift factor and (b) redshift decay parameter of critical emissions with $b = 2M$ and $q = 3M^2$, for orbits near the horizon at $r_H = M$, plotted against observation time for a $2.5M_\odot$ extremal ($a = M$) Kerr black hole.

As a result, the overall redshift will be of the form

$$\zeta(b, q, r_*, \sigma_r) = \frac{\nu_E}{\nu_*} = \sqrt{\frac{\Sigma\Delta}{A}} \left(1 - \frac{2Mra}{A}b\right)^{-1} \times \frac{\sqrt{1 - \beta_S^2}}{1 + \beta_S \cos \psi_S}. \quad (8.76)$$

An important difference of the rotating redshift from that of the non-rotating case is that it no longer approaches an exponential of constant decay parameter, as shown in Figures 8.16 and 8.17. It is most clear from the case of radial emissions, Figure 8.16, that the stronger the rotation is, the more it deviates from the exponentials described in Section 8.2.3. Furthermore, the much slower decline in the redshift curve of the critical emissions in Figure 8.17 hints at a further softening in the cut-off.

8.3.4 Ray Tracing and Luminosity Profile

The final luminosity profile is generated using the same ray-tracing Monte Carlo approach with some of the expressions updated. As mentioned in Section 8.3.2, the emitters are confined to the equatorial plane, and thus takes the form of a collapsing ring. The resulting cut-off profiles are shown in Figures 8.18 and 8.19. From Figure 8.18, one notices that rotation in general extends the tail of the cut-off profile. When compared to the Schwarzschild case, the extension of the tail in the moderate rotation case ($a = 0.5M$) is not evident. The extreme case ($a = M$), on the contrary, exhibits a much more significant modification, which is consistent with the observations in Figure 8.16. It is also evident from Figure 8.19 that the effects are mainly from the geodesics that appear to be directed inwards in the free-fall frame, whilst travelling outwards in the LNRF. Similar to observations in the redshift curves, the decay parameter of the cut-off profile does not approach a limiting value, but rather continues to increase in a manner that may be noticeable even before the time when neutrinos are redshifted below detectable energies.

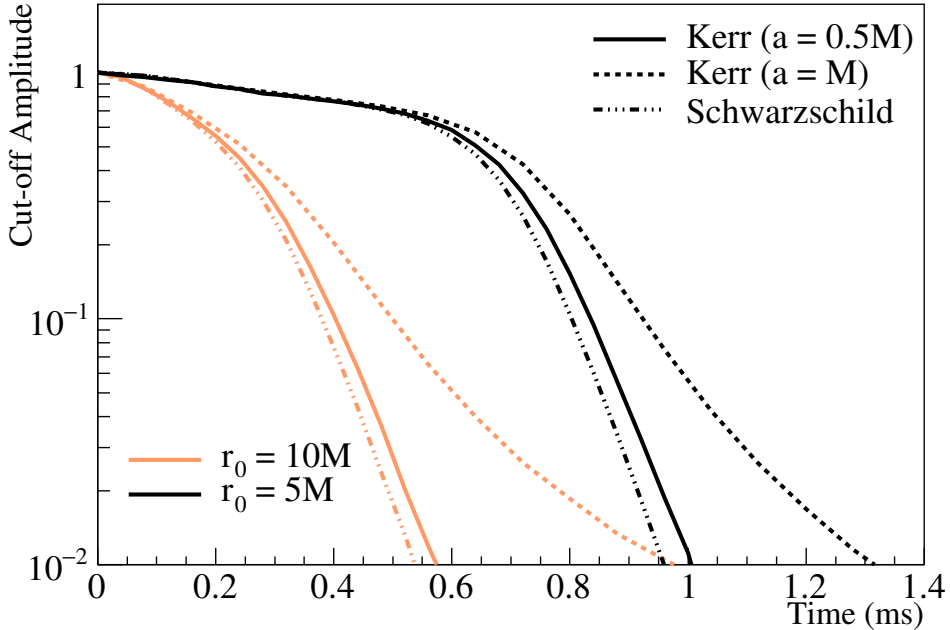


Figure 8.18: Luminosity profiles of the neutrino cutoff in Kerr geometry, with $a = 0.5M$ and $a = M$, and at different initial radii $5M$ and $10M$.

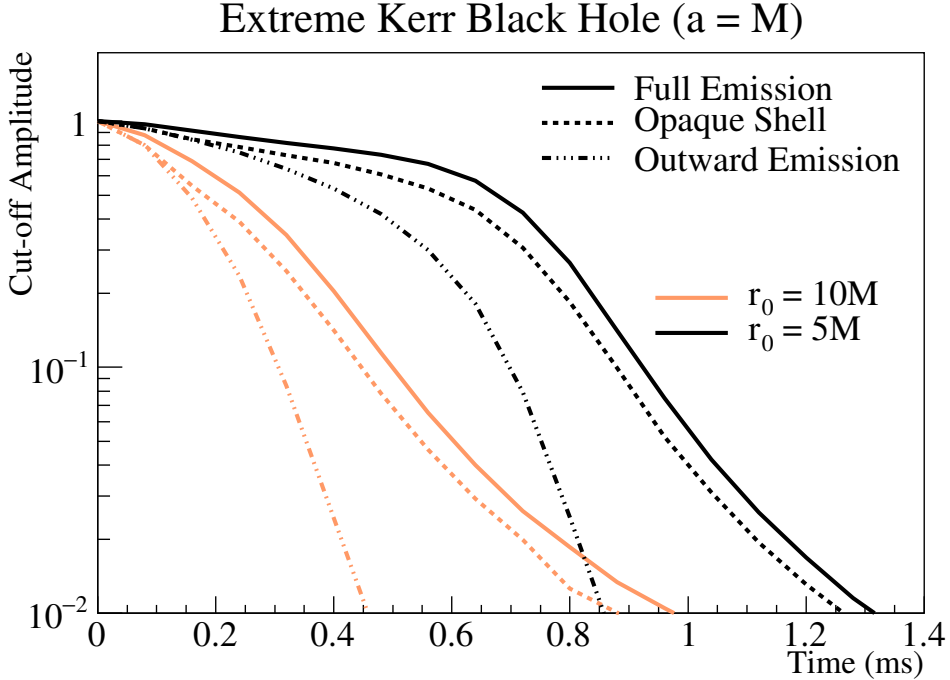


Figure 8.19: The three inward emission scenarios in an extreme Kerr black hole: transparent medium, with emissions allowed in all directions (solid); opaque inner medium, allowing only emissions which are outward in the free-fall frame (dotted); and allowing only emissions which are outward in the LNRF frame (dashed-dotted).

8.4 Measurement of the Black Hole Cut-Off

As demonstrated in Section 8.2, one of the most prominent features of the luminosity profile upon the formation of a non-rotating black hole is the universal exponential of decay parameter $3\sqrt{3}M$. To estimate the number of neutrino events that may be available for resolving the decay parameter, the cut-off profile is reduced to a constant pre-collapse luminosity followed by a simple exponential tail, neglecting the smooth transition of tenths of milliseconds as seen in Figure 8.6 and elsewhere. The number of events is simply calculated by integrating the exponential component.

As an example, the $40M_\odot$ model from Section 8.2.5 is invoked, assuming a distance of 10 kpc. A list of the event rates of possible neutrino detectors can be found in [239]. For Super-Kamiokande [240] and JUNO [205], one may expect to see an event rate of around 15 per millisecond before the cut-off, followed by a tail of approximately 0.7 events, which is an event yield unlikely to result in a measurement yet large enough to introduce a systematic uncertainty. This uncertainty

would affect applications such as the last-event method for multi-detector CCSN triangulation mentioned in Section 7.3.5. On the other hand, in the case of Hyper-Kamiokande [241], the estimated event rate would become roughly 100 events per millisecond before the sharp cut-off, followed by a tail of 5 events. This may very well lead to a crude measurement even taking into consideration the uncertainty in the starting time of the exponential. It is worth noting, nonetheless, that these late time events are likely to be mixed with those originating from other effects, for instance, an “echo” of neutrinos scattering off infalling material as explored in [239].

For rotating black holes, on the other hand, we note that the effect of rotation in the moderate case of $a = 0.5M$ is rather mild. The event yield of the exponential tail only sees an increase of about 20%. Nonetheless, the event yield increases rapidly with the increase in angular momentum. For the extreme case of $a = M$, the expected event yield doubles in the tail with respect to the non-rotating case. The detection of such deviations from the exponential tail provides a potential approach for measuring the rotation of the black hole.

8.5 Summary

In this chapter, the contribution of non-radial neutrino emissions to the neutrino luminosity profile expected upon black hole formation within a CCSN has been investigated. The toy model calculation based on null geodesic ray-tracing from a collapsing shell of matter, or ring, demonstrates that the cut-off profile starts out, in general, with a relatively slower decrease over several tenths of milliseconds, depending on the collapse velocity profile, and is then followed by a steep decline.

In the Schwarzschild case, the rapid decrease approaches an exponential of decay parameter $3\sqrt{3}M$, which is what was predicted by Podurets in the 1960s [207]. This exponential behaviour of the luminosity profiles persists across different modifications of the model, indicating that all such models end up with the long-lasting leakages from near the photon sphere. If this part of the cut-off can be resolved in time, it would represent an independent handle on the mass of the newly formed black hole.

In the case of a rotating black hole, it is discovered that even for rotations as large as $a = 0.5M$ the effect of rotation only introduces a mild softening to the cut-off profile, which does not lead to any noticeable modification to the decay parameters. As the black hole further spins up, however, the effect of rotation rapidly increases. When it reaches the extreme case ($a = M$), the tail will be significantly extended by the leakage from the critical orbits. Although it is usually considered unlikely, the case of extreme rotation highlights the desirability of resolving the shape of the cutoff, not just to measure rotation [242], but also to gauge the validity of using the time constant as a mass measurement.

This study is clearly very simplistic, it nonetheless suggests that in the observation of an abrupt drop in neutrino emission from a CCSN, signalling the formation of a black hole, it is worth examining the shape of the cut-off in more detail from both theoretical and observational perspectives. The advent of the next generation of larger detectors, as well as the combination of detectors via SNEWS, places such measurements in an increasingly feasible position.

Chapter 9

Conclusion

The main theme of this thesis is the detection of core-collapse supernovae (CCSNe) via the copious amount of neutrinos emitted in such events.

As a representative case of detecting supernova signals with neutrino detectors, the sensitivity of SNO+ to supernova neutrinos was investigated in this thesis. The analysis involved the complications of the evolving configuration during the water-to-scintillator transition and the varying radioactive background levels. With the bismuth-polonium (BiPo) coincidence identification, the internal ^{238}U and ^{232}Th chain concentrations were measured to be $(4.6 \pm 1.2) \times 10^{-17} \text{ g/g}$ and $(4.8 \pm 0.9) \times 10^{-17} \text{ g/g}$, respectively. Furthermore, the ^{214}Bi - ^{214}Po pairs served as a calibration source to evaluate the light yield level of the configuration. Having determined the background and light yield levels of the detector, a multi-threshold neutrino burst trigger was developed to detect supernovae by identifying the burst of neutrinos with relatively higher energies. Based on the simulated neutrino fluxes of [91, 132, 144], it was discovered that the SNO+ burst trigger, in the full-scintillator configuration, is able to maintain sensitivity greater than 50% at 100 kpc for most of the studied supernova models, excepting only the electron-capture supernova model (shen-s8.8). It should also be noted that the BiPo studies, whilst proven to be useful in supernova studies, is itself an essential part in achieving the main physics goal of the SNO+ experiment, as the ^{238}U and ^{232}Th chains constitute a sizeable fraction of the expected backgrounds for neutrinoless double beta decay ($0\nu\beta\beta$).

Besides the detection of higher energy neutrino bursts, the identification of inverse beta decays (IBD) is perhaps the most important handle for detecting supernova neutrinos. The coincident nature of the IBD guarantees the purity of the signals. With the coincidence tagging structure established in the BiPo studies, IBDs can be identified without much trouble in SNO+. By taking the identification of 2 IBD events within 10 s as the measure of the maximum sensitivity of SNO+, the sensitivity of the shen-s8.8 model at 100 kpc will be raised from 10% to about 45%, and the other

models above 90%. The only problem is that the identification of IBDs, just as with any coincidence identification, involves the spatial correlation between the prompt and delayed events, which usually relies on time-consuming position reconstruction. The **TimeCentroid** algorithm based on the comparison of the PMT hit patterns was, therefore, developed. **TimeCentroid** was able to achieve the same level of efficiency as the position reconstruction algorithms at the cost of only a few percent increase in the misidentification rate, and reduces the CPU time by three orders of magnitude. The implementation of this method, thus, enables a more prompt response in the measurements of pre-supernova and supernova $\bar{\nu}_e$, which are often constrained of time.

In addition, the relatively higher energy emission and high purity of the IBD signal makes it the common signal amongst water and scintillator detectors. This sets a common ground for the comparison of detected neutrino signals between neutrino detectors across the globe. One major application of such comparisons is the positioning of supernovae via multi-detector triangulation, which is valuable in guiding the subsequent electromagnetic wave and possible gravitational wave observations. The central part of this study is the determination of the detection time difference between a pair of neutrino detectors. A novel method of neutrino light curve matching, which exploits the underlying similarity between the observed $\bar{\nu}_e$ light curves, was developed to determine such time differences. Using, again, the supernova models in [91, 132, 144], this method was able to reduce the uncertainties from 5.7 ms [196] to 3.4 ms for the shen-s8.8 model and from 2.7 ms [197] to 1.8 ms for the $27M_\odot$ CCSN model (ls220-s27.0co). The method has also showed low biases in all cases and demonstrated robustness against possible backgrounds. During the study, it was discovered that the resolution power largely comes from the large derivatives of the time profiles.

Following this observation, it was noticed when examining the two $40M_\odot$ models that the sharp edge associated with black hole formation provided additional resolution power. This perfect cut-off is, however, an artifact of the termination of the simulations upon black hole formation. The actual cut-off associated with the formation of a black hole is expected to approach an exponential of decay constant $3\sqrt{3}M$ [207]. In this thesis, a ray-trace study was performed to give a comprehensive account on the effects of the contributions from non-radial neutrino emissions upon the formation of a non-rotating black hole. This extended tail introduces systematic uncertainties to the degree of how well one can localise the cut-off in time. Furthermore, the measurement of the asymptotic decay constant could possibly constitute an independent approach for the determination of the black hole mass.

Finally, this thesis also presents the first ray-tracing study on rotating black holes using the Kerr metric, with much of the formulation originally derived. The introduction of rotation was found to further extend the cut-off profile, and deviates from

the asymptotic exponential behaviour. This deviation provides a potential way of gauging the rotation of the black hole. With the next-generation large neutrino detectors, measurements to resolve the black hole cut-off profile are becoming increasingly attainable.

References

- [1] S. Al Kharusi *et al.*, “SNEWS 2.0: a Next-Generation Supernova Early Warning System for Multi-Messenger Astronomy,” *New J. Phys.*, vol. 23, p. 031201, 2021.
- [2] SNO+ Collaboration, “Current Status and Future Prospects of the SNO+ Experiment,” *Adv. High Energy Phys.*, vol. 2016, p. 6194250, 2016. arXiv: 1508.05759.
- [3] J. Wang, J. Tseng, S. Gullin, and E. O’Connor, “Non-Radial Neutrino Emission upon Black Hole Formation in Core Collapse Supernovae,” *Phys. Rev. D*, vol. 104, p. 104030, 2021. arXiv: 2109.11430 [astro-ph.HE and gr-qc].
- [4] S. Langrock, “Measurement of the Rayleigh Scattering Length and Background contributions during early data taking phases at SNO+,” Ph.D. dissertation, Queen Mary University of London, 2016.
- [5] M. Rigan, “SNO+ Supernova Sensitivity During Pure Scintillator Phase, Supernova Burst Trigger and PMT Calibration with TELLIE,” Ph.D. dissertation, University of Sussex, 2021.
- [6] C. Jensen, *Controversy and Consensus: Nuclear Beta Decay 1911-1934*. Springer Basel AG, 2000.
- [7] W. Pauli, “Pauli Letter Collection: Letter to Lise Meitner,” [Online]. Available: <https://cds.cern.ch/record/83282>.
- [8] E. Fermi, “Versuch einer Theorie der β -Strahlen. I,” *Z. Physik*, vol. 88, pp. 161–177, 1934.
- [9] C. Giunti and C. W. Kim, *Fundamentals of Neutrino Physics and Astrophysics*. Oxford University Press, 2007.
- [10] E. J. Konopinski and H. M. Mahmoud, “The Universal Fermi Interaction,” *Phys. Rev.*, vol. 92, p. 1045, 1953.
- [11] F. Reines and C. L. Cowan, “The Neutrino,” *Nature*, vol. 178, p. 446, 1956.

- [12] G. Danby *et al.*, “Observation of High-Energy Neutrino Reactions and the Existence of Two Kinds of Neutrinos,” *Phys. Rev. Lett.*, vol. 9, pp. 36–44, 1962.
- [13] M. L. Perl *et al.*, “Evidence for Anomalous Lepton Production in e^+e^- Annihilation,” *Phys. Rev. Lett.*, vol. 35, pp. 1489–1492, 1975.
- [14] K. Kodama *et al.*, “Observation of Tau Neutrino Interactions,” *Phys. Lett. B*, vol. 504, pp. 218–224, 2001.
- [15] C. S. Wu *et al.*, “Experimental Test of Parity Conservation in Beta Decay,” *Phys. Rev.*, vol. 105, p. 1413, 1957.
- [16] R. L. Garwin, L. M. Lederman, and M. Weinrich, “Observations of the Failure of Conservation of Parity and Charge Conjugation in Meson Decays: the Magnetic Moment of the Free Muon,” *Phys. Rev.*, vol. 105, p. 1415, 1957.
- [17] J. I. Friedman and V. L. Telegdi, “Nuclear Emulsion Evidence for Parity Nonconservation in the Decay Chain $\pi^+ \rightarrow \mu^+ \rightarrow e^+$,” *Phys. Rev.*, vol. 106, p. 1290, 1957.
- [18] T. D. Lee and C. N. Yang, “Parity Nonconservation and a Two-Component Theory of the Neutrino,” *Phys. Rev.*, vol. 105, p. 1671, 1957.
- [19] L. Landau, “On the Conservation Laws for Weak Interactions,” *Nucl. Phys.*, vol. 3, pp. 127–131, 1957.
- [20] A. Salam, “On Parity Conservation and Neutrino Mass,” *Nuovo Cim.*, vol. 5, pp. 299–301, 1957.
- [21] M. Goldhaber, L. Grodzins, and A. W. Sunyar, “Helicity of Neutrinos,” *Phys. Rev.*, vol. 109, pp. 1015–1017, 1958.
- [22] B. Pontecorvo, “Mesonium and Anti-Mesonium,” *Sov. Phys. JETP*, vol. 6, p. 429, 1957.
- [23] Z. Maki, M. Nakagawa, and S. Sakata, “Remarks on the Unified Model of Elementary Particles,” *Prog. Theor. Phys.*, vol. 28, p. 870, 1962.
- [24] S. Eliezer and A. R. Swift, “Experimental Consequences of Electron Neutrino Muon Neutrino Mixing in Neutrino Beams,” *Nucl. Phys. B*, vol. 105, pp. 45–51, 1976.
- [25] H. Fritzsch and P. Minkowski, “Vector-Like Weak Currents, Massive Neutrinos, and Neutrino Beam Oscillations,” *Phys. Lett. B*, vol. 62, pp. 72–76, 1976.
- [26] S. M. Bilenky and B. Pontecorvo, “Again on Neutrino Oscillations,” *Lett. Nuovo Cim.*, vol. 17, p. 569, 1976.

- [27] Q. R. Ahmad *et al.*, “Measurement of the Rate of $\nu_e + d \rightarrow p + p + e^-$ Interactions Produced by ${}^8\text{B}$ Solar Neutrinos at the Sudbury Neutrino Observatory,” *Phys. Rev. Lett.*, vol. 87, p. 071 301, 2001.
- [28] Y. Fukuda *et al.*, “Evidence for Oscillation of Atmospheric Neutrinos,” *Phys. Rev. Lett.*, vol. 81, pp. 1562–1567, 1998.
- [29] O. V. Lychkovskiy, “Neutrino Oscillations: Deriving the Plane-Wave Approximation in the Wave-Packet Approach,” *Phys. At. Nucl.*, vol. 72, pp. 1557–1559, 2009. arXiv: 0901.1198 [hep-ph].
- [30] L. L. Chau and W. Y. Keung, “Comments on the Parametrization of the Kobayashi-Maskawa Matrix,” *Phys. Rev. Lett.*, vol. 53, p. 1802, 1984.
- [31] S. Eidelman *et al.*, “Review of Particle Physics,” *Phys. Lett. B*, vol. 592, p. 1, 2004.
- [32] I. Esteban *et al.*, “The Fate of Hints: Updated Global Analysis of Three-Flavor Neutrino Oscillations,” *JHEP*, vol. 09, p. 178, 2020.
- [33] L. Stodolsky, “When the Wavepacket is Unnecessary,” *Phys. Rev. D*, vol. 58, p. 036 006, 1998.
- [34] A. D. Dolgov *et al.*, “Oscillations of Neutrinos Produced and Detected in Crystals,” *Nucl. Phys. B*, vol. 729, pp. 79–94, 2005. arXiv: 0505251 [hep-ph].
- [35] H. J. Lipkin, “Quantum Theory of Neutrino Oscillations for Pedestrians - Simple Answers to Confusing Questions,” *Phys. Lett. B*, vol. 642, pp. 366–371, 2006.
- [36] J. Beringer *et al.*, “Review of Particle Physics,” *Phys. Rev. D*, vol. 86, p. 010 001, 2012.
- [37] E. M. Lipmanov, “Quasi-Degenerate Neutrino Masses in Terms of Mass-Squared Differences,” *Phys. Lett. B*, vol. 567, pp. 268–272, 2003.
- [38] L. Wolfenstein, “Neutrino Oscillations in Matter,” *Phys. Rev. D*, vol. 17, p. 2369, 1978.
- [39] S. P. Mikheyev and A. Yu. Smirnov, “Resonance Amplification of Oscillations in Matter and Spectroscopy of Solar Neutrinos,” *Sov. J. Nucl. Phys.*, vol. 42, pp. 913–917, 1985.
- [40] S. P. Mikheyev and A. Yu. Smirnov, “Resonant Amplification of ν Oscillations in Matter and Solar-Neutrino Spectroscopy,” *Nuovo Cim. C*, vol. 9, pp. 17–26, 1986.
- [41] J. Xu *et al.*, “Detection of Supernova Neutrinos on the Earth for Large θ_{13} ,” *Commun. Theor. Phys.*, vol. 61, p. 226, 2014.

- [42] D. R. Williams, “Sun fact sheet,” 2013. [Online]. Available: <http://nssdc.gsfc.nasa.gov/planetary/factsheet/sunfact.html>.
- [43] A. S. Dighe and A. Yu. Smirnov, “Identifying the Neutrino Mass Spectrum from the Neutrino Burst from a Supernova,” *Phys. Rev. D*, vol. 62, p. 033 007, 2000.
- [44] H. Weyl, “Gravitation and the Electron,” *Proc. Natl. Acad. Sci. USA*, vol. 15, pp. 323–334, 1929.
- [45] S. M. Bilenky, “The History of Neutrino Oscillations,” *Phys. Scr.*, vol. 2005, p. 17, 2005.
- [46] E. Majorana, “Theory of the Symmetry of Electrons and Positrons,” *Nuovo Cim.*, vol. 14, pp. 171–184, 1937.
- [47] P. Minkowski, “ $\mu \rightarrow e\gamma$ at a Rate of One Out of 1-Billion Muon Decays?” *Phys. Lett. B*, vol. 67, p. 421, 1977.
- [48] M. Gell-Mann, P. Ramond, and R. Slansky, “Complex Spinors and Unified Theories,” in *Supergravity: proceedings of the Supergravity Workshop at Stony Brook*, North-Holland Publishing Company, 1979, pp. 315–321.
- [49] R. N. Mohapatra and G. Senjanovic, “Neutrino Mass and Spontaneous Parity Non-Conservation,” *Phys. Rev. Lett.*, vol. 44, p. 912, 1980.
- [50] S. Dell’Oro *et al.*, “Neutrinoless Double Beta Decay: 2015 Review,” *Adv. High Energy Phys.*, vol. 2016, p. 2 162 659, 2016.
- [51] M. Goeppert-Mayer, “Double Beta-Disintegration,” *Phys. Rev.*, vol. 48, pp. 512–516, 1935.
- [52] S. R. Elliott, A. A. Hahn, and M. K. Moe, “Direct Evidence for Two-Neutrino Double Beta Decay in ^{82}Se ,” *Phys. Rev. Lett.*, vol. 59, pp. 2020–2023, 1987.
- [53] C. Patrignani *et al.*, “Review of Particle Physics,” *Chin. Phys. C*, vol. 40, p. 10 001, 2016.
- [54] W. H. Furry, “On Transition Probabilities in Double Beta-Disintegration,” *Phys. Rev.*, vol. 56, pp. 1184–1193, 1939.
- [55] J. Schechter and J. W. F. Valle, “Neutrinoless Double- β Decay in $SU(2) \times U(1)$ Theories,” *Phys. Rev. D*, vol. 25, pp. 2951–2954, 1982.
- [56] E. Takasugi, “Can the Neutrinoless Double Beta Decay Take Place in the Case of Dirac Neutrinos?” *Phys. Lett. B*, vol. 149, pp. 372–376, 1984.

- [57] B. von Krosigk, “Measurement of Proton and α Particle Quenching in LAB Based Scintillators and Determination of Spectral Sensitivities to Supernova Neutrinos in the SNO+ Detector,” Ph.D. dissertation, Technischen Universität Dresden, 2015.
- [58] J. Engel and J. Menndez, “Status and Future of Nuclear Matrix Elements for Neutrinoless Double-Beta Decay: A Review,” *Rept. Prog. Phys.*, vol. 80, p. 046 301, 2017.
- [59] F. T. Avignone, S. R. Elliot, and J. Engel, “Double Beta Decay, Majorana Neutrinos, and Neutrino Mass,” *Rev. Mod. Phys.*, vol. 80, p. 481, 2008.
- [60] T. R. Rodriguez and G. Martinez-Pinedo, “Energy Density Functional Study of Nuclear Matrix Elements for Neutrinoless $\beta\beta$ decay,” *Phys. Rev. Lett.*, vol. 105, p. 252 503, 2010.
- [61] A. Bobyk, W. A. Kaminski, and F. Simkovic, “Neutrinoless Double-Beta Decay within Self-Consistent Renormalized Quasiparticle Random Phase Approximation and Inclusion of Induced Nucleon Currents,” *Phys. Rev. C*, vol. 63, p. 051 301, 2001.
- [62] J. Barea and F. Iachello, “Neutrinoless Double-Beta Decay in the Microscopic Interacting Boson Model,” *Phys. Rev. C*, vol. 79, p. 044 301, 2009.
- [63] J. Menendez *et al.*, “Disassembling the Nuclear Matrix Elements of the Neutrinoless beta beta Decay,” *Nucl. Phys. A*, vol. 818, pp. 139–151, 2009.
- [64] P. K. Rath *et al.*, “Uncertainties in Nuclear Transition Matrix Elements for Neutrinoless $\beta\beta$ Decay within the PHFB Model,” *Phys. Rev. C*, vol. 82, p. 064 310, 2010.
- [65] KamLAND-Zen Collaboration, “Search for Majorana Neutrinos Near the Inverted Mass Hierarchy Region with KamLAND-Zen,” *Phys. Rev. Lett.*, vol. 117, p. 082 503, 2016.
- [66] NEMO-3 and SuperNEMO Collaboration, “Latest Results of NEMO-3 Experiment and Present Status of SuperNEMO,” *Nucl. Part. Phys. Proc.*, vol. 273–275, pp. 1765–1770, 2016.
- [67] GERDA Collaboration, “Probing Majorana Neutrinos with Double- β Decay,” *Science*, vol. 365, pp. 1445–1448, 2019.
- [68] CUORE Collaboration, “New Results from the CUORE Experiment,” *Proc. Sci.*, vol. 390, pp. 13–22, 2021.
- [69] S. D. Biller, “Probing Majorana Neutrinos in the Regime of the Normal Mass Hierarchy,” *Phys. Rev. D*, vol. 87, p. 071 301, 2013.

- [70] S. M. Bilenky and C. Giunti, “Neutrinoless Double-Beta Decay. A Brief Review,” *Mod. Phys. Lett. A*, vol. 27, p. 1230015, 2012.
- [71] A. N. Cox, “Allen’s Astrophysical Quantities,” in Springer, New York, 2002, p. 648.
- [72] The XXVIII General Assembly of the International Astronomical Union, “Resolution B2 on the Re-Definition of the Astronomical Unit of Length,” 2012.
- [73] W. D. Arnett, J. N. Bahcall, R. P. Kirshner, and S. E. Woosley, “Supernova 1987A,” *Annu. Rev. Astron. Astrophys.*, vol. 27, pp. 629–700, 1989.
- [74] A. Mirizzi *et al.*, “Supernova Neutrinos: Production, Oscillations and Detection,” *Riv. Nuovo Cim.*, vol. 39, pp. 1–112, 2016. arXiv: 1508 . 00785 [astro-ph.HE].
- [75] E. N. Alexeyev *et al.*, “Detection of the Neutrino Signal from SN1987A using the INR Baksan Underground Scintillation Telescope,” *Phys. Lett. B*, vol. 205, pp. 209–214, 1988.
- [76] K. Hirata *et al.*, “Observation of a Neutrino Burst from the Supernova SN1987A,” *Phys. Rev. Lett.*, vol. 58, pp. 1490–1493, 1987.
- [77] R. Svoboda *et al.*, “Neutrinos from SN1987a in the IMB Detector,” *Nucl. Instrum. Meth. A*, vol. 264, pp. 28–31, 1988.
- [78] Garching Core Collapse Archive, [Online]. Available: <https://wwwmpa.mpa-garching.mpg.de/ccsnarchive/archive.html> (visited on 01/01/2020).
- [79] C. J. Hansen, S. D. Kawaler, and V. Trimble, *Stellar Interiors: Physical Principles, Structure, and Evolution*, ser. Astronomy and Astrophysics Library. Springer, New York, 2004.
- [80] E. Hertzsprung, “Über die Verwendung Photographischer Effektiver Wellenlaengen zur Bestimmung von Farbenaequivalenten,” *Publikationen des Astrophysikalischen Observatoriums zu Potsdam*, vol. 22, no. 63, A1–A40, 1911.
- [81] H. N. Russell, “Relations Between the Spectra and Other Characteristics of the Stars,” *Pop. Astron.*, vol. 22, pp. 275–294, 1914.
- [82] G. Laughlin, P. Bodenheimer, and F. C. Adams, “The End of the Main Sequence,” *Astrophys. J.*, vol. 482, p. 420, 1997.
- [83] F. J. Ballesteros, “New Insights into Black Bodies,” *Europhys. Lett.*, vol. 97, p. 34008, 2012.
- [84] W. Dehnen and J. J. Binney, “Local Stellar Kinematics from Hipparcos Data,” *Mon. Not. R. Astron. Soc.*, vol. 298, pp. 387–394, 1998.

- [85] M. Salaris and S. Cassisi, “Evolution of Stars and Stellar Populations,” in John Wiley & Sons, Ltd, 2005, p. 187.
- [86] H. J. G. L. M. Lamers and E. M. Levesque, “Understanding Stellar Evolution,” in IOP Publishing, 2017, pp. 18–13.
- [87] S. Chandrasekhar, “The Maximum Mass of Ideal White Dwarfs,” *Astrophys. J.*, vol. 74, p. 81, 1931.
- [88] S. Chandrasekhar, “On Stars, Their Evolution and Their Stability,” *Science*, vol. 226, pp. 497–505, 1984.
- [89] J. Th. van Loon, “On the Metallicity Dependence of the Winds from Red Supergiants and Asymptotic Giant Branch Stars,” in *Stellar Evolution at Low Metallicity: Mass Loss, Explosions, Cosmology*, ser. Astronomical Society of the Pacific Conference Series, vol. 353, Astronomical Society of the Pacific, 2006, p. 211. arXiv: astro-ph/0512326 [astro-ph].
- [90] C. L. Fryer, S. E. Woosley, and A. Heger, “Pair Instability Supernovae, Gravity Waves, and Gamma-Ray Transients,” *Astrophys. J.*, vol. 550, pp. 372–382, 2001.
- [91] S. E. Woosley, A. Heger, and T. A. Weaver, “The Evolution and Explosion of Massive Stars,” *Rev. Mod. Phys.*, vol. 74, pp. 1015–1071, 2002.
- [92] S. E. Woosley, S. Blinnikov, and A. Heger, “Pulsational Pair Instability as an Explanation for the Most Luminous Supernovae,” *Nature*, vol. 450, p. 390, 2007.
- [93] A. Heger *et al.*, “How Massive Single Stars End Their Life,” *Astrophys. J.*, vol. 591, pp. 288–300, 2003.
- [94] K. Nomoto, M. Tanaka, N. Tominaga, and K. Maeda, “Hypernovae, Gamma-Ray Bursts, and First Stars,” *New Astron. Rev.*, vol. 54, pp. 191–200, 2010.
- [95] G. J. Peters and R. Hirschi, “The Evolution of High-Mass Stars,” in *Planets, Stars and Stellar Systems*, Springer, Dordrecht, 2013, pp. 447–484.
- [96] D. Branch, “Spectra of Supernovae,” in *Supernovae*, ser. Astronomy and Astrophysics Library, Springer, New York, 1990, pp. 30–58.
- [97] E. Cappellaro and M. Turatto, “Supernova Types and Rates,” in *The Influence of Binaries on Stellar Population Studies*, ser. Astrophysics and Space Science Library, vol. 264, Springer, Dordrecht, 2001, pp. 199–214. arXiv: astro-ph/0012455 [astro-ph].
- [98] A. Gal-Yam, “Observational and Physical Classification of Supernovae,” in *Handbook of Supernovae*, Springer, Cham, 2017, pp. 195–237. arXiv: 1611.09353 [astro-ph.HE].

-
- [99] R. Minkowski, “Spectra of Supernovae,” *Publ. Astron. Soc. Pac.*, vol. 53, no. 314, p. 224, 1941.
 - [100] D. B. McLaughlin, “The Spectrum of the Supernova of 1954 in NGC 4214,” *Publ. Astron. Soc. Pac.*, vol. 75, no. 443, p. 133, 1963.
 - [101] J. H. Elias, K. Matthews, G. Neugebauer, and S. E. Persson, “Type I Supernovae in the Infrared and Their Use as Distance Indicators,” *Astrophys. J.*, vol. 296, pp. 379–389, 1985.
 - [102] D. Branch, “On the Relative Frequencies of the Kinds of Type I Supernovae,” *Astrophys. J. Lett.*, vol. 300, pp. L51–L54, 1986.
 - [103] J. C. Wheeler and R. P. Harkness, “Physical Models of Supernovae and the Distance Scale,” in *Galaxy Distances and Deviations from Universal Expansion*, ser. NATO ASI Series (Series C: Mathematical and Physical Sciences), vol. 180, Springer, Dordrecht, 1986, pp. 45–54.
 - [104] R. Barbon, F. Ciatti, and L. Rosino, “Photometric Properties of Type II Supernovae,” *Astron. Astrophys.*, vol. 72, pp. 287–292, 1979.
 - [105] A. Clocchiatti *et al.*, “A Study of SN 1992H in NGC 5377,” *Astron. J.*, vol. 111, p. 1286, 1996.
 - [106] A. Pastorello *et al.*, “Low-Luminosity Type II Supernovae: Spectroscopic and Photometric Evolution,” *Mon. Not. R. Astron. Soc.*, vol. 347, p. 74, 2004.
 - [107] A. V. Filippenko, “Supernova 1987K: Type II in Youth, Type Ib in Old Age,” *Astron. J.*, vol. 96, p. 1941, 1988.
 - [108] E. M. Schlegel, “A New Subclass of Type II Supernovae?” *Mon. Not. R. Astron. Soc.*, vol. 244, pp. 269–271, 1990.
 - [109] J. B. Doggett and D. Branch, “A Comparative Study of Supernova Light Curves,” *Astron. J.*, vol. 90, pp. 2303–2311, 1985.
 - [110] A. Burrows and D. Vartanyan, “Core-Collapse Supernova Explosion Theory,” *Nature*, vol. 589, p. 29, 2021.
 - [111] H. T. Janka, “Explosion Mechanisms of Core-Collapse Supernovae,” *Annu. Rev. Nucl. Part. Sci.*, vol. 62, pp. 407–451, 2012.
 - [112] E. O’Connor and C. D. Ott, “Black Hole Formation in Failing Core-Collapse Supernovae,” *Astrophys. J.*, vol. 730, p. 70, 2011.
 - [113] A. Kumar, “A Textbook Of Inorganic Chemistry,” in New Age International, 2007, p. 719.
 - [114] H. T. Janka *et al.*, “Theory of Core-Collapse Supernovae,” *Phys. Rept.*, vol. 442, pp. 38–74, 2007.

- [115] C. Iliadis and A. Champagne, “Review and Experiments on Nuclear Astrophysics,” *Proc. Sci.*, vol. GSSI 14, p. 009, 2015.
- [116] T. Rauscher and A. Patkós, “Origin of the Chemical Elements,” in *Handbook of Nuclear Chemistry*, Springer, Boston, MA, 2011, pp. 611–665.
- [117] H. T. Janka, “Neutrino Emission from Supernovae,” in *Handbook of Supernovae*, Springer, Cham, 2016, pp. 1–30.
- [118] Y. Suwa, “Neutrino Acceleration by Bulk Matter Motion and Explosion Mechanism of Gamma-ray Bursts,” *Mon. Not. R. Astron. Soc.*, vol. 428, pp. 2443–2449, 2013.
- [119] T. Fischer *et al.*, “Protoneutron Star Evolution and the Neutrino Driven Wind in General Relativistic Neutrino Radiation Hydrodynamics Simulations,” *Astron. Astrophys.*, vol. 517, A80, 2010.
- [120] R. Buras, M. Rampp, H. T. Janka, and K. Kifonidis, “Two-Dimensional Hydrodynamic Core-Collapse Supernova Simulations with Spectral Neutrino Transport. I. Numerical Method and Results for a $15 M_{\odot}$ Star,” *Astron. Astrophys.*, vol. 447, pp. 1049–1092, 2006.
- [121] E. O’Connor and C. Ott, “The Progenitor Dependence of the Pre-Explosion Neutrino Emission in Core-Collapse Supernovae,” *Astrophys. J.*, vol. 762, p. 126, 2013.
- [122] R. C. Tolman, “”Static Solutions of Einstein’s Field Equations for Spheres of Fluid”,” *Phys. Rev.*, vol. 55, pp. 364–373, 1939.
- [123] J. R. Oppenheimer and G. M. Volkoff, “On Massive Neutron Cores,” *Phys. Rev.*, vol. 55, pp. 374–381, 1939.
- [124] S. Mineshige *et al.*, “Black Hole Disk Accretion in Supernovae,” *Astrophys. J.*, vol. 489, p. 227, 1997.
- [125] M. T. Keil, G. G. Raffelt, and H. T. Janka, “Monte Carlo Study of Supernova Neutrino Spectra Formation,” *Astrophys. J.*, vol. 590, pp. 971–991, 2003.
- [126] H. T. Janka *et al.*, “Core-Collapse Supernovae: Reflections and Directions,” *Prog. Theor. Exp. Phys.*, vol. 2012, A309, 2012.
- [127] S. Fujibayashi, K. Takahashi, Y. Sekiguchi, and M. Shibata, “Ultra-Delayed Neutrino-Driven Explosion of Rotating Massive-star Collapse,” *Astrophys. J.*, vol. 919, p. 80, 2021.
- [128] K. Nomoto, “Evolution of 8-10 Solar Mass Stars Toward Electron Capture Supernovae. II - Collapse of an O + Ne + Mg Core,” *Astrophys. J.*, vol. 322, pp. 206–214, 1987.

-
- [129] K. Takahashi, T. Yoshida, and H. Umeda, “Evolution of Progenitors for Electron Capture Supernovae,” *Astrophys. J.*, vol. 771, p. 28, 2013.
 - [130] A. J. T. Poelarends, F. Herwig, N. Langer, and A. Heger, “The Supernova Channel of Super-AGB Stars,” *Astrophys. J.*, vol. 675, p. 614, 2008.
 - [131] S. Wanajo *et al.*, “Nucleosynthesis in Electron Capture Supernovae of AGB Stars,” *Astrophys. J.*, vol. 695, pp. 208–220, 2009.
 - [132] L. Hüdepohl *et al.*, “Neutrino Signal of Electron-Capture Supernovae from Core Collapse to Cooling,” *Phys. Rev. Lett.*, vol. 104, p. 251101, 2010.
 - [133] G. Rakavy and G. Shaviv, “Instabilities in Highly Evolved Stellar Models,” *Astrophys. J.*, vol. 148, p. 803, 1967.
 - [134] A. Heger and S. E. Woosley, “The Nucleosynthetic Signature of Population III,” *Astrophys. J.*, vol. 567, pp. 532–543, 2002.
 - [135] E. Cappellaro, R. Barbon, and M. Turatto, “Supernova Statistics,” in *Cosmic Explosions*, ser. Springer Proceedings in Physics, vol. 99, Springer, Berlin, Heidelberg, 2005, pp. 347–354.
 - [136] LSST Collaboration, “LSST Science Book, Version 2.0,” 2009. arXiv: 0912.0201 [astro-ph.IM].
 - [137] J. Vink, “Supernova 1604, Kepler’s Supernova, and Its Remnant,” in *Handbook of Supernovae*, Springer, Cham, 2016, pp. 1–22.
 - [138] S. Adams *et al.*, “Observing the Next Galactic Supernova,” *Astrophys. J.*, vol. 778, p. 164, 2013.
 - [139] B. Dasgupta and J. F. Beacom, “Reconstruction of Supernova ν_μ , ν_τ , anti- ν_μ , and anti- ν_τ Neutrino Spectra at Scintillator Detectors,” *Phys. Rev. D*, vol. 83, p. 113006, 2011.
 - [140] D. Vaananen and C. Volpe, “The Neutrino Signal at HALO: Learning About the Primary Supernova Neutrino Fluxes and Neutrino Properties,” *J. Cosmol. Astropart. Phys.*, vol. 1110, p. 019, 2011.
 - [141] C. Lujan-Peschard, G. Pagliaroli, and F. Vissani, “Spectrum of Supernova Neutrinos in Ultra-pure Scintillators,” *J. Cosmol. Astropart. Phys.*, vol. 1407, p. 051, 2014.
 - [142] B. Müller, H. T. Janka, and H. Dimmelmeier, “A New Multi-dimensional General Relativistic Neutrino Hydrodynamics Code for Core-Collapse Supernovae. I. Method and Code Tests in Spherical Symmetry,” *Astrophys. J. Suppl.*, vol. 189, pp. 104–133, 2010.

-
- [143] P. D. Serpico *et al.*, “Probing the Neutrino Mass Hierarchy with the Rise Time of a Supernova Burst,” *Phys. Rev. D*, vol. 85, p. 085 031, 2012.
 - [144] S. E. Woosley and T. A. Weaver, “The Evolution and Explosion of Massive Stars. II. Explosive Hydrodynamics and Nucleosynthesis,” *Astrophys. J. Suppl.*, vol. 101, p. 181, 1995.
 - [145] J. R. Stone, N. J. Stone, and S. A. Moszkowski, “Incompressibility in Finite Nuclei and Nuclear Matter,” *Phys. Rev. C*, vol. 89, p. 044 316, 2014.
 - [146] A. Z. Mekjian, S. J. Lee, and L. Zamick, “Nuclear Incompressibility at Finite Temperature and Entropy,” *Phys. Lett. B*, vol. 621, p. 239, 2005.
 - [147] J. M. Lattimer and F. D. Swesty, “A Generalized Equation of State for Hot, Dense Matter,” *Nucl. Phys. A*, vol. 535, pp. 331–376, 1991.
 - [148] H. Shen, H. Toki, K. Oyamatsu, and K. Sumiyoshi, “Relativistic Equation of State of Nuclear Matter for Supernova and Neutron Star,” *Nucl. Phys. A*, vol. 637, pp. 435–450, 1998.
 - [149] M. B. Aufderheide, E. Baron, and F. K. Thielemann, “Shock Waves and Nucleosynthesis in Type II Supernovae,” *Astrophys. J.*, vol. 370, p. 630, 1991.
 - [150] M. Ugliano, H. T. Janka, A. Marek, and A. Arcones, “Progenitor-Explosion Connection and Remnant Birth Masses for Neutrino-driven Supernovae of Iron-core Progenitors,” *Astrophys. J.*, vol. 757, p. 69, 2012.
 - [151] G. V. Domogatsky, R. A. Eramzhian, and D. K. Nadezhin, “Production of the Light Elements due to Neutrinos Emitted by Collapsing Stellar Cores,” *Astrophys. Space Sci.*, vol. 58, pp. 273–299, 1978.
 - [152] H. T. Janka and W. Hillebrandt, “Neutrino Emission from Type II Supernovae - An Analysis of the Spectra,” *Astron. Astrophys.*, vol. 224, pp. 49–56, 1989.
 - [153] E. S. Myra, J. M. Lattimer, and A. Yahil, “Neutrino Emission from Cooling Neutron Stars,” in *Supernova 1987A in the Large Magellanic Cloud*, Cambridge University Press, 1988, pp. 213–216.
 - [154] P. M. Giovanoni, D. C. Ellison, and S. W. Bruenn, “Neutrino Transport during the Core Bounce Phase of a Type II Supernova Explosion,” *Astrophys. J.*, vol. 342, p. 416, 1989.
 - [155] G. G. Raffelt, “Mu- and Tau-Neutrino Spectra Formation in Supernovae,” *Astrophys. J.*, vol. 561, p. 890, 2001.
 - [156] SNO Collaboration, “The Sudbury Neutrino Observatory,” *Nucl. Instrum. Meth. A*, vol. 449, pp. 172–207, 2000.

- [157] SNO+ Collaboration, “The SNO+ Experiment,” *J. Instrum.*, vol. 16, P08059, 2021.
- [158] P. K. F. Grieder, “Cosmic Rays at Earth: Researcher’s Reference Manual and Data Book,” in Gulf Professional Publishing, 2001, p. 482.
- [159] Cepsa, “PETRELAB 500-Q, C10-C13 Linear Alkylbenzene (LAB),” 2019. [Online]. Available: https://chemicals.cepsa.com/stfls/chemicals/Ficheros/PETRELAB_500_Q_Cepsa_Eng.pdf.
- [160] J. Rumleskie, “SNO+ Sensitivities to Pre-supernova and Supernova Neutrinos,” Ph.D. dissertation, Laurentian University, 2021.
- [161] SNO+ Collaboration, “Measurement of the ^8B Solar Neutrino Flux in SNO+ with Very Low Backgrounds,” *Phys. Rev. D*, vol. 99, p. 012012, 2019.
- [162] Borexino Collaboration, “The Liquid Handling Systems for the Borexino Solar Neutrino Detector,” *Nucl. Instrum. Meth. A*, vol. 609, pp. 58–78, 2009.
- [163] Borexino Collaboration, “Comprehensive Measurement of pp-Chain Solar Neutrinos,” *Nature*, vol. 562, pp. 505–510, 2018.
- [164] M. Stringer, “Sensitivity of SNO+ to Supernova Neutrinos,” Ph.D. dissertation, University of Sussex, 2018.
- [165] T. Kaptanoglu, “TeDiol (0.5%) Double Beta Counting Analysis,” 2019. SNO+ DocDB: 5009-v3.
- [166] C. Alduino *et al.*, “Measurement of the Two-Neutrino Double-Beta Decay Half-Life of ^{130}Te with the CUORE-0 Experiment,” *Eur. Phys. J. C*, vol. 77, p. 13, 2017.
- [167] J. Argyriades *et al.*, “Measurement of the Double Beta Decay Half-life of Nd-150 and Search for Neutrinoless Decay Modes with the NEMO-3 Detector,” *Phys. Rev. C*, vol. 80, p. 032501, 2009.
- [168] S. J. Brice *et al.*, “Photomultiplier Tubes in the MiniBooNE Experiment,” *Nucl. Instrum. Meth. A*, vol. 562, pp. 97–109, 2006.
- [169] G. Doucas *et al.*, “Light Concentrators for the Sudbury Neutrino Observatory,” *Nucl. Instrum. Meth. A*, vol. 370, pp. 579–596, 1996.
- [170] G. D. O. Gann, “Dealing With Time in RAT,” 2010. SNO+ DocDB: 481-v2.
- [171] GridPP Collaboration, “GridPP: Development of the UK Computing Grid for Particle Physics,” *J. Phys. G*, vol. 32, N1, 2005.
- [172] I. Antcheva *et al.*, “ROOT - A C++ Framework for Petabyte Data Storage, Statistical Analysis and Visualization,” *Comput. Phys. Commun.*, vol. 180, pp. 2499–2512, 2009.

- [173] I. Coulter, “Modelling and Reconstruction of Events in SNO+ Related to Future Searches for Lepton and Baryon Number Violation,” Ph.D. dissertation, University of Oxford, 2013.
- [174] RAT, [Online]. Available: <https://rat.readthedocs.io/en/latest/overview.html> (visited on 01/01/2022).
- [175] GEANT4 Collaboration, “GEANT4 - A Simulation Toolkit,” *Nucl. Instrum. Meth. A*, vol. 506, pp. 250–303, 2003.
- [176] GLG4sim, [Online]. Available: <https://www.phys.ksu.edu/personal/gahs/GLG4sim/> (visited on 01/01/2022).
- [177] M. de Bruin, “Glossary of Terms Used in Nuclear Analytical Chemistry,” *Pure Appl. Chem.*, vol. 54, pp. 1533–1554, 1982.
- [178] J. Hu, “Test the Partial Fitter When the Scintillator Filling is Near Completion,” 2021. SNO+ DocDB: 6813-v2.
- [179] I. Morton-Blake, “Scintillator Supported ^{222}Rn Concentration Measurement,” 2021. SNO+ DocDB: 6886-v1.
- [180] I. Morton-blake, “First Measurement of Reactor Antineutrinos in Scintillator at SNO+ and Study of Alternative Designs for Large-Scale Liquid Scintillator Detectors,” Ph.D. dissertation, University of Oxford, 2021.
- [181] S. Abe *et al.*, “Precision Measurement of Neutrino Oscillation Parameters with KamLAND,” *Phys. Rev. Lett.*, vol. 100, p. 221803, 2008.
- [182] G. Bellini *et al.*, “Observation of Geo-Neutrinos,” *Phys. Lett. B*, vol. 687, pp. 299–304, 2010.
- [183] J. F. Beacom, W. M. Farr, and P. Vogel, “Detection of Supernova Neutrinos by Neutrino-Proton Elastic Scattering,” *Phys. Rev. D*, vol. 66, p. 033001, 2002.
- [184] L. A. Ahrens *et al.*, “Measurement of Neutrino - Proton and Anti-Neutrino - Proton Elastic Scattering,” *Phys. Rev. D*, vol. 35, p. 785, 1987.
- [185] KARMEN Collaboration, “Measurement of the Weak Neutral Current Excitation $^{12}\text{C}(\nu, \nu')^{12}\text{C}^*$ (15.1 MeV) at $E(\nu) = 29.8$ MeV,” *Phys. Lett. B*, vol. 423, pp. 15–20, 1998.
- [186] T. Yoshida *et al.*, “Neutrino-Nucleus Reaction Cross Sections for Light Element Synthesis in Supernova Explosions,” *Astrophys. J.*, vol. 686, pp. 448–466, 2008.
- [187] E. Kolbe, K. Langanke, S. Krewald, and F. K. Thielemann, “Inelastic Neutrino Scattering on ^{12}C and ^{16}O Above the Particle Emission Threshold,” *Nuclear Physics A*, vol. 540, no. 3, pp. 599–620, 1992.

-
- [188] S. E. Woosley, D. H. Hartmann, R. D. Hoffman, and W. C. Haxton, “The ν -Process,” *Astrophys. J.*, vol. 356, p. 272, 1990.
 - [189] P. Antonioli *et al.*, “SNEWS: the SuperNova Early Warning System,” *New J. Phys.*, vol. 6, p. 114, 2004.
 - [190] C. J. Virtue, “SNO and Supernovae,” *Nucl. Phys. Proc. Suppl.*, vol. 100, pp. 326–331, 2001.
 - [191] SNO Collaboration, “Low-Multiplicity Burst Search at the Sudbury Neutrino Observatory,” *Astrophys. J.*, vol. 728, p. 83, 2011.
 - [192] J. F. Beacom and P. Vogel, “Can a Supernova be Located by Its Neutrinos?” *Phys. Rev. D*, vol. 60, p. 033 007, 1999.
 - [193] K. Abe *et al.*, “Real-Time Supernova Neutrino Burst Monitor at Super-Kamiokande,” *Astropart. Phys.*, vol. 81, pp. 39–48, 2016.
 - [194] B. P. Abbott *et al.*, “Multi-Messenger Observations of a Binary Neutron Star Merger,” *Astrophys. J. Lett.*, vol. 848, p. L12, 2017.
 - [195] M. G. Aartsen *et al.*, “Multi-Messenger Observations of a Flaring Blazar Coincident with High-Energy Neutrino IceCube-170922A,” *Science*, vol. 361, eaat378, 2018.
 - [196] N. B. Linzer and K. Scholberg, “Triangulation Pointing to Core-Collapse Supernovae with Next-Generation Neutrino Detectors,” *Phys. Rev. D*, vol. 100, p. 103 005, 2019.
 - [197] A. Coleiro *et al.*, “Combining Neutrino Experimental Light-Curves for Pointing to the Next Galactic Core-Collapse Supernova,” *Eur. Phys. J. C*, vol. 80, p. 856, 2020.
 - [198] R. V. Hogg and A. T. Craig, *Introduction to Mathematical Statistics*, 4th ed. Macmillan, New York, 1978.
 - [199] V. Brdar, M. Lindner, and X. Xu, “Neutrino Astronomy with Supernova Neutrinos,” *J. Cosmol. Astropart. Phys.*, vol. 1804, p. 025, 2018.
 - [200] L. Hüdepohl, “Neutrinos from the Formation, Cooling and Black Hole Collapse of Neutron Stars,” Ph.D. dissertation, Technische Universität München, 2014.
 - [201] SNOWGLOBES, [Online]. Available: <http://www.phy.duke.edu/schol/snowglobes> (visited on 01/01/2019).
 - [202] M. He, “Double Calorimetry System in JUNO,” 2017. arXiv: 1706.08761 [physics.ins-det].
 - [203] Y. Suzuki, “The Super-Kamiokande Experiment,” *Eur. Phys. J. C*, vol. 79, p. 298, 2019.

-
- [204] J. F. Beacom and M. R. Vagins, “GADZOOKS! Antineutrino Spectroscopy with Large Water Cerenkov Detectors,” *Phys. Rev. Lett.*, vol. 93, p. 171 101, 2004.
 - [205] F. An *et al.*, “Neutrino Physics with JUNO,” *J. Phys. G*, vol. 43, p. 030 401, 2016.
 - [206] M. Leyton and S. Dye, “Prospects for Long-Range Reactor Monitoring with Gadolinium-Loaded Water-Cherenkov Detectors,” 2018. arXiv: 1804 . 03696 [physics.ins-det].
 - [207] M. A. Podurets, “Asymptotic Behavior of the Optical Luminosity of a Star in Gravitational Collapse,” *Astr. Zh.*, vol. 41, p. 1090, 1964, [Sov. Astr. **8**, 868 (1965)].
 - [208] Ya. B. Zel'Dovich and I. D. Novikov, “Relativistic Astrophysics. I.,” *Usp. Fiz. Nauk*, vol. 84, p. 377, 1964, [Sov. Phys. Usp. **7**, 763 (1965)].
 - [209] W. L. Ames and K. S. Thorne, “The Optical Appearance of a Star that is Collapsing through its Gravitational Radius,” *Astrophys. J.*, vol. 151, p. 659, 1968.
 - [210] J. F. Beacom, R. N. Boyd, and A. Mezzacappa, “Technique for Direct eV Scale Measurements of the Mu and Tau Neutrino Masses using Supernova Neutrinos,” *Phys. Rev. Lett.*, vol. 85, p. 3568, 2000.
 - [211] J. F. Beacom, R. N. Boyd, and A. Mezzacappa, “Black Hole Formation in Core-Collapse Supernovae and Time-of-Flight Measurements of the Neutrino Masses,” *Phys. Rev. D*, vol. 63, p. 073 011, 2001.
 - [212] T. W. Baumgarte *et al.*, “Delayed Collapse of Hot Neutron Stars to Black Holes via Hadronic Phase Transitions,” *Astrophys. J.*, vol. 468, p. 823, 1996.
 - [213] L. Sarfati, R. S. L. Hansen, and I. Tamborra, “Triangulating Black Hole Forming Stellar Collapses through Neutrinos,” 2021. arXiv: 2110 . 02347 [astro-ph.HE].
 - [214] E. O’Connor, “An Open-Source Neutrino Radiation Hydrodynamics Code for Core-Collapse Supernovae,” *Astrophys. J. Suppl.*, vol. 219, p. 24, 2015.
 - [215] L. Walk *et al.*, “Neutrino Emission Characteristics of Black Hole Formation in Three-Dimensional Simulations of Stellar Collapse,” *Phys. Rev. D*, vol. 101, p. 123 013, 2020.
 - [216] K. Lake and R. C. Roeder, “Note on the Optical Appearance of a Star Collapsing through its Gravitational Radius,” *Astrophys. J.*, vol. 232, p. 277, 1979.
 - [217] S. L. Shapiro, “Thermal Radiation from Stellar Collapse to a Black Hole,” *Phys. Rev. D*, vol. 40, p. 1858, 1989.

- [218] S. V. Dhurandhar and C. V. Vishveshwara, “Neutrinos in Gravitational Collapse. I Analysis of Trajectories,” *Astrophys. J.*, vol. 245, p. 1094, 1981.
- [219] S. V. Dhurandhar and C. V. Vishveshwara, “Neutrinos in Gravitational Collapse: Analysis of the Flux Profile,” *Pramana*, vol. 22, p. 159, 1984.
- [220] S. W. Li, L. F. Roberts, and J. F. Beacom, “Exciting Prospects for Detecting Late-Time Neutrinos from Core-Collapse Supernovae,” *Phys. Rev. D*, vol. 103, p. 023016, 2021.
- [221] K. Schwarzschild, “Über das Gravitationsfeld eines Massenpunktes nach der Einsteinschen Theorie,” *Sitzber. K. Preuss. Akad. Wiss. Berlin, Math.-Phys. Kl.*, pp. 189–196, 1916.
- [222] R. M. Wald, *General Relativity*. The University of Chicago Press, Chicago, 1984.
- [223] E. Poisson, “A Relativist’s Toolkit: The Mathematics of Black-Hole Mechanics,” in Cambridge University Press, Cambridge, 2004, p. 189.
- [224] I. I. Shapiro, “Fourth Test to General Relativity,” *Phys. Rev. Lett.*, vol. 13, p. 789, 1964.
- [225] S. Chandrasekhar, “The Mathematical Theory of Black Holes,” in Oxford University Press, New York, 1983, pp. 127–130.
- [226] A. Arcones *et al.*, “Influence of light nuclei on neutrino-driven supernova outflows,” *Phys. Rev. C*, vol. 78, p. 015806, 2008.
- [227] E. O’Connor and C. D. Ott, “A New Open-Source Code for Spherically Symmetric Stellar Collapse to Neutron Stars and Black Holes,” *Classical Quant. Grav.*, vol. 27, p. 114103, 2010.
- [228] S. E. Woosley and A. Heger, “Nucleosynthesis and Remnants in Massive Stars of Solar Metallicity,” *Phys. Rep.*, vol. 442, p. 269, 2007.
- [229] W. H. Lee, E. Ramirez-Ruiz, and D. Page, “Opaque or Transparent? A Link between Neutrino Optical Depths and the Characteristic Duration of Short Gamma-Ray Bursts,” *Astrophys. J.*, vol. 608, p. L5, 2004.
- [230] R. P. Kerr, “Gravitational Field of a Spinning Mass as an Example of Algebraically Special Metrics,” *Phys. Rev. Lett.*, vol. 11, pp. 237–238, 1963.
- [231] R. H. Boyer and R. W. Lindquist, “Maximal Analytic Extension of the Kerr Metric,” *J. Math. Phys.*, vol. 8, p. 265, 1967.
- [232] B. Carter, “Global Structure of the Kerr Family of Gravitational Fields,” *Phys. Rev.*, vol. 174, p. 1559, 1968.

- [233] M. Walker and R. Penrose, “On Quadratic First Integrals of the Geodesic Equations for Type {22} Spacetimes,” *Commun. Math. Phys.*, vol. 18, p. 265, 1970.
- [234] J. M. Bardeen, W. H. Press, and S. A. Teukolsky, “Rotating Black Holes: Locally Nonrotating Frames, Energy Extraction, and Scalar Synchrotron Radiation,” *Astrophys. J.*, vol. 178, p. 347, 1972.
- [235] K. S. Thorne, R. H. Price, and D. A. MacDonald, “Black Holes: the Membrane Paradigm,” in Yale University Press, New Haven, 1986, p. 68.
- [236] T. Igata, K. Kohri, and K. Ogasawara, “Photon Emission from Inside the Innermost Stable Circular Orbit,” *Phys. Rev. D*, vol. 103, p. 104028, 2021.
- [237] K. Ogasawara and T. Igata, “Complete Classification of Photon Escape in the Kerr Black Hole Spacetime,” *Phys. Rev. D*, vol. 103, p. 044029, 2021.
- [238] J. B. Hartle, *Gravity: An Introduction to Einstein’s General Relativity*. Addison-Wesley, San Francisco, 2003.
- [239] S. Gullin, E. O’Connor, J. Wang, and J. Tseng, “Neutrino Echos following Black Hole Formation in Core-Collapse Supernovae,” *Astrophys. J.*, vol. 926, p. 212, 2022. arXiv: 2109.13242 [astro-ph.HE and gr-qc].
- [240] Y. Fukuda *et al.*, “The Super-Kamiokande Detector,” *Nucl. Instrum. Meth. A*, vol. 501, pp. 418–462, 2003.
- [241] K. Abe *et al.*, “Hyper-Kamiokande Design Report,” 2018. arXiv: 1805.04163 [physics.ins-det].
- [242] P. Podsiadlowski, “Supernovae and Gamma-Ray Bursts,” in *Planets, Stars and Stellar Systems Volume 4: Stellar Structure and Evolution*, Springer, Dordrecht, 2013, pp. 693–733.